NEW PHOTONIC DEVICES BASED ON NLO(NON-LINEAR OPTICAL) CRYSTALLINE WAVEGUIDES

Muhammad Ali Butt

ADVERTIMENT. L'accés als continguts d'aquesta tesi doctoral i la seva utilització ha de respectar els drets de la persona autora. Pot ser utilitzada per a consulta o estudi personal, així com en activitats o materials d'investigació i docència en els termes establerts a l'art. 32 del Text Refós de la Llei de Propietat Intel·lectual (RDL 1/1996). Per altres utilitzacions es requereix l'autorització prèvia i expressa de la persona autora. En qualsevol cas, en la utilització dels seus continguts caldrà indicar de forma clara el nom i cognoms de la persona autora i el títol de la tesi doctoral. No s'autoritza la seva reproducció o altres formes d'explotació efectuades amb finalitats de lucre ni la seva comunicació pública des d'un lloc aliè al servei TDX. Tampoc s'autoritza la presentació del seu contingut en una finestra o marc aliè a TDX (framing). Aquesta reserva de drets afecta tant als continguts de la tesi com als seus resums i índexs.

ADVERTENCIA. El acceso a los contenidos de esta tesis doctoral y su utilización debe respetar los derechos de la persona autora. Puede ser utilizada para consulta o estudio personal, así como en actividades o materiales de investigación y docencia en los términos establecidos en el art. 32 del Texto Refundido de la Ley de Propiedad Intelectual (RDL 1/1996). Para otros usos se requiere la autorización previa y expresa de la persona autora. En cualquier caso, en la utilización de sus contenidos se deberá indicar de forma clara el nombre y apellidos de la persona autora y el título de la tesis doctoral. No se autoriza su reproducción u otras formas de explotación efectuadas con fines lucrativos ni su comunicación pública desde un sitio ajeno al servicio TDR. Tampoco se autoriza la presentación de su contenido en una ventana o marco ajeno a TDR (framing). Esta reserva de derechos afecta tanto al contenido de la tesis como a sus resúmenes e índices.

WARNING. Access to the contents of this doctoral thesis and its use must respect the rights of the author. It can be used for reference or private study, as well as research and learning activities or materials in the terms established by the 32nd article of the Spanish Consolidated Copyright Act (RDL 1/1996). Express and previous authorization of the author is required for any other uses. In any case, when using its content, full name of the author and title of the thesis must be clearly indicated. Reproduction or other forms of for profit use or public communication from outside TDX service is not allowed. Presentation of its content in a window or frame external to TDX (framing) is not authorized either. These rights affect both the content of the thesis and its abstracts and indexes.

Muhammad Ali Butt

New photonic devices based on NLO (non-linear optical) crystalline waveguides

DOCTORAL THESIS

Supervised by
Dr. Rosa Maria Solé Cartañà
and
Dr. Maria Cinta Pujol Baiges

Departament de Química Física i Inorgànica
Física i Cristal·lografia de Materials i Nanomaterials

UNIVERSITAT ROVIRA I VIRGILI

Tarragona
2015

New photonic devices based on NLO (non-linear optical) crystalline waveguides

Muhammad Ali Butt

© Muhammad Ali Butt, 2015

Física i Cristal.lografia de Materials i Nanomaterials (FICMA-FICNA)

Departament de Química Física i Inorgànica

Universitat Rovira i Virgili

C/Marcellí Domingo, s/n

E-43007, Tarragona, Spain

DEPARTAMENT DE QUÍMICA FÍSICA
I INORGÀNICA

Campus Sescelades
Marcel·lí Domingo, s/n
43007 Tarragona
Tel. +34 977 55 81 37
Fax +34 977 55 95 63
www.quimica.urv.es

FAIG CONSTAR que aquest treball, titulat *"New photonic devices based on NLO(non-linear optical) crystalline waveguides"*, que presenta Muhammad Ali Butt per a l'obtenció del títol de Doctor, ha estat realitzat sota la meva direcció al Departament de Química Física i Inorgànica d'aquesta universitat.

Tarragona, 6 de febrer de 2015

Les directores de la tesis doctoral

Dra. Maria Cinta Pujol Baiges

Dra. Rosa Maria Solé Cartañà

UNIVERSITAT ROVIRA I VIRGILI
NEW PHOTONIC DEVICES BASED ON NLO(NON-LINEAR OPTICAL) CRYSTALLINE WAVEGUIDES
Muhammad Ali Butt

Abstract

$RbTiOPO_4$ (RTP) belongs to the non-centrosymmetric $KTiOPO_4$ (KTP) family of the non-linear optical crystals. It has high electro-optic coefficients and its optical damage threshold (approximately 1.8 GW/cm^2 for pulses with duration of 10 ns at 1064 nm) is twice as high as that of KTP crystals. These characteristics make it interesting for electro-optic applications such as modulators. Liquid phase epitaxial growth method can be used to obtain high quality step-index single crystal epitaxial systems, by adequate selection of the chemical composition of the epitaxial layer and the substrate. These step-index systems can be used as optical waveguides, which are the basic element of the integrated photonics (IP).

The aim of this doctoral thesis is to explore the use of RTP single crystal as a platform for the integrated photonics. Other isostructural materials such as K-doped RTP and Na-doped KTP are also studied in order to explore new KTP materials as a platform of IP. The thesis also focuses on the development of straight channel waveguides, Y-splitters and Mach-zehnder (MZ) structures on the (Yb,Nb):RTP/RTP(001) epitaxial systems by using chemical etching. The above mentioned waveguide structures are also fabricated in RTP (001) by Cs^+ ion exchange method, which reduces the cost at the ease of fabrication. The fabricated waveguides guide successfully visible and infrared wavelengths. Single mode guiding in MZ structures at 1550 nm has been obtained, which can be potentially used as a future sensor and/or EO modulator platform. The emphasis is given on 1550 nm which is the telecommunication wavelength.

Keywords: Crystal growth, Epitaxial growth, Rubidium Titanyl Phosphate, Mach-Zehnder, Reactive Ion etching, Inductively coupled plasma-Reactive ion etching, Ion exchange, channel waveguides, Integrated optics.

Preface

The Ph.D. investigation contained in this thesis has been carried out at the group of Física i Cristal·lografia de Materials i Nanomaterials (FiCMA-FiCNA) at the Departament de Química Física i Inorgànica of the Universitat Rovira i Virgili in Tarragona (Spain), and was supervised by Dr. Rosa Maria Solé and Dr. Maria Cinta Pujol.
This thesis has also involved active collaboration with: Departamento de Física de Materiales, led by Prof. Dr. Ginés Lifante at the Universidad Autónoma de Madrid, (Spain) and Optoelectronics Research Centre, group led by Prof. Dr. James S. Wilkinson at the University of Southampton, (UK).

This work was financed by the Spanish Government under Projects MAT2011-29255-C02-02, MAT2013-47395-C4-4-R and by the Catalan Authority under Projects 2009SGR235, 2014SGR1358. M. Ali Butt thanks the Catalan Government for the FI-DGR fellowship 2012FI-B 00192.

Muhammad Ali Butt
Tarragona, 2015

Acknowledgements

The four years of my PhD are the amazing time of my life. I have experienced the best part of my life among some great people of the different origins. Living alone away from my home was quite challenging but I really felt myself at home in such a beautiful city of Spain. So I can consider Tarragona as my second home because I have many memories connected to every corner of it. These four years taught me how to live, how to share, how to cook, how to make friends, how to behave, how to control your anger and above all how to love.

The accomplishment of this thesis would not have been possible without the support of many people. First of all, I would like to thank my supervisors/advisors Dra Maria Cinta Pujol and Dra Rosa Solé for their tireless efforts in enlightening me with their wonderful knowledge of crystallography, crystal growth technique and epitaxial layer growth method. I gained a lot from the excessive experience of Rosa in the field of crystal and epitaxial growth. I remember, during my first year, I was knocking at her office door all the time for asking some silly questions. But as it says that, **"the only stupid question is the one you don´t ask"**. I had my best time with Cinta not only because of her enthusiastic behavior towards work but also her conversations on different serious and non-serious topics that helped me a lot in viewing the world with a different perspective and a better point of view. She made me an organized man by forcing me to write the reports on daily basis.

I would like to convey my deepest gratitude to my Bosses Prof. Dr. Francesc Díaz(Quico) and Prof. Dra. Magdalena Aguiló for giving me the opportunity to join the FICNA-FICMA group and for their day to day involvement in this work. In this group, I really started from scratch. I learned growing crystals then obtaining substrates from them. I learned growing epitaxial layers, fabricating the channels, simulations and optical characterization. Believe me that knowledge of all fields really makes you **monster**. I really had many nice conversations with both of them about the waveguiding devices and the future of RTP crystals. During the first year, it was really hard for me to arrive to the office at sharp 9 am, not because that I was lazy just because that I used to work till late hours. But I became punctual because of Quico´s continuous invigilation. I can't forget his phrase when he used to tell us, **"You should to work from 9 to 6"**. One time, I got a warning note from him as I was 15 minutes late. And after that I was never late or he didn't notice ☺ so he not only helped me in scientific knowledge but also

brought a nice habit of punctuality in me. I hope I will not miss my first job interview now☺

I would like to acknowledge specially the other members of the FICNA-FICMA group Dr. Jaume Massons, Dr. Xavier Mateos, Dr. Airan Ródenas and Dr. Joan Carvajal for their collaboration and scientific discussions during my stay in this research group. All the time which Dr. Airan spent in optics lab with me was really great, that gave me confidence in performing the waveguiding experiments at my own.

I would like to acknowledge the technicians Agustí Montero, Nicolette Bakker and Laura Escorihuela for their invaluable contribution and support to this thesis. Sample cutting and polishing was the vital part of the research, without their contribution, I think this work wouldn't have moved at all. Sometime, they really got annoyed by me due to my crappy and small samples but at the end we tried to diffuse the situation with funny remarks.

My heartiest gratitude to all my colleagues of FICNA-FICMA group Muhammad Usman Qadri, Oleksandr Bilousov, Josue Mena, Marc Medina Martínez, Eric Pedrol, Josep Maria Serres, Oleksandr Savchuk, Javier Martinez, Irina Adell Barbará and Dat Huudt Nguyen; it has been a pleasure working with all of them. I will really miss the time when we all used to go for lunch, coffee and smoke and laugh out loud on silly things. It was a great opportunity to meet many talented people from different cultures and know about them.

I would like to thank especially all the team members of Servei de Recursos Científics I Técnics of University Rovira I Virgili. Without the cooperation of Dra Mercé Moncusí, Dra Mariana Stefanova, Dr. Rita Marimon, Nuria Argany and Dr Lukas Vojkuvka, it wouldn´t be easy for me to finish my work. I really appreciate the efforts of Lukas for what he made with me in order to handle the tiny samples which were hard to work with laser lithography equipment. And above all he taught me some funny kind of accent, that I can use with my friends to make them laugh☺

I am happy to acknowledge my debt to Prof. Ginés Lifante at Universidad Autonoma de Madrid for their support and scientific discussions during the designing of Machzehnder Interferometer devices. And I would like to thank Prof. James S. Wilkinson for accepting me to be the part of his wonderful and innovative lab of Optoelectronics Research Centre, ORC, at the University of Southampton. And I can't forget that how much he took care of me in the lab. And the amazing lunch with him and his wife at an Indian

restaurant and a Pakistani tea at their house. I owe my deep appreciation to Dr. Senthil Ganapathy for his precious time for helping me in the fabrication of waveguides and Neil Sessions for their expertise and advices in the clean room. I really enjoyed getting trained in the clean room and working as an independent user on many monster machines.

I am really grateful to all those precious friends who supported me and raised my morale when I was down. Despite the fact, that they are living in different countries but they are still close to me. I would like to acknowledge Luke Stam, Barbara Ludasz and Ewelina Kowal for sparing some time for me and coming to attend my defense from Ireland, Hungary and Poland respectively. Special thanks goes to Ewelina who sustained my bad mood and angry face when I used to go home with full of stress from work.

My deepest gratitude goes to my family who despite the geographical distance, were always close to my heart. My sisters, brother, nieces and nephews were the source of my motivation and they were proud that I was doing well. I would like to thank my parents who gave their full attention and better moral education which helped me to become a good human being and contribute positively towards the society. I believe that all the credit of my success goes to the non-stop prayers of my mother and father. They trusted me and let me travel thousands of miles away from them. Although I lost my mother in half of my journey to PhD. May her soul rest in peace. l felt all alone and I wish that she would smile from the heavens to see her son as a doctor.

Behind every successful man, there stands a woman

In loving

Memory

Of my

Beloved mother

Fazeelat Begum

(1949-2013)

List of publications

This doctoral thesis is partially based on the work contained in the following papers, referred by roman numerals in the text:

Paper I

"Crystal growth and characterization of epitaxial layers of the $RbTiOPO_4$ family of nonlinear optical crystals", M. A. Butt, R. Solé, M. C. Pujol, J. Cugat, M. Aguiló and F. Díaz. To be submitted to Optical Materials, 2015

Paper II

"Fabrication of Y-Splitters and Mach-Zehnder Structures on (Yb,Nb):$RbTiOPO_4$/$RbTiOPO_4$ Epitaxial Layers by Reactive Ion Etching" ,M. A. Butt, R. Solé, M. C. Pujol, A. Ródenas, G. Lifante, A. Choudhary, G. S. Murugan, D. P. Shepherd, J. S. Wilkinson, M. Aguiló, and F. Díaz. Accepted in Journal of Lightwave technology, 2014, DOI 10.1109/JLT.2014.2379091.

Paper III

"Channel waveguides in $RbTiOPO_4$ crystals produced by Induced Coupled Plasma-Reactive Ion etching", M. A. Butt, M. C. Pujol, R. Solé, A. Ródenas, G. Lifante, M. Aguiló, and F. Díaz. To be submitted to Journal of Lightwave Technology, 2015

Paper IV

"Channel waveguides and Mach-Zehnder structures on RbTiOPO4 by Cs+ ion exchange", M. A. Butt, M. C. Pujol, R. Solé, A. Ródenas, G. Lifante, J. S. Wilkinson, M. Aguiló and F. Díaz. Submitted to Optical Materials Express, 2015

Related publication not included in the thesis

"Effect of Doping on Crystalline Quality of Rubidium Titanyl Phosphate (RTP) Crystals Grown by the TSSG Method", J. Guo, B. Raghothamachar, M. Dudley, J. J. Carvajal, M. A. Butt, M. C. Pujol, R. Solé, X. Mateos, J. Massons, M. Aguiló, F. Díaz, MRS Proceedings, Volume 1698 (2014), DOI: http://dx.doi.org/10.1557/opl.2014.899.

"Low repetition rate femtosecond laser writing of optical waveguides in KTP crystals: analysis of anisotropic refractive index changes", M. A. Butt, H. D. Nguyen, A. Ródenas, C. R. Vázquez, P. M. Pedraz, J. R. V. Aldana, M. Aguiló, R. Solé, M. C. Pujol, F. Díaz. To be submitted to Optics Express 2015.

Table on Contents

Abstract……………………………………………………………………………..……i

Preface……………………………………………………………………………..…iii

Acknowledgments……………………………………………………………………v

List of publications……………………………………………………………..…xi

Chapter 1. Introduction…………………………………………………………..….1

1.1. Brief history of integrated photonics……………………………………………1

1.2. Optical waveguides…...…………………………………………………………....2

1.3. Integrated photonic devices……………………………………………………..…4

1.4. Materials used as a platform for Integrated photonics……………...................8

1.4.1. Electro-optic materials…………………………………………………8

1.4.2. Non-linear optical materials……………………………………………...9

1.5. Rubidium titanyl phosphate as a powerful candidate for integrated photonics...11

1.6. Integrated photonics based on RTP compounds………………………………15

1.7. Doctoral thesis aims…………………………………….............................16

Chapter 2. Experimental techniques…………………………………………………19

2.1. Crystal growth and processing of materials……………………………………..19

2.1.1. Top seeded solution growth - slow cooling method (TSSG-SC)…….19

2.1.2. Liquid phase epitaxy (LPE)……………………………………………..21

2.1.3. Sample cutting and polishing……………………………………...22

2.1.4. Microstructuring of epitaxial layers and substrates……. ……………23

2.1.4.1. Reactive ion etching (RIE)……………………………..........30

2.1.4.2. Inductively coupled plasma reactive ion etching (ICP-RIE)…………………………..................................32

2.1.4.3. Ion exchange………………………………………………37

2.2. Characterization techniques ……………………………………….............38

2.2.1. Microscopy techniques…………………………………………….38

2.2.1.1. Reflection and transmission optical microscopy…………...39

2.2.1.2. Environmental scanning electron microscopy (ESEM)…….39

2.2.1.3. Confocal microscopy………………………………………40

2.2.1.4. Atomic force microscopy (AFM)…………………………..41

2.2.2. Electron probe microanalysis (EPMA)………………………………43

2.2.3. X-Ray powder diffraction (XRPD) …………………………………46

2.2.4. Determination of refractive indices and dark mode spectra using a prism-coupler…………………………………………………………47

2.2.5. Waveguide laser set-up ……………………………………………49

2.2.6. Determination of the optical losses in waveguides…………………51

Chapter 3. Bulk single crystal and epitaxial growth………………………………...53

3.1. Bulk single crystal growth for substrates……………………………………...56

3.1.1. RTP bulk single crystal growth……………………………………56

3.1.2. K:RTP bulk single crystal growth…………………………………...58

3.1.3. Na: KTP bulk single crystal growth…………………………………59

3.2. Crystal growth of epitaxial layers……………………………………………..62

3.2.1. Lattice mismatch……………………………………………………62

3.2.2. Growth of (Yb,Nb):RTP epitaxial layers on RTP (001) substrates..63

3.2.3. Growth of RTP epitaxial layers on $Rb_{1-x}K_x TiOPO_4$ substrates……...67

3.2.4. Growth of KTP epitaxial layers on $K_{1-x}Na_xTiOPO_4$ (001) Substrates…………………………………………………………....70

3.3. Ferroelectric domains in RTP bulk crystals and epitaxial layers………………...71

Chapter 4. Waveguides fabrication……………………………………………………...73

4.1. Fabrication of Y-splitters and MZ structures on RTP(001) and (Yb,Nb):RTP/ RTP(001) by RIE……………………………..……………………......76

4.1.1. Pattern design……………………………………………………….76

4.1.2. Metal layer adhesion and morphology…………………………........77

4.1.3. Selectivity……………………………………………………………78

4.1.4. Etching rate and etching mechanism…………………………………79

4.1.5. Etched morphology…………………………………………..........81

4.2. Fabrication of straight channel waveguides on RTP/(Yb,Nb):RTP/RTP (001) by ICP-RIE……………………………………………………………………..83

4.2.1. Pattern design……………………………………………..........83

4.2.2. Improvement of the metal layer adhesion……………………...........84

4.2.3. Selectivity and etch rate……………………………………….........84

4.2.4. Etched morphology……………………………………………..........85

4.3. Fabrication of Y-Splitters and MZ structures on RTP (001) by Cs^+ ion exchange…………………………..……………………….……..........86

4.3.1. Pattern design……………………………………….………….86

4.3.2. Cs^+ exchange profile…………………………………………...........87

4.4. Fabrication of straight waveguides by ion exchange…………….…………..88

4.4.1. Pattern design………………………………………………................88

4.4.2. Morphological characterization and Cs^+ exchange profile……….........89

Chapter 5. Computer simulations and optical characterization……………………........91

5.1. Optical waveguides ....……………………….................................91

5.1.1. Classification of optical waveguides……………….........................92

5.1.2. Light propagation in channel waveguides…......................................94

5.1.3. Solution for step index channel waveguides by effective index method (EIM) 97

5.1.4. Finite differences Beam propagation method (FD-BPM).................100

5.2. Refractive index variation……………………………………………..........103

5.2.1. Refractive index contrast at 632 nm..103

5.2.2. Refractive index contrast at 1550 nm...103

5.3. Optical characterization of Y-splitters and MZ structures fabricated on (Yb,Nb):RTP/RTP(001) system ………………………………..............104

5.3.1. Computer simulations……………………..…………………......104

5.3.1.1. Cross-section dimensions……………………..….........104

5.3.1.2. Light propagation along the optical pathway……………..106

5.3.1.3. Coupling of light between the two arms of the MZ structure……………………………………………......107

5.3.2. Experimental characterization of the fabricated Y-splitters and MZ structures in step-index (Nb,Yb):RTP/RTP(001) waveguides…........110

5.3.2.1. Mode field characterization…………………………......110

5.3.2.2. Losses estimation………………………….....................111

5.4. Optical characterization of straight waveguides fabricated on RTP/(Nb,Yb):RTP/ RTP(001)…………………….………………......112

5.4.1. Computer simulations……………………………………………...112

5.4.2. Experimental characterization of the fabricated straight waveguides on RTP/(Nb,Yb):RTP/ RTP(001)....114

5.5. Optical characterization of Cs^+ exchanged waveguides....115

5.5.1. Expected refractive index contrast in Cs^+ exchanged waveguides....115

5.5.2. Experimental characterization of straight waveguides, S-bend waveguides and MZ structures on RTP (001) by Cs^+ ion exchange....115

5.5.3. Experimental characterization of straight waveguides fabricated by Cs^+ ion exchange....116

5.5.4. Losses estimation in Cs^+ exchanged waveguides....117

5.5.5. Preliminar study of SHG in Cs^+ exchanged waveguides....117

Conclusions....119

References....121

Appendix....133

Paper I....137

Paper II....157

Paper III....169

Paper IV....175

Chapter 1
Introduction

1.1. Brief history of integrated photonics

Optics is the branch of physical science which deals with the generation and propagation of light and its interaction with matter. In optics, we mainly talk about light in terms of electromagnetic radiations in the wavelength range extending from 50 nm (UV) to 1 mm (FIR). The invention of laser by the T. H. Maiman in 1960 brought a revolution in the modern optics [Maiman 1960].

Due to the advancement in technology of electronics and optics, many new disciplines related to optics have been originated such as electro-optics, opto-electronics, acousto-optics, quantum electronics, waveguide technology, etc. As a result, classic optics which was initially dealing with lenses, mirrors, filters, etc, has been transformed into much more complex discipline dealing with lasers, semiconductors, detectors, modulators, etc. These devices operate on the principle of optics and electronics and give rise to the discipline of **photonics**. If electronics describe the flow of electrons, the term photonics deal with the flow of photons. Moreover, these two disciplines clearly overlap in many cases, in case of detectors; photons can control the flux of electrons. In case of semiconductor lasers or electro-optic modulators; electrons themselves can determine the properties of light propagation. Integrated photonics is considered to constitute waveguide technology with other disciplines such as electro-optics, acousto-optics, non-linear optics and opto-electronics, as shown in figure 1.1.

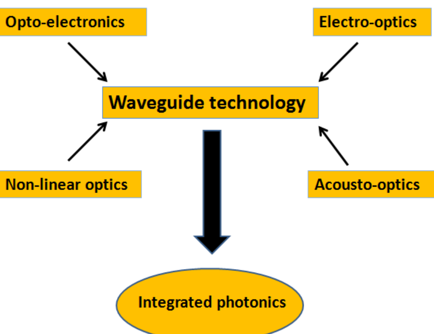

Figure 1.1. Confluence of various disciplines into integrated photonics [Lifante 2003]

In 1947, the development of transistors brought a revolution in processing and transmission of information based on electronics that used semiconductor devices for controlling the electronic flux. But at the beginning of 1980s, electronics was slowly supplemented and even replaced by optics, and electrons were substituted by photons as information carriers.

Integrated photonics deal with the fabrication and integration of several photonic components on a single platform. The components such as splitters, interferometers, couplers, detectors, gratings and many more can be used as building blocks to fabricate more complex planar devices which can perform a wide range of functions with applications in optical communication systems, instrumentation and sensors. The term integrated optics was first proposed by S. E. Miller [Miller 1969] in 1960 in order to emphasize the similarity between planar optical circuit technology and the well established integrated micro-electronic circuits. Miller proposed that various active as well as passive elements such as splitters, couplers, polarizers, modulators, switches and many more can be fabricated on a single platform combining and interconnecting them with the help of optical transmission lines called waveguides. The integration of multiple optical devices on a single substrate can clearly reduce the cost of advanced optical systems including optical communication networks.

The first bidimensional devices based on optical waveguides were fabricated on planar platforms at the end of 1960s. The successful operation of tridimensional devices was demonstrated in a variety of materials such as glasses, crystals and semiconductors in the mid of 1970s. Lithium niobate (LN) was rapidly known as one of the most promising dielectric platform for the fabrication of functional devices in waveguide geometries. Waveguide devices such as integrated intensity modulators based on LN up to 40 GHz and with integration levels of up to 50 switches fabricated on a single photonic chip have already been demonstrated in laboratory experiments [Burns 1999].

1.2. Optical waveguides

The basic concept in optical integrated circuits is based on the confinement of light. For example, in optical fibres, a medium (core) with higher refractive index surrounded by a medium (cladding) with lower refractive index acts as a trap. The light entering the core with acceptance angle cannot escape from the structure due to the phenomena of total internal reflection at the interfaces. Due to the confinement of light within the core, the

light can be able to propagate in integrated photonic chips or even long distance with the help of optical fibres. In planar waveguides, the region of high refractive index is a film acting as a core; the light is confined in one plane by total internal reflection in that film as described in ray optics. The film/core should be surrounded by a medium with lower refractive index known as substrate/cladding as can be seen in figure 1.2,a). In a channel waveguide, the light travels in a channel having a higher refractive index embedded in a planar substrate with low refractive index. The confinement of light takes place in two dimensions that's why these kinds of waveguides are also known as 2D waveguides as shown in figure 1.2,b). Buried waveguides can be fabricated by modifying the region of the substrate pre-defined by appropriate photolithographic masks by using diffusion process. This leads to the refractive index increase of the defined part of the substrate and because of that, the channel waveguides fabricated following this method give rise to graded-index profiles [Alferness 1990]. The main advantage of this type of channel waveguides, typical in glasses and ferroelectric materials, is the low propagation losses that can be achieved (less than 0.1 dB/cm). Also, buried channel waveguide geometry allows easy placing of metallic control electrodes, such as in the case of electro-optic modulators and switches. Figure 1.2,c) shows the geometry of an optical fibre, which can be considered as a cylindrical channel waveguide. The light is confined in the central part of the optical fibre known as core, surrounded by a medium of lower refractive index called cladding. Optical fibres have diversity in their applications such as communication, medical purposes, military, submarine networks and many more.

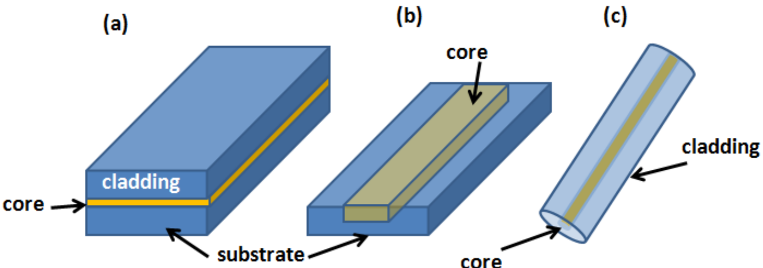

Figure 1.2. Basic waveguide geometries: a) Planar waveguide (1D), b) Channel waveguide (2D) and c) Optical fibre

1.3. Integrated photonic devices

Optical devices are key components for photonic and optoelectronic optical applications due to their simple structure, low losses and wide optical bandwidth. In integrated photonics, all the optical components are constructed with three building blocks that is straight waveguide, bend waveguide and power splitter. Table 1.1 shows several of these basic optical elements that perform some basic functions common in many integrated optical devices [Lifante 2003]. These structures in terms of splitters or couplers provide optical power splitting or combining respectively [Grossard 2007]. Optical splitters find application in optical fibre networks, particularly for broadcast optical signal distribution. It is known that the radiation losses increase with bend waveguides so it is significant to keep the angles at low value. So in order to keep the losses low, small branching angles and long structures are necessary.

Table 1.1. Integrated photonics elements [inspired by the book Integrated photonics fundamentals by Ginés Lifante].

Interconnect	Straight waveguide	Straight
	S-bend	S-bend
Power splitter 1x2	Y-splitter	Y-splitter
	Multimode interference (MMI)	MMI

Waveguide reflector	Mirror	
	Grating	
Intensity modulator	Mach-Zehnder Interferometer (MZ)	MZ Interferometer
TE/TM converter	EO-TE/TM converter	EO-TE/TM converter

UNIVERSITAT ROVIRA I VIRGILI
NEW PHOTONIC DEVICES BASED ON NLO(NON-LINEAR OPTICAL) CRYSTALLINE WAVEGUIDES
Muhammad Ali Butt

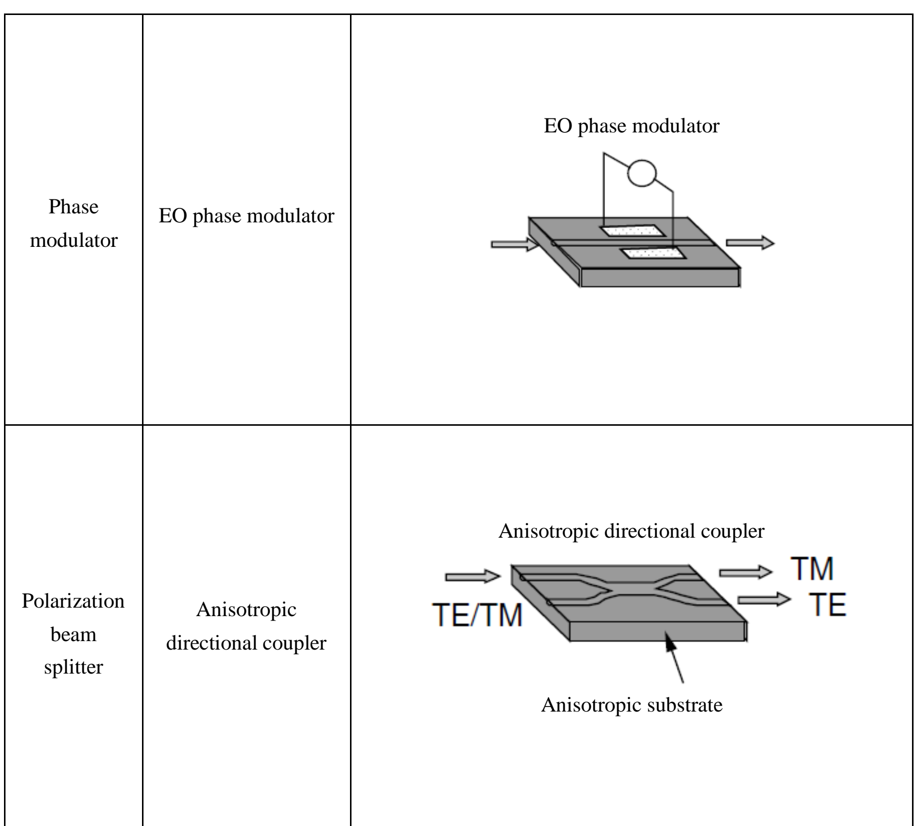

Phase modulator	EO phase modulator	
Polarization beam splitter	Anisotropic directional coupler	

Specific integrated photonic structures are fabricated in this work as straight waveguides for second harmonic generation (SHG), S-bend waveguides, Y-splitter and MZ structures.

Straight waveguides for SHG

Under normal conditions, when the light is incident on a non-linear optical material, its response is linear. But at sufficiently high light intensities, the response of the material depends on the light intensity which can lead to second harmonic, sum frequency and difference frequency generations. Nowadays, it is common to create blue or infrared laser light in the laboratories based on this effect where no alternative sources are available. Straight channel waveguides were fabricated along the phase matching direction of the incident wavelength and can be used for SHG generation.

UNIVERSITAT ROVIRA I VIRGILI
NEW PHOTONIC DEVICES BASED ON NLO(NON-LINEAR OPTICAL) CRYSTALLINE WAVEGUIDES
Muhammad Ali Butt

Bend waveguide

A bend waveguide is normally used to interconnect different elements which are not aligned with the optical axis of a chip or to separate the channel waveguides at the chip endfaces, in order to connect multiple fibres. Therefore these waveguides are often called offset waveguides.

Power splitter

A power splitter is usually a symmetric element which equally divides the power from a straight waveguide between two output waveguides. The simplest version of a power splitter is the Y-splitter. In order to minimize the power losses, it is important to carefully design the radius of curvature of the two bend waveguides as well as the junction.

Intensity modulator

One of the most important demands from integrated optics is to perform an intensity modulation of the light at very high frequencies. This can be done by fabricating an integrated MZI on a material with high electro-optic coefficients. The MZI consists of a monomode channel waveguide and then splits in two symmetric branches by means of a Y-branch and then two branches become parallel joining with the symmetric reverse Y-branch and ends in a straight waveguide. If the MZI structure is symmetric, then the light travels with the same phase and recombines constructively at the output but if there is a phase shift of 180° in one of the MZI´s arm, then the light recombine out of phase and will give rise to destructive interference with no light at the output. In practice, the phase shift of 180° in one arm is carried out by choosing the crystal orientation, polarization, electrode geometry and applied voltage across the waveguide in electro-optical material for a specific wavelength. MZ structure can also be used as a sensor where one arm acts as a reference arm and other acts as a sensing arm. Any change in the relative phase or the optical path length of the light from the two arms leads to displacement of the interference fringes.

1.4. Materials used as a platform for integrated photonics

Integrated optical devices based on glasses have the advantage of low cost and can be produced by ionic exchange processes [Najafi 1992]. Since the glasses are amorphous materials, they do not offer physical properties useful for the direct control of light that is why they are mainly used for the fabrication of passive devices. Nowadays glass optical fibres are used for high speed data transfer. However, they are not suitable for complex high density circuitry because they are difficult to fabricate and quite expensive.

Optical switches and arrayed waveguide gratings (AWGs) based on silica planar lightwave circuits (PLC) are predominant. However, the low wavelength tuning range and the temperature dependence of the central wavelength of silica based AWGs, are the major problems with this technology [Hui 2005].

Polymers are one of the attractive materials for highly integrated optical components and circuits because they offer rapid processibility, cost effectiveness, high yield, and high performance such as low optical losses and small birefringence as compared to silica. Furthermore, polymers provide an ideal platform for the incorporation of more complex material functionalities through selective doping, thereby enabling amplification and electro-optic effects [Ma 2002]. InP is the most widely used in commercially available photonic integrated circuits, it allows the integration of various optically active and passive functions on the same chip [Bente 2006]. Lithium niobate offers incredible versatility as a dielectric substrate for integrated optics. Many new optical devices such as waveguides, electro-optical wavelength filters and polarization controllers, lasers with remarkable properties, non-linear frequency converters of exceptional efficiency, ultrafast all-optical signal processing devices and single photon sources have been developed on this material [Sohler 2008]. But still active research is carried on in order to develop dielectric based optical integrated platform based on NLO materials with improved and attractive physical properties.

1.4.1. Electro-optic materials

In many applications such as modulation, switching, deflection, isolation, frequency shifting and polarization rotation of optical signals, it is important to control the optical signal with externally applied signals. The external signals can be in the form of electric field, magnetic field, an acoustic wave or another optical wave in order to control the

optical signal. All these interactions come under the umbrella of non-linear optical phenomena. Many useful devices such as modulators and optical switches are based on the electro-optic, magneto-optic and acousto-optic effects. Many dielectric materials change their optical properties under the influence of an externally applied electric field. A field applied to an anisotropic electro-optic material modifies its refractive indices and thereby its effect on polarized light. This phenomenon is known as linear electro-optic effect or the Pockels effect. Although, the change in the refractive index is very small but its effect on an optical wave propagating at a distance much greater than the wavelength of light in the medium can be significant. The majority of electro-optic devices are based on the Pockels effect. The effect has been characterized in a wide range of materials, including inorganic crystals (mostly ferroelectric compounds), organic and molecular crystals and crystalline and non-crystalline polymers. Non-linear inorganic materials such as $LiNbO_3$, $KTiOPO_4$, $KTiOAsO_4$, $RbTiOPO_4$ and $KNbO_3$ have orthorhombic mm2 symmetry. They have five large independent non-vanishing electro-optic coefficients in the $r_{\alpha k}$ matrix: r_{13}, r_{23}, r_{33}, r_{42} and r_{51} [Liu 2005]. Recently, there has been a great deal of interest in organic compounds for electro-optical and non-linear optical applications [Chemla 1987]. There are certain kinds of molecules that are symmetric and conjugated; that is to say, their structures have alternating single and double carbon-carbon bonds. These kinds of molecules possess very high molecular non-linearities β. As an example, 3-(1,1-dicyanothenyl)-1-phenyl-4,5-dihydro-1H-pyrazole (DCNP) polymer has been reported [Allen 1988] which can have high electro-optic coefficients. Over the last few years, polymeric materials are being studied, in which the highly non-linear molecules are dissolved in or attached to an inert polymeric matrix [DeMartino 1988]. Waveguide devices fabricated by using these materials have been demonstrated which showed high electro-optic coefficients comparable to those of lithium niobate [Lytel 1988].

1.4.2. Non-linear optical materials

There are many non-linear optical materials which are appropriate candidates to be used in integrated optics. One of the materials most widely used in the fabrication of integrated optical devices is $LiNbO_3$ (LN) [Prokhorov 1996]. LN crystallizes in the trigonal system and possesses relatively high non-linear optical (NLO) coefficients. It has a transmission range of 0.4-5 μm. It has valuable acousto-optic, electro-optic and piezo-electric effects. Because of these properties, this material is suitable for the

fabrication of functional devices such as phase modulators, switches, directional couplers, multiplexers, etc [Wooten 2000, Huo 2010, Aschieri 2011, Rottmann 1988]. Due to its birefringence, it can perform type I noncritical phase matching second harmonic generation (SHG) of 1064 nm at room temperature. It has high thermal conductivity. When illuminated with visible radiation, LN can suffer from photorefractive damage. Moreover photorefractive damage threshold can be increased by doping LN with Mg but doping seems to have some effect on the NLO coefficients of LN [Aillerie 2013]. Several techniques for waveguide fabrication in LN are now well established, including Ti or Zn metallic diffusion, photonic exchange, or even ion implantation. Conventional Ti diffused LN waveguide modulators have very low losses, typically 0.2 dB/cm [Hou 2004]. Integrated optical circuits technology based on LN substrates is now very well established and a great variety of devices based on this technology, mainly in the field of optical communications are now commercially available.

$KNbO_3$ (KN) is negative biaxial crystal and is known for its large NLO coefficients and birefringence among the commonly used inorganic crystals. It's transmission range is similar to that of LN. But it suffers from significant processing limitations due to low Curie temperature and its pyroelectric and ferroelastic character. This crystal is useful for surface acoustic wave devices [Yamanouchi 2001]. SHG and ion implanted planar waveguides have been demonstrated in this crystal [Pliska 1995].

β-BaB_2O_4 (BBO) and LiB_3O_5 (LBO) have found important applications for NLO devices [Gorazd 2009]. β-BaB_2O_4 has a wide transparent spectral range and good mechanical properties [Bosenberg 1989]. BiB_3O_6 is another outstanding NLO crystal suitable for ultrafast laser technology [Petrov 2008]. It is an appropriate material for phase matching condition for near infrared (NIR) wavelengths. It possesses high damage threshold and non-linear coefficients but is hygroscopic. $AgGaS_2$ [Elsaesser 1984], $AgGaSe_2$ [Fraser 1997] and $ZnGeP_2$ [Yang 2008] are also important compounds with broad transparency range, sufficient birefringence to enable phase matching and relatively high non-linear optical coefficients. But the optical losses are too high that clampdown the use of these crystals. $LiIO_3$ [Krykov 1977] has large birefringence which makes it useful for phase matching but it suffers large walk off effect. $KTiOPO_4$ (KTP) belongs to a family of compounds with the general formula $ABOXO_4$ where A=K, Rb, Na, Cs, Tl, NH_4; B= Ti, Sn, Sb, Zr, Ge, Al, Cr, Fe, V, Nb, Ta, and X= P, As, Si, crystallizing in the orthorhombic

system [Hagerman 1995]. These crystals have large non-linear optical coefficients. Perhaps most important for KTP are its very large thermal and angular phase matching bandwidths for SHG of fundamental wavelengths near 1064 nm. KTP has lower cost as compared to BBO and LBO. Several optical materials compatible with integrated photonic technology are also capable to incorporate optically active rare earth ions, which makes it possible to fabricate active integrated optical devices [Hubner 2001]. KTP could host lanthanides arising as a promising candidate for self-frequency doubling (SFD) material. But unfortunately the distribution coefficient of lanthanides were very low (typically about 10^{-3}) [Solé 1996].

In this work, we have used Rubidium titanyl phosphate (RTP) which belongs to the KTP family of non-linear optical crystals. This crystal is very interesting because of its excellent nonlinear and physical properties as explained in next section.

1.5. Rubidium titanyl phosphate as a powerful candidate for integrated photonics

Rubidium titanyl phosphate, $RbTiOPO_4$ (RTP), is an orthorhombic crystal, biaxial optical crystal which has high non-linear optical and electro-optical coefficients [Guillien 2003]. It belongs to the non-centrosymmetric space group $Pna2_1$ with unit cell parameters of a= 12.974(2) Å, b= 6.494(3) Å, c= 10.564(6) Å [Thomas 1992]; V=896.3(3) $Å^3$. RTP is isostructural with the already described well known KTP. Although less often used, but it has attracted a great attention as a NLO material.

RTP structure has a network of chains of distorted TiO_6 octahedra linked by PO_4 octahedra with periodic bond chains of $–PO_4$-TiO_6-, inside which rubidium cations are placed as shown in figure 1.3. Vertex sharing TiO_6 octahedra forms zig-zag chains along diagonals of the (010) face of a unit cell.

The optical non-linearity in this family of compounds is believed to be due to the markedly short Ti(1)-OT(2) and Ti(2)-OT(1) bonds [Zumsteg 1976]. However, by observing the Ti-OT bonds in Nb doped RTP and (Er:Nb):RTP, there is no clear or direct relationship between the difference in these bonds and SHG efficiency [Carvajal 2003a]. RTP has a less distorted octahedral coordination environment than KTP [Thomas 1990, Torjman 1974]. Therefore, it can be expected that the SHG properties of the RTP are weaker than that of KTP. Moreover, rubidium is more electropositive

element than potassium [Phillips 1990] therefore; its high ionic conductivity must result in stronger SHG properties. Moreover, the NLO coefficients of RTP and KTP are similar [Satyanarayan 1999].

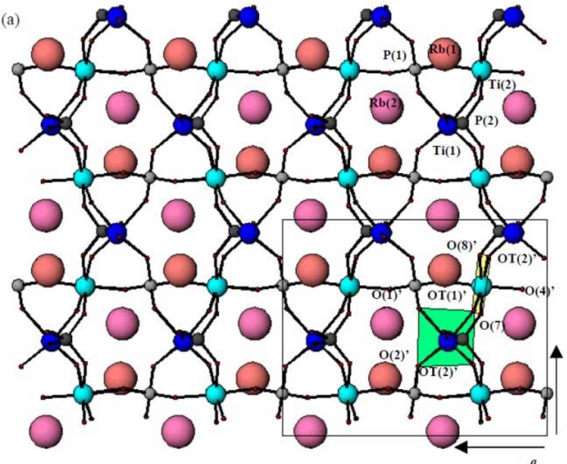

Figure 1.3. View of the RTP crystal structure illustrating the connected paths formed by alternating $Ti(1)O_6$ and $Ti(2)O_6$ octahedra. Projection parallel to the [010] direction.

It is interesting to dope RTP with Ln^{3+} to obtain self frequency doubling laser in a visible spectral range. The Ln^{3+} distribution coefficient in RTP is generally higher than in KTP but not enough to obtain efficient fluorescence. This can be solved by codoping RTP with Ln^{3+} and Nb^{5+} [Carvajal 2002]. The RTP crystals doped with niobium has the characteristic shape of RTP crystals, but its structure is flattened as explained by Carvajal *et al.* [Carvajal 2000]. When RTP crystal is doped with Nb^{5+} and Er^{3+}, these cations only go to Ti site. When the refinement of the structure is done, it is noted that Nb^{5+} cations exclusively substituted Ti(1) sites. However, the situation for Er is undistinguishable, as it is equally distributed between Ti(1) and Ti(2) sites. In case of Yb^{3+} doped RTP, the Yb^{3+} ions are also equally distributed in two different sites: Ti (1) and Ti(2). In Yb:Nb:RTP crystals, however, Yb^{3+} ions occupy likely Ti(2) sites only [Carvajal 2009].

Because of their non-centrosymmetry and non-linearity, they can be used for frequency doubling of lasers that emits in the IR spectral range [Zumsteg 1976]. In the non-linear process, the (001) plane is especially interesting because it contains the Yb^{3+} type-II phase matching direction and the ferroelectric vector is parallel to the [001] direction.

This enable domain is useful for Quasi Phase Matching (QPM) processes to be obtained. Moreover RTP can be doped with active ions to try to obtain a self frequency doubling (SFD) material, which are useful for compact and efficient laser sources in the visible range. The distribution coefficient of Yb^{3+} in RTP is higher than in KTP but it is still too low for laser operation, codoping with Nb^{5+} increases the concentration of Yb^{3+} in the crystal enough to obtain laser radiation [Carvajal 2000, Carvajal 2002, Mateos 2007]. Recently, laser operation has been demonstrated in a (Yb,Nb):RTP bulk single crystal [Mateos 2007]. Periodic poling of RTP for quasi-phase matching was demonstrated for the generation of blue light. RTP has an advantage over $LiNbO_3$ and $LiTaO_3$ because it has ten times low coercive field which requires low voltage for domain reversal [Karlsson 1999].

RTP can be considered as an interesting alternative to KTP for phase matched interactions, because its damage threshold is around 2 times larger than that of KTP which makes it useful in high power SHG and OPO applications [Oseledchik 1994, Guillien 2003]. While it has similar nonlinear optical coefficients [Cheng 1993b].

It is known that KTP has lower refractive indices than RTP and it is possible to grow single crystals of $Rb_{1-x}K_xTiOPO_4$ (K:RTP). Then it is reasonable to incorporate K^+ ions in the RTP structure for reducing the refractive indices [Satyanarayan 1999]. This is interesting because it offers the possibility to obtain epitaxial films of RTP over K:RTP substrates with high contrast in refractive indices. Also, Na:KTP single crystals were grown for producing substrates to be used for KTP epitaxial growth. Because of the lower values of refractive indices of Na: KTP as compared to KTP, these epitaxial layers could be used as waveguides. Some of the physical properties of the RTP single crystals are given in table 1.2.

Table 1.2. Selected physical properties of RTP crystal.

Properties	**Value**	**Reference**
Space group	$Pna2_1$	[Thomas 1992]
Z	4	
a [Å]	12.974(2)	
b [Å]	6.494(3)	

c [Å]	10.564(6)		
Hygroscopic	none	[Chaudhary 2006]	
Mohs Hardness	5		
Melting point [K]	1073	[Gier 1980]	
Curie temperature [K]	1058-1102	[Carvajal 2003]	
Optical transparency [μm]	0.35-4.3	[Loiacono 1992, Spence 1995, Oseledchik 1994]	
Laser damage threshhold	1.8 times greater than KTP	[Oseledchik 1994]	
Refractive indices @ 632.8 nm	n_x	1.7895	[Carvajal 2001]
	n_y	1.8015	
	n_z	1.8898	
EO coefficients [pm/V] at 0.633 μm	r_{33}	39.6	[Cheng 1994a, Roth 2000]
	r_{23}	17.1	
	r_{13}	12.5	
NLO susceptibilities [pm/V] at 1.064 μm	d_{33}	17.1	[Cheng 1993a, Cheng 1994b]
	d_{32}	4.1	
	d_{31}	3.3	
d_{eff} for type II SHG	2.51	[Oseledchik 1994, Cheng 1994a]	
Laser damage threshold J/cm^2 @ 1.064 μm	12 for x-cut RTP 6 for y-cut RTP	[Wagner 2007]	

- $n_x < n_y < n_z$ and $X \| \vec{a}$, $Y \| \vec{b}$, $Z \| \vec{c}$

1.6. Integrated photonics based on RTP compounds

KTP is recognized as a finer material for guided wave optics. KTP has shown to have attractive properties for SHG of the Nd:YAG and other Nd:doped lasers, sum and difference frequency mixing and optical parametric oscillation processes. KTP thin films offer a practical and cost effective alternative to single crystals with enhanced design and capability for integrated optic applications. Nowadays the literature related to integrated photonics in RTP is scarce as compared to KTP. Over the past few years, research has been conducted on RTP in order to explore its properties for the use in integrated photonics.

By the use of double crystal RTP EO modulator, a high repetitive rate 880 nm diode pumped EO Q-switched adhesive-free bond composite Nd:$GdVO_4$ laser was demonstrated for the first time [Yu 2013]. Recently, efficient RTP based OPO intracavity pumped by an acousto-optic Q-switched Nd:YVO_4 laser was demonstrated [Duan 2014]. Moreover, Pockel cell (Pismo Pulse picker 8/1) based on RTP crystal is commercially available. The frequency of the picked pulses start with single shot to 1 KHz for the basic model, and goes up to 100 KHz for the most advanced one. The electro-optics cell based on two RTP elements in a temperature compensating design that enables the use of these devices within a wide range of temperature range from -60 ^oC up to +70 ^oC. It can act as Q-switch, phase modulator, amplitude modulator, pulse picker, cavity dumper, shutter, attenuator and deflector. Figure 1.4.a) and 1.4.b) shows the commercially available pulse gating system based on RTP and electro-optics cell based on two RTP elements.

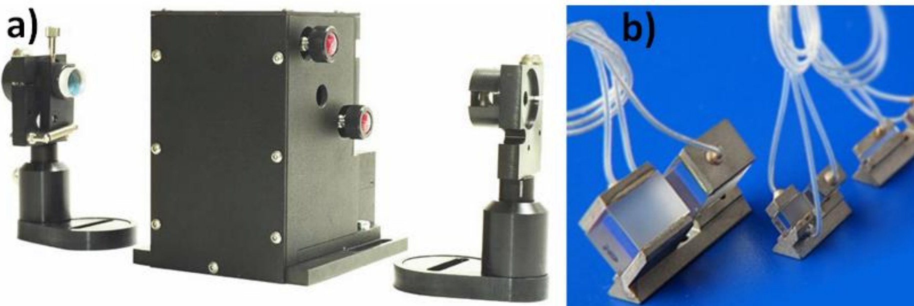

Figure 1.4. a) Pockels cell OG8/1-RTP with integrated HV generator, b) Electro-optics cells based on two RTP elements [www.dmphotonics.com ,www.raicol.com]

Moreover all the properties of RTP described above can be converged in waveguides for integrated photonics. A waveguide structure to confine the interacting optical waves enables compact and efficient devices to be constructed [Suhara 2003]. Efficient SHG of green light was obtained by using a Ba:Yb:Nb:RTP epitaxial layer grown on non-active RTP(001) substrate [Cugat 2011b]. Channel waveguides on RTP crystal by Cs^{+} ion diffusion was fabricated by Cugat *et al* [Cugat 2013b] and demonstrated type II SHG. Rib waveguides fabricated on (Yb,Nb):RTP by using Ar^{+} ion milling technique showed good optical confinement and generation of green light by type II second harmonic generation [Cugat 2013c].

1.7. Doctoral thesis aims

As explained in this chapter about the exceptional NLO and EO properties of RTP, the objective of this thesis is to make use of this crystal as a base for designing, fabrication and characterization of different waveguide structures with interesting applications in integrated optics. The study is divided in the following steps.

- ✓ Growth of substrates and epitaxial layers of high quality for the fabrication of optical devices.
- ✓ Investigation of Na:KTP and K:RTP crystals in order to provide a platform material for integrated optics.
- ✓ Designing of optimum structures of MZ and Y-splitters in RTP substrate.
- ✓ Fabrication and characterization of MZ and Y-splitter structures on (Yb,Nb):RTP/RTP(001) epitaxial system by using etching techniques.
- ✓ Fabrication and characterization of straight waveguides, MZ and Y-splitter structures on RTP compounds by ion exchange method.

The structure of this manuscript is of the following:

The main experimental techniques used in this thesis work are described in chapter two. Top seeded solution growth slow-cooling technique (TSSG-SC) was employed for obtaining bulk single crystals and the epitaxial layers that constitute the waveguides were grown by liquid phase epitaxy (LPE), reactive ion etching (RIE), inductively coupled plasma-reactive ion etching (ICP-RIE) and Cs^{+} ion exchange were the main source of waveguides fabrication techniques used. The chemical composition of the crystals and the epitaxial layers were determined by Electron Probe Micro Analysis

(EPMA). Through X-ray powder diffraction (XRPD), lattice parameters of bulk crystals were determined, which were used in the calculation of the lattice mismatch between the substrate and the epilayer. Information about the refractive indices of the substrates and the epitaxial layers was obtained by the dark mode spectrum method. Many microscopic techniques such as reflection and transmission optical microscopy, environmental scanning electron microscopy (ESEM), atomic force microscopy (AFM) and confocal imaging profilometry were used to obtain images of the samples. The waveguide laser experiments set-up is also described in chapter two as well as the techniques used to quantify the optical losses in different waveguides.

Chapter three explains the growth of bulk single crystals as well as the epitaxial layers. In this chapter, we present the growth of RTP, K:RTP and Na:KTP single crystals as possible substrates for integrated optics. As an interest in waveguides, different epitaxial layer systems have been studied for instance the growth of (Yb,Nb):RTP on RTP(001), epitaxial layers of RTP on K:RTP(001) and K:RTP(100) and finally epitaxial layers of KTP on Na:KTP(001).

Chapter four deals with the fabrication of Y-splitters and MZ structures on RTP (001) and (Yb,Nb):RTP/RTP(001) samples by using RIE technique, straight channel waveguides on RTP (001) samples by using ICP-RIE technique and, at the end, Y-splitters, MZ structures and straight channel waveguides along the basic principle axis and phase matching directions of RTP(001) and (Yb,Nb):RTP/RTP(001) samples were fabricated by Cs^+ ion exchange. The pattern designs, etched morphologies, etch rate and etch mechanism of these samples is also presented in this chapter. A brief study on the adhesion of different metals on RTP substrates which acted as a hard mask during etching and exchange processes is also carried out. It was investigated that, the ferroelectric domains of RTP can influence the exchange profile, so RTP bulk crystal domain map is also reported.

Chapter five deals with the optical simulations and characterization of the waveguides as mentioned in chapter 4. Chapter 5 begins with a review of the fundamental theory of planar and channel waveguides along with their solution of modes. Refractive indices of RTP substrates and the epitaxial layers were measured at 1550 nm at room temperature. The optimum parameters for designing Y-splitters and MZ structures which can support a single fundamental mode were determined with the help of simulation tool.

UNIVERSITAT ROVIRA I VIRGILI
NEW PHOTONIC DEVICES BASED ON NLO(NON-LINEAR OPTICAL) CRYSTALLINE WAVEGUIDES
Muhammad Ali Butt

Experimental characterization and the losses estimation of waveguides are also presented in this chapter.

Finally, the conclusions give an overview of the main results obtained and the accomplishment of the objectives described above.

Chapter 2

Experimental techniques

In this chapter, we summarize the main experimental techniques used in the growth of bulk single crystals and epitaxial layers, and their microstructuring and morphological, structural, compositional and optical characterization. The single crystals were grown from high temperature solutions using the top seeded solution growth-slow cooling technique, while the epitaxial layers were obtained by liquid phase epitaxy. This chapter is divided into two parts: the first part covers the growth, cutting, polishing and structuring techniques such as reactive ion etching, inductively coupled plasma and Cs^+ ion exchange. The second part is mostly related to the techniques used to characterize the samples such as electron probe microanalysis, X-Ray powder diffraction, refractive index measurement, and microscopy techniques including atomic force microscopy, confocal microscopy and environmental scanning electron microscopy. Waveguides characterization including near field pattern and optical losses calculation in the waveguides are also carried out.

2.1. Crystal growth and processing of materials

2.1.1. Top seeded solution growth-slow cooling method (TSSG-SC)

The top seeded solution growth-slow cooling technique (TSSG-SC) was used to grow undoped and doped RTP and KTP single crystals, which were used for substrates after cutting and polishing processes. In the single crystal growth, the supersaturation of the solution needed for crystal growth was obtained by slow cooling of the solution.

All growth experiments were performed in a vertical tubular single-zone furnace equipped with a mechanical structure which allows the vertical displacement and rotation of an alumina rod which supports the crystal seed. The furnace is thermally isolated from the environment by means of insulator bricks. The crucible is placed inside an alumina tube helicoidally wrapped in Kanthal resistance wire, which provides the heat. The temperature is measured by an S type thermocouple plugged to an Eurotherm 903 controller/programmer that allows cooling rates as low as 0.01 K/h. The power supplied to the furnace is regulated by a tyristor in a phase angle mode, according to a DC signal received from the controller/programmer. A DC motor is used to rotate the

alumina rod with the crystal seed. A rotatory handle is used for vertical displacement of the alumina rod with the crystal seed towards the crucible and solution in the furnace, and after growing the crystal, to remove it from the solution and from the furnace when the furnace has cooled down to room temperature. The crucible must be located in a suitable position in the furnace in order to ensure the optimum thermal gradient, keeping the surface of the solution colder than the bottom of the crucible (see figure 2.1). The growth/dissolution of the oriented seed depending on the temperature is measured with a micrometer with an accuracy of 10 µm, and the saturation temperature is accurately determined. The supersaturation of the solution is then obtained by applying a slow cooling to the solution, typically in the range between 0.05 K/h and 0.1 K/h. During the cooling process, the crystal growth was produced on an oriented seed, generally with the same composition as the crystal to be grown, in contact with the center of the solution's surface. The crystal rotation can be diminished as the crystal grows in order to try to maintain the convection pattern in the solution. In several experiments, when the crystal size in the plane parallel to the solution surface is large enough, a typical pulling rate of 1 mm per day can be applied in order to increase the crystal's dimension in the direction perpendicular to the solution's surface. When the crystal was fully grown, it was slowly extracted from the solution and maintained slightly above the solution's surface while the furnace was cooled to room temperature at a typical rate of 30-40 K/h. The slow cooling process of the system prevents the crystal from cracking due to thermal shocks.

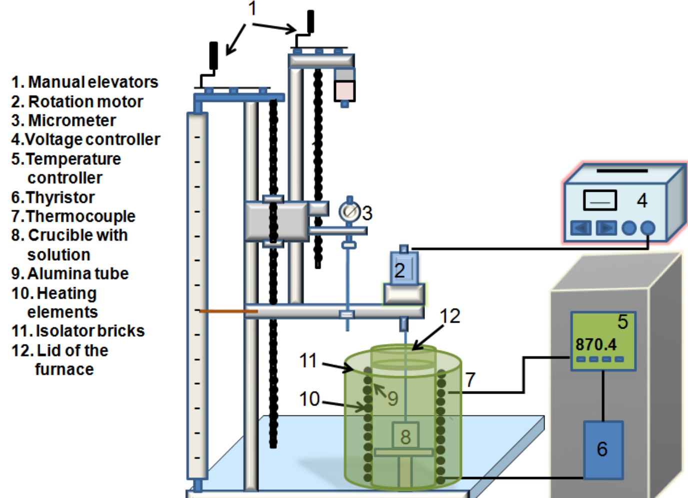

Figure 2.1. Diagram of the furnace used for single crystal growth

2.1.2. Liquid phase epitaxy (LPE)

LPE is a technique used to grow a single crystalline thin layer on an orientated substrate, which generally belongs to the same crystalline family as the layer to be grown. If the substrate and the crystalline layer belong to the same crystalline family and the lattice mismatch is low enough, the layer should possess the same orientation as the substrate and the crystalline quality should be high. For high mismatches between the substrate and the epitaxial layer, the structural stress at the substrate/layer interface increases, and can lead to a higher density of defects. Among the various techniques used to grow epitaxial films, the LPE technique is one of the most widely used to produce optoelectronic devices [Ferrand 1999].

The LPE process uses the same experimental set-up as the TSSG-SC technique, but in a well isolated cylindrical vertical furnace with a central area with practically no thermal gradients. After homogenizing the solution, its saturation temperature is accurately determined in a similar way to the procedure in the single crystal growth process, and the kinetics of growth/dissolution of a crystal seed at temperatures slightly above and below the saturation temperature of the solution must also be determined in order to decide the growth conditions for epitaxial growth. The well-polished substrates must be carefully cleaned before being placed in the furnace. In our case, we used a mixture of HNO_3/H_2O in the ½ ratio in volume for cleaning the substrate for 5 min, followed by dipping them in distilled water (5 min), in acetone (5 min) and finally in ethanol (5 min). All these cleaning steps are made with substrate rotation. After that, the substrates are slowly introduced into the furnace with the help of a stepper motor to avoid thermal shocks. Before sinking the substrate into the solution, it is maintained at a few mm above the surface of the solution for at least 1 h in order to obtain a thermal equilibrium between the solution and the substrate. The substrate is then dipped into the solution with a temperature typically 1 K above the saturation temperature for 5 min in order to dissolve the outer layer of the substrate. The growth time usually ranges from 2 to 4 h, depending on the experiment. After the epitaxial growth process, the sample is taken out of the solution very slowly and maintained at a few mm above the solution, while the furnace is cooled down to room temperature at a typical rate of 25 K/h to avoid thermal shocks.

2.1.3. Sample cutting and polishing

For substrates: After the crystals have been obtained using the TSSG-SC technique, they are cut into slices with a known crystallographic orientation, which after a polishing process will be used for substrates in the LPE experiments. The top of the crystal, which has grown entirely on the solution's surface, is generally not flat due to growth instabilities on the solution's surface and requires polishing in order to have a well-oriented and smooth plane for using as reference for subsequent oriented cuts. The polishing process was performed with a Logitech PM5 polishing machine.

After obtaining the well oriented and polished flat plane, the crystal is placed in a Minitom Struers diamond disk saw to obtain plates 1.5-2 mm thick, and perpendicular to the crystallographic direction which has been chosen for epitaxial growth. In our case, for the growth of epitaxial layers of the RTP family, we chose substrates perpendicular to the ***c*** crystallographic direction because of the low lattice mismatch between the substrate and the layer and the favorable optical properties on this plane. In few cases, we have used substrates perpendicular to the ***a*** crystallographic direction. The disk that is usually used for cutting the slices is 0.12 mm thick, although other disks are available if needed. Using this equipment, we can make a precise cut of the substrates without any crack.

Polishing the raw substrates involve three steps, with which surface roughness can be reduced to below 20 nm with a bend radius of above 80,000 mm. Reduced surface roughness provides a smooth interface between the epitaxial layer and the substrate, which in turn produce less defects and roughness on the epitaxial layer. First, the substrates are polished with 9 µm alumina powder which removes the major roughness of the substrates. 3 µm and 1 µm diameter alumina powder are then used to create high optical quality surfaces. All these steps are performed with the help of the commercially available polishing suspension SF1 from the Logitech Company.

For epitaxies: Once the substrates are obtained, they are used to grow epitaxial layers over them using the LPE technique. In order to obtain the epitaxial layer with the required thickness and flatness after the polishing process, the epitaxial layer on one face of the substrate is removed for easy collimation and to measure the thickness of the remaining epitaxial layer. The remaining epitaxial layer is then polished, repeating the same procedure as described above in order to obtain the required thickness, roughness

UNIVERSITAT ROVIRA I VIRGILI
NEW PHOTONIC DEVICES BASED ON NLO(NON-LINEAR OPTICAL) CRYSTALLINE WAVEGUIDES
Muhammad Ali Butt

and flatness. After this process, the sample is ready for fabrication of channels on the epitaxial layer.

The end faces of the waveguides must be polished before optical characterization of the microstructures. This process is done by machinating the sample between two flint glass blocks on the substrate and epitaxial layer sides. Flint glass is used by taking into account the hardness of RTP and flint glass which is ~5 Mohs and ~7 Mohs, respectively [www.redphotonics.com, www.tedpella.com].

2.1.4. Microstructuring of epitaxial layers and substrates

Preliminary processing on the substrates/epitaxies is required for the fabrication of channel waveguides or any other structures like Y-splitters and Mach-Zehnder structures. This involves clamping substrates on glass to extend the surface area, the deposition of a metal layer which acts as a hard mask, spin coating to perform photolithography and finally etching/or ion exchange to obtain the required dimensions of the channels.

Sample preparation: The sample is glued on a glass substrate with unibond power epoxy resin in order to increase the area for further processing. This step is important in fabrication because the obtained samples are not large and are difficult to handle in spin coating and photolithography processes. The curing time of epoxy is usually around 6-7 hours, and it can sustain heating at 423 K without becoming detached from the glass. A sample cured in resin is shown as an example in figure 2.2.

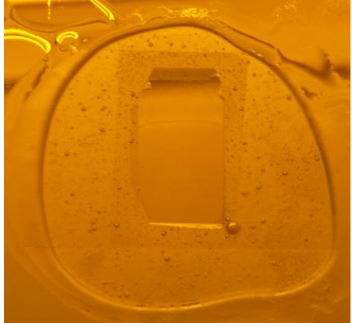

Figure 2.2. (Yb,Nb):RTP/RTP(001) sample cured in Unibond power epoxy resin

Metal deposition: A thin layer of metal acts as a hard mask for RIE and ICP-RIE, so that the required thickness of metal layer is determined by analyzing the selectivity between the metal layer and the material to be etched. Cr, Ni, Ti and Al layers have been deposited on RTP substrates in order to check the selectivity, layer quality and adhesion of these metals on RTP.

Two kinds of metal deposition techniques are applied in this study - sputtering and e-beam evaporation. The sputtering technique is available in the URV clean room, the device used is from AJA International Inc. ATC ORION/8/HV. E-beam evaporation was performed at the ORC clean room, University of Southampton, with a BOC Edwards auto500 system device.

In the e-beam evaporation technique, the metal to be deposited on the substrate is heated by an electron beam to a point where it starts to boil and evaporate. It is then allowed to condense on the substrate. This process takes place inside a vacuum chamber, enabling the material to evaporate freely in the chamber. Chromium layers of 700-800 nm were deposited using this technique under high vacuum, with a deposition rate of 0.2-0.3 nm/sec at a current intensity of 20-40 mA.

Sputtering is a technique used to deposit thin films of material onto substrates by creating gaseous plasma and then accelerating the ions from this plasma into a source material (target). These energetic ions erode the source material, and neutral particles in the form of individual atoms, clusters of atoms or molecules are emitted. These neutral particles travel in a straight line unless they come into contact with the substrate and a thin layer of source material is deposited.

For ion-exchange experiments, a thin layer of 200 nm of Ti is sputtered at 200 W with deposition rate of 0.4 Å/sec on the RTP substrate which acts as a hard mask for ion exchange.

Photoresist deposition: Prior to lithography, a thin layer of photoresist (PR) is deposited to transfer the designed patterns to the metal layer in the case of RIE and ICP-RIE. PR is considered to be the radiation sensitive compound that can be used to form a patterned coating on the sample. It consists of three components; a photosensitive compound, a base resin and an organic solvent. PRs are categorized in two types: positive or negative PR.

In positive PR, the UV exposed parts become more soluble in the developer and are removed. Before exposure, the photosensitive compound is unsolvable in the developer solution. However, during exposure, the photosensitive compound is able to absorb radiations in the exposed patterns. This helps to change its chemical structure, which becomes soluble in the developing solution and the exposed areas are removed after development, as shown in figure 2.3.

In a negative PR, the exposed regions become less soluble in the developer and it creates the reverse patterns on the PR as found on the mask. The basic phenomenon behind this sort of feature is that the negative photoresist causes a polymer crosslinking due to chemical reaction after exposure. The crosslinked polymer has a higher molecular weight and becomes insoluble in the developer. As a result the unexposed parts are removed after development, as shown in figure 2.3.

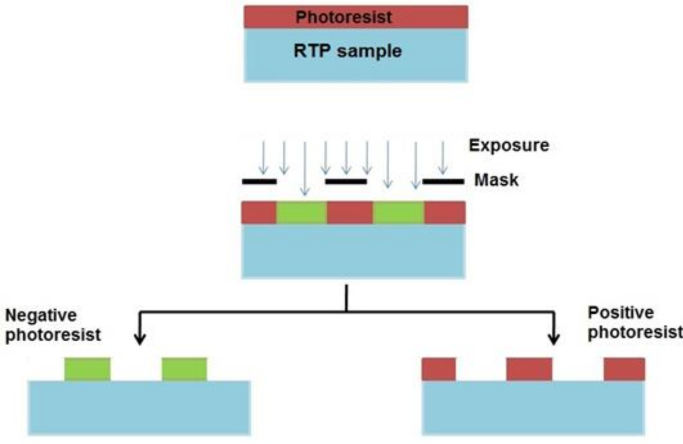

Figure 2.3. Demonstration of negative and positive photoresist. The exposed part of the PR is shown in green and the non-exposed part is shown in dark red

In this thesis, we have used two kinds of positive PR for RIE experiments; a thin layer of positive PR S1813 was deposited on the metal layer, using a spin coater at 5,000 rpm for 60 sec. PR thickness of 1.3 µm was obtained with this rotation. In order to obtain thick PR layer, S1828 photoresist was deposited on the sample by spin coating at 2,500 rpm. The coating was repeated twice in order to increase the thickness of the resist, to obtain a layer with a thickness of 8 µm. This kind of PR is available in the clean room of Optoelectronic Research Center (ORC), Southampton.

The second kind of positive PR which was used for RIE experiments was AZ 1505, spun on the samples at 5,000 rpm for 45 sec to obtain a thickness of 0.45-0.5 µm with the help of a standard spin coater. This kind of PR was also used for samples fabricated by ICP-RIE and ion exchange process. These spin coatings were performed in the URV clean room.

Photolithography and laser lithography: Photolithography is a process in which patterns are transferred from a photomask to a thin coat of photosensitive material - a PR layer covering the surface of the sample. These patterns are merely temporary features on the PR, in order to obtain the waveguide features and they must be transferred onto the underlying layers of the device [Jansen1996].

The photomask is an important part of the transfer of patterns on the PR coated samples when working with a photolithography. In this study, we used two kinds of photomasks: a light field mask and a dark field mask. The light field mask is used to transfer the patterns on the epitaxial layer grown samples, as it only protects the desired channels, leaving behind the unwanted part which can be removed afterwards with the help of etching, as can be seen in figure 2.4. The photomasks usually consist of glass with a patterned Cr layer on it.

The dark field mask is used to transfer the patterns directly onto the RTP substrates. As a result, the desired inverted channels are obtained by an etching process and then filling these cavities by growing an epitaxial layer inside them, as can be seen in figure 2.4. In this thesis, the commercial photomasks were adquired by Compugraphics International Ltd (UK), and used for RIE. The mask design is reported in the appendix.

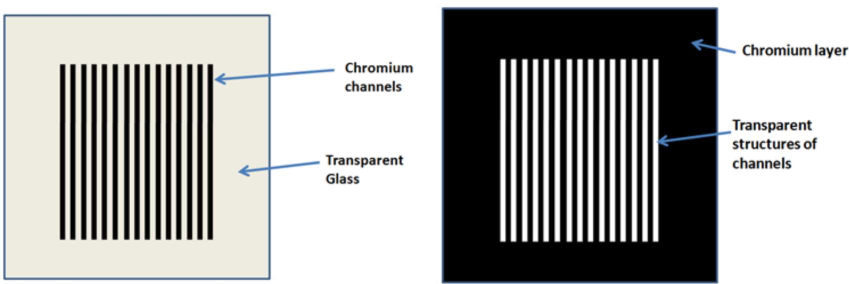

Figure 2.4. Top view of light field mask (left) and dark field mask (right)

For ion exchange experiments, a dark field mask was fabricated on a commercially available glass (50 x 50 x 2 mm^3) coated with Ti layer and PR. The patterns were transferred to that photoresist-Ti-glass with the help of Heidelberg Instruments DWL 66 fs laser lithography equipment, available in the URV clean room, followed by development of the PR.

Photolithography should take place in a clean processing room. This is a requirement due to the fact that dust particles in the air can remain on the sample or mask and can cause defects in the circuit features. The dilemma even becomes worse when the dust particle sticks to the photomask, as it behaves as an opaque pattern and is transferred to the PR and finally to the circuit features, as shown in figure 2.5.

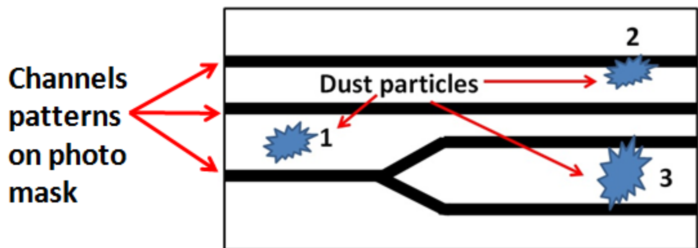

Figure 2.5. Various ways in which particles can interfere with photomask patterns

As an example, figure 2.5 shows three dust particles which are adhered to the photomask. Particle 1 can result in the development of a pinhole in the device feature. Particle 2 is adhered on the edge of the pattern, and can cause a limitation of the light flow. Particle 3 may be responsible for a short junction between two optical structures and renders the structures ineffective. For the fabrication of most integrated optical structures, a class 100 clean room is therefore necessary, which means that the dust count must be four orders of magnitude lower than that of ordinary room air. However, a class 1 or class 10 clean room is required for photolithography in which the dust count is even lower.

There are many lithographic techniques, e.g. UV lithography, extreme UV lithography, X-Ray lithography, electron beam lithography and nanoimprint lithography. The main difference between these techniques is the resolution limit.

In contact lithography, the mask is in direct contact with the wafer, which is known as contact printing. A collimated beam of UV light is exposed on the photoresist for a fixed

time. This gives a very high resolution of ~ 1µm. The basic set-up of contact printing is shown in figure 2.6.

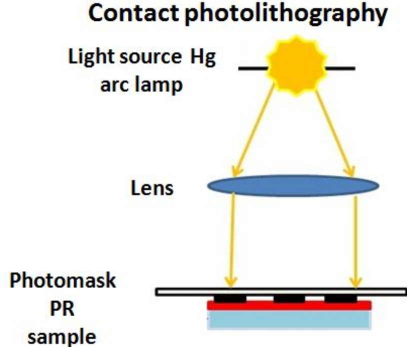

Figure 2.6. Diagram of the contact photolithography method

However, there is one major disadvantage to this method, which is that a dust particle may become embedded in the mask when it is brought near the contact with the wafer. This dust particle can permanently damage the mask [Jansen1996].

The second way of lithography is proximity lithography which is also known as proximity printing, and involves a small gap of 10-50 µm between the photomask and the wafer during exposure. This method is used to minimize the chances of photomask damage, but reduces the resolution to a 2-5 µm range, due to the optical diffraction at the feature edges. The basic set-up of this method is shown in figure 2.7.

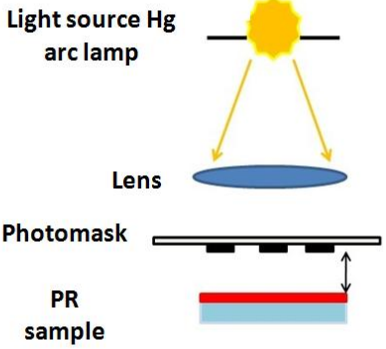

Figure 2.7. Diagram of the proximity photolithography method

Laser lithography is a maskless technique that is used to write complex designs with small structures, with the help of a focused laser beam. It provides much better quality and throughput. This technique can write arbitrary microstructures with minimum feature sizes down to 500 nm on almost any material. It is commonly used in mask-making or the direct writing of microstructures for production and R&D. It eliminates the turnaround time needed for the mask-making process and makes it quick and easy to adjust a prototype design.

In this thesis, both kinds of lithography techniques, laser lithography and photolithography techniques are used depending on the size of the sample. If the sample is too small and could not possible to perform laser lithography then photo masks are fabricated by using laser lithography. Laser lithography (Heidelberg Instrument DWL 66fs) was used in the URV clean room, with energy of 20 W, 2100 defocus with 1% filter. These parameters are obtained by optimizing the energy and defocus of the laser, as high energy can lead to overexposure.

For RIE experiments, we used proximity photolithography performed in the clean room available at ORC with a SussMicrotec Mask Aligner 6 with a 365 nm mercury lamp working at 16.5 mW/cm^2 for 12-13 sec. For the ion exchange and ICP-RIE experiments; we used contact photolithography with the help of the MG 1410 mask aligner with an exposure time of 1-2 sec depending on the reflectivity of the metal masks used. This equipment is available at the URV's facilities.

PR Developing: We used two kinds of developers to remove the exposed part of the photoresist. In order to remove the AZ1505 photoresist used in the URV clean room, we adopted AZ®726(MIF), which contains 2.38 % tetramethyl ammonium hydroxide (TMAH) in H_2O with surfactants added for fast and homogeneous substrate wetting. This PR developer is obtained from Microchemicals Company. In the ORC clean room, we tried the MF 319 developer, which is an alkaline corrosive solution containing tetramethylammonium hydroxide in order to remove photoresist S1813 and S1828.

Metal chemical etching: Metal chemical etching was used to remove the unwanted parts of metal from the sample in order to expose the desired part of the sample for etching. For instance, Ti, Al and Cr, were etched using three different kinds of chemical etchants. A mixture of H_2O_2 and NH_4OH with a molar proportion of 2:1 was used to

remove Ti. In the case of Al and Cr, commercially available Aluminium etchant and Chromium etchant was used respectively.

2.1.4.1. Reactive Ion Etching (RIE)

Reactive Ion etching (RIE) is a dry etching process in which the substrate is basically etched by a combination of chemical and physical interactions between the etching gas and the substrate. The physical mechanism deals with the bombardment of high energy ions that decompose the material, and the chemical mechanism forms volatile species from the induced reactions on the material surface with the species from the plasma. The etch rate and sidewall angle can be optimized by varying the combination of chemical and physical parameters of the etching process [Winnall 2000]. The integrated optical devices obtained by RIE generally have low propagation losses with smooth sidewalls, so the sidewall slope is a vital factor in characterizing device performance. The RIE process also produces some contaminants that are considered unsuitable for microelectronic processing. Plasma is created from a suitable feed gas (e.g SF_6 for RTP etching) by electron-impact dissociation/ionization of the gas phase into an etching environment which contains neutrals, electrons, photons, radicals (F^*) and positive (SF_3^+) and negative (F^-) ions. Reactive radicals are transported from the plasma to the surface of the substrate. Etching is assisted by the positive ions, which are forced to move towards the substrate from the glow region. Reactive radicals adsorb on the sample’s surface, which produces active sites since it helps to eliminate the top layer which may otherwise passivate the surface. The adsorbed species must start the chemical reaction with the sample. In the case of fluorine based etching of RTP, chemical reactions between the F species and the surface produce either volatile species or their precursors. This mechanism is known as ion-induced RIE. If the reaction products are volatile then it is easier to convert the reaction product into the gas phase. To accelerate this process, chemical etching is assisted with physical etching by ion bombardment with the help of sputtering. This mechanism is known as ion inhibitor RIE. In order to avoid the redeposition of the desorbed species, these by-products should be pumped out from the chamber [Jansen 1996].

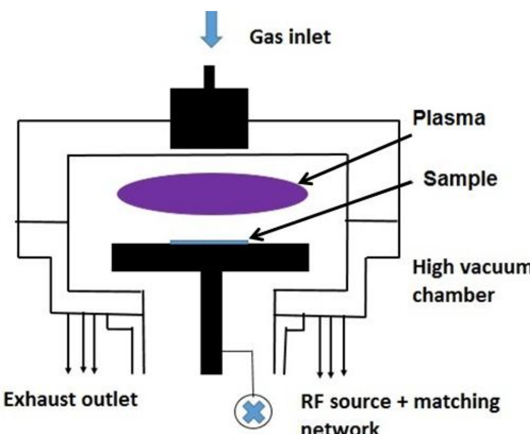

Figure 2.8. A schematic diagram of the RIE system

Mainly, all the RIE experiments were performed at the Optoelectronics Research Centre, at the University of Southampton. A Plasmalab 80 plus RIE system (Oxford Instruments) with a RF frequency of 13.56 MHz was used, with a recipe of 250 W, 40 mTorr pressure and a gas combination of Ar(10) and SF_6(10) kept at 20 sccm. The diagram of the RIE system is shown in figure 2.8.

The fabrication involves a series of steps to reach the point of etching, which are summarized in figure 2.9.

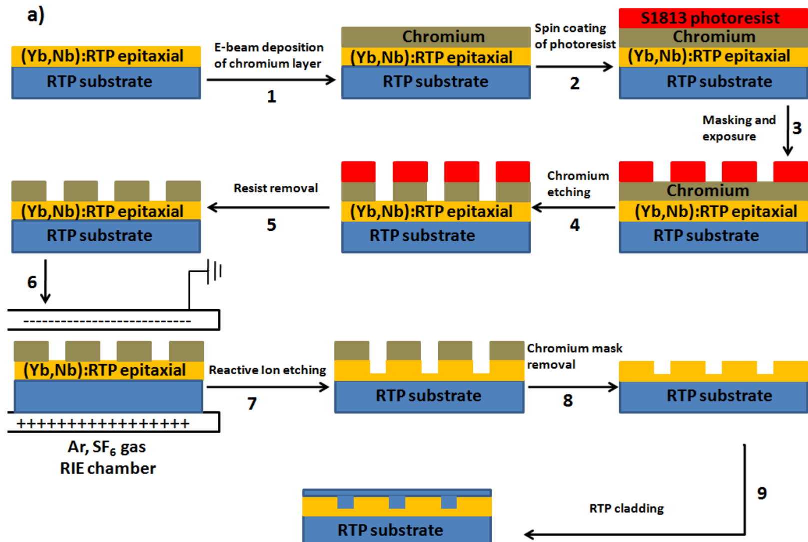

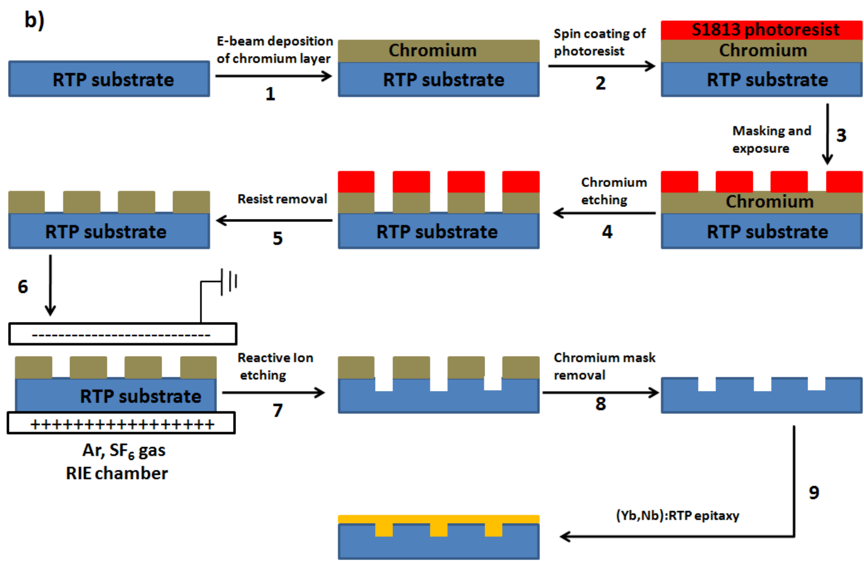

Figure 2.9. Steps involved in the fabrication process of rib waveguides, a) in the epitaxial layer, b) in the substrate

2.1.4.2. Inductively coupled plasma reactive ion etching (ICP-RIE)

Plasma is a partially ionized gas which is created by the collision of free electrons with neutral atoms/molecules resulting in two electrons and one ion through a dissociative process. This collision can also result in other species, such as negative ions, excited molecules, neutral atoms and ions depending on the energy of incoming electrons. The light emitted by the plasma is due to the return of excited electrons to their ground state. Each gas emits light at specific wavelength because the energies between the electron states are well defined which gives the possibility to analyze the plasma.

Reactive ion etching (RIE) is the dominant etching process for the transfer of fine features from the hard mask to the wafers. In standard capacitively coupled RIE systems, the ion energy is controlled through chamber pressure or applied RF power. The fact is that, chemical concentrations in the plasma can be changed by changing the power and changing pressure effects the uniformity of the etching process across the wafer [Mauer 1979, Kao 1990].

Capacitively coupled RF plasmas are the most commonly used plasmas in dry etching. In general, the power is applied to the upper or lower electrode having a frequency of 13.56 MHz. As a result a dark sheath is formed on all the surfaces in the reactor, electrodes and walls which acts as some kind of dielectric or a capacitor helping to transfer the applied power to the plasma. As the electrons are lighter than positive ions, they travel much longer distances and in this way, they collide more frequently with the reactor walls and electrodes and consequently are removed from the plasma. This would leave the plasma positively charged but it has to remain neutral. To ensure the neutrality of the plasma, a DC electric field is formed by the capacitor between power generator and electrode which repel the electrons from the walls as shown in figure 2.10.

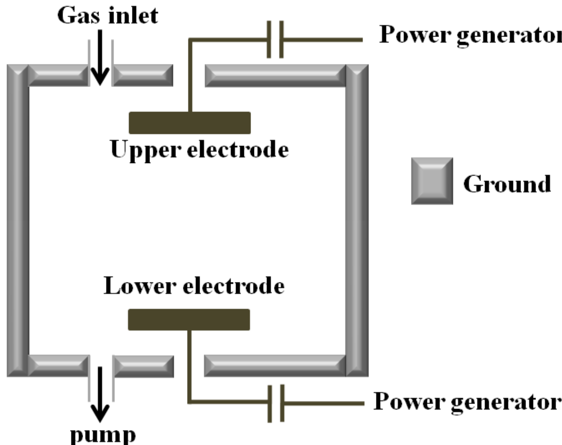

Figure 2.10. A schematic diagram of the RIE system

During the first few cycles, the capacitor is negatively charged because the electrons generated in the plasma accumulate on the electrode. In this way, a negative DC bias voltage is formed on the electrode, which repels the electrons. The AC voltage becomes then superposed on this negative DC voltage as shown in figure 2.11.

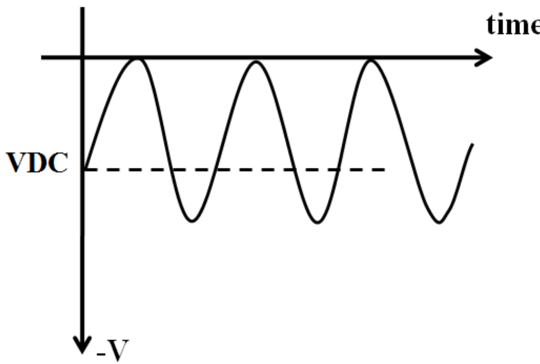

Figure 2.11. DC and AC voltage on the powered electrode

The dimensions of the reactor are fixed, so process parameters can influence the DC voltage. DC voltage is created to repel electrons therefore, if the electron density and electron energy are higher, more negative voltage is necessary to repel a large number of electrons. By following this reasoning, the tendencies of the DC bias voltage can be determined.

The electronegativity of used gas or gases can determine the DC voltage. Gases such as O_2, N_2, etc are less electronegative therefore they have very high negative DC bias voltage. The atoms of group VII are prone to absorb any free electron which passes nearby. Flourine, chlorine and bromine containing gases are much more electronegative therefore these gases can decrease the density of the free electrons in the plasma. Flourine containing gases are more electronegative than chlorine and bromine containing gases. In the case of fluorine based etching of RTP, chemical reactions between the F atoms and the surface produce either volatile species or their precursors. This mechanism is known as ion-induced RIE and acts as ion inhibitor RIE. In order to avoid the redeposition of the desorbed species, these by-products should be pumped out from the chamber [Jansen 1996]. Plasma is created by electron-impact dissociation/ionization of the gas phase into an etching environment which contains neutrals, electrons, photons, radicals (F^*) and positive (SF_3^+) and negative (F^-) ions. SF_6 is a very electronegative gas; the DC voltage of its plasma can be a factor of 10 times less than the DC voltage of N_2 plasma. In general, the DC bias tends to become rapidly more negative when a small flow of gas with low electronegativity is entered in the plasma. Small flows of electronegative gases do not influence the DC bias very much.

At higher pressure, the electrons have the higher tendency to collide with the molecules in order to generate new free electrons and positive ions. As a result, an increase in pressure can increase the number of free electrons turning the DC voltage more negative. The DC voltages are also a function of the energy of the free electrons. At higher pressure, electrons suffer more collisions; therefore they gain less energy between collisions. The electron energy decreases with pressure.

The influence of power is straightforward: an increase of power increases both the density and the energy of the free electrons. Therefore, the DC voltage becomes more negative with increasing power.

The etching mechanism explained here is valid for all types of plasmas etching. In general, plasma etching is a chemical etching, not a physical etching. This means, a molecule is formed due to the chemical reaction takes place between the sample and the gas atoms, which is removed from the sample. Some sputtering is always present due to the existing DC bias. For the large majority of the etching processes, this physical etching component is so small that it can be neglected. If the reaction products are volatile then it is easier to convert the reaction product into the gas phase. To accelerate this process, chemical etching is assisted with physical etching by ion bombardment with the help of sputtering.

The main steps in the etching process are:

1) Formation of the reactive particles.
2) Arrival of the reactive particles at the surface to be etched.
3) Adsorption of the reactive particles at the surface
4) Chemisorption of the reactive particles at the surface.
5) Formation of the product molecules.
6) Desorption of the product molecules.
7) Removal of the product molecules from the reactor.

Inductively coupled RF plasmas: In capacitively coupled RF plasmas, it is not possible to generate plasmas at low pressure: 10 mTorr is typically the lowest pressure at which plasma can be sustained. In the field of integrated optics, high aspect ratios are required which can only be obtained if the ions come in at nearly perpendicular angles. For this

condition to be fulfilled, a large mean free path is required which means that there should be little or no collisions of the ions in the dark sheath. Therefore the pressure must be reduced as much as possible which helps to obtain an anisotropic etch process by the use of a passivation layer at the vertical surface. Inductively coupled plasmas and electron cyclotron resonance plasmas are 2 types of plasmas which combine the quality of high density plasma at a low pressure.

In the beginning of the 1990s, the inductively coupled plasma has been increasingly used in the industry. In this decade, inductively coupled plasma sources are known to etch aluminium. The beauty of this technique is: the generation of high density and uniform plasma at low pressure, the electrons and ion density can be controlled independently from the energy of the ions which collide the substrate. These properties make this technique more powerful than a capatively coupled source. There are two kinds of inductively driven sources using cylindrical or planar geometries as shown in figure 2.12. It is not vital to use the multipole permanent magnets but the density and uniformity of plasma increases when they are present. An RF voltage is applied to the coil which produces an RF current as a result magnetic field is induced in the reactor. Therefore, the magnetically conductive walls are not important but they should be dielectric. In order to increase the ion bombardment on the substrate, it is possible to apply a low extra (RF, low frequency or DC) bias voltages to the substrate holder which does not play any role in plasma generation. The ions and electrons are mainly generated by the inductive coupling. By using this configuration, it is possible to control the plasma density and the energy of incoming ions independently.

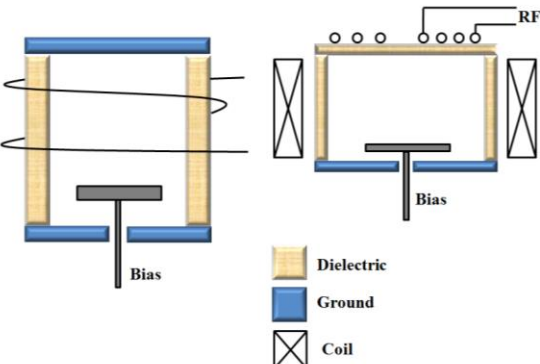

Figure 2.12 a): Inductively coupled plasma reactor, using a cylindrical coil, b) Inductively coupled plasma reactor, using a planar coil

The most common geometry for commercial equipment is with the planar coil together with multipole magnets, results in high density and uniform plasmas [Lieberman 1994, Paranjpe 1994]. Apart from this, it also requires less dielectric material which makes this geometry easy to fabricate. Quartz would be a suitable dielectric but it etches when fluorine containing plasmas are used. Therefore, the preferred dielectric material is alumina (Al_2O_3) which has excellent dielectric properties but its hard and expensive to manufacture. Pressure lower than 20 mTorr can produce ion densities of the order 10^{11} to 10^{12} per cm^3, which are two orders of magnitude higher than for the traditional capacitively coupled plasmas. However, an RF power of at least 100 W is required to maintain the inductively coupled plasma. It should be noted that, in addition to the inductive coupling there is a small contribution from capacitive coupling which is produced by the dielectric walls acting as a dielectric of the capacitor formed between the lower part of the coil and plasma. Therefore, a capacitively coupled plasma is also formed which helps to strike and maintain the plasma. Etch rate of the order of 1 μ/min can easily be obtained at pressures around 10 mTorr. At this low pressure, it is easier to obtain walls with a well-controlled vertical profile [Hill 1996].

2.1.4.3. Ion exchange

Various methods to produce graded index waveguides such as ion exchange, proton exchange and ion implantation on KTP have been successfully implemented in the literature. In this study, we created channels by Cs^+ exchange in RTP substrates in order to obtain a refractive index contrast between the ion exchange region and the surroundings. The exchange process takes place in a $CsNO_3$ melt at 698 K for two hours.

The homemade photomask, described in section 2.1.4, is used to transfer the patterns to the (001) oriented sample aligned along the desired crystallographic direction. A thin layer of 200 nm of Ti is sputtered on the RTP substrate, which acts as a hard mask for diffusion. A thin layer of photoresist AZ1505 is coated on the Ti sputtered substrate. The sample is exposed by mask aligner photolithography with the help of a prepared photomask for 1 s (due to the high reflectivity of Ti, the exposure time is short, otherwise the channels would be wider than expected), which transfers the patterns onto the resist and the same process is then repeated to etch Ti as in the mask preparation.

The metal channel pattern must stay on the sample during the diffusion process in order to have a selective ion exchange, otherwise Cs^+ ions can diffuse all over the sample and

the result will be a planar waveguide. A platinum crucible filled with 25 g of $CsNO_3$ is maintained at 698 K for 1-2 hours. The processed sample is then dipped in the $CsNO_3$ melt 6 mm below its surface at 698 K for 2 hours at a rotation of 40 rpm. The diagram of the Cs^+ ion exchange process is shown in figure 2.13.

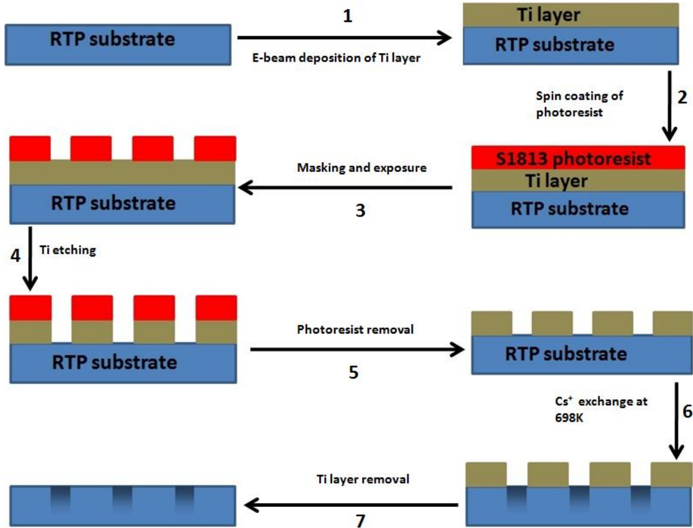

Figure 2.13. Steps involved in the process of Cs^+ exchange on RTP substrate

2.2. Characterization techniques

In this section, we have given a detailed description of the experimental equipment, with a precise description and the schematic views of the systems used to measure the spectroscopic and non-linear optical properties. These experimental techniques are available at the Rovira i Virgili University and at the University of Barcelona, Spain.

2.2.1. Microscopy techniques

In this section, we describe the main characteristics of the microscopy techniques used to observe the surfaces of the samples before and after processing.

2.2.1.1. Reflection and transmission optical microscopy

Reflected light microscopy, often termed incident light or metallurgical microscopy, is used to observe specimens that are opaque/transparent and which reflect back the light to the microscope objective by either specular or diffused reflectance. The high contrast enhances the observation of details on the sample surface, and there is no need for special preparation of the sample. An Olympus BH-2 microscope is used in this study. In transparent samples, this microscope also allows observation using transmitted light. In this technique, the light is transmitted from the source, and passes through a condenser to focus it on the sample to obtain very high illumination. After the light passes through the specimen, its image is magnified with the help of objective lenses and viewed.

2.2.1.2. Environmental scanning electron microscopy (ESEM)

Scanning Electron Microscopy (SEM) is an imaging and analytical technique which started to appear commercially in mid 1960s. It requires a high vacuum pressure, which is its primary limitation. Another limitation is that sample has to be clean, dry and electrically conductive. Non-conductive samples have to be coated with a conductive film of gold in order to avoid sample charging.

ESEM was introduced in the mid-1980s and enables its users to vary the sample environment across a range of pressures, temperatures and gas compositions. ESEM contains all the features of the conventional SEM, and the limitation of high vacuum pressure is removed. Furthermore, samples which are wet, dirty, oily and non-conductive can be used for examination remaining in their natural state without any modification or preparation. Samples with any composition can be examined with high resolution secondary electrons, backscattered electrons or current imaging in a gaseous environment at pressures as high as 50 Torr and temperatures as high as 1773 K.

A conventional ESEM consists of an electron column which creates a beam of electrons which interacts with the sample placed in a sample chamber. When an inner shell electron is displaced from an atom, a higher energy outer shell electron jumps in to fill the gap and releases an X-ray photon. The energy differences between the shells are well-defined and specific to each element, so this energy of the X-ray can be associated with the emitting atom. The spectrometer counts and sorts the X-rays, usually on the basis of energy (Energy Dispersive Spectrometry, EDS). The numbers of X-rays are then

plotted on a vertical axis against the energy on the horizontal axis. The peaks on the spectrum are the elements present in the sample. The energy level of the peak gives an indication about the element. The number of counts in the peak indicates the concentration of the element. The electrons with energies ranging from a few hundreds to tens of thousands of electron volts are directed by an electrostatic field through a very small spot called the crossover, entered in the sample chamber and focused as the smallest possible spot on the sample surface. As the beam penetrates the sample, energy is produced in different ways. Two major ways of emission are secondary electrons (SE) and backscattered electrons (BSE).

Electrons which are emitted by the interaction of the primary electrons of the beam with the sample are known as secondary electrons. These electrons have very low energy and can only escape from a very shallow region on the sample surface. A hillock emits more electrons than a valley, and hillocks are therefore brighter than valleys. On the other hand, backscattering electrons (BSE) are the primary beam electrons which are scattered back out of the sample by elastic collisions with the nuclei of the sample atoms. Elements with a high atomic number backscatter more electrons, which creates bright areas in the image and gives important information about the sample composition. Both emission modes are potentially a signal which can be used to create an image.

In this study, a FEI QUANTA 600 ESEM, which is available at Servei de Recursos Científics i Tècnics of the Universitat Rovira i Virgili, is used to obtain the morphology of the samples, the cross-sectional view and EDS which gives identifies the elements present in the sample.

2.2.1.3. Confocal Microscopy

Confocal microscopy is a non-contact technique used to measure the profile of the samples and surface metrology. It creates sharp images of the specimen with less haze and better contrast than when using a conventional microscope. It is capable of building three dimensional (3D) reconstructions of a surface of the specimen by aligning a series of thin slices taken along the vertical axis and surface topographies on a millimeter to nanometer scale.

In order to understand the confocal microscopy, it is necessary to imagine a pair of lenses that focuses the light from the focal point of one lens to the focal point of the

other lens. This is illustrated by the red rays in figure 2.14. The green rays represent light from another source (with the same wavelength as red) in the specimen, which is not falling at the focal point of the left hand side lens. It is obvious that the image of the red point is not at the same location as the image of the green point. It is not important that the points (red and green) fall at the focal point of the lens to form an image in the system of lenses. In confocal microscopy, the aim is only to observe the image of the red point by placing a screen with a pinhole on the other side of the lens system.

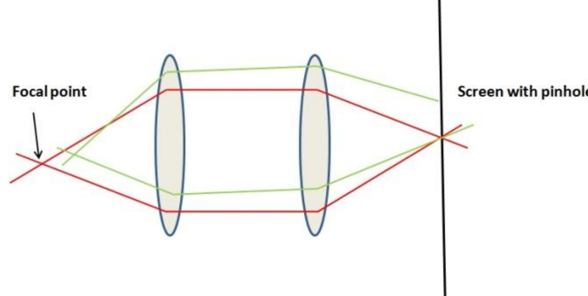

Figure 2.14. Confocal microscopy diagram

The confocal microscope works using point-by-point illumination of the sample, and rejects the out of focus light. In confocal microscopy, only a few photons are emitted and collected at any given moment. To avoid receiving a noisy image, each point has to be illuminated for a long time to collect enough light to make an accurate measurement. This increases the time needed to create a point-by-point image. A high intensity light source can be used to reduce the time for measuring the sample.

In this study, a Sensofar PLμ 2300 Optical imaging profile with a wavelength of 470 nm is used to observe the surface quality of as-grown and polished epitaxies, and to measure the roughness, bent radius and the profile of the epitaxial layers which helps polish the layers until a certain thickness is achieved.

2.2.1.4. Atomic force microscopy (AFM)

Atomic force microscopy (AFM) was invented by Binning *et al.* in 1986 [Binnig 1986]. It is based on the measurement of the forces acting between a fine tip and a sample which depends on their distance. The forces measured by AFM can be classified into

long range forces and short range forces. Long range forces work on the principle of the Van der Waals force and capillary forces due to the thin water layer that is often present in an ambient environment. However, when the scanning tip is in contact with the surface of the sample, quantum mechanical forces are used. This technique is applied to various environments (air, liquid, vacuum) and can be used to examine many materials, including metal semiconductors, soft biological samples, conductive and non-conductive materials. A tip is attached to a free end of a cantilever and brought very close to the surface. If the tip is far from the surface of the sample, then the force is attractive and at close contact the force is repulsive. Based on this attractive or repulsive force between the tip and the sample surface, a positive or negative bending of the cantilever is caused, which is detected by means of a laser beam which is focused on the back side of the cantilever. The reflected beam is collected by a photodiode, which is divided into four parts. When the laser is displaced vertically, this indicates a bending due to topography, while in the case of horizontal movement; it produces torsion due to friction (lateral force).

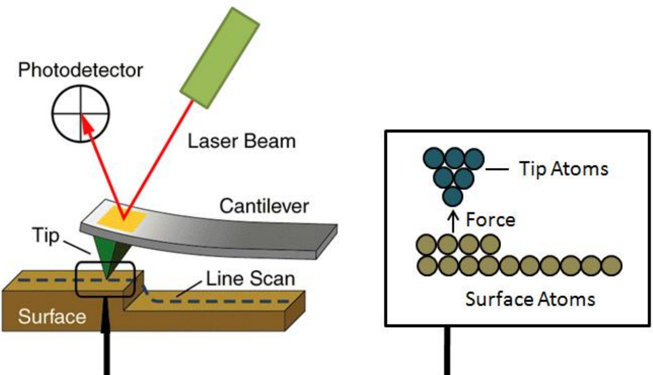

Figure 2.15. Principle of AFM. Picture inspired from Agilent technology website [www.agilent.com]

Various modes of operation can be used with AFM for the examination of samples: the contact mode, non-contact mode and tapping mode. In the contact mode, there is a soft physical contact between the tip and the surface of the sample, while in the non-contact mode the probe operates in the attractive force region, and the tip-sample interaction is minimized. In this study, we used the tapping mode, in which the cantilever oscillates close to its resonance frequency, which is controlled by an electronic feedback which ensures that the oscillation amplitude is constant throughout the feedback loop. When the tip passes over a hill, its vibration amplitude decreases, and when it passes over a

depression its vibration amplitude increases. This change in amplitude is detected by the optical system, and the tip-sample separation is adjusted in order to maintain the oscillation amplitude constant, and consequently the force on the sample is also maintained constant. This mode has an advantage over other modes in that it can eliminate many of the permanent shearing forces, causing less damage to the sample surface even with stiffer probes. It has a high lateral resolution, ranging from 1 nm to 5 nm, but the scan speed is slower than in contact mode.

An Agilent 5500 Atomic Force Microscope in the tapping mode was used in this study, with a Si tip with of 10 nm in diameter, oscillating at a resonance frequency of 75 KHz.

2.2.2. Electron probe microanalysis (EPMA)

EPMA with wavelength dispersive spectroscopy (WDS) is a technique for non-destructive X-ray microanalysis and imaging of solid materials performed using a specially designed electron microscope. It is equipped with four wavelength dispersive spectrometers and a high resolution energy dispersive solid state detector. The target material is focused with an electron beam of less than 1 μm diameter so that it produces secondary electrons, backscattered electrons, cathodoluminescence and X-rays. The interaction between electron beam and sample also produces characteristic X-rays that have a wavelength and energy characteristic of the atom from which they are produced. This electron microscope is considered hybrid as it combines the capabilities of both scanning electron microscope (SEM) and X-ray flourescence spectrometer (XRF). It has some other extended features such as fine spot focusing (~1 micrometer), optical microscope imaging and precision automated sample positioning. These advanced features help the user to perform measurements while observing the sample with an optical microscope or a secondary/backscattered electron image.

The incident electron beam on the sample may inelastically interact with the orbital electrons and cause them to dislocate from their shells around nuclei of atoms comprising the sample. As a result, the atom becomes excited and seeks to return to an unexcited state. There are two possible ways in which electron energy transition can occur. One way is the energy difference experienced by the removal of outer shell electrons. This is known as the Auger process. The second possibility for an atom to become unexcited occurs when the electron from the higher orbital jumps into the vacant

space of the lower orbital. This is accompanied by the emission of energy and a single X-ray of a narrow energy range. This is the basis for production of characteristic X-ray radiation.

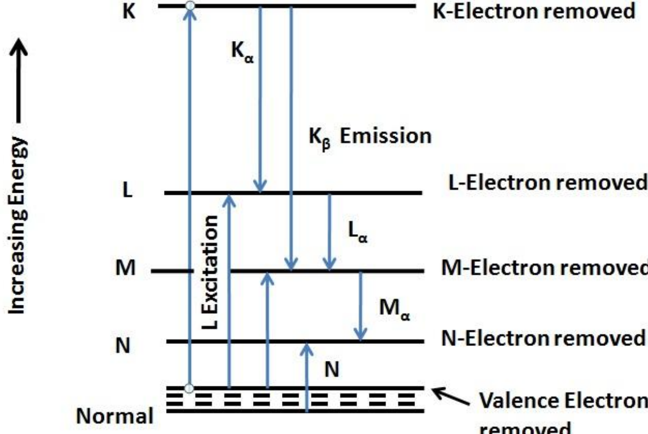

Figure 2.16. Energy level diagram for an atom, illustrating the excitation of the K, L, M and N shells and the formation of K_α, K_β, L_α, and M_α X rays

For instance, if an inner K shell electron is knocked out of its orbit by an incident electron, this gap is covered by the electron from L shell by emitting a K_α X-ray on some wavelength; there will be low probability of an M shell electron falling in and yielding a K_β X-ray. Similarly, M orbital electrons are more likely to fall in and yield L_α X-rays compared to N-orbital electrons producing L_β. The energy level diagram for an atom with the excitation of K, L, M and N shells is shown in figure 2.16.

This technique is able to provide a high spatial resolution of ~1µm, and high analytical sensitivity of less than 0.5 % for major elements and a detection limit of ~100 ppm for trace elements. It can have up to five wavelength dispersive spectrometers.

The equipment used in this study is a Cameca SX-50 microprobe analyzer available at Servei de Recursos Cientifico-Tecnics of the University of Barcelona. EPMA can perform fully qualitative and quantitative non-destructive elemental analysis of micron sized volumes on the surface of materials, with sensitivity at ppm level. For quantitative analysis, the X-ray spectrum of the single element is used for comparison with the known standard, to provide a very precise analysis of the chemical composition of the

sample. This method can determine the chemical composition of all the elements ranging from fluorine to uranium. The experimental conditions under which the EPMA measurements were performed are summarized in table 2.1.

Table 2.1. Measurement conditions used in EPMA analysis.

Element	**Line**	**Standard**	**Crystal**
O	K_α	RTP	PC1
P	K_α	RTP	PET
Ti	K_α	RTP	PET
Rb	L_α	RTP	TAP
K	K_α	KTP	PET
Nb	L_α	Nb	PET
Yb	L_α	YbF_3	LiF
Cs	K_α	CsI	PET
Na	K_α	Albite	PET

All the samples were prepared in the same way - by putting a small piece of crystal in a cylindrical container, to which we added a polyester resin with the proper catalyst, and let it cure. Both surfaces of the solid cylindrical sample (which contains the small crystal to be analysed) are lapped with a SiC disk, and the surface containing the crystal is then polished to optical quality with diamond powder of 3 and 1 μm.

The surface of the polished cylinder was sputtered with carbon to obtain a thickness approximately equal to the thickness in the standards used. The electron beam used to focus the sample has an intensity of 15nA and an acceleration voltage of 20 keV, depending on the concentration of the elements to be determined. The spectrometer crystals used are lithium fluoride 200 (LIF) (2d=4.028 Å), pentaerythritol 002(PET)

(2d=2.8742 Å), thallium acid phthalate 1011 (TAP) (2d=25.75 Å), and PC1 (W/Si multilayered with 2d=60 Å). The wavelengths covered by these spectrometer crystals range from 1 to 24 Å.

2.2.3. X-ray powder diffraction (XRPD)

In 1913, two English physicists, Sir W.H. Bragg and his son Sir W.L. Bragg, developed a relationship to explain why X-ray beams reflect off the faces of crystals at certain angles of incidence (θ), and they proposed an equation which relates the incident light to diffracted light. The planes act as reflecting mirrors, and the waves reflected by these lattice planes interfere constructively only if $n\lambda = 2\, d_{hkl} \sin\theta$, where λ is the wavelength of the radiation, n is an integer number (nλ is the path difference between the waves scattered by adjacent lattice planes with equivalent indices), d_{hkl} is the spacing distance between two consecutive planes in the atomic lattice and θ is the angle between the incident ray and the scattering plane. This equation is known as Bragg's law [Bragg 1912]. In 1919, A.W. Hull mentioned in his article [Hull 1919] that every crystalline material produces a specific pattern. In the case of different compounds, each material produces its own pattern independently of the others. The X-ray diffraction pattern of a pure substance is considered a fingerprint of the substance.

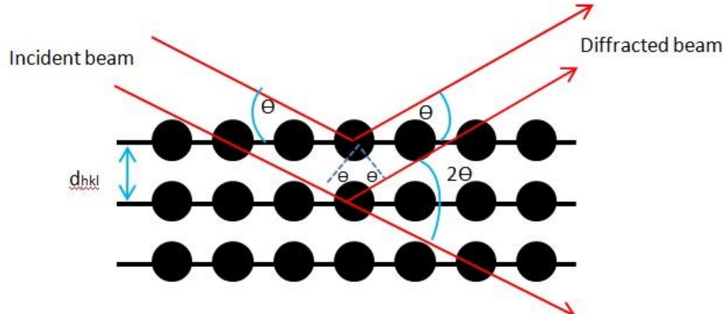

Figure 2.17. Diagram of the diffraction of the lattice planes according to W .L. Bragg

XRPD is therefore a suitable method for the characterization and identification of polycrystalline phases. In this study, the X-ray powder diffraction data are used to determine the cell parameters of the crystals in order to calculate the lattice mismatch between the substrate and the epitaxial layer. In this technique, the crystals are crushed

into a fine powder to reduce the size of the particles, each particle has a random crystal orientation, and a beam of monochromatic X-ray is allowed to fall on it. This is performed with a Siemens EM10110BU model D5000 X-ray diffractometer, using Bragg-Brentano parafocusing geometry and θ-θ configuration. It has an X-ray standard Cu-tube, the radiation used was $K_{\alpha 1}$ (λ_1=1.540560Å) and the detector was a double collimated scintillation counter. Cu $K_{\alpha 1}$ radiations were operated at 40 kV and 40 mA. The measurements were carried out in step-scanning mode with a diffraction angle (2θ) ranging from 10º to 70°. The X-ray powder diffraction patterns were recorded at step size=0.05°, step time=3 s to identify the crystalline phases and at step size=0.02°, step time=16 s to refine the unit cells. This equipment is available at Servei de Recursos Científics i Tècnics at the Universitat Rovira i Virgili. After obtaining the diffraction pattern, the precise cell parameters were obtained using the FULLPROF program based on the Rietveld method [Rodriguez- Carvajal 2000, Rietveld 1969, Young 1995].

2.2.4. Determination of refractive indices and dark mode spectra using a prism-coupler

Knowledge of the refractive indices of the materials used for research in waveguides is of great importance for computer modeling the waveguides in order to predict their optical response. If the refractive index contrast between the core and the cladding of a waveguide is known, it is therefore possible to predict the confinement level and propagation properties. In this study, a Metricon prism-coupler 2010 was used to couple the light into the waveguide in order to study the dark modes spectra to determine the refractive indices. Figure 2.18 shows the optical set-up used to measure the refractive indices of the substrates and epitaxial layers at 633 nm and 1550 nm. It is very simple, with a He-Ne laser source, a rotator stage table and a prism-coupler. The information from the detector is sent to the PC to calculate the refractive indices. Figure 2.19 shows a detail of the prism-coupler with the sample located between the prism and the coupling head.

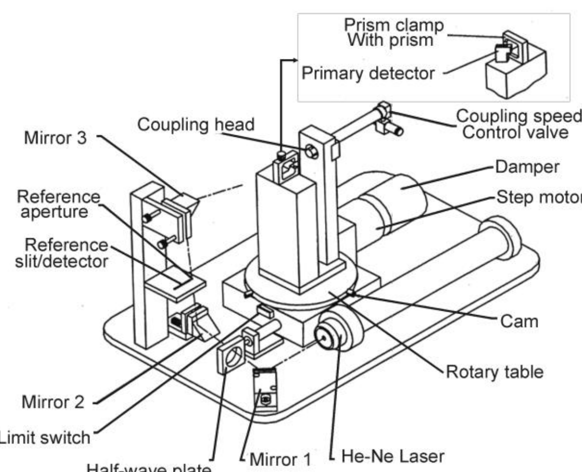

Figure 2.18. Optics module of Metricon prism-coupler model 2010. Picture reproduced from the user's manual provided by Metricon

In order to determine the refractive indices of the substrates and the different epitaxial layers, the refractive index of the prism should be higher than those of the substrates and epilayers. The phenomenon of total internal reflection thus takes place and the large intensity of reflected beam goes to the detector. As the table rotates, the sample coupled with the prism also rotates and the incidence angle of the beam falling on the prism also changes. This causes the reading on the detector to fluctuate, and for the particular angles known as mode angles, the light falling on the prism/film interface tunnels through the small air gap into the waveguide. This causes the null at the detector and a fall in intensity can suddenly be seen. By monitoring the angles at which the tunneling effect takes place, the thickness and refractive indices of the film can be calculated using computer modeling techniques. It is important to apply sufficient pressure between the prism and film; this reduces the air gap between the two materials, resulting in the maximum coupling to the waveguide.

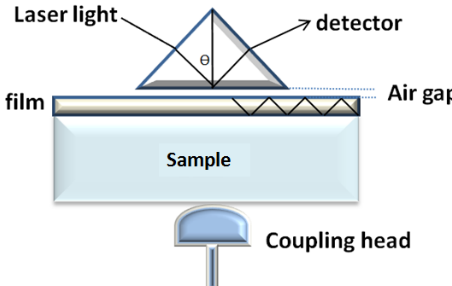

Figure 2.19. Experimental arrangement of the prism-coupler.

Either the refractive index or thickness of the film can be determined with the detection of one mode. However, when two modes are detected, both the index and the thickness can be determined and when more than two modes are found, a standard deviation and mean value for both the index and thickness can be determined. A low standard deviation value indicates the validity of the measurements of the refractive indices and thickness.

2.2.5. Waveguide laser set-up

In order to characterize the straight waveguides, bend waveguides, MZ structures and Y-splitters fabricated using different techniques, it is important to have a sound knowledge of optics in order to understand the properties of light travelling through the channels. The basic setup used to carry out this study consists of three precision 3-axis mobile stages. One is used to hold the sample; it has freedom to tilt the sample vertically and horizontally in order to correct the angle. The other two precision mobile stages are used to carry the input and output microscope objectives. In the optical set-up, there are many optical components that help in obtaining the near field pattern of the waveguides, such as mirrors, filters, polarizers and USB camera. Mirrors are used to direct the light from laser source to the input microscope objective. Normally two or more mirrors are used in the optical set-up in order to align the light vertically and horizontally with respect to the input and out objectives. If the laser light is not perfectly aligned or flat with respect to the optical bench, then there are chances that light can be lost without properly travelling in the waveguide. Sometimes, when high power lasers are used to couple the waveguides, the filters are necessary to attenuate the light in order not to saturate/damage the camera. Polarizers are the optical component which changes the

polarization of the laser light because sometimes the waveguides guide only one polarization (TE or TM), that is why it is mandatory to check the waveguides for different polarizations. Before starting the characterization of the sample, it is very important to align the set-up in order to obtain the real waveguide modes. USB camera can also be used to check the alignment of the waveguides with the input microscope objective by observing the parallelism of the end face of the sample with the objective. As a starting point, it is always better to couple the light with low numerical aperture objectives. The numerical aperture of a microscope objective is a measure of its ability to gather the light and resolve fine specimen detail at a fixed objective distance. The objectives with low numerical aperture have large working distance, bigger spot size which provides ease in coupling. But it totally depends on the size of the waveguides and hence numerical aperture (NA) of the waveguide. If the waveguide dimensions are too small then ideal coupling is carried out by objectives with higher numerical aperture otherwise low NA objectives can cause bad coupling and most of the light can be lost in the substrate. The output beam from the waveguide is out-coupled with a microscope objective. It is convenient to use the output objectives with low numerical aperture which makes it easy for mode observation. The near field pattern of the waveguide modes are collected with visible/ IR camera, which gives the intensity of the mode profile in pixels, and which has to be calibrated with a target sample for conversion back into microns. The laser sources used in this study are 632 nm, 1064 nm and 1520 nm HeNe lasers. The waveguiding setup is shown in figure 2.20.

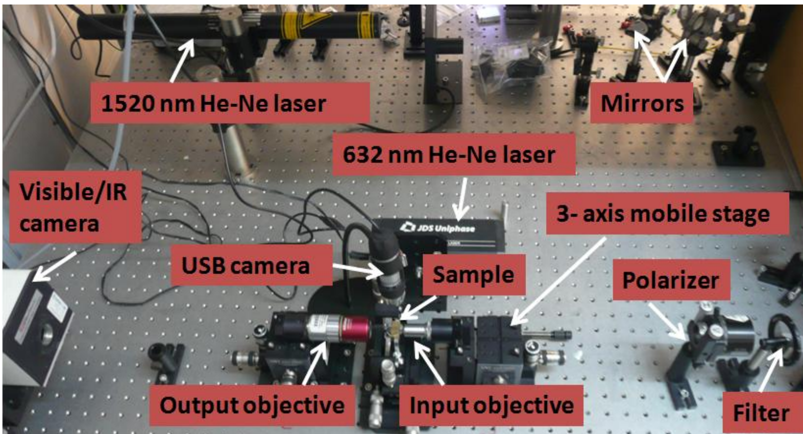

Figure 2.20. Experimental set-up for waveguiding.

2.2.6. Determination of the optical losses in waveguides

Single pass transmission method: Waveguide loss is one of the key parameters for the fabrication of efficient guided wave devices such as frequency doublers and electro-optic modulators. There are many different loss-measurement methods, such as cut-back for optical fibers (destructive), Fabry-Perot (requires single mode lasers), Prism coupling method (requires a minimum waveguide length of several centimeters) and many others. In this thesis, optical losses are measured by the simple method known as single pass transmission method. It uses the same optical setup used for measuring the input power before it enters the waveguide with the help of a power meter. Output power is recorded by placing the power meter behind the output objective after propagating through the waveguide. In order to calculate the propagation losses, we need to know the total losses. The total waveguide losses, L_T(dB) can therefore be determined by $L_T = -10\log(P_{total}/P_{in})$. The total losses depend on three factors - overlapping, fresnel and propagation losses as given by expression (2.1).

$$P_{\text{total}} = P_{\text{overlapping}} + P_{\text{fresnel}} + P_{\text{propagation}} \qquad (2.1)$$

Overlapping is the ratio between the input beam size and the waveguide mode size. This can be calculated by $1/e^2$, the Gaussian fit and the matrix method. Basically, overlapping is the mismatch between the focus of the microscope's objective and the area of the channel or rib. If the mismatch is high then most of the light does not enter the channel and can ultimately affect the waveguide's efficiency.

Fresnel losses are due to the reflectance from both the end facets of the waveguide. If the reflectance of the waveguide is high enough then the transmittance is low and this can affect the efficiency of the waveguides. In particular, the reflectance of both faces of RTP and its compounds is around 9%.

Propagation losses are then calculated by subtracting the overlapping losses and Fresnel losses from the total losses as in the above formula.

UNIVERSITAT ROVIRA I VIRGILI
NEW PHOTONIC DEVICES BASED ON NLO(NON-LINEAR OPTICAL) CRYSTALLINE WAVEGUIDES
Muhammad Ali Butt

Chapter 3
Bulk Single crystal and epitaxial growth

The history of KTP is dated back since 1890, when Ouvrard [Ouvrard 1890] first synthesized this crystal. This crystal cannot be grown directly from its melt because it melts incongruently at 1445 K when it is heated in air [Hagerman 1995, Satyanarayan 1999]. Traditionally KTP single crystals have been grown from high temperature solution (HTS) or by hydrothermal method. KTP single crystals were first grown on crystal seeds from the self-flux solution by *Gier* [Gier 1980]. Voronkova *et al.* applied a growth process, in which crystals were grown by the slow cooling of the saturated solution [Voronkova 1988a] and [Jacco 1984] demonstrated a growth with gradient transport at a constant ΔT. *Voronkova* and *Yanovskii* were the first to study the crystallization region of KTP in the K_2O- P_2O_5-TiO_2 system [Voronkova 1988b], later Iliev *et al.* [Iliev 1990] studied it in detail. Lliev *et al.* also determined the phase diagram of KTP in the K_2O- P_2O_5-TiO_2-WO_3 system as well as the viscosity of these solutions [Iliev 1990].

In phosphate solutions, a constant decrease in the temperature increases the viscosity of the solutions and creates supersaturation gradients in it. As a result, spurious nucleation may take place and crystals with inclusions could be obtained. These inclusions can be a source of cracks when the crystal is cooled to the room temperature by cooling the furnace. Bordui *et al.* and Vartak *et al.* [Bordui 1989, Vartak 2000] demonstrated that inclusion free crystals can be obtained by improving the mass transport in the solution by rotation of the seed in the solution. Seed rotation can be performed centrically or eccentrically of the surface of the solution. In centrically seed rotation, the crucible space is more efficiently used as compared to the eccentric rotation [Bordui 1987, Sasaki 1993]. But in accentrically rotation, there is an improvement of mass transport, especially if a centrically stirrer is added, thus minimizing the problems associated with non-homogeneous supersaturation in these viscous solutions [Carvajal 2000]. Sasaki *et al.* reported the crystallization of large KTP inclusion free crystal by controlling the cooling rate and crystal weight changes [Sasaki 1993].

Top Seeded Solution Growth (TSSG) is a flux growth technique generally used to grow crystals from high temperature solutions. HTS are used for growing crystals with incongruent melting and in the case with polymorphic transitions before melting. High

quality large single crystals of the KTP family can be grown by this technique in a single-zone furnace, as Cheng *et al.* [Cheng 1991a] have already demonstrated. In TSSG, crystal grows in a crystal seed placed in contact with the surface of solution that is why this technique is different from other flux techniques. With this technique, when the solution is cooled slowly, the crystal starts to grow in the supersaturated solution and continues to grow while the temperature decreases steadily. High quality inclusion-free single crystals with appropriate dimensions are obtained which are suitable for optical investigations.

When the crystals are grown at high cooling rate in viscous solutions, dendritic structures on the crystal surface and flux inclusion in the bulk crystals can be formed due to the rapid increase in the supersaturation of the solution [Dhanaraj 1992, Dhanaraj 1990]. TSSG has also been applied to grow KTP bulk single crystals by applying a pulling technique [Bolt 1991, Angert 1994]. Bolt *et al.* claimed that by avoiding the multifacet shape of the crystals by pulling during growth, the cutting of optical elements would be more efficient [Bolt 1991].

RTP was first grown by Zumsteg *et al*. by using the hydrothermal method in 1976 [Zumsteg 1976]. Oseledchik *et al.* determined the phase diagram of RTP in the phosphate system in the temperature range of 873-1373 K and obtained rhombic and cubic crystalline phases of RTP [Oseledchik 1992]. In order to avoid the problem associated with the non-homogeneous supersaturation in the self-flux RTP viscous solutions, a method to improve the mass transport in the solution was developed. It consists of a mixing system formed by a stirrer immersed 1.5-2 cm in the growth solution and two crystal seeds symmetrically distributed at several mm from the rotation axis in contact with the surface of the solution. The crystal seeds eccentrically distributed rotated with the same angular velocity than the stirrer [Carvajal 2000]. Carvajal *et al.* also introduced WO_3 in the solution to decrease its viscosity for improving the mass transport. They determined the primary crystallization region of RTP in self-flux and WO_3 containing solutions and observed that the RTP primary crystallization region was displaced to Rb_2O rich regions when the concentration of WO_3 was increased as shown in figure 3.1. For WO_3 concentrations higher than 20 mol%, the RTP crystallization region became narrow. The use of WO_3 solvent helps to decrease the homogenization time, the crystals can be grown at large cooling interval and the cooling process to obtain high quality crystals could be made faster than in self flux solutions [Carvajal 2000].

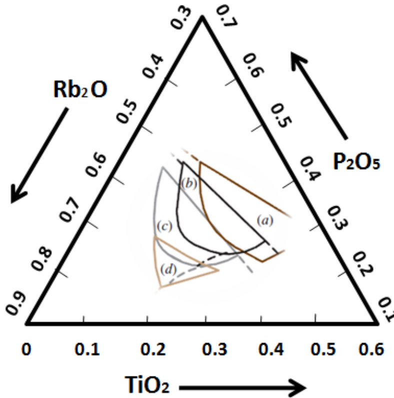

Figure 3.1. Crystallization region of $RbTiOPO_4$ in the system Rb_2O- P_2O_5-TiO_2-WO_3 for a) 0 mol % WO_3 b) 10 mol % WO_3 c) 20 mol % WO_3 and d) 30 mol % WO_3 in solution. [Inspired from Dhanaraj 2010]

Taking into account this previous knowledge in the bibliography, in this work KTP and RTP bulk single crystals will be grown by TSSG - slow cooling technique; using WO_3 as modifier in the solution, with centric seed, rotation, and pulling will be also applied in some cases, to enlarge the size of the obtained bulk single crystals.

There are different techniques to fabricate waveguides and these techniques can be classified in two families. Deposition techniques, consisting of deposition of high index thin film onto a low index substrate and exchange or diffusion techniques, where the principle is to create a high refractive index region in the substrate by introducing new atoms. More recently, a novel technique for the fabrication of step-index channel waveguides by refractive indices modification of the substrate by means of 3D direct laser has been demonstrated [Ródenas 2011]. Among all these techniques, in this work, we used liquid phase epitaxy (LPE) with posterior structuration and Cs^+ ion exchange method to fabricate channel waveguides. LPE is a technique that allows growing a homogeneous single crystal film on a substrate, obtaining the desired thickness of the film by adjusting the growth temperature and growth time. Cheng *et al.* used tungstate and pure phosphate arsenate self fluxes to demonstrate the growth of thin films of $KTiOP_xAs_{1-x}O_4$ (KTA) on KTP substrates by using LPE method [Cheng 1991b] and demonstrated the fabrication of step-index waveguides in the KTP family of crystals by using the LPE method [Cheng 1991c]. The KTA epitaxial layers were grown on KTP substrates, because the substitution of arsenic for phosphorus provides the desired refractive index contrast without altering the non-linear optical properties of the material.

In order to have defect free epitaxial layers, it is important to control the lattice mismatch between the substrate and the epitaxial layer. Good quality single crystal epitaxial layers of KTP were grown on substrates of the same family by using LPE method. Solé *et al.* [Solé 2002a, Solé 2002b] produced KTP thin films grown on $KTi_{1-x}Ge_xOPO_4$ substrates also using both tungstate and pure phosphate self-fluxes. Prior to epitaxial growth, substrate cleaning with dilute hydrochloric acid seems to improve the quality of the epitaxial layer on {100}, {011}, {110} and {201} oriented plates cut from a single crystal grown by the flux method. But the main interest lies in the {001} oriented plane because of the higher d_{33} non-linear optical coefficients of KTP and RTP. Cugat *et al.* demonstrated the growth of epitaxial layers of RTP doped with Yb and Nb on {001} RTP substrates [Cugat 2011a].
In this chapter, we summarize the growth of bulk single crystals by the TSSG and epitaxial layers by the LPE techniques.

3.1. Bulk single crystal growth for substrates

3.1.1. RTP bulk single crystal growth

The solution composition Rb_2O-P_2O_5-TiO_2-WO_3 = 44.24-18.96-16.8-20 (mol %) was chosen on the basis of the primary crystallization region of RTP in the Rb_2O-P_2O_5-TiO_2-WO_3 system with 20 mol % of WO_3 [Carvajal 2000]. The use of 20 mol % of WO_3 in the solution is interesting because it decreases the solution viscosity, as has been proved in solutions used to grow crystals of the same family [Iliev 1990].

The solution was prepared by mixing the desired quantities of Rb_2CO_3, $NH_4H_2PO_4$, TiO_2 and WO_3 used as initial reagents. In these experiments, a cylindrical Pt crucible of 125 cm^3, filled with about 170 g of solution was used. The axial thermal gradient in the solution was 1.5 K/cm for the first centimeter (near to the surface of the solution) and 0.8 K/cm for the next 1.5 cm. The bottom was hotter than the surface of the solution. The radial gradient was 1.8 K/cm and the crucible wall was hotter than the centre of the solution surface. The saturation temperature is defined as the temperature at which there is no apparent growth/dissolution of a seed when is immersed in the solution. The solution temperature was kept at about 80 K above the expected saturation temperature (T_s) for about 6 h to homogenize the solution. Subsequently, the saturation temperature was accurately determined by repeated seeding. The saturation temperature of the above RTP solution composition is around 1163 K. The supersaturation of the solution, needed

for crystal growth was obtained by slowly decreasing the temperature of the solution at a rate of 0.1 K/h for several K and then the cooling rate was reduced to 0.05 K/h for slow and steady growth. Normally, the cooling interval used for crystal growth is around 27-35 K, depending on the size of the crystal. The velocity of rotation was constant at 60 rpm during the initial stage of growth and then reduced in several steps till 40 rpm when the crystal gained in size. Once, we have obtained the sufficiently big size of the (001) plane, we pull the crystal 1 mm every day in order to increase the size of the crystal along the ***c*** crystallographic direction and pulling can be done for several days. As can be seen in table 3.1, different growth conditions were used. The crystals obtained were generally colorless, transparent and free of inclusions and cracks.

Table 3.1. Growth conditions, dimensions and weight of some crystals grown for obtaining RTP substrates.

Experiment number	**Cooling interval [K]**	**Cooling ramp [K/h]**	**Total pulling [mm]**	**Crystal dimensions a x b x c [mm]**	**Crystal weight [g]**
1	30	0.1 for 15 K, 0.05 for 15 K	0	15.3 x 18.3 x 12.35	5.74
2	33	0.1 for 15 K, 0.05 for 18 K	0	15.7 x 16.6 x 15.3	5.98
3	31	0.1 for 15 K, 0.05 for 16 K	0	13.6 x 18.4 x 14.2	5.59
4	34.5	0.1 for 15 K, 0.05 for 19.5 K	2	18.3 x 16.0 x 13.9	6.21
5	32	0.1 for 15 K, 0.05 for 17 K	3	14.5 x 15.8 x 15.9	5.60
6	27	0.1 for 15 K, 0.05 for 12 K	4	17.3 x 18.7 x 20.4	9.37

From the table 3.1, it can be seen that pulling seems to help in increasing the dimension of the ***c*** crystallographic direction without creating any effects in the crystal quality. As

UNIVERSITAT ROVIRA I VIRGILI
NEW PHOTONIC DEVICES BASED ON NLO(NON-LINEAR OPTICAL) CRYSTALLINE WAVEGUIDES
Muhammad Ali Butt

an example, Figure 1 of **paper I** shows the images of crystals with and without pulling obtained in this work. To obtain substrates, the crystals were cut in plates perpendicular to the ***c*** crystallographic direction and polished to optical quality, so that the roughness of the surfaces was lower than 10 nm and the curvature was 8-20 m.

3.1.2. K:RTP bulk single crystal growth

For the bulk single crystal growth of K:RTP, we also used the TSSG technique and the supersaturation of the solution was also obtained by slow-cooling. The solution composition used was Rb_2O-K_2O-P_2O_5-TiO_2-WO_3=39.51-4.39-23.6-22.5-10 (mol %). We used a Pt cylindrical crucible of 100 cm^3 in volume, 5 cm in diameter, filled with about 195 g of solution. In the first experiment the vertical thermal gradient, ∇T in the solution was 3 K/cm. The temperature was kept at 75-100 K above the expected saturation temperature for 3-5 h to homogenize the solution. The velocity of rotation was constant in all experiments (65-70 rpm). When the thermal ramp of cooling, which was of 0.1 K/h for the firsts 15 K and 0.05 K/h for the next 15 K, was finished; we extracted the crystal slowly from the solution to minimize the thermal stress and decreased the temperature of the furnace to room temperature. The saturation temperature of the above mentioned K:RTP solution is around 1155 K which is a bit lower than the saturation temperature of RTP solution with the same basical composition (without K substitution). No pulling along ***c*** crystallographic direction was applied.

Table 3.2 shows the growth parameters of K:RTP single crystals and the dimensions and weight of the crystals obained. In the first experiment, some problems appeared with the quality of the crystals, because it was dissolving at the tip of the crystal and shape was rounded. In order to overcome this problem, in second experiment, we reduced the vertical thermal gradient, ∇T, of the solution to 2.4 K/cm, obtaining by this way the desired morphology of the crystals.

Table 3.2. Growth conditions, dimensions and weight of some crystals grown for obtaining K:RTP substrates.

Experiment number	Cooling interval [K]	Cooling ramp [K/h]	∇T [K/cm]	dimensions [mm]	weight [g]
1	29.7	0.1 for 15 K, 0.05 for 14.7 K	3.0	16.7 x 7.4 x 6	5.30
2	30	0.1 for 15 K, 0.05 for 14.7 K	2.4	14.8 x16.0 x 10.4	4.44
3	29.2	0.1 for 15 K, 0.05 for 14.2 K	2.4	18. 9 x 15.1 x 9.5	4.57

Figure 3.2 shows as-grown K:RTP crystals grown in the three experiments of table 3.2. As it can be seen, the first crystal has large area in the (001) plane but the size along the ***c*** crystallographic direction is short, maybe due to the high vertical thermal gradient in the solution. Experiments number 2 and 3 show an enlargement in the size along ***c*** crystallographic direction. This could be due to lower thermal gradient as compared to the first experiment.

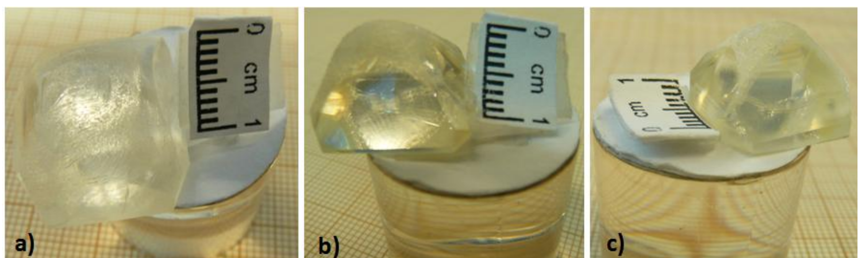

Figure 3.2. As-grown K:RTP single crystal, a) experiment number 1, b) experiment number 2 and c) experiment number 3

3.1.3. Na:KTP bulk single crystal growth

Before the bulk single crystals of $K_{1-x}Na_xTiOPO_4$ were grown, small crystals were grown to be analyzed for identification of the crystalline phase and measuring the chemical composition. In order to maintain the Na:KTP orthorhombic phase during the crystal growth, a solution composition was selected in the crystallization region of KTP with 30 mol % of WO_3 [Iliev 1990] which was far from the boundaries of this KTP

crystallization region. The solution composition used was ((1-x) K_2O- x Na_2O)-TiO_2-P_2O_5-WO_3= 37.8-4.2-14-14-30 (mol %) with 10 mol % of K_2O substituted by Na_2O (x = 0.1). The saturation temperature of this solution is around 1221 K, which is higher than the saturation temperature of the RTP and K:RTP solutions used in this work. Note that the RTP and K:RTP solutions contain less WO_3 than the Na:KTP solution.

The small crystals were obtained from 15 g of solution, contained in a 25 cm^3 platinum crucible. After the solution had been homogenized, its temperature decreased by 10 K every 30 min until small single crystals had appeared on a platinum rod immersed in the solution. Once the crystals had appeared on the platinum rod, the solution temperature was maintained constant for 24 h so that the crystals could grow. When the crystals on the platinum rod were reasonably big in size, they were slowly extracted from the solution. These crystals were not useful for obtaining substrates but they were useful for obtaining lattice parameters and identify the crystalline phase of the crystal. The crystalline phase of Na:KTP crystals was identified by comparing with the powder diffraction pattern of KTP entry 80-0893 of the data base maintained by the Joint Committee for Poweder Diffraction Studies (JCPDS). As it can be observed in figure 3.3, the obtained crystalline phase is orthorhombic and isostructural to KTP.

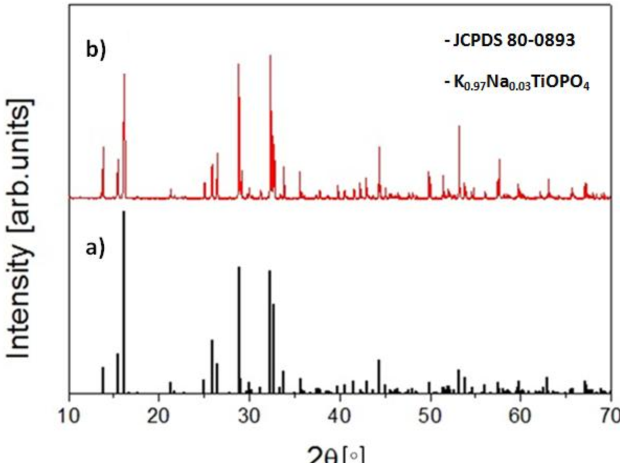

Figure 3.3. X-ray powder diffraction analysis: a) KTP crystalline powder (JCPDS 80-0893), b) $K_{0.97}Na_{0.03}TiOPO_4$

The composition of these crystals was measured by EPMA. From the EPMA results, we calculated the coefficient of distribution of Na^+ in KTP for 10 mol % substitution of K_2O

by Na_2O in solution and its value is 0.3. While 10 mol % of K_2O has been replaced by Na_2O in the solution, only a 3 mol % of Na substitutes K in the Na:KTP crystals, as it has been probed by EPMA analysis. Thus, the chemical composition of the bulk single crystals determined by electron probe microanalysis was $K_{0.97}Na_{0.03}TiOPO_4$. Bulk single crystals of Na:KTP were grown from the the same solution composition that was used to obtain small crystals. For these growth experiments, a 100 cm^3 platinum crucible was filled with 150 g of solution. The vertical thermal gradient in the solution was 3.8 K/cm. After determining the saturation temperature of the solution, a cooling rate of 0.1 K/h was applied for 15 K and 0.05 K/h for the next 11-14 K. Sometimes, pulling was also applied in order to increase the size of the crystal in ***c*** direction. During few days of crystal growth, the rotation was maintained at 60 rpm and then reduced gradually as the crystal grew. Table 3.3 summarizes the experiments for the growth of Na:KTP single crystals. As we can see clearly, the pulling increases the size of the crystal along the ***c*** crystallographic direction. As it was expected, the Na:KTP crystals obtained were larger in size than the RTP and K:RTP crystals obtained before because of the higher quantity of WO_3 (30 mol %) contributes to decrease the solution viscosity.

Table 3.3. Experimental conditions of the crystal growth of Na: KTP crystals for substrates preparation.

Experiment number	**Cooling interval [K]**	**Cooling ramps [K/h]**	**Total Pulling [mm]**	**Crystal dimensions a x b x c [mm^3]**	**weight [g]**
1	28.7	0.1 for 15 K, 0.05 for 13.7 K	0	17.9 x 21.6 x 8.2	5.55
2	27.3	0.1 for 15 K, 0.05 for 12.3 K	3	11.9 x 23 x12.5	5.39
3	26.2	0.1 for 15 K, 0.05 for 11.2 K	4	18.2 x 16.5 x 13.47	5.70

Figure 3.4 shows an as-grown Na:KTP single crystals used for obtaining substrates. The crystals obtained were generally transparent, inclusion free and without any cracks.

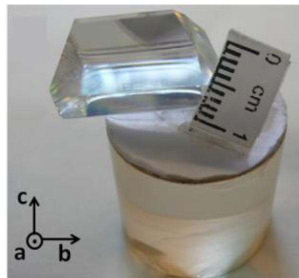

Figure 3.4. As-grown Na:KTP crystal

3.2. Crystal growth of epitaxial layers

3.2.1. Lattice mismatch

From the unit cell parameters of the substrate and epitaxial layer, the lattice mismatch was calculated according to the expression:

$$\mathbf{F_{(hkl)} = (S_{L(hkl)} - S_{S(hkl)})/S_{S(hkl)}}$$

where (hkl) refers to the plane of the substrate and epitaxial layer, $S_{S(hkl)}$ and $S_{L(hkl)}$ are the areas defined by the periodicity vectors of the substrate and the epitaxial layer, respectively [Cugat 2011a].

High values of lattice mismatch can increase the stress in the substrate/epitaxial layer interface and can produce microscopic or macroscopic defects (cracks and /or inclusions) with sizes of the order of the wavelength of the light to be guided or higher and increase the optical losses in the light guiding process. The chemical composition of the guiding layer should then be carefully optimized in terms of lattice parameters in order to minimize the lattice mismatch with respect to the substrate, neither tension nor compression have to be exerted by the substrate to the guiding layer, whenever possible.

Table 4 of **paper I** shows the lattice mismatch between the different epitaxial layer/substrate systems explained in the next sections 3.2.2, 3.2.3 and 3.2.4. The unit cell parameters used to calclulate the lattice mismatches are reported in table 3 of **paper I**. The lattice mismatch of the $RbTi_{0.971}Yb_{0.015}Nb_{0.014}OPO_4/RbTiOPO_4$ (001) epitaxial layer grown from a self-flux solution calculated by Cugat *et al.* is 0.473 [Cugat 2011a]. This value is slightly higher than the ones obtained in this work (see table 4 of **paper I**). Cugat *et al*. reported that at these values of mismatch, the obtained epitaxial layer presented high crystalline quality and no visible defects in the interface; so we can expect that with similar values, the quality of the interface of the epitaxial layers will be

maintained. In case of RTP/K:RTP system, (001) plane has higher lattice mismatch as compared to (100) plane, and both are lower than the ones reported for (Yb,Nb) doped RTP on RTP (001), so it could be expected, as well, a high quality crystalline interface. Finally, if we compare these values with the ones reported in the literature, for previous KTP epitaxial systems, these values are higher as compared to the ones obtained in $KTP/KTiGeOPO_4$, which lattice mismatch values were around -0.156 for $f_{(110)}$ [Solé 2002a]. In all our cases, the lattice mismatch values obtained are positive, meaning a compressive strain in the epilayer.

3.2.2. Growth of (Yb,Nb): RTP epitaxial layers on RTP (001) substrates

From the past experience of the group in the growth of (Yb,Nb):RTP/RTP(001) epitaxial layers [Cugat 2010, Cugat 2011a], several basic solution compositions and also several TiO_2 substitutions for Nb_2O_5 and Yb_2O_3 were used for growing epitaxies by the LPE technique. We have used a suitable solution composition in order to obtain high quality thin layers of (Yb,Nb):RTP over RTP(001) substrates [Cugat 2011a]. The solution composition is Rb_2O-P_2O_5-TiO_2-Nb_2O_5-Yb_2O_5-WO_3=43.9-23.6-20.7-0.45-1.35-10 (mol %). This composition contains 10 mol % of WO_3 which helps in decreasing the viscosity of the solution and improve the growth conditions; higher contents of WO_3 can lead detrimental effects in the crystal properties due to W^{6+} incorporation in the crystal.

This composition has been chosen near the centre of the RTP crystallization region in solutions containing 10 mol % of WO_3 [Carvajal 2000], because the dopant elements can displace the boundaries of the crystallization region, as reported by Carvajal *et al.* [Carvajal 2002]. The growth details of the epitaxial layers are mentioned in section 2.12. Usually, we slightly dissolve the substrates for 5 minutes at 1 K above the saturation temperature and after that, we grew the epitaxial layer at 3-6 K below the saturation temperature for 50-380 min, in order to obtain 23-105 µm thickness of epitaxy.

The surface morphologies of the as-grown epitaxial layers were studied with a confocal microscope. Figure 3.5 shows the topography of an as-grown epitaxial layer. The defects aligned along the ***b*** crystallographic direction could be due to the high growth rate of (Yb,Nb):RTP in WO_3 containing solutions as a consequence of the supersaturation of the solution and lower viscosity compared with self-flux solutions. Besides, the (001) face is not a natural face, so the growth rate in this face can be expected to be high. At less growth time, these defects are larger and more in number but as the growth time increases, they tend to reduce in size and density.

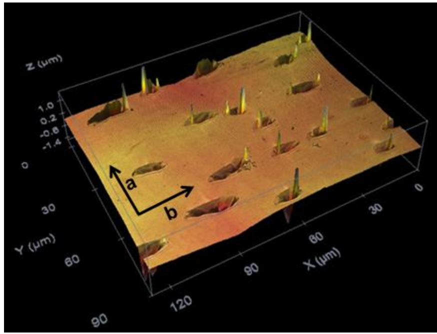

Figure 3.5. Topography of an as-grown epitaxial layer with defects aligned along ***b*** crystallographic direction

Different growth times and different growth temperatures have been tried in order to observe if there are any changes in the quality of the epitaxial layers. Table 3.4, shows the degrees below the saturation temperature decreased to supersaturate the solutions for growing the epitaxial layers, the growth times and the results obtained of epitaxial thickness and growth rate.

Table 3.4. Conditions for growing the epitaxial layers, thickness and quality of the (Yb.Nb): RTP/ RTP (001) epitaxies obtained.

Experiment number	**Degrees below the saturation temperature [K]**	**Growth time [min]**	**Thickness [µm]**	**Growth rate [µm/min]**
1	3	240	75	0.31
2	3	320	100	0.31
3	4	140	62	0.44
4	4	150	60	0.40
5	4	90-150-210-270-330	5.5-10.7-15-20.7-28	0.09
6	6	130	82	0.63
7	6	180	105	0.58
8	6	50-110-170-230-320-380	23-34-50.5-69-78-93	0.21

As it was expected, the growth rate increases by increasing the supersaturation of the solution. Even at higher growth rates, the quality of the epitaxial layers was good. Figure 2 of **paper I** shows an as-grown (Yb,Nb):RTP/RTP (001) epitaxial layer. As it can be seen in the Figure, the layer is transparent and free of macrodefects.

To study how the growth time affects the quality of the surface of the epitaxial layers and the growth rate of the epitaxial layers, we dipped a substrate in the solution for several millimeters. After an initial growth of 50 or 90 minutes, depending on the experiment, the substrate was pulled in different steps; usually 2 mm every 60 min. The growth morphologies were observed with a confocal microscope.

In experiment number 5, an (Yb,Nb):RTP stepped epitaxy was grown on a RTP(001) substrate of dimensions 12.3 x 11.2 x 1.5 mm^3 (along ***a***, ***b*** and ***c*** crystallographic directions), at 4 K below the saturation temperature for times ranging from 90 to 330 minutes, with substrate rotation at 60 rpm. The substrate was orientated with ***a*** crystallographic direction perpendicular to the surface of the solution. In every step, substrate was pulled 2 mm up from the solution. Figure 3.6 shows the epitaxial thickness as a function of growth time of the epitaxial layers performed in experiment number 5. As can be seen, the epitaxial layer thickness has a linear dependence on growth time with a growth rate of 0.09 µm/min.

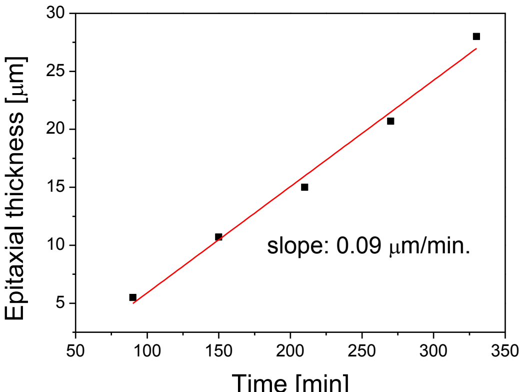

Figure 3.6. Epitaxial thickness vs growth time of (Yb,Nb):RTP/RTP(001) exitaxial layer grown in different steps

Images of each growth step were obtained with a confocal microscope using 20x microscope objective and are shown in figure 3.7. As can be seen in the figure, during

the first steps of growth there was a high density of defects of the order of several hundreds of µm and during growing the defects decrease in number and size.

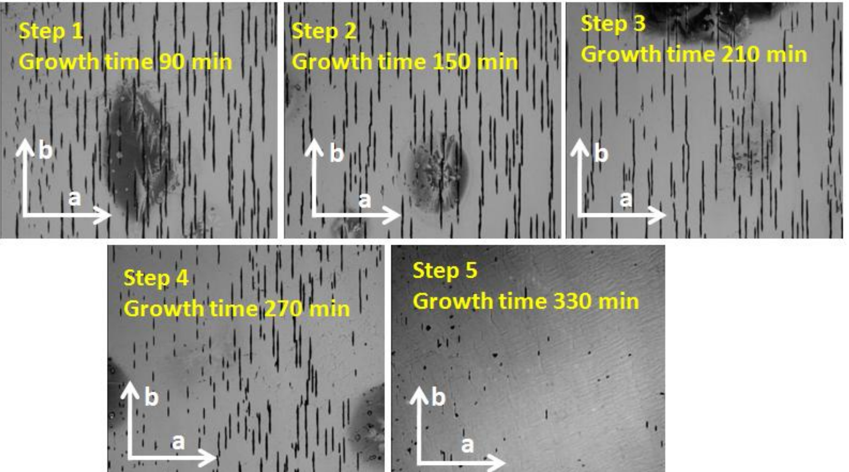

Figure 3.7. Confocal images of different steps of (Yb,Nb):RTP/RTP(001) in experiment number 5

In experiment number 8, an (Yb,Nb): RTP stepped epitaxial layer was grown on a RTP (001) substrate of dimensions 12 x 6 x 1.5 mm^3 (along ***a, b*** anc ***c*** crystallographic directions), at 6 K below the saturation temperature rotating at 60 rpm for times ranging from 50 minutes to 380 minutes. The substrate was orientated with ***a*** crystallographic direction perpendicular to the surface of the solution. In every step, the substrate was pulled 2 mm up from the solution. The evolution of the epitaxial thickness with time in this experiment can be seen in figure 3 of **paper I.** In this case, the growth rate of epitaxial layer is 0.21 µm/min. Images of the different steps of growth in this experiment taken with a confocal microscope with 20X objective are shown in figure 4 of **paper I.**

After observing figures 3.7 and figure 4 of **paper I**, we can conclude that, the defects always are oriented along the ***b*** crystallographic direction (indicated in the figure) and they are few hundred nanometers holes in depth which can be easily removed during polishing. The density and size of defects depends on the growth time; higher time of growth reduces the defects. This effect have been observed in experiments number 5 and 8 of table 3.4, where in the last steps of these experiments, the number of defects are clearly reduced in relation with the first step. A possible explanation of this effect is that near the substrate/epitaxial layer interface, the defects are higher in number and size due to the substrate/layer mismatch and when the thickness of the epitaxial layer increases

these defects can be partially overcome. Figure 3.6 and figure 3 of **paper I** shows the linear tendency of the epitaxy thickness over growth time at least up to 330 and 380 min respectively. In experiment number 8, the growth rate was 0.21 µm/min.

3.2.3. Growth of RTP epitaxial layers on $Rb_{1-x}K_x TiOPO_4$ substrates

The growth of RTP epitaxial layers on $Rb_{1-x}K_xTiOPO_4$ (001) substrates has interest for changing the refractive index contrast between the substrate and the epitaxial layer by introducing a lighter ion in the substrate. The refractive indices and the contrast of refractive indices between the substrate and the material forming an epitaxial layer when a 10 at. % of Rb is substituted by K in the substrate are given in table 5 and 6 of **paper I** respectively. After obtaining K:RTP (001) substrates (described in section 3.1.2), epitaxial layers of RTP were grown on these substrates by LPE (described in chapter 2) with a solution composition of Rb_2O-P_2O_5-TiO_2-WO_3 = 44.24-18.96-16.8-20 (mol %). After determining accurately the saturation temperature of the solution and the kinetics of growth/dissolution of an RTP seed in this solution, different growth temperatures and growth times were applied for LPE growth. Details of the different epitaxial growth experiments are given in table 3.5. In the first epitaxial growth experiment, a bad quality epitaxial layer was obtained due to the high super-saturation of the solution, because the epitaxial growth was produced at 6K below the saturation temperature and also the growth time was too high. After that, when the epitaxial layers were grown at low super-saturation (epitaxial growth at 2-3 K below saturation temperature) and low growth time, good quality epitaxial layers were obtained.

Table 3.5. Conditions for growing epitaxial layers and thickness and quality of the RTP/ $Rb_{1-x}K_x TiOPO_4$ (001) epitaxies obtained.

Experiment Number	Degrees below the saturation temperature [K]	Growth time [min]	Thickness [µm]	Growth rate [µm/min]
1	6	360	-	
2	3	120	80	0.67
3	2	120	55	0.46
4	2	60	29	0.48

As an example of defects observed, Figure 3.8.a, shows a detail of an as-grown epitaxial layer where some growth steps are observed and after polishing sometimes appeared cracks that could be due to the stress existing in the substrate/epitaxial layer interface (figure 3.8.b). This morphology is different than the observed in the growth of (Yb, Nb): RTP/RTP (001) epitaxial layers (see figure 3.5 and 3.7). In general, the crystals grow with planar faces known as habit faces from the solution.Those faces with low surface energy tends to grow slowly and determine the final morphology of the crystal [Wulff 1901]. During the first growth, if the surfaces are not cut in a plane of a natural face, facets of habit faces and terraces of these faces tends to be formed. The facets become bigger and the terraced regions grow out until a single edge between the two habit faces is formed [Herring 1951, Herring 1953]. These healed out regions often takes the shape of caps (capping region). In figure 3.9, a capping habit of growth in RTP layer observed in experiment 4 is shown.

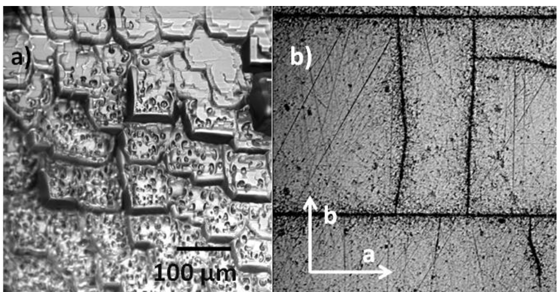

Figure 3.8. a) As-grown RTP epitaxy over a K:RTP (001) substrate. b) Epitaxial layer polished till 7 µm thickness shows some cracks appeared after polishing

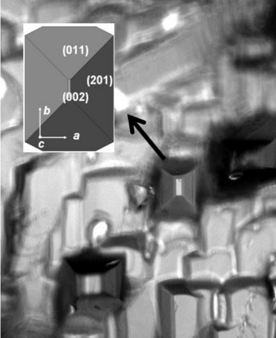

Figure 3.9. As-grown RTP epitaxial layer over a K:RTP(001) substrate shows capping habit

The epitaxial layer of RTP grown in experiment 2 was used to study the compositional change in the substrate/epitaxial layer interface by electron probe microanalysis

(EPMA). The results are shown in Figure 5 of **paper I**. It can be seen that, there is a region of about 35 μm where there is diffusion of K^+ ions. This means that there is a graded interface between the substrate and the epitaxial layer, while in (Yb,Nb):RTP/RTP epitaxial layers the interface was sharp [Cugat 2011a].

The measurements of the concentration of K^+ taken in two different parts of the epitaxial layer showed that the compositional change with the depth was the same in different parts of the epitaxial growth. According to Gavaldà *et al* [Gavaldà 2009], the ionic conductivity of RTP and its isostructural compounds is higher along ***c*** crystallographic direction than along ***a*** and ***b*** crystallographic directions. This causes the high mobility of K^+ in the RTP/K:RTP(001) channels parallel to ***c*** crystallographic direction.

As along the ***a*** crystallographic direction the ionic conductivity of RTP and its isomorphs is lower than along the ***c*** direction, we grew a RTP epitaxial layer on a K:RTP (100) substrate in order to try to reduce the K^+ diffusion from the substrate to the epitaxy. The lattice mismatch between the substrate and the epitaxial layer in the (100) plane is very low as compared to (001) plane as can be seen in table 4 of **paper I** and additionally it is a natural face of RTP parallel to the (100) plane. Although a priory, it seemed that the K^+ diffusion through the interface could be lower using a (100) substrate, the experimental results showed that the level of K^+ diffusion is similar than in the case of using (001) substrates. Figure 3.10 shows the concentration of K^+ ions in the region near the substrate/epitaxial layer interface.

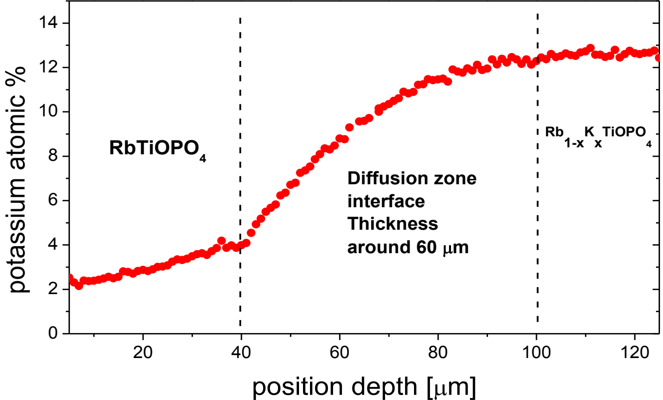

Figure 3.10. K^+ ion concentration in the region around the substrate/epitaxial layer interface

Thus, the RTP/K:RTP(001) and RTP/K:RTP(100) epitaxial layers are not suitable for fabricating step-index waveguides due to the diffusion of K^+ ions from the substrate to the epitaxial layer. But they can be used as graded index waveguides because of their index profile which is similar to the ion exchange waveguides.

3.2.4. Growth of KTP epitaxial layers on $K_{1-x}Na_xTiOPO_4$ (001) substrates

The growth of KTP epitaxial layers on $K_{1-x}Na_xTiOPO_4$ (001) substrates with x = 0.1 has interest of changing the refractive index contrast between the substrate and the epitaxial layer by introducing a lighter ion in the substrate and to obtain KTP waveguides. The solution composition used was ((1-x) K_2O- x Na_2O)-TiO_2-P_2O_5-WO_3= 37.8-4.2-14-14-30 (mol %) with 10 mol% of K_2O substituted by Na_2O (x = 0.1). The refractive indices and the contrast of refractive indices between the substrate and the material forming the epitaxial layer when doped with 10 at. % of Na is substituted by K in the substrate are given in table 5 and 6 of **paper I** respectively. After obtaining the Na:KTP (001) substrates (described in section 3.1.3), epitaxial layers of KTP were grown on it with a solution composition of K_2O-P_2O_5-TiO_2 =48-32-20 (mol %) by LPE (described in chapter 2). Usually, we slightly dissolve the substrates for 5 minutes at 1 K above the saturation temperature and after that, epitaxial layer is grown at 1 K below the saturation temperature for 1 h. It can be seen from figure 3.11, that the layer is transparent and free of macrodefects. The epitaxial layer thickness obtained in this case is around 25 μm with a growth rate of 0.41 μm/min.

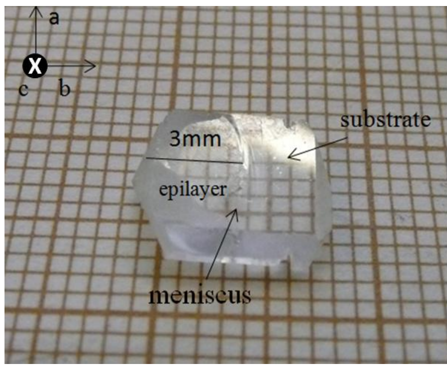

3.11. As-grown KTP epitaxy over a Na:KTP (001) substrate

3.3. Ferroelectric domains in RTP bulk crystals and epitaxial layers

We have studied the ferroelectric domain structures in an RTP bulk single crystal and in (Yb,Nb):RTP/RTP epitaxial layer. The variety of the domain boundaries depends directly on the growth sector number, the kinetics of growth of them, and then directly from the growth method and composition of the flux used for growth; so the description here is for the crystals grown as described in section 3.1.1.

Two single crystals have been cut in slices perpendicular to ***c*** crystallographic direction. The resulting plates have been submitted to a selective chemical etching in a 2:1 (molar ratio) solution of KOH: KNO_3 for 30 min at 353 K for visualizing the domains. It is known that molten salts containing hydroxide attack the negative ferroelectric face (c^-), while the positive ferroelectric face (c^+) is left essentially untouched.

Roth *et al.* [Dhanaraj 2010] reported the growth sectors present in KTP and RTP crystals. As can be seen in the Figure 4 of **paper IV**, mainly in the plates perpendicular to the ***c*** direction, there are four main growth sectors, displayed and labelled trough the developed faces in the morphology, the {201} and the {011}sectors, as observed before [Dhanaraj 2010]. It has been reported that in KTP, these two sectors are usually monodomain; however as it can be observed in the Figure 4 of **paper IV**, it seems that in RTP the {201} is grown as monodomain, but the {011} sector is multidomain. The domain presents in the {201} sector has a domain boundary coincident with the edge boundary of the growth sector, and can be labelled as a full-size edge; but the small domains with irregular shape located inside the {011} growth sector, they present intrasector domain boundaries dispersed type.

For the epitaxial doped sample, they are also grown over the Curie temperature (it is expected that the T_c is decreased with the presence of Nb, so they are grown as paraelectric samples and no transfer of the domain structure of the substrate can be done. The transition to ferroelectric is down through the cooling period. In this case, as the samples are grown by LPE method on the (001) face, which is not a natural face, it is expected also a ferroelectric multidomain. In Figure 5 of the **paper IV** shows an epitaxial sample after the wet etching. As it can be observed, it is as expected, multidomain.

Chapter 4
Waveguides fabrication

As mentioned in the introduction, RTP/KTP maybe is an ideal alternative NLO crystal to the well known Lithium niobate. Lithium niobate ($LiNbO_3$, LN hereafter) is a suitable material as a waveguide platform because it constitutes an interesting non-linear optical crystal. LN is a negative uniaxial material ($n_e< n_o$) and belongs to ABO_3-type ferroelectrics. Due to its ferroelectricity, LN is a non-centrosymmetric crystal below the Curie temperature. At the temperature above the Curie temperature, it is in para-electric phase [Räu 1978, Che 2003]. As its curie temperature is relatively high (1483 K), it allows the use of many techniques for optical waveguide fabrication, as depolarization of the crystal does not occur. The first waveguides based in lithium niobate based on titanium (Ti) doping were performed by Schmidt and Kaminow [Schmidt 1974]. These came after attempts to fabricate waveguide by Li_2O exo-diffusion which allowed only a weak index increase and high losses [Kaminow 1973]. LN waveguides were also achieved by ion exchange, in particular, Ag ions using a solution of $AgNO_3$ [Shah 1975]. Proton exchange was also recently developed, many research activities are currently dealing with this technique in order to understand and control all the mechanisms governing the fabrication process [Jackel 1982, Ganshin 1988, Jackel 1991, Chanvillard 2000, Suchoski 1988]. In recent years, the ionic implantation, in particular by using light ions, has been successfully employed for the development of waveguides with very good optical qualities in this material. Nowadays, many optoelectronic components are commercially available based on $LiNbO_3$ waveguides [Ari 2004].

Like in the case of lithium niobate, for KTP, several techniques for index graded optical waveguide fabrication have been studied and developed such as ionic exchange [Boudrioua 2009], ionic diffusion [Boudrioua 2009] and ionic implantation [Tow 1994]. Among these, only ionic implantation makes it possible to produce waveguides in samples cut according to all the principal axes: X, Y and Z. The exchange techniques and ionic diffusion do not allow this because the ionic conductivity of material is different according to the direction of the principal axes [Zha 1992]. Nevertheless, the use of this technique in the KTP family of compounds has not been largely explored [Boudrioua 2009].

Plasma etching is relatively new techniques in the fabrication of integrated circuits. It was introduced in the seventies, mainly for stripping resists. In the eighties, plasma etching became a mature technique to etch layers and was introduced in the production of integrated circuits. Reactive ion etching was the main technology, but new techniques were developed. In the nineties new techniques, such as electron cyclotron resonance (ECR) and inductively coupled plasmas (ICP) were introduced, with mixed success. The use of plasma etching is widespread in the industry, but contrary to other techniques (e.g lithography), the theoretical understanding of the different mechanisms involved in plasma etching is still very poor. This explains why no reliable simulator for plasma etching exists (yet). Reactive ion etching (RIE) is a dry etching process that has become really popular for structuring different dielectric materials such as SiO_2 and $LiNbO_3$. The fabrication of single mode rib waveguides was demonstrated for the first time in (Yb,Nb):$RbTiOPO_4$ by using reactive ion etching technique by Choudhary *et al.* [Choudary 2013]. The plasma etching involves two dominant etch mechanisms: physical and chemical. The physical mechanism is the high-energy ion bombardment that erodes the material and the chemical mechanism is the formation of volatile species from reactions on the material surface with the species from the plasma.

Ion exchange has been used exactly for one century to modify the surface properties of glass; Schülze in 1913 [Schulze 1913] was in fact the first to demonstrate that monovalent cations contained in glass would be exchanged when a soda lime silicate glass was immersed into a bath of molten silver nitrate. Ion exchange is a process by which species are transferred from one phase to another phase when the two phases are brought into contact. The process is motivated by the random jumping of atoms between adjacent sites. When a solid matter containing a cation α^{A+} is introduced into a melt or hot solution containing a diffusing cation β^{A1+}, χ_2 ions of β^{A1+} are driven into the solid phase due to an interphase chemical potential gradient, and in order to maintain charge neutrality, χ_1 ions of α^{A+} are released into the melt or solution. This ion exchange process can be represented by an overall chemical reaction as follows [Garfinkel 1968].

$$\chi_2\, \beta^{A1+}\,(\text{liquid}) + \chi_1\, \alpha^{A+}\,(\text{solid}) \longleftrightarrow \chi_2\, \beta^{A1+}\,(\text{solid}) + \chi_1\, \alpha^{A+}\,(\text{liquid})$$

The main objective of the ion exchange process in waveguide formation is to obtain a positive change in the refraction index of the active layer, and therefore the choice of appropriate ion exchanged pairs is typically carried out by comparing the electron

polarizabilities of ions. As a rule, the higher the value of electron polarizability, the higher the refractive index increases.

Waveguides have been fabricated by ion exchange when the univalent ions such as Rb^+, Cs^+ and Tl^+ replace the potassium ions of KTP [Bierlein 1987]. Divalent ions are usually added to the melt to increase the rate and infirmity of the ion exchange [Bierlein 1988]. It has been shown that divalent ions Ba^{2+} and Sr^{2+} are incorporated at relatively high concentrations into KTP by ion exchange from nitrate melts. Such doping greatly increases both the rate of exchange of univalent ions (e.g., K^+ and Rb^+), and the ionic conductivity [Roelofs 1991]. The exchange of potassium ions by protons in a crystal of KTP makes it possible to obtain effective waveguides [Ris 1996, Roe 1993]. Waveguides in KTP based on $K_{0.5}$ $(NH_4)_{0.5}TiOAsO_4$ and $Na_xK_{1-x}TiOPO_4$ have been carried out by ion exchange of ammonium and sodium from crystals containing initially only potassium [Richard 1989, Phillips 1989]. Recently, Cs^+ ion exchange channel waveguides on RTP has been reported [Cugat 2013b]. Cs^+ ions were used for exchange process because it produces an increase in the refractive index and its ionic radius is not far from the Rb^+ radius. It is known that the ionic conductivity of the KTP crystals along the [001] direction is around 100 factor higher than RTP along [001] direction [Bierlein 1986]. The ionic conductivity of RTP along the [001] direction is lower than that of KTP, but also higher than the ionic conductivity along the other directions [Bierlein 1987, 1989]. The ionic radius of Rb^+ and K^+ is different, that contributes in the difference in ionic conductivity between KTP and RTP. Hence the mobility through the channels along ***c*** crystallographic direction is reduced due to the higher ion radius of Rb^+. In any case, the ionic conductivity of RTP along ***c*** direction is high enough to allow Cs^+ exchange into the RTP crystal lattice with levels high enough to allow the formation of optical waveguides with vertical optical channel walls parallel to the polar [001] axis.

The LPE technique enables growth of a homogeneous single crystal film and provides the better control of the thickness by adjusting the supersaturation of the solution and the growth time. Thin films with well defined step-like refractive index profile can be grown directly on the substrates by LPE [Cheng 1991]. Thin films of $KTiOP_xAs_{1-x}O_4$ were grown by Cheng *et al.* on KTP substrates using both tungstate and the pure phosphate-arsenate self-fluxes [Cheng 1991a]. For device applications, films with KTP (001) orientations are preferred as they provide the largest nonlinear optical coefficients in this plane. High quality KTP (001) films have not been successfully grown due to the fast growth and c-capping habit of KTP. The same problem was observed when growing thin

epitaxial layers of KTP on (010) substrates. It should be noted that the use of substrates cut from hydrothermally grown crystals leads to optical degradation with the formation of fine white filaments in the substrate due to the precipitation of fine water-based inclusions [Cheng 1991]. RTP has an advantage over KTP single crystal because active ions doped epitaxial layers can be grown on RTP(001) substrates. The fabrication of planar waveguide on RTP(001) substrate by the epitaxial growth of (Yb,Nb):RTP, which allows the propagation of light along TM polarization was demonstrated by Cugat *et al.* [Cugat 2011]. By the incorporation of these active ions, it can also be possible to produce second harmonic generation in the planar waveguides [Cugat 2011]. Also, structuring of epitaxial layer of (Yb,Nb):RTP over RTP(001) was demonstrated by Cugat *et al* with the help of femtosecond-laser [Cugat 2013a].

In this chapter, we summarize the main results after applying the experimental techniques used for the fabrication of rib waveguides, stripe loaded waveguides and ion-exchanged waveguides on RTP (001) and (Yb,Nb):RTP/RTP(001). Also their morphological characterization is shown.

4.1. Fabrication of Y-splitters and MZ structures on RTP(001) and (Yb, Nb):RTP/RTP(001) by RIE

In this section, we have described the reactive ion etching technique (RIE) with the help of which we have fabricated Y-Splitters and MZ on RTP and (Yb,Nb):RTP/RTP (001). Reactive ion etching technique was used to fabricate these devices on (Yb,Nb):RTP/RTP(001) and at the end, an undoped RTP cladding layer was grown.

4.1.1. Pattern design

The design of the pattern is shown in Figure 4.1. A balanced single mode MZ design without any geometrical path length difference between the two arms and with two identical symmetric Y-structures, in which one acts as a splitter and one as a combiner, is shown in Figure 4.1.a. On the other hand, Figure 4.1.b shows a Y-structure with similar design parameters to act only as a splitter. To obtain the optimized designs for Y-splitters and MZs, different geometrical parameters have been designed. We have designed MZs and Y-splitters of length 9 mm with radius of curvature ranging from 50 mm to 80 mm. It was expected that the Y-junction design, based on an S-line pattern, would give low losses and a large enough separation between the two arms so that there

is no evanescent coupling between the branches. It was also expected to give the maximum length in the branches for future applications as an electro-optical modulator. In order to obtain single-mode MZ and Y-splitters at the selected wavelength, the core width and height of the waveguides must be limited depending on the refractive contrast Δn between the waveguide core and the substrate. The guiding properties of the MZ's and Y-splitters were modelled with Rsoft BeamPro [Rsoft BeamPROP software, v2013.12.] at a wavelength of 1.5 µm. The dimensions of the designed structures are channels with a width of 6 µm and 5 µm depth. (The depth of the channels was optimized in simulations in chapter 5, section 5.3.1.1) These dimensions were chosen in order to support a fundamental guided optical mode at a wavelength of 1.5 µm. The parameters of the designs are given in Table I of **paper II**.

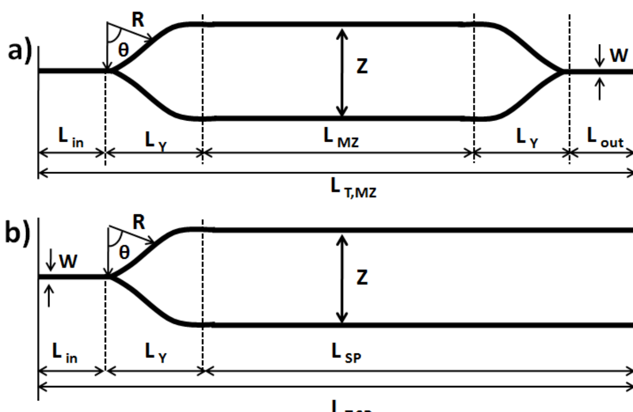

Figure 4.1. a) MZ structure, b) Y-splitter design

4.1.2. Metal layer adhesion and morphology

Sample preparation details were explained in section 2.1.4 and different tests were conducted in order to check the adhesion of Ti, Ni, Al and Cr metal mask over the RTP composites.

Deep etching can only be possible by using a high selective metal mask. Different metal mask, for instance Ti, Ni, Al and Cr were tested as possible candidates. The topography and surface roughnesses of the deposited metal layers, analysed by AFM, are shown in Figure 3 of **paper II**. Surface roughness *rms* values calculated with the WSxM software were 2.8 nm, 2.6 nm, 150 nm and 100 nm for Ti, Ni, Al and Cr layers, respectively. As it

can be observed in the case of Al and Cr, the layers are composed of grains; which are larger for Al. The presence of these grains contributes to the higher value of roughness for Al and Cr layers.

In order to analyze the adhesion and durability of the metal layer on the RTP surface, we performed a tape test five times on each metal layer to check its adhesion. The Ti layer was completely or partially removed during the first attempt, as can be seen in Figure 3 of **paper II**. In the case of Ni, in the first attempt significant parts of the Ni layer were removed (possibly due to some defects prior to deposition) but in second attempt, Ni was removed as can be seen from Figure 3 of **paper II.** A scratch test was also performed on the Ni layer but didn't show any significant influence on the adhesion. Finally, in the case of Al and Cr, there was no observed removal during the tape test. The scratch test on Al and Cr layer showed a good adhesion. Thus the results indicate that Al and Cr are good candidates to be used for metal mask.

4.1.3. Selectivity

A preliminary test was performed to determine the etch rates in undoped RTP, (Yb, Nb):RTP, photoresist and the metal layers using the etching conditions described above. The samples were etched for 60 min and the etch rates obtained are summarized in Table II of **paper II.**

Selectivity is defined as the ratio of etch rate of the RTP substrate compared to the etch rate of applied mask. The selectivity for RTP compounds against the photoresist is around 3, this means that it would require a thickness of photoresist around 15 μm to etch 5 μm of RTP, so it is not possible to obtain a smooth and homogeneous thick layer of this photoresist eliminating the possibility of using only this photoresist as a mask. The selectivity for RTP against Cr (the ratio of the etch rate of RTP compared the etch rate of Cr) was found to be 19 and the selectivity for (Yb,Nb):RTP against Cr was found to be 29. For Al, the selectivity against RTP was 5 and against (Yb,Nb):RTP was 7. It has previously been reported [Lazar 2006] that Al masks used in RIE processes using SF_6/O_2 gases show the effect of micromasking if the etched matter from the mask is not properly evacuated and is instead deposited the formed Al_2O_3 on exposed surfaces. Using SF_6, we can also create the AlF volatile species and AlF_3 as non-volatile species, which can also originate micromasking. Chromium and nickel seem to be perfect mask materials. They are minimally sputtered at bias energies up to 200 eV [Jansen 1996].

4.1.4. Etching rate and etching mechanism

Table 4.1 summarizes all the RIE experiments performed with their different experimental parameters. We expected the volatile species to be TiF_4 (temperature of sublimation 557 K), PF_3 (boiling point 172 K), NbF_5 (boiling point 502 K) and PF_5 (boiling point 198 K) [Köhler 1999]. As mentioned above the RIE process employed 250 W RF power, 40 mTorr pressure and gas combination of Ar (10 sccm) and SF_6 (10 sccm) in order to etch the samples.

Table 4.1. Parameters of the RIE experiments.

<table>
<tr><th>Sample</th><th>Compound</th><th>M</th><th>t_{epi}[µm]</th><th>t [min]</th><th>w_{exp} [µm]</th><th>w_r [µm]</th><th>d [µm]</th><th>Etch rate [nm/min]</th></tr>
<tr><td rowspan="2">1</td><td rowspan="2">(Yb,Nb):RTP</td><td rowspan="2">Cr</td><td rowspan="2">3.2</td><td rowspan="2">213</td><td>4</td><td rowspan="2">6.86-7.63</td><td rowspan="2">1.8</td><td rowspan="2">8.2</td></tr>
<tr><td>6</td></tr>
<tr><td rowspan="2">2</td><td rowspan="2">(Yb,Nb):RTP</td><td rowspan="2">Cr</td><td rowspan="2">8.8</td><td rowspan="2">387</td><td>4</td><td rowspan="2">7.5-10</td><td rowspan="2">2.6</td><td rowspan="2">6.7</td></tr>
<tr><td>6</td></tr>
<tr><td rowspan="2">3</td><td rowspan="2">(Yb,Nb):RTP</td><td rowspan="2">Cr</td><td rowspan="2">5</td><td rowspan="2">333</td><td>5</td><td rowspan="2">5.9-8.2</td><td rowspan="2">2.8</td><td rowspan="2">8.4</td></tr>
<tr><td>7</td></tr>
<tr><td rowspan="2">4</td><td rowspan="2">(Yb,Nb):RTP</td><td rowspan="2">Cr</td><td rowspan="2">5</td><td rowspan="2">333</td><td>4</td><td rowspan="2">5.8-6.75</td><td rowspan="2">2.9</td><td rowspan="2">8.7</td></tr>
<tr><td>6</td></tr>
<tr><td>5</td><td>(Yb,Nb):RTP</td><td>Al</td><td>5</td><td>624</td><td>7</td><td>6.41-7.19</td><td>2.5</td><td>4.0</td></tr>
<tr><td rowspan="2">6</td><td rowspan="2">RTP</td><td rowspan="2">Al</td><td rowspan="2">-</td><td rowspan="2">480</td><td>5</td><td rowspan="2">13-15</td><td rowspan="2">2.5-3.5</td><td rowspan="2">6.2</td></tr>
<tr><td>7</td></tr>
<tr><td rowspan="2">7</td><td rowspan="2">RTP</td><td rowspan="2">Al</td><td rowspan="2">-</td><td rowspan="2">810</td><td>5</td><td rowspan="2">19.25-21.58</td><td rowspan="2">2.6</td><td rowspan="2">3.2</td></tr>
<tr><td>7</td></tr>
</table>

M: Metal, t_{epi} : epitaxial layer thickness, w_{exp}: expected width
w_r: real width, d: depth

In Figure 5 of **paper II**, we can observe the etch rate obtained in undoped RTP and (Yb, Nb):RTP in relation to the etching time used. The average etch rate obtained is in the

range of 3.2 to 8.7 nm/min; this etch rate is larger than previously reported for standard RIE of $LiNbO_3$ (around 4 nm/min) [Winnall 2000], although we note that the etching rate of $LiNbO_3$ can be increased after proton exchange to values of 10 nm/min [Hu 2006].

It can be observed that in the case of the chromium mask with short etching times, there is a linear reduction in the etching rate with the time. The potential causes of the low etch rate include too high pressure of the etching gases, increasing the number of collisions in the gas and a decreasing the number of reactive species reaching the surface. Another possible reason, could be an increase of the chemical etching, leading to the formation of sub-products acting as inhibitors on the surface of the etch material, blocking the etching process. Furthermore, in the case of long etching times, there is a significant linear decrease of the etching rate using aluminium as metal mask, both for undoped RTP and (Yb,Nb):RTP; this could be related to the fact that at long etching times, the etching was not only in vertical direction but also in the plane of the sample.

According to Ren *et al*. [Ren 2008], during RIE, etching using gases such as SF_6, CHF_3 etc; gas components could penetrate into the sample, in our case to form bonds with the RTP sample. In order to detect any contamination of the sample by these gases, we have measured the composition of the sample by EDAX. Sample 7 and sample 2 were examined for the detection of Al, Cr, Rb, Ti, O, P, S, F and Ar. As it can be observed in the graph of figure 4.2(b) and figure 4.2(d), only the peaks of the constituent elements of the sample have been observed; there was no detected presence of any element originating from the gases (S, F and Ar) or from the hard mask (Al or Cr).The analysis was made inside the channels of the sample 7 coated with Cr mask. And in case of sample 2 coated with Al mask, analysis was made on the surface which was etched while creating a rib.

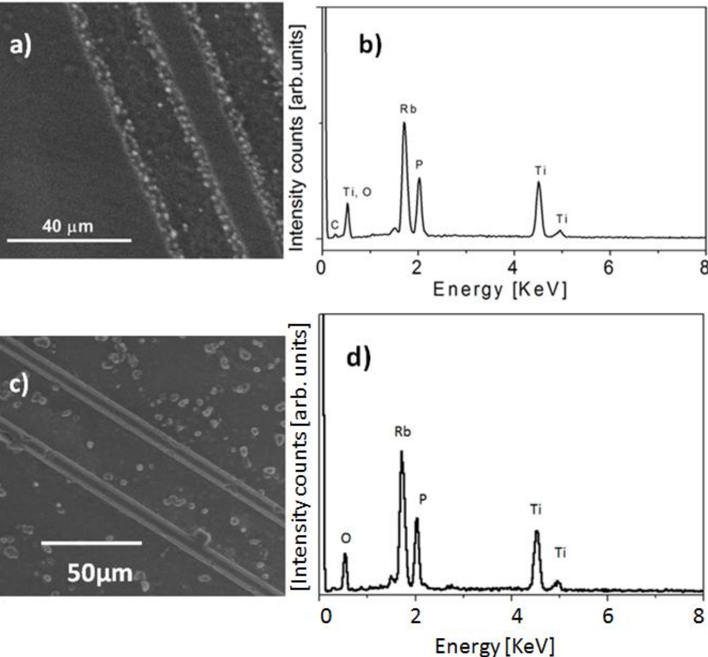

Figure 4.2. a) ESEM image of sample 7, b) energy dispersive X-Ray spectrum of etched RTP sample using Al mask (sample 7), c) ESEM image of sample 2, and d) energy dispersive X-Ray spectrum of etched RTP sample using Cr mask (sample 2)

4.1.5. Etched morphology

The dimensions of the fabricated structures were evaluated by confocal interferometry, and the results are given in Table 4.1. The actual width was observed using an ESEM in sample 2 and sample 6.

It is observed that the width of the structures is always larger than expected, especially in the case of the Al mask. In order to elucidate the reason for these results, different photoresist exposure times on the different metal layers were investigated. It was observed that longer exposure times lead to a larger broadening of the channels for an Al mask than in the case of Cr. It can be deduced that Al required less exposure time in order to obtain the desired width of the channels in the photoresist and this can be related to the larger reflectivity (R) of Al versus Cr in the UV region (R of Al is 92% and R of Cr is 51%). The broadening of the channels obtained in the case of an Al mask could also be due to the fact that, as shown in Table III of **paper II**, the etching rate of Al is larger than for Cr. Therefore, in the case of long etching times, the Al layer could be

totally removed, causing etching of the RTP material to take place along the plane as well as perpendicular to the surface.

The surface topography of the rib waveguide for sample 2, measured with confocal microscope, is shown in Figure 7.a of **paper II**. The epitaxial layer roughness before etching was measured to be around 5 nm and after reactive ion etching it was around 15 nm at the etched region. An ESEM image of a part of the set of 9-mm-long MZs fabricated on the (Yb, Nb):RTP deposited on RTP (sample 2) is shown in Figure 7.b of **paper II**. It can be seen that rather homogenous etching is obtained along the full length of the MZs.

Then these samples were etched in RIE with the gas combination of Ar(10) and SF_6(10) kept at 20 sccm at 250 W power and 40 mTorr pressure. This etch recipe was optimized in the work of Choudhary *et al.* [Choudhary 2013]. In Figures 4.3.a and 4.3.b, ESEM images of the cross section of a RIE channel realized in a (Yb,Nb):RTP/RTP epitaxial layer (sample 2) are shown. A cladding layer of undoped RTP was also grown on the (Yb,Nb):RTP etched layer. After etching for 387 min, an etch depth of around 2.6 μm in an 8.8-μm-thick epitaxial layer is obtained. As can be observed in Figure 4.3.c, the slab height is around 6 μm with a rib height of 2.6 μm. The channel width is 7.3 μm at the base, making a trapezoid with an angle of 30°. As in the previous case, no visible defects are observed in the interface between the active layer and the cladding.

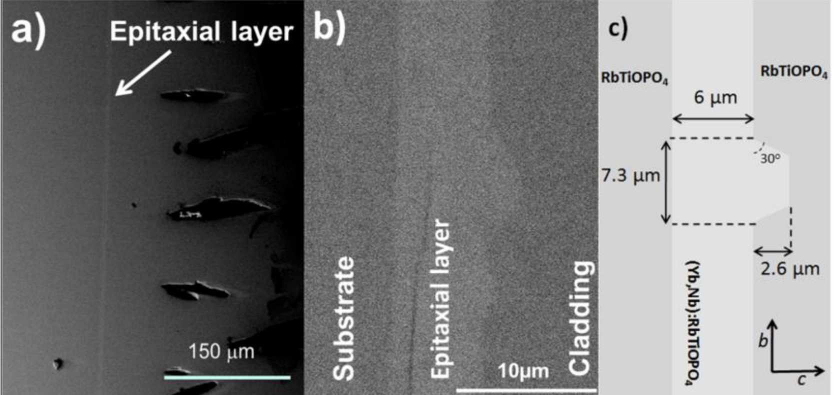

Figure 4.3. a) ESEM image of the general view of the cross section of RIE etched (Yb,Nb):RTP layers and RTP cladding grown also by LPE. b) ESEM image of a detailed cross section of RIE etched (Yb,Nb):RTP layers and RTP cladding and c) cross sectional scheme and dimensions of the figure 4.3 b

In Figure 4.4, we can observe a cross-sectional ESEM image of the channels fabricated by RIE in a RTP substrate (sample 6), using an Al mask with designed structures of 7 µm in width. The etching time was 480 min and the etch depth obtained was around 2.5-3.5 µm. The next step was the growth of an (Yb, Nb):RTP layer by LPE. Ribs with trapezoidal cross section were obtained and there are no appreciable defects at both interfaces, between the epitaxial layer and the RIE etched substrate and between the cladding and the epitaxial layer. The bottom of the channels is found to be approximately 13-15 µm in width, while at the top the channels width is around 3-5 µm. The height of the channels is 2.5-3.5 µm and the side wall angle is around 20-30º.

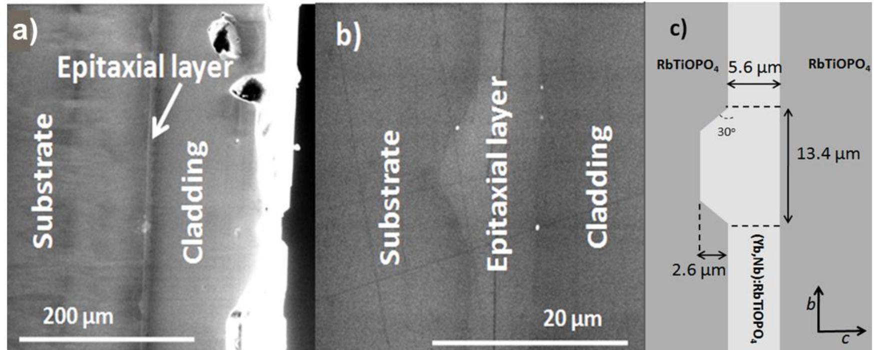

Figure 4.4. (a) ESEM image of the general view of the cross section of RIE channels on RTP filled by (Yb,Nb):RTP by LPE and RTP cladding grown also by LPE. (b) ESEM image of the detailed cross section of the RIE channels and (c) cross sectional scheme with dimensions of the figure 4.4 b

4.2. Fabrication of straight channel waveguides on RTP/(Yb,Nb):RTP/ RTP(001) by ICP-RIE

In this section, we have described the Inductively coupled plasma- reactive ion etching (ICP-RIE) technique with the help of which we have fabricated the straight channel waveguides by structuring the cladding layer of RTP grown on (Yb,Nb):RTP/RTP(001) system.

4.2.1. Pattern design

For these kind of straight channel waveguides, an appropriate thickness of epitaxial layer and dimensions of cladding layer are important. For this reason, we have fabricated different set of straight channel waveguides in order to pattern the cladding layer. The channels with width of 20 µm, 25 µm and 30 µm are designed by using OlympiOs

integrated optics software as shown in figure 4.5. The height of the cladding layer can be controlled by careful etching.

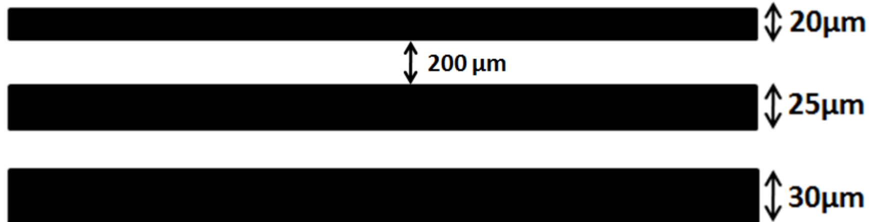

Figure 4.5. Mask design of straight waveguides

4.2.2. Improvement of the metal layer adhesion

Some test experiments were conducted in order to determine the etching rate of metal layer and RTP with ICP-RIE. Among all the other metal layers as mentioned in table 4.2, we tried the combination of Al and Cr with different thicknesses.The reason of using the combination of Al and Cr was that, Al showed good adhesion on RTP substrates and Cr has higher selectivity among all the other metal layers as experimented in section 4.1. But the combination of Al and Cr at higher layers thickness, for instance 500 nm each was not good; the layers were lifted off during cleaning the sample with acetone.

The etch rate of Cr is very low and it can work as a perfect hard mask for deep etching but sometimes we faced some problems with the adhesion of Cr with the sample. It could sustain the tape and scratch test but during cleaning the sample with acetone and ethanol, the layer was removed very fast. In order to ensure the good adhesion of Cr on RTP, we deposited a thin layer of TiO_2 then progressively decrease the oxygen content in the chamber and moved to Ti. Then started enriching Ti with Cr upto pure Cr. This technique really helped to improve the adhesion of the metal layers which was proved by tape and scratch test.

4.2.3. Selectivity and etch rate

The preliminary test was performed to determine the etch rates of undoped RTP and Cr metal layer by using Ar (10 sccm), SF_6 (sccm), Power=150 W, ICP=300 W and Pressure=15 mTorr. The process was controlled by laser camera with end point feature, which means that the etching process stops when the metal layer is completely removed from the surface of the substrate. The etching rate of RTP and metal layers is shown in

table 4.2. As it can be seen that the selectivity of Ti-Cr layer combination is relatively higher than Al-Cr layer combination which allows the fabrication of rib waveguides with greater heights.

Table 4.2. Parameters of ICP-RIE process.

Etch time [min]	Cr layer thickness [nm]	Ti layer thickness [nm]	Al layer thickness [nm]	Etching rate of RTP [nm/min]	Etching rate of metal layers [nm/min]	Selectivity
18	250	10	-	95	14	6.78
30	400	-	400	133	26.66	4.98
45	800	10	-	127	17.8	7.13

4.2.4. Etched morphology

The sample was etched in ICP-RIE with a gas combination of Ar (10), SF_6 (10) kept at 20 sccm at 150W power, 300W ICP power and 15mTorr pressure. This etch recipe is obtained after optimizing different parameters. After the fabrication process, the samples were examined by ESEM with an acceleration voltage of 20 kV at a working distance of 10 mm. Table 4.3 summarizes the dimensions of the straight waveguides.

Table 4.3. Etched dimensions.

Actual width [µm]	Obtained top width [µm]	Obtained bottom width [µm]	Rib height [µm]	Rms value [nm]
20	14.60	21.8	5.75	7.66
25	17.70	25.47	5.43	7.34
30	25.28	31.53	5.70	7.12

In Figure 4.6, we can observe a cross-sectional ESEM image of the channels fabricated by ICP-RIE in a RTP cladding, using an Ti-Cr mask with designed structures of 30 µm in width. The etching time was 45 min and the etch depth obtained was around 5.7 µm. Ribs with trapezoidal cross section were obtained in the cladding layer. There are no appreciable defects at the interfaces between the RTP substrate- epitaxial layer and the epitaxial layer-cladding layer. The bottom of the channels is found to be approximately 31 µm in width, while at the top the channels width is around 25 µm.

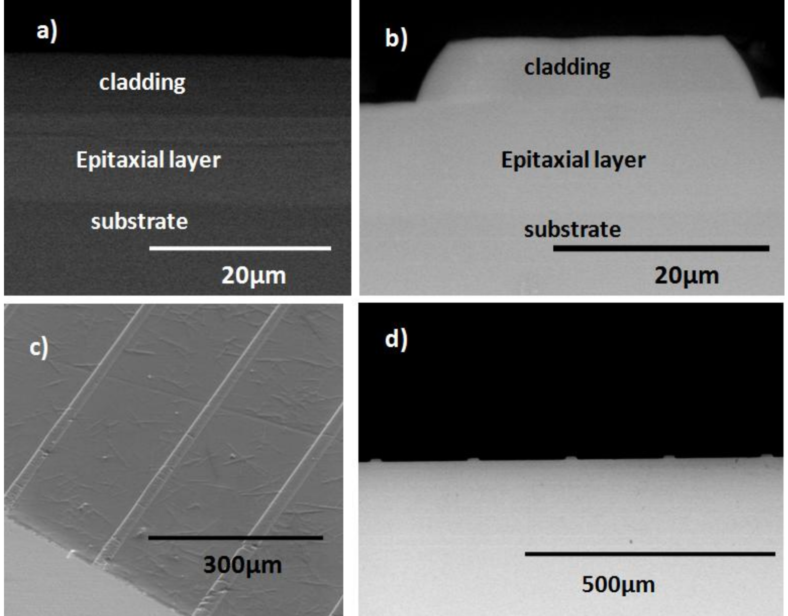

Figure 4.6.a) ESEM image of the sample before etching process, b) ESEM image of the 30 µm rib structure, c) ESEM image of the top view of the sample, d) ESEM image of the cross-sectional view of the sample

4.3. Fabrication of Y-Splitters and MZ structures on RTP (001) by Cs^+ ion exchange

4.3.1. Pattern design

In a previous work of our group, planar waveguides and channel waveguides were fabricated by Cs^+ ion exchange method [Cugat 2013b]. Cs^+ ions were used for exchange process because it produces an increase in the refractive index and its ionic radius is not

far from the Rb^+ radius and free ion polarizability of Cs^+ (3.34) is higher than Rb (1.98) [Tessman 1953]. Different experiments were conducted in order to test the parameters of ion exchange process. In this work, we used the optimized parameters in order to create straight lines, S-bends, Y-splitters and MZs structures on RTP (001) substrates. All these structures were oriented along the ***b*** crystallographic direction.

The designed mask was prepared by using the parameters shown in table I of **paper IV**. The structures were transferred to the sample (Ti layer + RTP(001)) by means of laser lithography as explained in section 2.1.4 of chapter 2. The ion exchange took place for 2 h at a temperature of 698 K and a rotation of 60 rpm in all the samples mentioned below. Design patterns of MZI, bend and straight- waveguide are shown in figure 2 of **paper IV**.

4.3.2. Cs^+ exchange profile

Sample was prepared in an epoxy and analysed for the compositional analysis of the element as can be seen in the figure 4.7. To obtain the Cs^+ ion analysis detail, the profile was taken vertically down from the surface along the channel. The exchange of Cs^+ as a function of the depth in the RTP samples was measured by electron probe microanalysis.

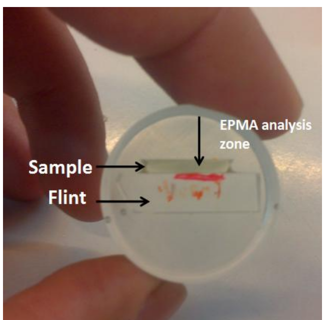

Figure 4.7. Cs:RTP sample embedded in a glue for EPMA analysis

Figure 4.8 shows the Cs concentration in weight per cent as a function of the distance to the crystal surface in three different channels in the RTP and two other channels in a (Yb,Nb):RTP epitaxial layer. As can be observed, there's no reproducibility of the Cs^+ exchange in the different channels, maybe due to the fact that each channel can be located in a different crystal growth sector, and then, different ferroelectric domains.

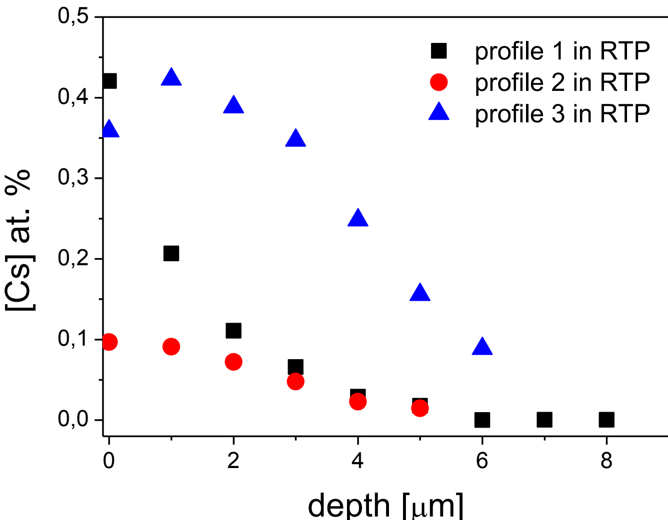

Figure 4.8. Cs^+ concentration in the channel as a function of the depth in the RTP substrate

4.4. Fabrication of straight waveguides by ion exchange

4.4.1. Pattern design

Set of ten waveguides of 10 μm in width and 10 mm in length were designed by using olympiOs software. The mask design for channel waveguides is shown in figure 4.9.

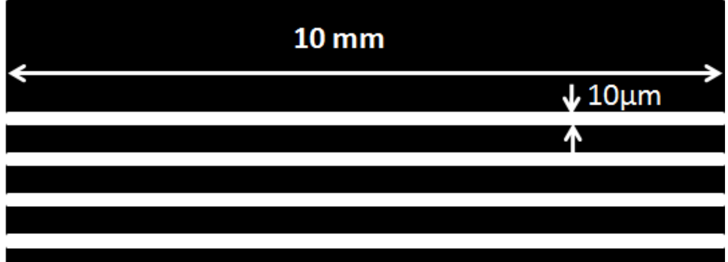

Figure 4.9. Pattern design of straight waveguides

In this work, Cs^+-exchange RTP WGs were fabricated along three different crystallographic directions (see table 2 of **paper IV**). For future applications in self-frequency doubling (SHG) in RTP and self-frequency doubling (SFD) in Yb-doped RTP, the straight channel WG propagation directions were chosen to be parallel to the direction of type II ($e^{\omega}+o^{\omega}\rightarrow e^{2\omega}$) phase matching for a wavelength of 1.05 μm. These

directions are along the [180] direction in RTP (θ=90º, φ=75º) and along the [120] direction (θ=90º, φ=45º) in (Yb,Nb):RTP. Epitaxial layer of (Yb, Nb) doped RTP with a solution composition mentioned in section 3.2.2 was grown on RTP(001) substrate. The thickness of epitaxial layers was kept at 20 μm in order to avoid the Cs^+ exchange till RTP substrate. RTP (001) sample was cut along 45° is shown in figure 4.10. For the design pattern, same mask was used as shown in fig 4.5.

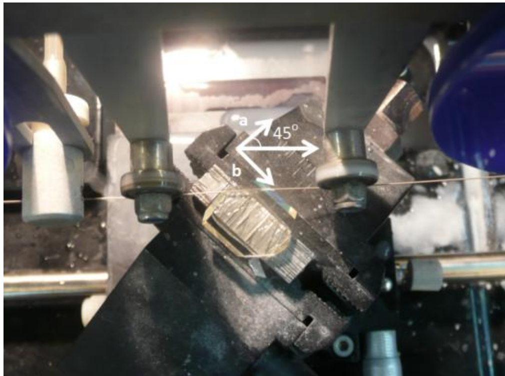

Figure 4.10. Cutting of a RTP (001) substrate along [120] direction with a diamond cutting wire

The processed sample was dipped in the $CsNO_3$ melt 6 mm below the surface at 698 K for 2 hours at rotation of 40 rpm. And when the process was finished, the sample was extracted and suspended 6 mm above the melt and allowed the cooling of the furnace at 30 K/ h to avoid thermal shocks.

4.4.2. Morphological characterization and Cs^+ exchange profile

The ion exchange time of these waveguides was also 2 h at 698 K with a rotation rate of 60 rpm. After the ion exchange process, when these samples were examined with ESEM, it was observed that Ti mask layer was removed from the edges along the waveguides allowing the Cs^+ ions to diffuse in these parts which in turn forms a wider dimension of waveguides than expected as shown in figure 7 of **paper IV**. This kind of Ti layer removal was observed in all parts of the waveguides. This can be due to the bad adhesion of Ti layer at the edge of the waveguide or over etching the Ti mask. And it can also be seen in figure 7.a) and b) of **paper IV** that the part of the substrate which was directly exposed with the Cs melt shows some etching.

If we compare the Cs^+ ion concentration in the channel as a function of the depth in RTP substrate and Cs^+ ion concentration in the channel as a function of depth in (Yb,Nb):RTP epitaxial layer from figure 4.8 and 4.11, it can be also observed that the quantity of Cs^+ ions introduced in RTP is larger than in the doped (Yb,Nb):RTP. This fact could be expected due to the similar or lower ionic conductivity when RTP is doped with Yb and Nb [Gavaldà 2012]. In this reference, the Nb content of the sample was larger than in the epitaxial sample as reported in this work, and the ytterbium concentration is similar; and as observed by Gavaldà *et al*. (Yb,Nb):RTP has similar ionic conductivity than RTP along ***c*** crystallographic direction. The codoping with Nb and Yb reduces the effects of niobium ion, and shows the ionic conductivity similar to that of RTP. Generally, the Cs^+ concentration decrease exponentially with the depth and the ion exchange region is as minimum 6-7 μm.

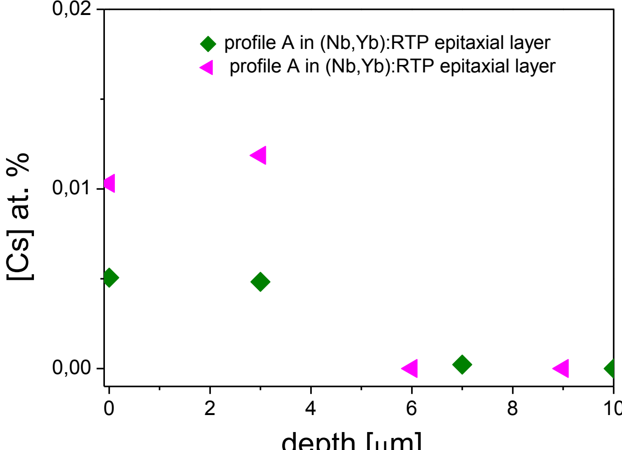

Figure 4.11. Cs^+ ion concentration in the channel as a function of the depth in (Yb,Nb):RTP epitaxial layer

Chapter 5
Computer simulations and optical characterization

Waveguides are the basic building block of the integrated photonics. By using different kinds of waveguides, we can construct complex devices. Therefore, the proper characterization helps us to understand the guiding properties of the waveguides. Computer simulations are the first step in order to design a specific device and estimate the guiding properties. The losses estimation of the waveguides and the near field pattern gives the information about the guiding process in the waveguides. Hence, the simulated and experimental results can be correlated. In this work, the optimum dimensions of Y-splitters and MZ structures were carefully determined in order to guide the single fundamental mode. In this chapter, the basic concept of ray optical treatment is described and some typical geometry of optical waveguides including planar waveguides and channel waveguides are presented. By using the channel waveguides geometry, straight waveguides, Y-splitters and MZ structures are fabricated and their characterization is explained in this chapter.

5.1. Optical waveguides

The basic elements in integrated photonics technology, which is based on the processing of light confined in optical structures, are known as optical waveguides. A waveguide works on the principle of total internal reflection by confining the light within its boundaries. For total internal reflection phenomena to happen, it is necessary to fabricate a guiding medium (where most of the radiation energy is concentrated) with high refractive index surrounded by low refractive index media. For instance: light confinement happens in a planar film of glass with refractive index $\boldsymbol{n}$ situated in air. When the ray enters the film and propagates with the internal angle $\boldsymbol{\theta}$ greater than the critical angle $\boldsymbol{\theta_c}=\sin^{-1}(1/n)$, total internal reflection takes place. And this ray remains trapped inside the film, this kind of arrangement of film and air acts as an optical waveguide.

When the thickness of the guiding film is reduced progressively till it reaches the size of the order of the wavelength of radiation, a new phenomenon take place. The reflected wave coming from the total internal reflection at the upper boundary and the reflected

wave coming from the lower interface interferes and allows the light to propagate in only a discrete set of angles. For each permitted angle of propagation, the transversal structure of the electromagnetic field associated with the radiation is maintained as the light beam propagates along the film; these characteristic form a ***propagation mode***. So a propagation mode is the outcome of combining total internal reflection and constructive interference. This assumption of propagation modes was based on considering the light as plane waves, or in other words, that the direction of the light propagation within the waveguide can be explained by using rays. Although, the ray optics treatment can give some interesting information, for a complete understanding of light propagation within guiding structures, it is necessary to consider light as electromagnetic waves.

5.1.1. Classification of optical waveguides

I) Planar waveguides (1D): Planar waveguides are optical structures that confine the optical radiation in only one dimension. Depending on the refractive index distribution in the planar structure, planar waveguides can be classified as step-index waveguides or graded-index waveguides.

a) Step-index planar waveguides

The step index planar waveguides can be fabricated by growing a uniform planar epitaxial layer with a constant refractive index (n_{epi} = constant) on a substrate with refractive index n_{sub} and a cladding layer of refractive index n_{clad} grown on the film as is shown in figure 5.1 [Lifante 1997]. Usually, the refractive index of the cladding is lower than or equal to the refractive index of the substrate $n_{clad} \leq n_{sub}$, and in this way, we have $n_{epi} > n_{sub} \geq n_{clad}$. In fact, in many cases the cladding medium is air, therefore $n_{clad} = 1$, which fulfils the condition of $n_{clad} \leq n_{sub}$.

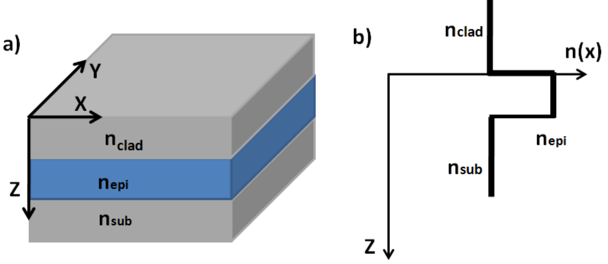

Figure 5.1. a) Symmetric step index planar waveguide, b) refractive index profile, where $n_{epi} > n_{sub} = n_{clad}$

b) Graded-index planar waveguides

If the refractive index of the surface layer of the substrate is not constant, but varies with depth (along the z-axis), the structure is called a graded index planar waveguide [Nevado 2001]. In these kinds of waveguides, the refractive index is maximum at the top surface and its value decreases with depth until it reaches the value corresponding to the refractive index of the substrate as shown in figure 5.2. These kind of waveguides can be fabricated by the surface modification of a substrate, whether by physical processes such as ion implantation, metal diffusion etc or by chemical modification of the substrate such as ion exchange methods.

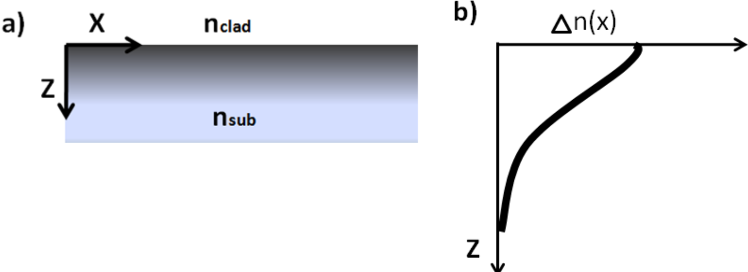

Figure 5.2. a) Graded-index planar waveguide, b) Refractive index profile inside the active layer

II) Channel waveguides (2D): In planar waveguides the light confinement is restricted in one dimension (for example to z-axis), and if the light propagates along the y axis, the light can spread out in x-direction due to diffraction. In order to avoid this situation, the total reflection should not have to take place at only upper and lower interfaces but also at the lateral boundaries. In this way, light beam can be confined in channel waveguides or 2D waveguides, in which the core region has a refractive index greater than any of the surrounding media. These waveguides can also be classified as step-index and graded-index waveguides similar to above mentioned planar waveguides but with the difference that, now it has an extra dimension which characterizes the waveguide structure. There are many different types of channel waveguides but in this chapter, we have only mentioned the ones we worked on. These waveguides are rib waveguides, ion exchanged waveguides and stripe loaded waveguides.

a) Rib waveguides

Rib waveguides can be fabricated by growing an epitaxial layer on a substrate and structuring it by etching. If the etching process is not complete and does not reach the

substrate, a channel waveguide is also produced, providing that the thickness and height of the rib are conveniently tailored. Figure 5.3.a shows a scheme of a rib waveguide structure.

b) Ion exchanged waveguides

Another common type of channel waveguides in integrated photonics is the diffused channel waveguides which are fabricated by introducing a local increase of the substrate´s refractive index performed by diffusion methods [Pernas 2000] as can be seen in figure 5.3.b.

c) Stripe loaded waveguides

In these types of waveguides, the planar waveguide has high refractive index as compared to substrate and structured cladding layer known as stripe. Figure 5.3.c shows a scheme of a stripe loaded waveguide. Within the region of the strip, most of the energy is confined in the film with refractive index higher than the surroundings. Requirements of the edge roughness of the strip are no longer as severe as in rectangular film waveguides and therefore it is easier to fabricate strip loaded structures.

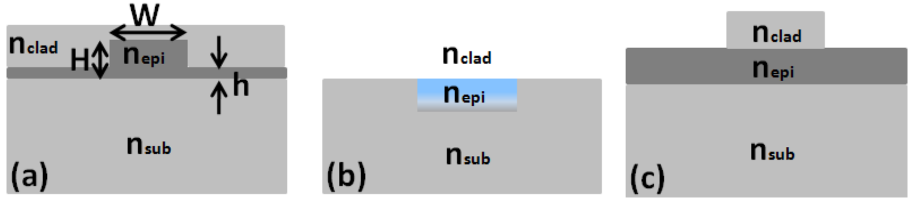

Figure 5.3. Three main types of channel waveguides (2D waveguides): a) rib waveguide; b) diffused channel waveguide; c) stripe loaded waveguide

5.1.2. Light propagation in channel waveguides

In general, the integrated photonic waveguides presented in chapter 4 are based on channel (2D) waveguides, in which the light is confined in two directions, allowing the propagation in only one direction. In this way, radiation travelling in channel waveguides can propagate without spreading in a direction perpendicular to the propagation direction, which contributes to decrease the power losses. Therefore, for performing functions such as modulation, switching, amplification, etc., the channel waveguides are the right choice for the fabrication of integrated optical devices.

Light behaviour in an optical waveguide can initially be analysed by examining the case of planar waveguides from the point of view of ray optics. Let us consider a planar waveguide, where the refractive index of the epitaxial layer n_{epi} is higher than the refractive index of the substrate n_{sub} and the cladding layer n_{clad} ($n_{epi} > n_{sub} > n_{clad}$). The critical angle that defines the total internal reflection for the cladding-epitaxial layer interface and the epitaxial layer-substrate boundary are given by (5.1) and (5.2):

$$\theta_{clad-epi} = sin^{-1}\left(\frac{n_{clad}}{n_{epi}}\right) \tag{5.1}$$

$$\theta_{epi-sub} = sin^{-1}\left(\frac{n_{sub}}{n_{epi}}\right) \tag{5.2}$$

In this case, $n_{epi} > n_{sub} > n_{clad}$, therefore the critical angles fulfil the relation of $\theta_{epi-sub} > \theta_{clad-epi}$. When the ray enters the epitaxial layer with an internal angle θ lower than the critical angle corresponding to the cladding-epitaxial layer interface ($\theta_{clad-epi}$), the light penetrates the cladding as well as the substrate. Therefore the light travels in three regions; hence there is no confinement of light in the epitaxial layer. This situation corresponds to radiation modes as shown in figure 5.4.a. In the case of light entering the epitaxial layer with an internal angle θ which fulfils $\theta_{clad-epi} < \theta < \theta_{epi-sub}$, it totally reflects at the epitaxial layer-cladding interface due to total internal reflection phenomena but it can still penetrate the substrate because $\theta < \theta_{epi-sub}$. This leads to the substrate radiation modes or substrate modes as shown in figure 5.4.b. And if the light fulfils the total internal reflection phenomena at both the interfaces by following $\theta > \theta_{clad-epi} > \theta_{epi-sub}$, then the radiation is totally confined and cannot escape the film. This situation gives rise to guided mode as shown in figure 5.4.c which are the most interesting case as these guided modes propagate through the waveguide.

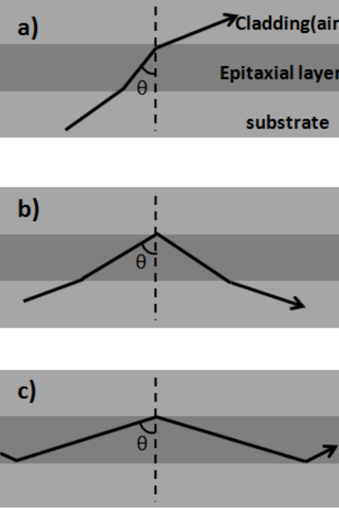

Figure 5.4. a) Radiation mode in a step-index planar waveguide, b) substrate mode and, c) guided mode

The ray optic approach can be used for the qualitative description of light behaviour in an optical waveguide. This approach helps to determine the types of mode that can be found in such structures, the number of guided modes supported by a waveguide and the propagation constant can be determined. But for many applications, it is important to have the knowledge about the electric field distribution of the radiation within the waveguide structure. Electromagnetic theory of light helps to determine the optical fields or the intensity distribution associated with the light propagation in the waveguide structures. The electromagnetic fields in a given structure are solved by the Maxwell´s equations and the solutions for the field correspond to the propagation modes. Maxwell´s equations are used to develop the wave equations for TE (the electric field associated with the mode has only a transversal component) and TM (the electric field associated with the mode has only a parallel component) propagations that govern light behaviour in planar waveguides. Assuming that the light is propagating through a dielectric, non-magnetic and linear material, Maxwell´s equations are used to provide the wave equations for TE and TM modes indicated by (5.3) and (5.4) respectively.

$$\frac{d^2E_y(x)}{dx^2} + [k_o^2n^2(x) - \beta^2]E_y(x) = 0 \qquad (5.3)$$

$$\frac{d^2H_y(x)}{dx^2} + [k_o^2n^2(x) - \beta^2]H_y(x) = 0 \qquad (5.4)$$

where k is the wavenumber and β is the propagation constant of the modes.

In case of channel waveguides, some approximate methods such as effective index method and Marcatili´s method can be applied to calculate the propagation modes in 2D structures. Maxwell´s equations provide the way to establish an equation for the longitudinal component of the electric field E_z and the magnetic field H_z. These two equations are referred to as the reduced wave equations for the channel waveguides, and are given by (5.5) and (5.6):

$$\frac{\partial^2 E_z}{\partial x^2} + \frac{\partial^2 E_z}{\partial y^2} = [\beta^2 - k_o^2 n^2(x,y)]E_z \tag{5.5}$$

$$\frac{\partial^2 H_z}{\partial x^2} + \frac{\partial^2 H_z}{\partial y^2} = [\beta^2 - k_o^2 n^2(x,y)]H_z \tag{5.6}$$

An exact treatment of the modal characterisation in 2D waveguides is not possible, even in the simplest case of a symmetric rectangular channel waveguide. In this chapter, the effective index method is explained. With this method, we can obtain the optical modes supported by a channel waveguide with arbitrary geometry, even with graded index regions.

5.1.3. Solution for step index channel waveguides by effective Index method (EIM)

The effective index method (EIM) is used to perform approximate analysis for calculating the propagation modes of channel waveguides. Two dimensional structures can be solved by applying the tools developed for planar waveguides [Chiang 1986]. The modal fields and the propagation constant in channel waveguides with arbitrary geometry and index profiles can be obtained by using this approximation method. It consists of solving the problem in one dimension, described by the $\boldsymbol{x}$ coordinate, in such a way that the other coordinate (the $\boldsymbol{y}$ coordinate) acts as a parameter. In this way, a y-dependent effective index profile is obtained; then this index profile is processed once again as a one dimensional problem from which the effective index of the propagating mode is finally obtained.

The propagation constants supported by a 2D channel waveguide having a refractive index profile which depends on two coordinates $n=n(x,y)$ are then calculated by solving the propagation modes for two 1D planar waveguides. The EIM treats the channel waveguide as the superimposition of two 1D waveguides as shown in figure 5.5.

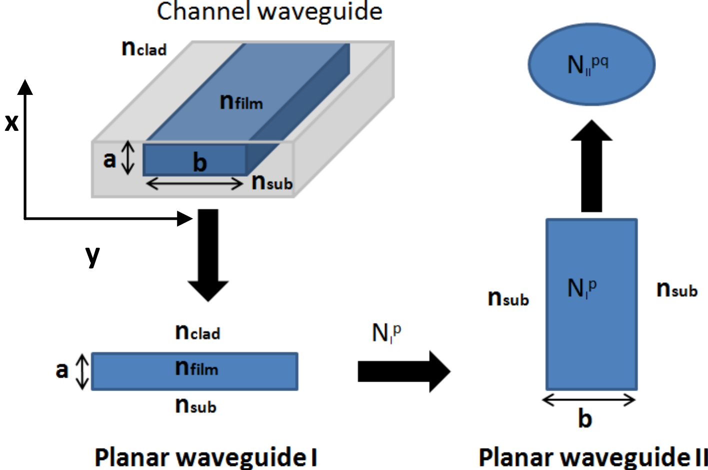

Figure 5.5. Scheme of the effective index method for solving the propagation constant of a step index channel waveguide. To solve the problem of a 2D waveguide, it is splitted into two step-index planar waveguides.

As we can see in Figure 5.5, the planar waveguides I and II confine the light in $\boldsymbol{x}$ and $\boldsymbol{y}$ directions respectively. For propagation modes polarised mainly along the x direction (E_{pq}^{x}), we have seen that the major field components are E_x, H_y and E_z. The propagation of these polarised modes is similar to the TM modes in a 1D planar waveguide, and their solutions will correspond to the effective indices N_I.

Now the waveguide II is considered to consist of a guiding layer of refractive index N_I, which has previously been calculated. In this second planar waveguide, the modes are TE polarised and the major field components are E_x, H_y and H_z components, because the light is mainly polarised along the $\boldsymbol{x}$ direction. From equation (5.5), the wave equation for modes propagating in a channel structure defined by its refractive index function given by n(x, y) can be written as:

$$\frac{\partial^2 E(x,y)}{\partial x^2} + \frac{\partial^2 E(x,y)}{\partial y^2} + [k_0^2\, n^2(x,y) - \beta^2]E(x,y) = 0 \qquad (5.7)$$

where $k_o = 2\pi / \lambda$, λ with the wavelength of the radiation, and β is the propagation constant of the mode, $\beta = k_o N$ with N the effective refractive index. The EIM is based on the assumption that the function describing the optical field admits a factorisation of the form:

$$E(x,y) = \Theta(x,y)\,\Phi(y) \tag{5.8}$$

By substituting this proposed solution into the wave equation for channel waveguides (5.7), we obtain a system of two coupled differential equations:

$$\frac{\partial^2 \Theta(x,y)}{\partial x^2} + [k_o^2 n^2(x,y) - k_o^2 N(y)^2]\Theta(x,y) = 0 \tag{5.9}$$

$$\frac{\partial^2 \Phi}{\partial y^2} - \left(\frac{2}{\Theta}\frac{\partial \Theta}{\partial y}\right)\frac{\partial \Phi}{\partial y} + \left(k_o^2 N^2(y) + \frac{1}{\Theta}\frac{\partial^2 \Theta}{\partial y^2} - \beta^2\right)\Phi = 0 \tag{5.10}$$

The differential equation (5.9) is solved by using the ***y*** coordinate as a parameter which is the basic requirement in the EIM procedure. An effective index profile (N_y) obtained by the eigenvalue solution of (5.9) explicitly depends on the ***y*** coordinate which is thus introduced in the second differential equation (5.10) in the problem resolution.

The approximation used by the effective index method based on the fact that function Θ(x, y) has a slowly variation respect to the y coordinate [Liñares 2000]. So it is reasonable to eliminate the second and fourth terms in differential equation (5.10) that involve partial derivatives of the function Θ(x,y) respect to *y* coordinate. This approximation leads to:

$$\frac{\partial^2 \Phi}{\partial y^2} + [k_0^2 N^2(y) - \beta^2]\Phi = 0 \tag{5.11}$$

The differential equation obtained by solving the equation (5.10) is similar to the wave equation for planar waveguides. Thus the solution of equation (5.11) finally provides the effective index of the propagating mode in the channel waveguide. This effective index is defined by two integer numbers *p* and *q*, reflecting the *p*th and *q*th order solution of (5.9) and (5.11) respectively.

The electromagnetic wave propagation as we have explained above, can be described by Maxwell´s equations. However a direct solution of Maxwell´s equations is usually difficult and the exact analytical expressions for such a solution can be found only for a few cases. Numerical solutions can be possible for more complex problems which cannot be solved analytically. To make the numerical solution possible, certain

assumptions have to be made to simplify Maxwell´s equations for specific applications [Xu 1995]. For different interests and applications, Helmholtz equations are derived directly from Maxwell´s equations which are used by the BeamProp software for solving the modes. The BeamProp software used in this thesis to perform simulations is based on the Beam propagation method by finite differences (FD-BPM), described in next section.

5.1.4. Finite Differences Beam propagation method (FD-BPM)

In beam propagation method (BPM), the light propagation in the waveguides is solved by applying the solution to the Helmholtz equation or the Fresnel equation. There are two numerical schemes in order to solve the Fresnel equation: fast fourier transform (FFT-BPM) and finite difference method (FD-BPM). In FFT-BPM, the optical propagation is modeled as a plane wave spectrum in the spatial frequency domain. In this way, the effect of medium inhomogeneity is interpreted as a correction of the phase in the spatial domain at each propagation step. Besides the conventional FFT-BPM, the beam propagation method using finite differences, called FD- BPM, to solve the scalar paraxial wave equation has also been developed [Chung 1990] and compared to FFT-BPM [Chung 1990, Scarmozzino 1991].

In this section, finite differences method is developed for 1D waveguides, in order to solve the optical propagation in 2D waveguides; we need to reduce the 2D problem to a 1D problem through the EIM. This course of action gives very good results in general and saves processing time. However, finite difference schemes for 2D structures can also be developed [Huang 1992].

The Fresnel or paraxial equations is as follow:

$$2iK\frac{\partial u}{\partial z} = \left(\frac{\partial^2}{\partial x^2} + \frac{\partial^2}{\partial y^2}\right)u + (k^2 - K^2)u \qquad (5.12)$$

where K is a constant which represents the characteristic propagation wave vector, K= $n_o\omega$/c and k(x,y,z)= k_on(x,y,z), n_o can be the refractive index of the substrate or cladding. It is the starting equation for the description of optical propagation in inhomogeneous media. The partial derivatives of Helmholtz scalar wave (*5.12*) are approximated by a finite difference scheme which can be expressed as:

$$2iK\frac{u_j(z+\Delta z)-u_j(z)}{\Delta z}=\frac{u_{j-1}(z)-2u_j(z)+u_{j+1}(z)}{\Delta x^2}+k_o^2(n^2-n_o^2)u_j(z) \qquad (5.13)$$

where $u_j(z)$ is the optical field at the position (jΔx, z) with j= 1, 2…... N. In finite differences, this scheme is known as *forward-difference* which uses the information of field u_j (z) at position z and facilitates us to calculate the optical field $u_j(z+\Delta z)$ after a propagation step of Δz [Press 1996a]. Finite difference method based on forward difference scheme is accurate to the first order; moreover, from a numerical point of view, it is conditionally a stable method. In finite difference scheme, there is another way to calculate the optical field and that is known as backward-difference [Press 1996b]. The Helmholtz scalar equation expressed backward-difference as:

$$2iK\frac{u_j(z+\Delta z)-u_j(z)}{\Delta z}=\frac{u_{j-1}(z+\Delta z)-2u_j(z+\Delta z)+u_{j+1}(z+\Delta z)}{\Delta x^2}+k_o^2(n^2-n_o^2)u_j(z+\Delta z) \qquad (5.14)$$

By using this method, the solution obtained in the simulation is similar to the forward difference method, but it has an advantage of being unconditionally stable. But we cannot obtain more accuracy by this method.

Superior to these above mentioned methods, there is another method which is a linear combination of *forward-difference* and *backward-difference* method known as Crank-Nicolson scheme [Press 1996b]. It is not only unconditionally stable but also provides more accurate solutions than the two previous methods.

The paraxial propagation equation to be solved by finite difference method following a Crank-Nicolson scheme can be represented as:

$$[2K+i\,\Delta z\,\alpha\,H]u(z+\Delta z)=[2K-i\,\Delta z\,(1-\alpha)\,H]u(z) \qquad (5.15)$$

where the operator *H* is defined as:

$$Hu\equiv\frac{u_{j-1}-2u_j+u_{j+1}}{\Delta x^2}+(n_j^2-n_o^2)k_o^2u_j \qquad (5.16)$$

By using finite differences, the next equation is obtained:

$$2iK\big[u_j(z+\Delta z)-u_j(z)\big]=k_o^2(n^2-n_o^2)\big[\alpha u_j(z+\Delta z)-(1-\alpha)u_j(z)\big]\Delta z+\left[\alpha\frac{u_{j-1}(z+\Delta z)-2u_j(z+\Delta z)+u_{j+1}(z+\Delta z)}{\Delta x^2}-(1-\alpha)\frac{u_{j-1}(z)-2u_j(z)+u_{z+1}(z)}{\Delta x^2}\right]\Delta z \qquad (5.17)$$

This expression relates the optical field u(z+Δz) at z+Δz with the optical field u(z) at z. Rearranging terms in the (5.17) equation, we can obtain:

$$a_j u_{j-1}(z+\Delta z) + b_j u_j(z+\Delta z) + c_j u_{j+1}(z+\Delta z) = r_j(z) \qquad (5.18)$$

where a_j, b_j, c_j, and r_j coefficients are:

$$a_j = -\propto \frac{\Delta z}{\Delta x^2}$$

$$bj = 2 \propto \frac{\Delta z}{\Delta x^2} - \alpha\, \Delta z[n_j^2(z+\Delta z) - n_o^2]k_o^2 + 2iK$$

$$c_j = -\alpha \frac{\Delta z}{\Delta x^2}$$

$$r_j = (1-\alpha)\frac{\Delta z}{\Delta x^2}[u_{j-1}(z) + u_{j+1}(z)] + \left\{(1-\alpha)\Delta z[n_j^2(z) - n_o^2]k_o^2 - 2(1-\alpha)\frac{\Delta z}{\Delta x^2} + 2iK\right\} u_j(z) \qquad (5.19)$$

Equation 5.18 in addition to the coefficients defined by *(5.19)*, forms a tridiagonal system of N linear equations (j=1,2,…….N), which can be solved very efficiently. This tridiagonal system can be solved by using the Thomas method [Press 1996a] which shows an excellent numerical stability. Thomas algorithm is a simplified form of Gaussian elimination that can be used to solve tridiagonal systems of equations.

The Crank- Nicolson scheme is stable for $\alpha > 0.5$, if the refractive index is independent of *x* and *z*. It provides a good approximation to the exact solution of the problem by establishing a second order approximation in the propagation step $O(\Delta z^2+\Delta x^2)$. Therefore, the finite difference method is a powerful numerical method which allows the use of large propagation steps which implies less computational time.

Boundary conditions

The computational domain in BPM calculations is finite therefore, it is important to define the boundary conditions for the optical field at the limits of the computational window. These boundary conditions should be properly chosen so that, they should not introduce any error in the propagation description of the optical field otherwise, the radiations can reflect on the limits of the computational window and interferences are produced. In order to solve this problem, an algorithm known as *transparent boundary condition* (TBC) [Hadley 1992] is used to implement the realistic boundary conditions from a physical point of view. It allows the wave to leave the computational region when it reaches the window limits without any reflection coming back to the domain. It does not require adjustable parameters and is problem independent so it can be directly applied to any waveguide structure. Additionally, it is easily incorporated into a standard

Crank-Nicolson differencing scheme in both two and three dimensions, and it is applicable to longitudinally varying structures of importance for integrated photonic devices [Hadley 1992]. These transparent boundary conditions have been applied in the simulations reported in this thesis.

5.2. Refractive index variation

5.2.1. Refractive index contrast at 632 nm

We have measured the refractive indices at 632 nm of different layer systems with light polarized parallel to ***a***, ***b*** and ***c*** crystallographic directions (X, Y and Z, respectively) at room temperature. The refractive indices of substrates and epitaxial layers were measured by following the procedure as mentioned in section 2.2.3. The refractive indices and refractive indices variation of the epitaxial layer systems is shown in tables 5 and 6 respectively of **paper I.**

In table 6 of **paper I**, we can see that, in (Yb,Nb):RTP/RTP (001) system, $\Delta n_z > \Delta n_y > \Delta n_x$. So in case of channel waveguides, the better light confinement is along z-direction and x-direction is used as a propagation direction. In the case of RTP/K:RTP(001), RTP/K:RTP(100) and KTP/Na:KTP(001) waveguide systems, Δn_x, Δn_y and Δn_z are all positive and can confine the light (confinement can vary depending on the value of refractive index contrast between the two layers) in all the directions at 632 nm. Potentially, these waveguides should have step index profile but the refractive index was graded in the case of RTP/K:RTP(001) and RTP/K:RTP(100) as explained in section 3.2.3 of chapter 3.

5.2.2. Refractive index contrast at 1550 nm

We have measured the refractive indices of RTP and (Yb,Nb):RTP (epitaxial layer) with light polarized parallel to the ***a***, ***b*** and ***c*** crystallographic directions in order to determine the refractive index contrast at 1550 nm at room temperature for each polarization. The refractive indices in the three dielectric axes are shown in table 5.1.

Table 5.1. Refractive index measurement of RTP substrate and (Yb,Nb):RTP at 1550 nm.

	n_x	n_y	n_z
RTP	1.7559	1.7630	1.8375
(Yb,Nb):RTP/RTP	1.7516	1.7633	1.8425
Δn	-0.0043	0.0003	0.0050

As it can be seen from table 5.1, the refractive index contrast along ***b*** and ***c*** crystallographic directions is positive which is suitable to confine the light in the waveguide and negative along ***a*** crystallographic direction which has no confinement and ***a*** crystallographic direction is used to propagate the light.

5.3. Optical characterization and computer simulation of Y-splitters and MZ structures fabricated on the (Yb,Nb):RTP/RTP(001) system

5.3.1. Computer simulations

5.3.1.1. Cross-section dimensions

After obtaining the information about the refractive index contrast between undoped RTP and (Yb,Nb):RTP doped samples at a wavelength of 1550 nm, it is possible to design the dimensions of the waveguides in order to obtain the fundamental single mode and examine the propagation of light by using BeamProp software [RsoftBeamPROP].
Nowadays, an increasing number of optical modulators, filters and other functions relevant for telecommunication networks have been proposed as integrated or embedded in dielectric rib/ridge waveguides. Many of them share the widespread feature of being based on the propagation of the light beam inside a waveguide which has been designed to sustain only its fundamental mode of propagation to allow lower insertion losses when coupled to optical fibres. To fulfil this, waveguides with slightly large cross-section are designed (that is with lateral dimension and height much greater than the optical wavelength).

We have performed many simulations in order to choose the appropriate dimensions of the rib waveguide which can support only fundamental mode at 1.5 µm. Three

parameters were taken into account while designing the single mode waveguides that is *h, H* and *W*. Where *h* is the height of the slab, *H* is the slab height plus rib height and *W* is the width of the rib as can be seen in figure 5.3.a.

In figure 5.6, the dimensions suitable for single and multi-mode waveguides are presented. It can be seen that the region defined by the black triangles are the dimensions of waveguides which can only support a fundamental single mode and the region above it which is defined by red triangles can be used for multi modal waveguides. The black triangle marked with circle represents the dimensions of the waveguide used as starting point. The green triangles represent the experimental data taken from Figures 8 and 9 of **paper II** (which are the real dimensions of our waveguides). We have produced this graph inspired by the work of Pogossian *et al.* [Pogossian 1998] where they have determined the single mode condition for semiconductor rib waveguides with large cross-sections. We have taken the ratios between h/H and W/H and then simulated each point with BeamProp software in order to calculate the modes.

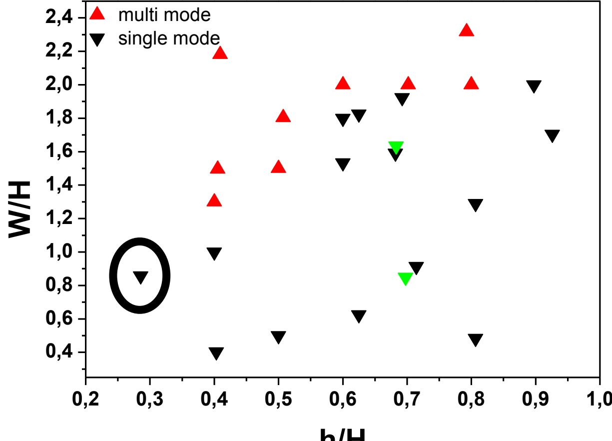

Figure 5.6. Single and multi modal waveguides dimensions. Black and red triangles represent single and multi modal waveguide dimensions respectively. Green and black triangle marked with circle, represent experimental and starting point of waveguide dimension

It can be seen from figure 5.6 that the ratios of h/H lower than 0.5 is multimodal for the ratios of W/H higher than 1.2. The waveguides behave as a single mode for the values of h/H higher than 0.5 and lower than 1.9 for W/H. In electro-optic devices like MZIs, it is important to have waveguides that can only support a fundamental single mode

otherwise it can create confusion and wrong interpretation during modulation. The refractive indices difference between substrate and epitaxial layer at 1.5 µm allows only guiding in TM polarization whatever the size of the waveguide but it will be single mode by choosing the appropriate channel waveguide dimensions. As a starting point, we choose a rectangular waveguide with a dimension of 5 µm and 6 µm as height and width of the waveguide respectively, with a slab height of 2 µm, expecting that these dimensions will support a fundamental TM mode at 1.5 µm. We use the simulations as a tool to optimize the width of the channel. Figure 11 of **paper II** shows the result of the simulation assuming a rectangular 2D channel, in which the height is 5 µm and width is 6 µm (x, y and z are the optical axis of our samples, being the crystallographic *a, b* and *c* directions, respectively). Figure 11 a) of **paper II** corresponds to the map of refractive index used in simulation; figure 11 b) is the confined TM mode and figure 11 c) shows the inexistence of the TE mode with the measured refractive index contrast and with these dimensions.

5.3.1.2. Light propagation along the optical pathway

The total length of the MZ and Y-splitter structures were dependent on the size of the RTP substrate. Also some part of the substrate is needed for collimating the sample for polishing the epitaxial layer. So our design was limited to 9 mm in length which includes 1 mm of straight waveguide as input, 2 mm of bend waveguides, 3 mm for the straight waveguides acting as the arms, 2 mm of bend waveguides and 1 mm of straight waveguide for output. The separation between the two arms varies between 38-42 µm as mentioned in table I of **paper II**.

By using the starting parameters mentioned above, we have also obtained the simulations for the propagation of the light and launch power in every section of the MZ structure by using launch dimensions (input spot) of 7 µm in width and height as an input. Figure 5.7.a) shows the propagation of light in 9 mm long MZ structure. In ideal case, light should be divided equally in pathway 1 and pathway 2 and combines at the output. As the MZ structure is symmetrical, the launch power in only pathway 1 is shown in figure 5.7.b). The input mode is first cleaned itself during the first few microns and then the power in the input straight waveguide become stable. Then the light splits and the power is divided in two parts and propagated in two arms, then it is combined at

the output with almost the same input power. The simulated power losses of the MZ structure were obtained which was 0.72 dB.

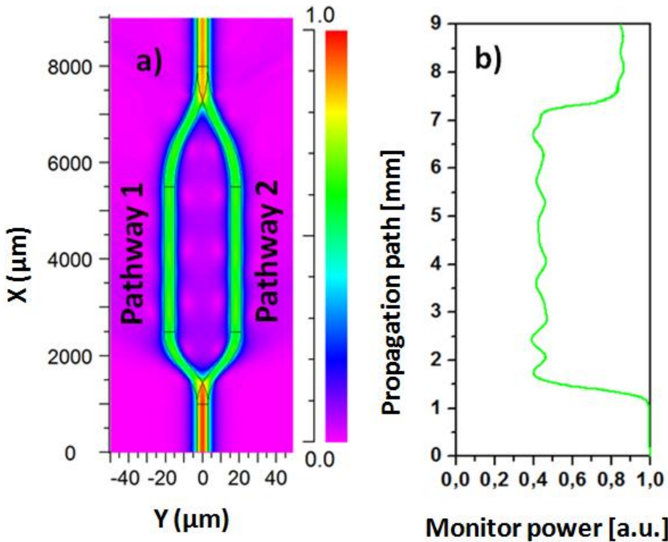

Figure 5.7.a) Propagation of light in 9 mm long MZ structure, b) Variation of launch power in one branch of the MZ structure.

There are different parameters that should be taken care of: such as the separation between the two arms, the radius of curvature of the channels and the dimensions of the channels. So due to the limitation on the length of the structures, only other parameters (as mentioned above) were examined for the optimum design.

5.3.1.3. Coupling of light between two arms of the MZ structure

Before designing a MZ structure, it is important to check the safe distance of the two arms in order to do not couple the light from one arm to the other. For that purpose, we have made some simulations with the waveguides dimensions (10 µm in width and 5 µm in height) equal to the preliminary parameters of the MZ design and keeping them apart at distance (Z) of 15, 25 and 35 µm from centre to centre.

In a first simulation, the distance between the two channels was kept at 15 µm and the second channel starts 3 mm away from the origin. In this way the mode takes some time in order to stabilize itself as it can be seen in the figure 5.8.a, where the power has some oscillations in the beginning but after 2 mm it stabilizes. It can be seen that the power

was propagating along the first channel at certain level but when the second channel start it transfers the energy to the second channel due to evanescence effect and its power reduces to zero. So 15 μm were not the safe distance between two channels in order to create a MZ structure. At the separation of 25 μm between two channels, the coupling effect reduces a lot but there is still a low transfer of energy from first channel to the second. Figure 5.8.b shows the propagation in the channel and the energy transfer when the separation between them is 25 μm. In order to be sure about the safe distance between the two channels where there is no transfer of energy between them, we have selected the separation distance of 35 μm and the simulation result is shown in figure 5.8.c.

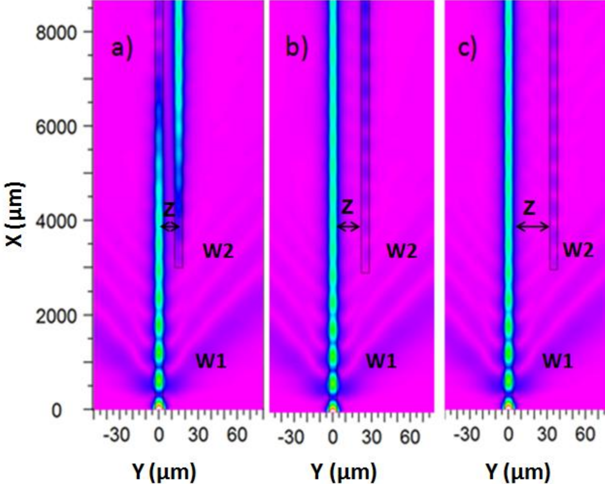

Figure 5.8. Propagation and coupling of light in two waveguides separated, a) 15 μm, b) 25 μm, and, c) 35 μm

Figure 5.9 shows the transfer of power from one waveguide to another, studied in three different cases that are at the separation (Z) of 15 μm, 25 μm and 35 μm. WG1 is the master waveguide where light is propagated and WG2 is the waveguide which is under the consideration for coupling effect. And it can be seen in figure 5.9 (green- blue line), when the channels have a separation of 15 μm, the power is coupled from the first channel to the other and the power in the first channel is reduced to zero which shows the strong coupling between waveguides. In figure 5.9 (red- light blue line) the coupling is reduced a lot at the separation of 25 μm. In the last case, where separation between the two waveguides is 35 μm, there is practically no coupling which is shown in figure 5.9 (black- grey line).

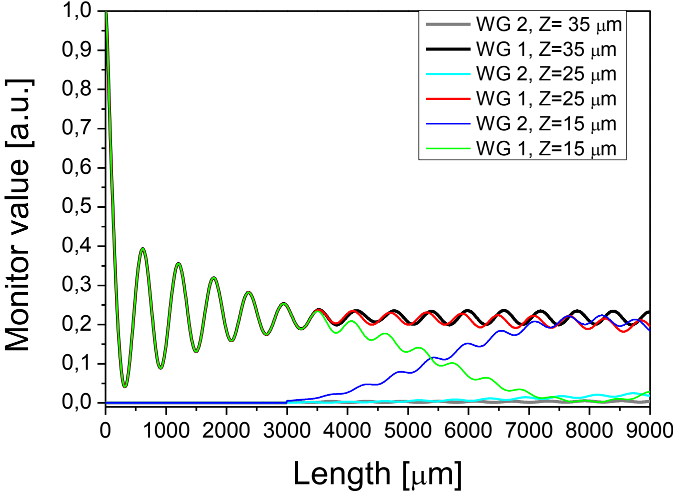

Figure 5.9. Coupling effect between two waveguides at separation of 15 μm, 25 μm and 35 μm

By keeping the optimum separations between the two arms free from coupling effect, we can choose a high value of radius of curvature in order to provide a smooth bending to the propagation light. There are three kinds of bends that can be used by using OlympiOs integrated Optics software: Bend, SB-Bend and S-Bend [OlympiOs integrated optics software 2002]. We have used S-bend waveguides with fixed radius of curvature ***R*** to design the Y-splitters and MZ structures. The S-shaped bent waveguide connects two parallel waveguides separated by the distance Z/2 by two arcs of circumference of the same radius as it is shown in figure 5.10. S-bend waveguides are important as input/output waveguides for directional couplers and as waveguide path transformers in various circuits. There are basically two kinds of S-bend waveguides; the S-bend waveguide consisting of a fixed radius of curvature R as shown in figure 5.10 and S-bend waveguide with the functional shape of y= $az + b\sin(cz)$ in which radius of curvature varies continuously. But in our designs, we have used S-bends with fixed radius of curvature; range between 50 mm- 80 mm.

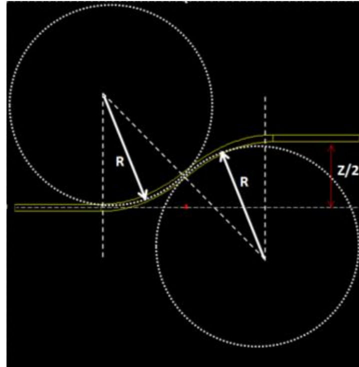

Figure 5.10. S-shaped bent waveguide

5.3.2. Experimental characterization of the fabricated Y-splitters and MZ structures in step-index (Nb,Yb):RTP/RTP(001) waveguides

5.3.2.1. Mode field characterization

Once the structuration of the Y-splitters and MZ structures has been done, their morphology was examined by ESEM and computer simulations were carried out by using the real channel dimensions in order to check the behaviour of the waveguides. These new simulations were needed because after the fabrication process which includes photolithography, wet chemical etching and RIE, the dimensions of the waveguides were not exactly the mask dimensions and the shape and height were not exactly the expected ones. We obtained channels with trapezoidal shape with broad channel widths than the mask dimensions and less height than expected and these modifications can influence the propagation modes in the channels. A simulation using the measured parameters for sample 2 (as mentioned in table I of **paper II**) was carried out in order to check the guiding of optical modes at 1.5 μm with vertically polarized light (polarization parallel to ***c***//z direction). These simulation results were compared with the experimental ones and they were quite in agreement with each other as can be seen in figures 12 and figure 13 of **paper II**.

To experimentally characterize the propagation modes, we polished the sample faces perpendicular to the crystallographic *a* direction. The near-field pattern was observed using an IR camera in order to visualize the mode intensity profile at the output of the MZ structure. Figure 12.a) of **paper II** shows the near-field pattern of the output mode for MZ structure. The horizontal and vertical fundamental mode field diameters (MFD)

at $1/e^2$ intensity (see in Figures 12.c) and figure 12.d), respectively of **paper II**) were measured to be 17.6 µm and 8.3 µm, along the ***b*** (horizontal) and ***c*** (vertical) directions, respectively. Figure 12.b) of **paper II** shows the output mode obtained by simulation. The dimensions of the simulated guided mode are 23.3 µm and 9.6 µm along ***b*** (horizontal) and ***c*** (vertical) directions, respectively.

A 9-mm-long Y splitter, fabricated on sample 2, was also characterized and the near-field patteren observed is shown in Figure 13.a) of **paper II**. From the figure, we can conclude that the Y –splitter is rather well balanced, obtaining an output flux power ratio between the two branches of 0.91. The horizontal and vertical fundamental mode field diameters (MFD) at $1/e^2$ intensity (shown in Figures 13.c) and figure 13.d), respectively of **paper II**) were measured to be 19 µm and 16.7 µm (right and left branches, respectively) along the ***b*** direction and 9.6 µm and 9.9 µm (right and left branches, respectively) along the ***c*** direction. The simulation of the modes is plotted in figure 13. b of **paper II**). The MFD for the simulated modes were 8.4 µm and 17.6 µm, for the vertical and horizontal directions, respectively. In the near field pattern, the separation between the centers of two modes propagated in the two respective arms is around 36 µm.

5.3.2.2. Losses estimation

We have estimated the total transmission losses corresponding to a single pass transmission as L_T= -10 log (P_{out}/P_{in}), where P_{out} is the power measured after the output microscope objective and P_{in} is the power measured before the input microscope objective. In the case of MZ and Y-splitter structures, the total transmission losses measured should be the result of the addition of the optical insertion, the Fresnel and the propagation losses; and in the last term, are included the propagation losses of the straight portions of the MZ and the Y-splitter structures (L_{in}, L_{MZ} and L_{SP}) and the propagation losses due to the S-bends and the Y-junctions.

The optical insertion losses measured by calculating the $1/e^2$ overlapping between the input laser mode and the output guided mode; are around 1.2 dB for the MZ and 1.5 dB (left output) and 1.2 dB (right output), for the Y-splitter. The Fresnel losses are in both cases around 0.8 dB.

The measured total transmission losses, L_T, for the MZ were 8.75 dB. Accounting for the insertion losses (1.2 dB) and the Fresnel losses (0.8 dB) we can approximate the

propagation losses as 6.7 dB, including the bending and Y-junction losses. For the Y-splitter, the measurement of the total transmission losses were 7.08 dB, making a similar calculation, the total propagation losses (including bending and Y-junction) are around 4.9 dB (assuming 0.9 cm length, they are 5.4 dB/cm). These values are in agreement with the previous reported values, published by Choudhary *et al*. [Choudhary 2013], in channel WGs fabricated also by RIE, in which the transmission losses were >3.5 dB/cm at 980 nm.

5.4. Optical characterization of straight waveguides fabricated on RTP/ (Nb,Yb):RTP/ RTP(001)

5.4.1. Computer simulations

In order to characterize the straight waveguides, we have tested different parameters such as dimensions of cladding structures, cladding thickness, epitaxial layer thickness. A scheme of this straight waveguide is shown in figure 2 of **paper III**. For instance, in these simulations, we studied the effect of varying epitaxial layer thicknesses on the different cladding thicknesses and widths. Also different dimensions of cladding structures were taken into account. The details about the parameters used in the simulation are shown in table 5.2.

Table 5.2. Parameters for stripe loaded waveguides used in simulation.

Simulation number	Epitaxial layer thickness (µm)	Cladding layer thickness (µm)	Cladding width top(µm)	Cladding width bottom(µm)
a	5	5	15	25
b	5	5	29	35
c	5	5	9.5	15
d	7	5	15	25
e	7	2.5	19	25
f	7	8.5	16.5	25

In accordance to the simulations, the near-field pattern of the modes were obtained and are given in figure 5.11. The simulation results showed in this figure corresponds to the parameters of table 5.2. If we look carefully, we can see that all the stripe loaded waveguides are guiding a single mode with high intensity but the mode profile of simulation number 3 has very low intensity which means that the dimensions used in this waveguide are not appropriate for guiding the light with high intensity.

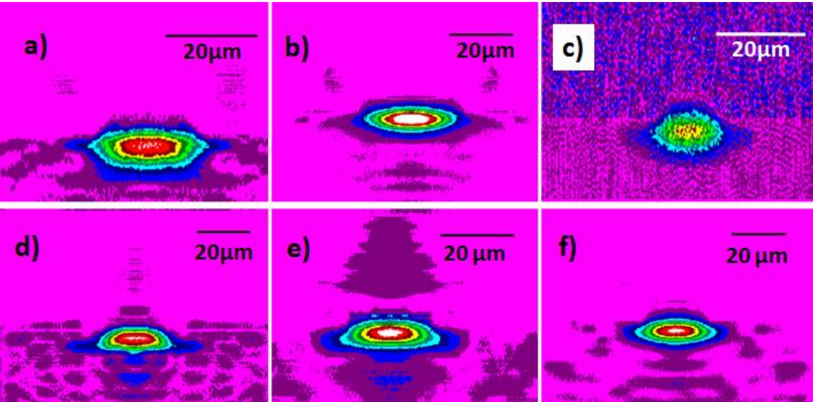

Figure 5.11. Simulation results for cladding waveguide at different parameters. The letters a), b), c), d), e) and f) correspond to the simulations with the parameters of table 5.2

Simulation (b) was further examined from the side view in order to check the penetration of the propagation beam into the substrate or cladding and the losses as shown in figure 5.12. Fig 5.12 b), it can be observed that there is a small amount of light which penetrate in the substrate depending on the size of the input spot used to couple the waveguide and the total losses also depend on the input beam size. As an example, an input mode of 25 µm and 8 µm in size in horizontal and vertical directions, respectively was used and the total losses obtained were around 0.75 dB.

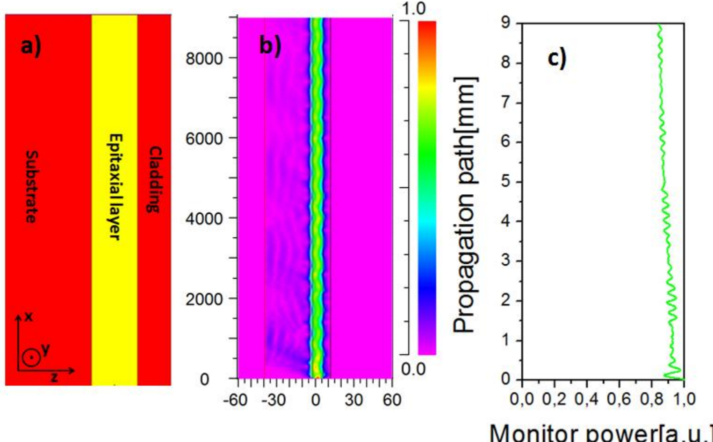

Figure 5.12. a) Side view of the straight waveguide b) Propagation of light in the straigth loaded waveguide c) Variation of launch power in the straight waveguide

5.4.2. Experimental characterization of the fabricated straight waveguides on RTP/ (Nb,Yb):RTP/ RTP(001)

A vertically polarized 1520 nm HeNe laser radiation with a maximum output power of 1 mW was coupled to the 9 mm long stripe loaded waveguides. The waveguide mode was excited via careful alignment using a xyz translation stage. To experimentally characterize the propagation mode, we polished the faces perpendicular to the crystallographic ***a*** direction. The near field pattern was measured using an IR camera in order to visualize the mode intensity profile at the output of the straight waveguide. Figure 7.a) of **paper III** shows the near-field pattern of the output mode for the straight waveguide. The horizontal and vertical fundamental mode field diameters (MFD) at $1/e^2$ intensity are shown in Figures 7.c) and 7.d) of **paper III** respectively, were measured to be 26.5 µm and 20.7 µm, along the ***b*** (horizontal) and ***c*** (vertical) directions, respectively. Figure 7.b) of **paper III** shows the output mode obtained by simulation. The dimensions of the simulated guided mode are 24.7 µm and 12.2 µm along ***b*** (horizontal) and ***c*** directions (vertical), respectively.

We have estimated the total transmission losses corresponding to a single pass transmission as L_T= -10log (P_{out}/P_{in}), where P_{out} is the power measured after the output microscope and P_{in} is the power measured before the input microscope objective, then the L_T was around 7 dB in the stripe loaded waveguide, taking into account the fresnel and overlapping losses, the propagation losses were 0.37 dB/cm. The propagating mode

was confined in the region far from the lateral walls of the ridge, thus avoiding the losses that could arise from the roughness of the etched walls.

5.5. Optical characterization of Cs^+ exchanged waveguides

5.5.1. Expected refractive index contrast in Cs^+ exchanged waveguides

According to the Bierlein *et al*. investigation on the diffusion of Cs^+ ions in z-cut KTP substrates, the Δn was found to be 0.028 and 0.019 for TE and TM polarizations respectively [Bierlein 1987]. Bierlein and Vanherzeele (1989), fabricated the Cs^+ ion diffused KTP waveguides, reported that Δn was isotropic ($\Delta n_x=\Delta n_y=\Delta n_z= 0.023$) [Bierlein 1989]. Cugat *et al*. investigated the Cs^+ ion diffused RTP waveguides and reported a refractive index contrast (Δn_x) of 0.038 at the surface of the z-cut RTP substrate [Cugat 2013b].

As we have mentioned in section 4.3.2 of chapter 4, the diffusion of Cs^+ in RTP substrate and (Yb,Nb):RTP epitaxy is different depending the region of the sample (due to the different ferroelectric domains). Then we can also expect a variation of the refractive indices contrast along the sample.

5.5.2. Experimental characterization of straight waveguides, S-bend waveguides and MZ structures on RTP(001) by Cs^+ ion exchange

To characterize the straight waveguides, S-bend waveguides and MZ structures, the near field pattern of the guided modes must be obtained. A 20X microscope objective was used to couple the 632 nm light into the input side of the devices and images were collected with a visible camera through 20X microscope output objective.

In all the straight waveguides, S-bends and MZs, the light of 632 nm was guided only in TM polarization. It can be found a correlation between the horizontal dimension of the waveguides and the sizes of the mode in horizontal dimension, observing at the ESEM images of the “exchanged region”(as an example see Figure 7 of **paper IV**). In a previous work where the Cs^+ diffusion was done also in a channel parallel to ***b*** direction in a RTP (001) substrate with the same experimental conditions [Cugat 2013b], the size of the mode obtained for guided light at 632 nm, was 9.7 µm x 7.5 µm, horizontal and vertical dimensions, respectively, despite the observed diffusion depth was around 20

µm. Figure 8.a) of **paper IV**, shows the near field pattern of a straight waveguide with mode dimensions of 43 µm x 22 µm in horizontal and vertical directions, respectively. Figure 8.b) of **paper IV** shows the near field pattern of an S-bend waveguide with mode dimensions of 33 µm x 18 µm in horizontal and vertical directions respectively. Figure 8.c) of **paper IV** shows the near-field pattern of a MZ structure with mode dimension of 52 µm x 26 µm in horizontal and vertical directions, respectively.

5.5.3. Experimental characterization of straight waveguides fabricated by Cs^+ ion exchange

In this work Cs^+ ion exchange RTP and (Yb,Nb):RTP waveguides were fabricated parallel to the direction of type II second harmonic generation (SHG) in RTP and (Yb,Nb):RTP respectively, at a wavelength of 1050 nm. These directions are parallel to the [180] direction in RTP (θ=90°, φ=76°) and along [120] direction (θ= 90°,φ= 45°) in (Yb,Nb):RTP as described in [Peña 2007].

Cs:RTP straight waveguides fabricated along the [180] direction were characterized by using the same optical set-up as mentioned above with three different wavelengths, 633 nm, 1064 nm and 1520 nm at TE and TM polarizations. The near field patterns of the straight waveguides are shown in Figure 9 of **paper IV**.

It can be observed that almost all the waveguides are multimode and can support more modes at shorter wavelengths. The guiding in both polarizations may allow type II SHG in future applications. Also, for this last sample, we have observed the TE_{01} and TM_{11} modes at 633 nm, which means that this waveguide can support at least two TE modes and four TM modes which indicates that $\Delta n_{(001)\ plane} < \Delta n_z$.

It is interesting to fabricate straight waveguides by Cs^+ ion exchange on (Yb,Nb) doped RTP to study the effect of the active ions on Cs^+ exchange. Straight waveguides fabricated by Cs^+ exchange in (Yb,Nb):RTP/RTP(001) along [120] direction were characterized by using the same optical set-up as mentioned above at 633 nm with TM polarization. In this case the light was only confined and guided with TM polarization. The near-field patterns of the modes guided in straight waveguides are shown in figure 10 of **paper IV**.

When comparing the guiding properties of the Cs^+ diffused sample in RTP along [180] direction versus the (Yb,Nb):RTP also with Cs^+ diffusion but in the [120] direction, it

can be inferred that it exists larger refractive index contrast in the RTP samples (in agreement with the EPMA measurements), in which guiding has been observed in both polarizations, TE and TM; and also the TM_{11} mode has been observed, implying the existence of confinement of a minimum of five modes.

5.5.4. Losses estimation in Cs^+ exchanged waveguides

The propagation losses of the channel WGs were estimated by exciting the fundamental mode in the channel using an x-y-z stage. The output microscope objective with 20X magnification was used to collect the transmitted light. In order to calculate the total losses in the channel waveguides, the beam power was measured before the input microscope objective as well as after the output microscope objective. The expression applied to estimate the total insertion losses, L_I, was the corresponding to the single pass transmission method, $L_I = -10*\log_{10}(P_{wg}/P_{no\text{-}wg})$, where P_{wg} is the power measured after the output microscope objective with the WG inserted, and $P_{no\text{-}wg}$ is the power measured with both input and output objectives aligned but without the WG.

The Fresnel losses L_{Fr}, coupling losses L_C, and the propagation losses L_{Prop}, are the terms whose summation is assumed to give the total transmission insertion losses, $L_I = L_{Fr} + L_C + L_{Prop}$. Coupling losses were evaluated by calculating the overlapping integral of WG output modes and input objective focal spot intensity distributions. Details of the losses for different types of waveguides are summarized in table 3 of **paper IV**. The losses of the graded-index waveguides are higher as compared to the step-index waveguides. This difference could be due to the high insertion losses in the structures made by Cs^+ exchange because of bad coupling in this kind of the waveguides. Another reason for the higher losses in Cs^+ diffused samples with respect to the structures fabricated by RIE could be due to different existing domains in the RTP substrate which hinders the homogenous diffusion of Cs ions as explained in chapter 3 section 3.3.

5.5.5. Preliminar study of SHG in Cs^+ exchanged waveguides

Cs^+-diffused RTP waveguides of 10 µm in width were fabricated for second harmonic generation (SHG) studies. These waveguides [180] propagation directions were parallel to the direction of type II ($e^{\omega}+o^{\omega} \rightarrow e^{2\omega}$) phase matching for 1050 nm wavelength. The sample was excited at 1050 nm with pulse duration of 6.1 ns with a corresponding pulse

repetition frequency of 39 KHz. The power of the pulse laser was 0.5 mW. The average power of the laser was attenuated by blocking the light with the help of multiple filters. The pulsed laser at 1050 nm with TE polarization enters the half wave plate parallel to the plane where its polarization transforms from horizontal to circular. The circular polarization is then allowed to pass through the polarizer at 45° which pass the light with two orthogonal polarizations and finally enters the channels.

The green light generated during SHG has TE polarization. The obtained near-field pattern of IR and green collected by a CCD camera can be seen in figure 5.13.b and 5.13.c respectively.

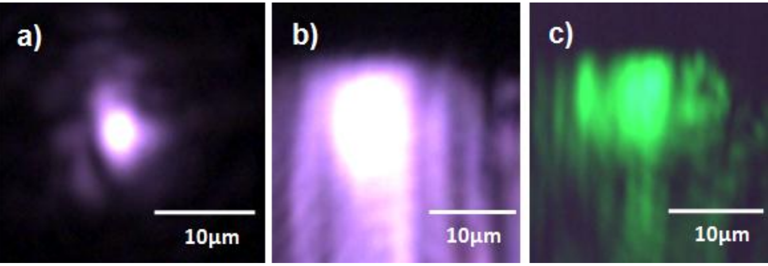

Figure 5.13.a) CCD images of the input spot at 1050 nm , b) IR near-field mode at 1050 nm, and c) visible near field mode at 522 nm generated by SHG

The exact wavelength of the green light was measured with the help of spectrum analyser. The optical spectrum of the green light at 522 nm is shown in figure 5.14.

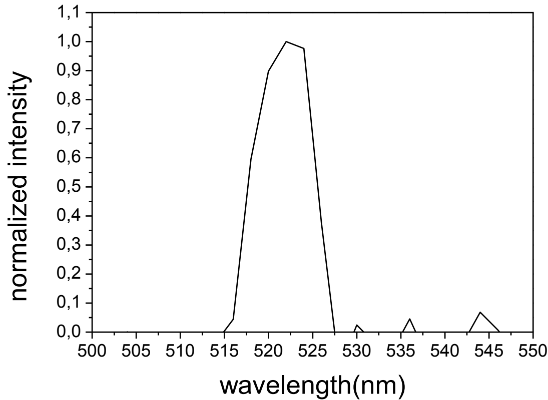

Figure 5.14. Spectra of green light measured with optical spectrum analyser.

Conclusions

We have successfully grown bulk single crystals of RTP, K:RTP and Na:KTP by using TSSG-SC technique. The crystals obtained were free of cracks, inclusions and other macroscopic defects and they were used to obtain substrates. Epitaxial layers of (Yb,Nb):RTP were grown on RTP (001) substrates, RTP epitaxial layers were grown on K:RTP (001) and K:RTP (100) substrates and finally KTP epitaxial layers were grown on Na:KTP (001) substrates. Among all the epitaxial layer systems under study, one of our focus was on (Yb,Nb):RTP/RTP (001) in order to use it for the fabrication of straight waveguides, S-bends, Y-splitters and MZIs. RTP cladding layers of few microns were also grown over epitaxial layers by the LPE method.

Al and Cr metal layers were deposited on RTP substrates to be used as a hard mask for the channel waveguides fabrication and both metals showed good adhesion on RTP substrates but Cr was selected as a hard mask due to its high selectivity. Moreover, the adhesion of Cr hard mask on the substrate was improved by depositing a thin layer of TiO_2, progressively decreasing the oxygen content in the chamber and moved to Ti, and finally enriching Ti with Cr up to pure Cr.

Channel waveguides such as straight waveguides, S-bends, Y-splitters and MZ structures were fabricated by using RIE with an etch rate of 3.2-8.7 nm/min depending on the substrate/epitaxial layer and the hard mask used. The surface roughness produced by long RIE process was approximately 15 nm.

We have tried to reproduce these structures by using ICP-RIE in order to compare the etch rate, morphology and roughness. The etch rate obtained was 127 nm/min with a surface roughness of 7 nm. This clearly shows that ICP-RIE has advantage over conventional RIE due to high etch rate and less surface roughness, which in turn reduce the fabrication cost and have less propagation losses.

Another fabrication technique used in this work to produce straight waveguides, S-bend waveguides, Y-splitters and MZ structures was Cs^+ ion exchange. These waveguides have graded refractive index along the ***c*** crystallographic direction. The exchange process depends on the ferroelectric domains of the substrate which can highly influence the exchange profile and lately the refractive index gradient. The straight waveguides, S-bends and MZ structures were fabricated by Cs^+ ion exchange on RTP (001) substrates and were oriented along the *b* crystallographic direction. At the end, straight channel

waveguides of Cs^+ exchanged in RTP of 10 µm in width were fabricated for applications in self-frequency doubling (SHG) in RTP, since the straight channel WG propagation directions were parallel to the direction of type II ($e^{\omega}+o^{\omega} \rightarrow e^{2\omega}$) phase matching for 1050 nm wavelength. This direction is along the [180] direction in RTP (θ=90º, φ=75º). The characterization of type II SHG showed that 1050 nm radiation is converted to the green light at 522 nm.

The devices fabricated by RIE have propagation losses > 3.5 dB/cm in fundamental TM mode propagating along ***a*** direction at 1550 nm, which are higher than the propagation losses of the straight waveguides fabricated by ICP-RIE propagating along same direction and polarization. The propagation losses at 1550 nm of these structures fabricated by ICP-RIE are 0.37 dB/cm. The propagation losses depend on several factors such as the roughness of the waveguides and its high value in the waveguides fabricated by RIE can introduce greater losses than in the waveguides fabricated by ICP-RIE. And also in case of straight waveguides fabricated by ICP-RIE, the propagation of light in the epitaxial layer is far away from the etched surface.

By the efficient use of modelling software BeamProp, we have designed Y-splitters, MZs, S-bends, straight waveguides and studied their propagation of light modes and losses. This inturns help us in the fabrication of real devices.

The propagation losses of straight waveguides, S-bends and MZ structures fabricated by ion exchange along ***b*** direction were 11.3, 15.8 and 10.4 dB/cm at 633 nm with TM polarization, respectively. Additionally, we have fabricated straight channel waveguides in RTP along the [180] crystallographic direction (001) which is the type II phase matching direction of RTP at 1050 nm. The propagation losses of these waveguides were measured with TE polarization and were 5.7 dB/cm, 18.8 dB/cm, 6.6 dB/cm for 633, 1064 and 1520 nm, respectively. Also the propagation losses of these waveguides were measured with TM polarization, which were 15.9 dB/cm, 26.1 dB/cm, 4.97 dB/cm for 633, 1064 and 1520 nm respectively. Straight channel waveguides were also fabricated on (Yb,Nb):RTP/RTP (001) along the [120] crystallographic direction which is the phase matching direction of (Yb,Nb):RTP at 1050 nm. The propagation losses of these waveguides were 15.5 dB/cm measured at 633 nm with TM polarization. If we compare the losses of the waveguides/devices fabricated by the three different fabrication techniques explained above, we can observe that the straight channel waveguides fabricated by ICP-RIE technique has lower optical losses.

References

[Aillerie 2013] M. Aillerie, P. Bourson, M. Mostefa, F. Abdi, M. D. Fontana, "Photorefractive damage in congruent $LiNbO_3$. Part II. Magnesium doped lithium niobate crystals", *J. Phys: Conf. Ser.* **416**, 012002, 2013.

[Alferness 1990] R. C. Alferness, "Titanium-diffused lithium niobate waveguide devices, in guided wave optoelectronics", T. Tamir (ed.), Springer-Verlag, Berlin, 1990.

[Allen 1988] S. Allen, T. D. McLean, P. F. Gordon, B. D. Bothwell, M. B. Hursthouse, S.A. Karaulov, "A novel organic electro-optic crystal: 3-(1,1-dicyanoethenyl)-1-phenyl-4,5-dihydro-1H-pyrazole", *J. Appl. Phys*. **64**, 2583-2590, 1988.

[Angert 1994] N. Angert, L. Kaplun, M. Tseitlin, E. Yashchin, M. Roth, "Growth and domain structure of potassium titanyl phosphate crystals pulled from high-temperature solutions", *J. Cryst. Growth* **137**, 116-122, 1994.

[Ari 2004] L. Arizmendi, "Photonic applications of lithium niobate crystals", *Phys. Stat. Sol.* (a) **201**, 253-283, 2004.

[Aschieri 2011] P. Aschieri, M. P. de Micheli, "Highly efficient coupling in lithium niobate photonic wires by the use of a segmented waveguide coupler", *Appl. Opt.* **52**, 3885-3888, 2011.

[Bente 2006] E. Bente, M. Smit, "Ultrafast InP optical integrated circuits", *Proc. SPIE*, **6124**, 612419 (1-10), 2006.

[Bierlein 1986] J. D. Bierlein and C. B. Arweiler, "Electro-optic and dielectric properties of $KTiOPO_4$", *Appl. Phys. Lett.* **49**, 917-919, 1986.

[Bierlein 1987] J. D. Bierlein, A. Ferretti, L. H. Brixner, W. Y. Hsu, "Fabrication and characterization of optical waveguides in $KTiOPO_4$", *Appl. Phy. Lett.* **50**, 1216-1218, 1987.

[Bierlein 1988] J. D. Bierlein, A. Ferretti, M. G. Roelofs, " $KTiOPO_4$ (KTP): A new material for optical waveguide applications", *Proc. SPIE* **994**, Optoelectronic materials, devices, packaging and interconnects II, 160, 1988.

[Bierlein 1989] J. D. Bierlein, H. Vanherzeele, "Potassium titanyl phosphate: properties and new applications", *J. Opt. Soc. Am*. B **6**, 622-633, 1989.

[Binnig 1986] G.Binnig, C.F.Quate, Atomic force microscope, *Phys. Rev. lett.* **56**, 930-933, 1986.

[Bolt 1991] R. J. Bolt, M. H. van der Mooren, H. de Haas, "Growth of $KTiOPO_4$ (KTP) single crystals by means of phosphate and phosphate/sulphate fluxes out of a three-zone furnace", *J. Cryst. Growth* **114**, 141-152, 1991.

[Bordui 1987] P. F. Bordui, J. C. Jacoo, G. M. Loiacono, R. A. Stolzenberger, J. J. Zola, "Growth of large single crystals of $KTiOPO_4$ (KTP) from high temperature solution using heat pipe based furnace system", *J. Cryst. Growth* **84**, 403-408, 1987.

[Bordui 1989] P. F. Bordui, S. Motakef, "Hydrodynamic control of solution inclusion during crystal growth of $KTiOPO_4$ (KTP) from high-temperature solution", *J. Cryst. Growth*. **96**, 405-412, 1989.

[Bosenberg 1989] W. R. Bosenberg, W. S. Pelouch, C. L. Tang, "High efficiency and narrow-linewidth operation of a two crystal β- BaB_2O_4 optical parametric oscillator", *Appl. Phys. Lett.* **55**, 1952-1954, 1989.

[Boudrioua 2009] A. Boudrioua, ''Photonic waveguides: Theory and Applications'', ISTE ltd and John Wiley & Sons, Inc, 2009.

[Bragg 1912] W. L. Bragg, "The specular reflection of X-rays", *Nature* **90**, 410-410, 1912.

[Burns 1999] W. Burns, M. Howerton, R. Moeller, R. McElhanon, S. Greenblatt, "Low drive voltage, 40 GHz $LiNbO_3$ modulators", in OFC '99, San Diego, CA, paper ThT1, 1999.

[Carvajal 2000] J. J. Carvajal, V. Nikolov, R. Solé, Jna. Gavaldá, J. Massons, M. Rico, C. Zaldo, M. Aguiló, F. Díaz, "Enhancement of the erbium concentration in $RbTiOPO_4$ by codoping with niobium", *Chem. Mater.* **12**, 3171-3180, 2000.

[Carvajal 2001] J. J. Carvajal, R. Solé, J. Gavaldà, J. Massons, M. Rico, C. Zaldo, M. Aguiló, F. Díaz, "Growth and characterization of $RbTiOPO_4$:Nb crystals as a host for rare earth ions", *J. All. Comp*. **323-324**, 231-235, 2001.

[Carvajal 2002] J. J. Carvajal, V. Nikolov, R. Solé Jna. Gavaldà, J. Massons, M. Aguiló, F. Díaz, "Crystallization region, crystal growth, and characterization of rubidium titanyl phosphate codoped with niobium and lanthanide ions", *Chem. Mater.* **14**, 3136-3142, 2002.

[Carvajal 2003] J. J. Carvajal, R. Solé, Jna. Gavaldà, J. Massons, F. Díaz, M. Aguiló, "Phase transitions in $RbTiOPO_4$ doped with niobium", *Chem. Mater.* **15**, 2730-2736, 2003.

[Carvajal 2003a] J. J. Carvajal, J. L. García-Muñoz, R. Solé, Jna. Gavaldà, J. Massons, X. Solans, F. Díaz, M. Aguiló, "Charge self-compensation in the non-linear optical crystals $Rb_{0.855}Ti_{0.955}Nb_{0.045}OPO_4$ and $RbTi_{0.927}Nb_{0.056}Er_{0.017}OPO_4$", *Chem. Mater.* **15**, 2338-2345, 2003.

[Carvajal 2009] J. J. Carvajal, G. Ciatto, A. Peña, M. C. Pujol, J. Gavaldà, F. Díaz, M. Aguiló, "Lattice location and short range ordering of doping ions in $RbTiOPO_4$", *Appl. Phys. Lett*. **94**, 061908 (1-3 pages), 2009.

[Chanvillard 2000] L. Chanvillard, P. Aschieri, P. Baldi, D. B. Ostrowsky, M. De Micheli, L. Huang, D. J. Bamford, "Soft proton exchange on periodically poled $LiNbO_3$: a simple waveguide fabrication process for highly efficient nonlinear interactions", *Appl. Phys. Lett.* **76**, 1089-1091, 2000.

[Chaudhary 2006] A. K. Chaudhary, G. C. Bhar, P. Kumbhakar, "Generation of tunable infrared radiation in rubidium titanyl phosphate crystal for the optical measurement of number density, absorption cross-section of methane gas", *J. Quant Spectrosc. and Rad. Trans*. **98**, 157-166, 2006.

[Chemla 1987] D. S. Chemla, J. Zyss (eds.), "Nonlinear optical properties of organic molecules and crystals", **1-2**, *Academic Press*, Orlando, USA, 1987.

[Cheng 1991] L. K. Cheng, J. D. Bierlein, "Crystal growth of $KTiOPO_4$ isomorphs from tungstate and molybdate fluxes", *J. Cryst. Growth* **110**, 697-703, 1991.

[Cheng 1991a] L.K. Cheng, J.D. Bierlein, A.A. Ballman, "$KTiOP_xAs_{1-x}O_4$ optical wave-guides grown by liquid-phase epitaxy", *Appl. Phys. Lett.* **58**, 1937-1939, 1991.

[Cheng 1991b] L. K. Cheng, J. D.Bierlein, A. A. Ballman, "$KTiOP_xAs_{1-x}O_4$ optical wave-guides grown by liquid-phase epitaxy", *Appl. Phys. Lett*. **58**, 1937-1939, 1991.

[Cheng 1991c] L. K. Cheng, J. D. Bierlein, C. M. Foris, A. A. Ballman, "Growth of epitaxial thin-films in the $KTiOPO_4$ family of crystals", *J. Cryst. Growth* **112**, 309-315, 1991.

[Cheng 1993a] L.K. Cheng, J.D. Bierlein, "KTP and isomorphs- recent progress in device and material development", *Ferroelect.* **142**, 209-228, 1993.

[Cheng 1993b] L.T. Cheng, L. K. Cheng, J. D. Bierlein, "Linear and nonlinear optical properties of the arsenate isomorphs of KTP", *Proc. SPIE* **1863**, 43-53,1993.

[Cheng 1994a] L. K. Cheng, L. T. Cheng, J. D. Bierlein, "Phase matching property optimization using birefringence tuning in solid solutions of $KTiOPO_4$ isomorphs", *Appl. Phys. Lett.* **64**, 1321-1323, 1994.

[Cheng 1994b] L. K. Cheng, L. T. Cheng, J. Galperin, P. A. Morris Hotsenpiller, J. D. Bierlein, "Crystal growth and characterization of $KTiOPO_4$ isomorphs from the self- fluxes", *J. Cryst . Growth*. **137**, 107-115, 1994.

[Chiang 1986] K. S. Chiang, "Dual effective –index method for the analysis of rectangular waveguides", *Appl. Opt*. **25**, 2169-2174, 1986.

[Choudary 2013] A. Choudary, J. Cugat, K. Pradeesh, R. Solé, F. Díaz, M. Aguiló, H. M. H. Chong, D.P. Shepherd, "Single-mode rid waveguides in (Yb,Nb):$RbTiOPO_4$ by reactive ion etching", *J. Phys. D: Appl. Phys.* **46**, 145108, 2013.

[Chung 1990] Y. Chung, N. Dagli, "An assessment of finite difference beam propagation method", *IEEE J. Quant. Electron* **26**, 1335-1339, 1990.

[Cugat 2010] J. Cugat, R. Solé, M. C. Pujol, J. J. Carvajal, X. Mateos, F. Díaz, M. Aguiló, "Waveguiding demonstration on Yb: Nb:$RbTiOPO_4$/$RbTiOPO_4$ (001) epitaxies grown by LPE", *Opt. Mater.* **32**, 1648-1651, 2010.

[Cugat 2011a] J. Cugat, R. Solé, J.J. Carvajal, M.C. Pujol, X. Mateos, F. Díaz, M. Aguiló, "Crystal growth and characterization of $RbTi_{1-x-y}Yb_xNb_yOPO_4/RbTiOPO_4(001)$ non-linear optical layers", *CrystEngComm,* **13**, 2015-2022, 2011.

[Cugat 2011b] J. Cugat, R. Solé, M. C. Pujol, J. J. Carvajal, X. Mateos, F. Díaz, M. Aguiló, "Efficient second harmonic generation green light in RTP planar waveguides", *Phys. Stat. Sol. C* **8**, 2946-2949, 2011.

[Cugat 2013a] J. Cugat, A. Ruiz de la Cruz, R. Solé, A. Ferrer, J. J. Carvajal, X. Mateos, J. Massons, J. Solís, G. Lifante, F. Díaz, M. Aguiló, "Femtosecond-laser Microstructuring of Ribs on Active (Yb,Nb):RTP/RTP planar waveguides", *J. Lightwave Technol.* **31**, 385-390, 2013.

[Cugat 2013b] J. Cugat, R. Solé, J.J. Carvajal, X.Mateos, J. Massons, G. Lifante, F.Diaz, M. Aguilo, "Channel waveguides on $RbTiOPO_4$ by Cs^+ ion exchange'', *Opt. Lett.* **38**, 323-325, 2013.

[Cugat 2013c] J. Cugat, A. Choudhary, R. Solé, J. Massons, D. Shepherd, F. Díaz, M. Aguiló, "Ar^+ ion milling rib waveguides on nonlinear optical (Yb,Nb): RTP/RTP epitaxial layers", *J. Opt Mat. Express,* **3**, 1912-1917, 2013.

[Demartino 1988]. R. N. Demartino, E. W. Choe, G. Khanarian, D. Hass, T. Leslie, G. Nelson, J. Stamatoff, D. Stuetz, C.C. Teng, H. Yoon, "Development of polymeric nonlinear optical materials" in nonlinear optical and electroactive polymers (P.N. Prasad and D.R. Ulrich, eds.), 169-188, Plenum Press, New York, 1988.

[Dhanaraj 1990] G. Dhanaraj, H. L. Bhat, "Dendritic structures on habit faces of potassium titanyl phosphate crystals grown from flux", *Mater. Lett.* **10,** 283-287, 1990.

[Dhanaraj 1992] G. Dhanaraj, T. Shripathi, H.L. Bhat, "Defect characterization of KTP single-crystals", *Bull. Mater. Sci.* **15**, 219-227, 1992.

[Dhanaraj 2010] G. Dhanaraj, K. Byrappa, V. Prasad, M. Dudley, Handbook of Crystal Growth, Springer-Verlag Berlin Heidelberg, 2010.

[dmphotonics] www.dmphotonics.com

[Duan 2014]. Y. Duan, H. Zhu, Y. Ye, D. Zhang, G. Zhang, D. Tang, "Efficient RTP based OPO intracavity pumped by an acousto-optic Q switched $Nd:YVO_4$ laser", *Opt. Lett.* **39**, 1314-1317, 2014.

[Elsaesser 1984] T. Elsaesser, A. Seilmeir, W. Kaiser, P. Koidl, G. Brandt, "Parametric generation of tunable picoseconds pulses in the medium infrared using $AgGaS_2$ crystals", *Appl. Phys. Lett.* **44**, 383-385, 1984.

[Ferrand 1999] B. Ferrand, B. Chambaz, M. Couchaud. "Liquid phase epitaxy: A versatile technique for the development of miniature optical components in single crystal dielectric media", *Opt. Mater.* **11**, 101-104, 1999.

[Fraser 1997] J. M. Fraser, D. Wang, A. Haché, G. R. Allan, H. M. van Driel, "Generation of high-repetition- rate femtosecond pulses from 8 to 18 µm", *Appl. Opt*. **36**, 5044-5047, 1997.

[Ganshin 1988] V. A. Ganshin, Y. N. Korkishko, V. Z. Petrova: "Reverse proton-exchange in H:$LiNbO_3$ lightguides", *Sov. Phys. Tech. Phys.* **33**, 686, 1988.

[Garfinkel 1968] Garfinkel, H. M, "Photochromic glass by silver ion exchange", *Appl. Opt.* **7**, 789-794, 1968.

[Gavaldà 2009] Jna. Gavalda, J. J. Carvajal, X. Mateos, M. Aguiló, F. Díaz, "Composition-dependent dielectric properties of $RbTiOPO_4$ single crystals", *Appl. Phys. Lett.* **95**, 182902 (3 pages), 2009.

[Gavaldà 2012] J. Gavaldà, J. J. Carvajal, X. Mateos, M. Aguiló and F. Díaz, "Dielectric properties of Yb^{3+} and Nb^{5+} doped $RbTiOPO_4$ single crystals", *J. Appl. Phys.* **111**, 034106 (1-8), 2012.

[Gier 1980] T. E. Gier, "Method for flux growth of $KTiOPO_4$ and its analogues", *U.S. Patent No*. **4**, 231, 838, 1980.

[Gorazd 2009] P. Gorazd, D. Riccardo, M. Carolina, G. Peter, "UV integrated optics devices based on beta- barium borate", *Opt. Mat.* **31**, 1049-1053, 2009.

[Grossard 2007] N. Grossard, J. Hauden, H. Porte, "Low loss and stable integrated optical Y-junction on lithium niobate modulators", *European Conference on Integrated Optics*, ThG08, 2007.

[Guillien 2003] Y. Guillien, B. Menaert, J. P. Feve, P. Segonds, J. Douady, B. Boulanger, O. Pacaud, "Crystal growth and refined Sellmeier equations over the complete transparency range of $RbTiOPO_4$", *Opt. Mater.* **22**, 155-162, 2003.

[Hadley 1992] G. R. Hadley, "Transparent Boundary condition for the beam propagation method", *IEEE J. Quant. Electron* **28**, 363-370, 1992.

[Hagerman 1995] M. E. Hagerman, K. R. Poeppelmeier, "Review of the structure and processing defect property relationships of potassium titanyl phosphate: a strategy for novel thin film photonic devices", *Chem. Mater.* **7**, 602-621, 1995.

[Herring 1951] C. Herring, "Some theorems on the free energies of crystal surfaces", *Phys. Rev.* **82**, 87-93, 1951.

[Herring 1953] C. Herring, "The use of classical macroscopic concepts in surface energy problems", Structure and properties of solid surface, ed. By R.G. Gromer, pp. 5-72, C.S. Smith, Univeristy of Chicago Press, Chicago, 1953.

[Hill 1996] R. Hill, "Characterization of a low pressure, high ion density, plasma metal etcher", *J. Vac Sci.Technol*. B, 14, 547-551, 1996.

[Hou 2004] X. Hou, "A leaky waveguide all-optical analog-to-digital converter", A PhD thesis, Drexel University, 2004.

[Hu 2006] H. Hu, A. P. Milenin, R. B. Wehrspohn, H. Hermann, W. Sohler, "Plasma etching of proton-exchanged lithium niobate," *J. Vac. Sci. Technol. A,* **24**, 1012-1015, 2006.

[Huang 1992] W. Huang, C. Xu, S. Chu, K. Chaudhuri, "The finite-difference vector beam propation method: Analysis and Assessment", *J. Lightwave Technol.* **10**, 295-305, 1992.

[Hubner 2001] J. Hubner, S. Guldberg-Kjaer, M. Dyngaard, Y. Shen, C. L.Thomsen, S. Balslev, C. Jensen, D. Zauner, T. Feuchter, "Planar Er- and Yb-Doped amplifiers and lasers", *Appl. Phys.* B **73**, 435-438, 2001.

[Hui 2005] R. Hui, Y. Wan, J. Li, S. Jin, J. Lin, H. Jiang, "III- Nitride- based planar lightwavecircuits for long wavelength optical communications", *J. Quan. Elec*. **41**. 100-110, 2005.

[Hull 1919] A.W. Hull, "A new method of chemical analysis", *J. Am. Chem. Soc.* **41**, 1168-1175, 1919.

[Huo 2010] J. Huo, K. Liu, X. Chen, "1x2 precise electro-optic switch in periodically poled lithium niobate", *Opt. Express* **18**, 603-608, 2010.

[Iliev 1990] K. Iliev, P. Peshev, V. Nikolov, I. Koseva, "Physicochemical properties of high-temperature solutions of the K_2O-P_2O_5-TiO_2-WO_3 system, suitable for the growth of $KTiOPO_4$ (KTP) single-crystals", *J. Cryst. Growth* **100**, 219-224 ,1990.

[Jacco 1984] J. C. Jacco, G.M. Loiacono, M. Jaso, G. Mizell, B. Greenberg, "Flux growth and properties of $KTiOPO_4$", *J. Cryst. Growth* **70**, 484-488, 1984.

[Jackel 1982] J. L. Jackel, C. E. Rice, J. J. Veselka: "Proton exchange for high index waveguides in $LiNbO_3$", *Appl. Phys. Lett*. **41,** 607-608, 1982.

[Jackel 1991] J. L. Jackel, J. J. Johnson, "Reverse proton exchange method for burying proton exchanged waveguides", *Electron. Lett.* **27**, 1360-1361, 1991.

[Jansen 1996] H. Jansen, H. Gardeniers, M. de Boer, M. Elwenspoek, J. Fluitman, "A survey on the reactive ion etching of silicon in microtechnology" , *J. Micromech. Microeng*. **6**, 14-28, 1996.

[Kaminow 1973] I. P. Kaminow, J.R. Carruthers, "Optical waveguiding layer in $LiNbO_3$ and $LiTaO_3$", *Appl. Phys. Lett*. **22**, 326-328, 1973.

[Kao 1990] A. S. Kao and H. G. Stenger, "Analysis of non-uniformities in plasma etching of silicon with carbon tetraflouride in oxygen", J. Electrochem. Soc. 137, 954-960, 1990.

[Karlsson 1999] H. Karlsson, F. Laurell, L.K. Cheng, "Periodic poling of $RbTiOPO_4$ for quasi phase matched blue light generation", *Appl. Phys. Lett.* **74**, 1519-1521, 1999.

[Köhler 1999] M. Köhler, "Etching in microsystem technology", Weinheim; New York; Chichester; Brisbane; Singapore; Toronto, Wiley-VCH, 1999.

[Krykov 1977] P.G. Krykov, Y. A. Matveets, D.N. Nikogosyan, A.V. Sharkov, E.M. Gordeev and S.D. Franchenko, "Generation of frequency-tunable single ultrashort light pulses in an $LiIO_3$ crystal", *Sov. J. Quant. Electron* **7**, 127-128, 1977.

[Lazar 2006] M. Lazar, H. Vang, P. Brosselard, C. Raynaud, P. Cremillieu, J.L. Leclercq, A. Descamps, S. Scharnholz, D. Planson, "Deep SiC etching with RIE", *Superlattice Microst.* **40**, 388-392, 2006.

[Lieberman 1994] M. A. Lieberman, A. J. Lichtenberg, "Principles of plasma discharges and materials processing", John Wiley and Sons Inc, 1994.

[Lifante 1997] G. Lifante, T. Balaji, A. Muñoz-Yagúe, "Planar optical waveguides fabricated by molecular beam epitaxy of Pd-doped CaF_2 layers", *App. Phys. Lett.* **70**, 2079-2081 1997.

[Lifante 2003] G. Lifante, "Integrated Photonics fundamentals", John Wiley & Sons Ltd, The Atrium, Southern Gate, Chichester, West Sussex PO19 8SQ, England, 2003.

[Liñares 2000] J. Liñares, V. Moreno, M. C. Nistal, "Designing of monomode step index channel guides with quasi-exact modal solutions by the effective index method", *J. Mod Opt.* **47**, 599-604, 2000.

[Liu 2005] Jia-Ming Liu, "Photonic Devices", Cambridge University Press, 2005.

[Loiacono 1992] G.M. Loiacono, D. N. Loiacono, J.J. Zola, R.A. Stolzenberger, T. McGee, R.G. Norwood, "Optical properties and ionic conductivity of $KTiOAsO_4$ crystals", *Appl. Phys. Lett.* **61**, 895-897, 1992.

[Lytel 1988] R. Lytel, G.F. Lipscombe, M. Stiller, J.I. Thackara, A.J. Ticknor, "Organic electro-optic waveguide modulators and switches" in "Nonlinear optical properties of organic materials" (G. Khanarian, ed.), *Proc. SPIE* **971**, 218-229, 1988.

[Ma 2002] H. Ma, A.K. Y Jen, L.R. Dalton, "Polymer based optical waveguides: material processing and devices", *Adv. Mater.* **14**, 1339-1365, 2002.

[Maiman 1960] T.H. Maiman, "Stimulated optical radiation in ruby", *Nature.* **187** (4736), 493-494, 1960.

[Mateos 2007] X. Mateos, V. Petrov, A. Peña, J. J. Carvajal, M. Aguiló, F. Díaz, P. Seconds, B. Boulanger, "Laser operations of Yb^{3+} in acentric $RbTiOPO_4$ codoped with Nb^{5+} ", *Opt. Lett*, **32**, 1929-1931, 2007.

[Mauer 1979] J. L. Mauer and J. S. Logan, "Reactive supply in reactive ion etching", J. Vac.Sci. Technol. 16, 404-406, 1979.

[Miller 1969] S. E. Miller, "Integrated optics, An introduction", *The Bell Sys. Techn. Journal*, **48**, 2059-2068, 1969.

[Najafi 1992] S. I. Najafi, "Introduction to glass integrated optics", Ed. Artech House, Boston, 1992.

[Nevado 2001] R. Nevado, G. Lifante, "Low loss, damage-resistant optical waveguides in Zn-Diffused $LiNbO_3$ by a two step procedure", *Appl. Phys*. A. **72**, 725-728, 2001.

[OlymiOs 2002] OlympiOs Integrated Optics Software, Alcatel Optronics Version 5.0, 2002.

[Oseledchik 1992] Y. S. Oseledchik, S. P. Belokrys, V. V. Osadchuk, A. L. Prosvirnin, A. F. Selevich, V. V. Starshenko, K. V. Kuzemchenko, "Growth of $RbTiOPO_4$ single crystals from phosphate systems", *J. Cryst. Growth* **125**, 639-643, 1992.

[Oseledchik 1994] Y. S. Oseledchik, A. I. Pisarevsky, A. L.Prosvirnin, V. V. Starshenko, N. V. Svitanko, "Nonlinear optical properties of the flux grown $RbTiOPO_4$ crystal", *Opt. Mater*. **3**, 237-242, 1994.

[Ouvrard 1890] L. Ouvrard, "Recherches sur les phosphates doubles de titane, d'étain et de cuivre", *Compt.Rend.* **111**, 177-179, 1890.

[Paranjpe 1994] A. P. Paranjpe, "Modeling an inductively coupled plasma source", *J. Vac Sci.Technol.* A, 12, 1221-1228, 1994.

[Peña 2007] Ytterbium and erbium doped $RbTi_{1-x}M_xOPO_4$ (M=Nb or Ta) crystals. New laser and nonlinear bifunctional materials, Alexandra Peña Revellez, Thesis 2007.

[Pernas 2000] P. L. Pernas, M. J. Hernández, E. Ruíz, E. Cantelar, R. Nevado, C. Morant, G. Lifante, F. Cussó, "Zn-Vapor diffused Er:Yb:$LiNbO_3$ channel waveguides fabricated by means of SiO_2 electron cyclotron resonance plasma deposition", *Appl. Surf. Sci*. **161**, 123-130, 2000.

[Petrov 2008] V. Petrov, A. Gaydardzhiev, I. Nikolov, I. Buchvarov, P. Tzankov, F. Noack, "The application of the monoclinic BiB_3O_6 nonlinear crystal in ultrafast laser technology", *Proc. of SPIE*, 6875, 68750X (1-14), 2008.

[Phillips 1989] M. L. F. Phillips, W. T. A. Harrison, T. E. Gier, G. D. Stucky, "SHG tuning in the KTP structure field", *Proc. SPIE* **1104**, 225-231, 1989.

[Phillips 1990]. M. L. F. Phillips, W. T. A. Harrison, T. E. Gier, G. D. Stucky, G. V. Kulkarni, J. K. Buerdett, "Electronic effects of substitution chemistry in the potassium titanyl phosphate ($KTiOPO_4$) structure field: structure and optical properties of potassium vanadyl phosphate", *Inorg. Chem.* **29**, 2158-2163, 1990.

[Pliska 1995] T. Pliska, F. Mayer, D. Fluck, P. Gunter, D. Rytz, "Non-linear optical investigation of the optical homogeneity of $KNbO_3$ bulk crystals and ion-implanted waveguides", *J. Opt. Soc. Am.* B, **12**, 1878-1887, 1995.

[Pogossian 1998] S. P. Pogossian, L. Vescan, A. Vonsovici, "The Single-mode condition for semiconductor rib waveguides with large cross section", *J. Lightwave Technol.* **16**, 1851-1853, 1998.

[Press 1996a] W. H. Press, S. A. Teukolsky, W. T. Vetterling, B. P. Flannery, "Numerical Recipes in Fortran 77: The art of Scientific Computing", Chapter 2, Cambridge University Press, New York, 1996.

[Press 1996b] W. H. Press, S.A. Teukolsky, W.T. Vetterling, B.P. Flannery, "Numerical Recipes in Fortran 77: The Art of Scientific Computing", Chapter 19, Cambridge University Press, New York, 1996.

[Prokhorov 1996] A. M. Prokhorov, Y. S. Kuz´minov, O. A. Khachaturyan, "Ferroelectric Thin-film waveguides in Integrated Optics and Optoelectronics", Cambridge International Science Publishing, 1996.

[Raicol] www.raicol.com

[Räu 1978] A. Räuber, "Chemistry and physics of lithium niobate", *Curr. Top. in Mater. Sci*. **1**, 481-601, Amsterdam, 1978.

[Ren 2008] Z. Ren, P. J. Heard, J. M. Marshall, P. A. Thomas, S. Yu, "Etching characteristics of $LiNbO_3$ in reactive ion etching and inductively coupled plasma", *J. Appl. Phys.* **103**, 034109, 2008.

[Richard 1989] A.S. Richard, C.C.Hsu, N. Peyghambarian, J. J.E. Reid, R.A. Morgan, "Type II sum frequency generation in flux and hydrothermally grown KTP at 1.319 and 1.338 µm", *IEEE phot tech lett.* **1**, 446-448, 1989.

[Ris 1996] W. P. Risk, G. M. Loiacono, "Fabrication and characterization of ion-exchanged waveguides in potassium titanyl arsenate", **69**, 4157-4158, 1996.

[Ródenas 2011] A. Rodenas, A. K. Kar, "High/contrast step/index waveguides in borate non-linear laser crystals by 3D laser writing", *Opt. Express* **19**, 17820-17833, 2011.

[Rodriguez-Carvajal 2000] J. Rodriguez-Carvajal, "An Introduction to the program Fullprof 2000", Laboratoire Léon Brillouin (CEA-CNRS), Saclay, France, 2000.

[Roe 1993] M. G. Roelofs, A. Ferretti, J.D. Berlein, "Proton and ammonium exchanged optical waveguides in $KTiOPO_4$", *J. Appl. Phys*. **73**, 3608-3613, 1993.

[Roelofs 1991] M. G. Roelofs, P. A. Morris, J. D. Bierlein, "Ion exchange of Rb, Ba, and Sr in $KTiOPO_4$", *J. Appl. Phys*. **70**, 720-728, 1991.

[Roth 2000] M. Roth, N. Angert, M. Tseitlin, G. Wang, T. P.J. Han, H. G. Gallagher, N.I. Leonyuk, E.V. Koporulina, S. N. Barilo, L. A. Kurnevich, "Recent developments in crystal growth and characterization of nonlinear optical borate and phosphate materials", *Proc. 3rd Int. Conf. Single Crystal Growth, Strength Probl. Heat Mass Transf*. **2**, 416-426, ed By V.P. Ginkin (Uchlzd, Obninsk 2000).

[Rottmann 1988] F. Rottmann, A. Neyer, W. Mevenkamp, E. Voges, "Integrated optic wavelength multiplexers on lithium niobate based on two mode interference", *J. lightwave Technol.* **6**, 946-952, 1988.

[Rsoft BeamPROP 2013] Rsoft BeamPROP software, Synopsys Optical solutions, v2013.12, 2013.

[Sasaki 1993] T. Sasaki, A. Miyamoto, A. Yokotani, S. Nakai, "Growth and optical characterization of large potassium titanyl phosphate crystals", *J. Cryst. Growth.* **128**, 950-955, 1993.

[Satyanarayan 1999] M. N. Satyanarayan, A. Deepthy, H. L. Bhat, "Potassium titanyl phosphate and its isomorphs. Growth, properties, and applications", *Critical Rev. Sol. State Mater. Sci*. **24**, 103-191, 1999.

[Scarmozzino 1991] R. Scarmozzino, R. M. Osgood, "Comparison of finite-difference and Fourier transform solutions of the parabolic wave equation with emphasis on integrated optics applications", *J. Opt. Soc. Am. A* **8**, 724-731, 1991.

[Schmidt 1974] R. V. Schmidt, J. P. Kaminow, "Metal-diffused optical waveguide in $LiNbO_3$", *Appl. Phys. Lett.* **25**, 458-460, 1974.

[Schulze 1913] G. Schulze, "Versuche über die diffusion von Silber in Glas", *Annalen der Physik* **345**, 335-367, 1913.

[Shah 1975] M. L. Shah, "Optical waveguides in $LiNbO_3$ by ion exchange technique", *Appl. Phys. Lett*. **26**, 652-653, 1975.

[Sohler 2008] W. Sohler, H. Hu, R. Ricken, V. Quiring, C. Vannahme, H. Herrmann, D. Büchter, S. Reza, W. Grundkötter, S. Orlov, H. Suche, R. Nouroozi, Y. Min, "Integrated optical devices in lithium niobate", *Opt. and Phot. News* **19**, 24-31, 2008.

[Solé 1996] R. Solé, X. Ruiz, R. Cabré, Jna. Gavaldá, M. Aguiló, F. Díaz, V. Nikolov, X. Solans, "$KTiOPO_4$ single crystals grown from neodynium modified fluxes", *J. Cryst. Growth* **167**, 681, 1996.

[Solé 2002a] R. Solé, V. Nikolov, A. Vilalta, J. J. Carvajal, J. Massons, Jna. Gavaldá, M. Aguiló, F. Díaz, "Liquid phase epitaxy of $KTiOPO_4$ on $KTi_{1-x}Ge_xOPO_4$ substrates", *J. Cryst. Growth.* **237-239**, 602-607, 2002.

[Solé 2002b] R. Solé, V. Nikolov, A. Vilalta, J. J. Carvajal, J. Massons, Jna. Gavaldà, M. Aguiló, F. Díaz, "Growth of $KTiOPO_4$ films on $KTi_{1-x}Ge_xOPO_4$ substrates by liquid-phase epitaxy", *J. Mater. Res*. **17**, 563-569, 2002.

[Spence 1995] D. E. Spence, C. L. Tang, "Characterization and applications of high repetition rate, broadly tunable, femtosecond optical parametric oscillators", *IEEE J. Sel. Top. Quant. Electron*. **1**, 31-43, 1995.

[Suchoski 1988] P. G. Suchoski, T. K. Findalky, F. J. Leonberger, "Stable low loss proton exchanged lithium niobate devices with no electro-optic degradation", *Opt. Lett.* **13**, 1050-1052, 1988.

[Suhara 2003] S. Suhara, M. Fujimura, "Waveguides and nonlinear-optic Devices", Springer, Photonics, **11**, 2003.

[Tessman 1953] J.B. Tessman, A.H. Kahn, W.S. Shockley, " Electronic polarizabilities of ions in crystals", *Phys. Rev*. **92**, 890-895, 1953.

[Thomas 1990] P.A. Thomas, A. M. Glazer, B.E. Watts, "The crystal structure & Nonlinear optical properties of $KTiOPO_4$ and its structural analogue $KSnOPO_4$", *Acta. Cryst. Sect. B: Sctruct. Sci.* **46**, 333-343, 1990.

[Thomas 1992] P. A. Thomas, S. C. Mayo, B. E. Watts, "Crystal structures of $RbTiOAsO_4$, $KTiO(P_{0.58}As_{0.42})$, $RbTiOPO_4$ and $(Rb_{0.465}K_{0.535})TiOPO_4$, and analysis of pseudosymmetry in crystals of the $KTiOPO_4$ family", *Acta. Crystallogr*. B **48**, 401-407, 1992.

[Torjman 1974] I. Torjman, R. Masse, J. C. Guitel, "Structure crystalline du monophosphate $KTiPO_5$", *Z. Kristallogr.* **139**, 103-115, 1974.

[Tow 1994] P. D. Townsend, P.J. Chandler, L. Zhang, "Optical effects of ion implantation", Cambridge University Press, 1994.

[Vartak 2000] B. Vartak, Y. I. Kwon, A. Yeckel, J. J. Derby, "An analysis of flow and mass transfer during the solution growth of potassium titanyl phosphate", *J. Cryst. Growth*. **210**, 704-718, 2000.

[Voronkova 1988a] V. I. Voronkova, V. K. Yanovskii, "Growth of $KTiOPO_4$-group crystals from a solution in a melt and their properties", *Inorg. Mater.* **24**, 205-208, 1988.

[Voronkova 1988b] V. I. Voronkova, V. K. Yanovskii, " Flux growth and properties of the $KTiOPO_4$ family crystals", *Neorg. Mater.* **24**, 273-277, 1988.

[Wagner 2007] F. R. Wagner, A. Hildenbrand, J. Y. Natoli, M. Commandré, F. Théodore, H. Albrecht, " Laser damage resistance of $RbTiOPO_4$: evidence of polarization dependent anisotropy", *Opt. Express* **15**, 13849 (1-8 pages), 2007.

[Winnall 2000] S. Winnall, S. Winderbaum, "Lithium niobate reactive ion etching, electronic warfare division electronics and surveillance research laboratory", DSTO-TN-0291, Salisbury South Australia, 2000.

[Wooten 2000]. Ed L. Wooten, K. M. Kissa, A. Y. Yan, E. J. Murphy, D. A. Lafaw, P. F. Hallemeier, D. Maack, D. V. Attanasio, D. J. Fritz, G. J. McBrien, D. E. Bossi, "A review of lithium niobate modulators for fiber-optic communications systems", *IEEE J. Selected Topics in Quant. Electron*. **6**, 69-82, 2000.

[Wulff 1901] G. Wulff, "Zur frage der geschwindigkeit des wachstums und der auflosung der krystallflachen", *Z. Kristallogr*. **34**, 449-530, 1901.

[Xu 1995] C.L. Xu, W.P.Huang, "Finite-difference beam propagation method for guide wave optics", *Prog. Electromagnetic Res.* **11**, 1-49, 1995.

[Yamanouchi 2001] K. Yamanouchi, Y. Wagatsuma, H. Odagawa, Y. Cho, "Single crystal growth of $KNbO_3$ and application to surface acoustic wave devices", *J. European Ceram. Soc*. **21**, 2791-2795, 2001.

[Yang 2008] T. Yang, S. Song, H. Dong, R. Ba, "Waveguide structures for generation of terahertz radiation by electro-optical process in GaAs and $ZnGeP_2$ using 1.55 µm fiber laser pulses", *Progress in Electromag. Res. Lett.* **2**, 95-102, 2008.

[Young 1995] R. A. Young, "The Rietveld method", International Union of Crystallography, Monographs on crystallography 5, Oxford University Press, Oxford, 1995.

[Yu 2013] Y. J. Yu, X. Y. Chen, C. Wang, C. T. Wu, M. Yu, G. Y. Jin, "High repetition rate 880 nm diode-directly-pumped electro-optic Q-switched Nd:$GdVO_4$ laser with a double-crystal RTP electro-optic modulator", *Optics Comm.* **304**, 39-42, 2013.

[Zha 1992] L. Zhang, P. J. Chandler, P. D. Townsend, P.A. Thomas, "Helium ion implanted optical waveguide in $KTiOPO_4$", *Electronics Lett*. **28**, 650-653, 1992.

[Zumsteg 1976] F. C. Zumsteg, C. J. Bierlein, T. E. Gier, "Kx Rb1-x TiOPO4: A new nonlinear optical material", *J. Appl. Phys.* **47**, 4980-4985, 1976.

Appendix

Mask design for waveguides fabrication

To obtain the commercial mask, the design was made in OlympiOs Integrated Optics software and sent to Compugraphics International Ltd (UK). In this mask, different sets of devices were designed. For example, it contain fields of A1,A2, B1, B2, C1, C2, D1, D2, E1, E2, F1, F2, G1, G2, H1,H2. All these set contains 3 straight waveguides, 5 bend waveguides, 5 splitters and 5 MZI. The mask also has four sets of MZI (each set contains 10 MZI of 9mm in length and 10 MZI of 12 mm in length). These sets are made in order to use these MZI in E-O modulation. The mask design is shown in figure A.1.

And the detail of one set of the mask which is 9mm long is shown in figure A.2. It has 3 straight waveguides (4µm, 5 µm and 30 µm), 5 Y-splitters of 6 µm width with varying radius of curvature, 5 MZI of 6 µm widths with varying radius of curvature and 5 bend waveguides with the same parameters as that of Y-splitter and MZI.

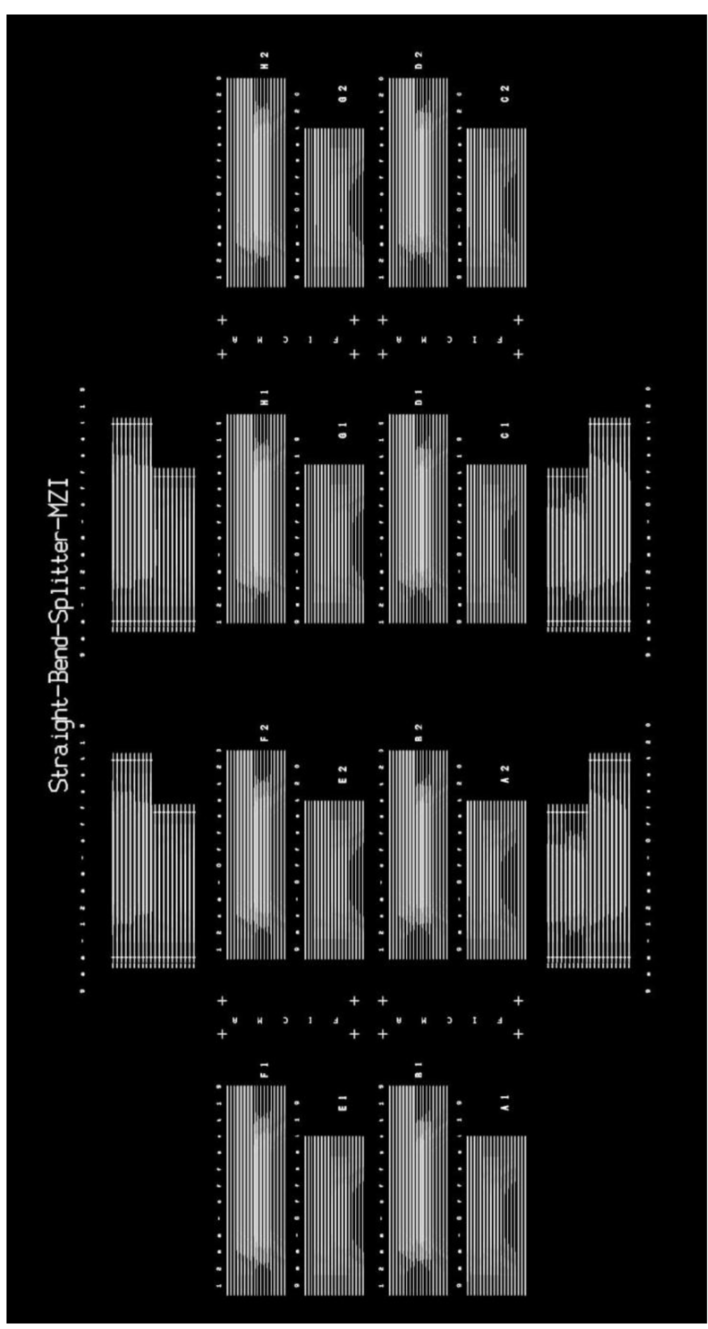

Figure A.1. Complete mask design containing different sets of straight waveguides, bend waveguides, Y-splitters and MZ

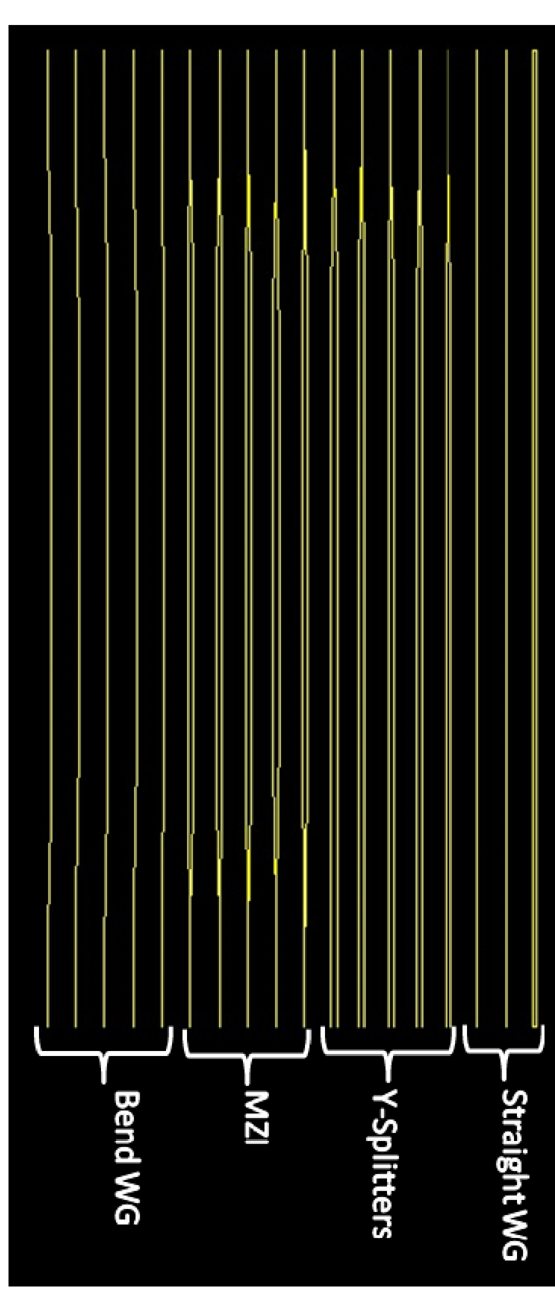

Figure A.2. One set of the mask containing straight WG, bend WG, Y-splitters and MZ

UNIVERSITAT ROVIRA I VIRGILI
NEW PHOTONIC DEVICES BASED ON NLO(NON-LINEAR OPTICAL) CRYSTALLINE WAVEGUIDES
Muhammad Ali Butt

Paper I

"Crystal growth and characterization of epitaxial layers of the $RbTiOPO_4$ family of nonlinear optical crystals"

M. A. Butt, R. Solé, M. C. Pujol, J. Cugat, M. Aguiló and F. Díaz

To be submitted to Optical Materials, 2015

Crystal growth and characterization of epitaxial layers of the $RbTiOPO_4$ family of nonlinear optical crystals

M. A. Butt, R. Solé, M. C. Pujol, J. Cugat, M. Aguiló and F. Díaz

Física i Cristal·lografia de Materials i Nanomaterials (FiCMA-FiCNA) and EMaS, Universitat Rovira i Virgili (URV), Marcel·lí Domingo 1, E-43007 Tarragona, Spain

*rosam.sole@urv.cat, mariacinta.pujol@urv.cat

Abstract

Epitaxial layers based on $RbTiOPO_4$ and $KTiOPO_4$ non-linear optical materials have been grown by liquid phase epitaxy. The crystalline quality of the epitaxial layers on the (001) and (100) faces are good, being a non-natural face and a natural face, respectively. Both planes contain the phase-matching direction for type-II second harmonic generation in the wavelength range from 980 to 1140 nm, and from 1000 to 1500 nm, respectively. The lattice mismatch between the epitaxial layers and the substrates are low enough to obtain high quality epitaxial layers. The refractive indices contrast between the epitaxial layer and the substrate has been analyzed for each epitaxial system.

1. Introduction

In the field of integrated optics, the interest in novel structures based on dielectric materials with different capabilities such as non-linearity and/or electro-optic properties is increasing. Among the known crystals with high non-linear optical and electro-optical (EO) coefficients, $KTiOPO_4$ (hereafter KTP) and its isomorphs $RbTiOPO_4$ (hereafter RTP) offer great possibilities for integrated optics, although their use in this field is scarce. KTP and RTP are orthorhombic crystals, which crystallize in the $Pna2_1$ space group and point symmetry mm2 [1,2]. Optically, they are positive biaxial crystals with $n_x>n_y>n_z$ (being ***a***, ***b*** and ***c***, the dielectric axes X, Y and Z, respectively)

The knowledge of the different possibilities for growing epitaxial layers of crystals of the RTP family with different refractive index variation to be used as a platform for these applications is necessary. Cugat *et al.* [3] already demonstrated that the epitaxial layer system based on (Yb,Nb) doped RTP on RTP(001) substrates assures a high refractive index contrast in n_z polarization; and using different techniques such as RIE and Ar ion milling it is possible to create 2D channels to be used as waveguides. More recently, Butt *et al.* [4] have used these epitaxial systems to create MZ and Y-splitter structures to be used as future platforms for EO modulators and/or optical sensors.

The objective of this work is to explore the possibilities of other epitaxial systems changing the chemical composition of the epitaxial layer and of the substrate and in addition to continue with the study of the (Yb,Nb):RTP/RTP epitaxial growth. The use of undoped epitaxial layers grown on doped substrates has the advantage that the non-linear optical and electro-optical coefficients of the layers are the high values corresponding to the undoped KTP and RTP, while the doping is in the substrate. These doping in the substrates has been always for the K^+/Rb^+ ion. As these materials are well-known by their high ionic conductivity along the ***c*** crystallographic direction [5], special emphasis has been taken to analyze the chemical composition of the epitaxial layer and the substrate to study the possibility of ion-exchange. On the other hand, the use of (Yb,Nb):RTP/RTP epitaxial layers have the advantage that the layer contains a lanthanide ion, Yb^{3+}, with concentration that could be enough for laser action [6]. A previous work on epitaxial layers of (Yb,Nb):RTP/RTP(001) was carried out in our group by J. Cugat *et al.* [3,7]. In this work we continue with the study of epitaxial growth of (Yb,Nb):RTP/RTP(001) and in addition we grew (Yb,Nb):RTP/RTP (001), RTP/K:RTP (001), RTP/K:RTP (100) and KTP/Na:KTP(001) epitaxial layers using the liquid phase epitaxy (LPE) method.In addition, the refractive indices of the substrates and the epitaxial layers have been measured to check the refractive indices contrast between the epitaxial layer and the substrate of great importance in waveguiding.

2. Experimental

2.1 Single crystal growth by Top Seeded Solution Growth-slow cooling method for substrates

RTP, K:RTP and Na:KTP single crystals were grown from high temperature solutions using the Top Seeded Solution Growth (TSSG) technique and the supersaturation was obtained by slow cooling. We used WO_3 containing solutions with the aim to decrease the viscosity of the solutions for improving the mass transport in the solutions. The solution compositions were chosen taking into account the crystallization regions of KTP and RTP in solutions containing WO_3 [8,9]. The reagents used were Rb_2CO_3, K_2CO_3, Na_2CO_3, TiO_2, $NH_4H_2PO_4$ and WO_3. For these experiments we used Pt cylindrical crucibles of 125 cm^3 filled with 150-200 g of solution. The solution compositions were Rb_2O-P_2O_5-TiO_2-WO_3 = 44.24-18.96-16.8-20 (mol %), Rb_2O-K_2O-P_2O_5-TiO_2-WO_3=39.51-4.39-23.6-22.5-10 (mol %) and was K_2O-Na_2O-TiO_2-P_2O_5-WO_3= 34.02-3.78-4.2-14-14-30 (mol %) for growing RTP, 10 at.% K:RTP and 10 at. %

Na:RTP single crystals, respectively. We choose the suitable WO_3 concentration in each case as a compromise between the decreasing of the solution viscosity and the difference of the cell parameters between these crystals that will be used for substrates and the cell parameters of the layers which will be grown by LPE on these substrates (see section 3 on lattice mismatch). The vertical axial thermal gradient in the solutions was between 1.5 and 3.0 K/cm, while the radial thermal gradient was around 1.8 K/cm, with the cooler place at the center of the surface of the solution. We used seeds oriented along ***c*** crystallographic direction because in previous works it has been proved that the crystals grow good with this orientation and these crystals are with enough size for cutting several crystallographic oriented substrates from each single crystal with suitable dimensions for fabricating optical waveguides. Once the solutions were homogeneous, its saturation temperature was measured by repeated seeding and the crystal growth was produced by decreasing the solution temperature from the saturation temperature at a rate of 0.05-0.1 K/h for 27-35 K with rotation between 40-60 rpm. In the initial stages of growth, the velocity of rotation generally was 60 rpm and it was reduced in several steps till 40 rpm when the crystal gained in size. In some experiments a pulling of the crystal (1 mm per day) for obtaining higher crystal dimension in ***c*** direction was applied at the final stages of the crystal growth. The growth conditions are summarized in Table 1.

2.2 Lattice mismatch

Before liquid phase epitaxial growth, the lattice mismatch between the substrates and the epitaxial layers have been calculated in order to obtain information about the possible stresses in the substrate/layer interface due to the different composition of the layer and the substrate.

Small single crystals were grown from the same solution composition detailed above. The crystals were grown from 15 g of solution contained in a 25 cm^3 platinum crucible. After homogenizing the solution, a Pt rod was immersed in it and the solution temperature was decreased 10 K every 30 minutes until the appearing of crystals on the Pt rod. After that, the solution was maintained at this temperature for 24 h in order to growth the crystals. These crystals were used for X-ray powder diffraction studies using a Siemens D-5000 equipment. The measurements were made using Bragg Brentano parafocusing geometry with θ-θ configuration and Cu K_α radiation. The data were collected with 2θ range from 10 to 70 °, step scan of 0.02 ° and step time of 16 s. Using these diffraction data, the unit cell parameters of the crystals obtained were refined using the Fullprof program based on the Rietveld method [10].

2.3 Liquid phase epitaxial growth

The LPE growth experiments were carried out in a very well isolated furnace in order to obtain practically zero thermal gradients in the solution. We used Pt cylindrical crucibles, 30 mm in diameter and 40 mm in height, filled with about 80 g of solution. The saturation temperature of the solution, as well as, the kinetics of growth/dissolution at several degrees below/above the saturation temperature was studied before the LPE growth. The substrates were cleaned by dipping them in HNO_3/H_2O in a molar ratio ½ (5 minutes), in distilled water (5 minutes), in acetone (5 minutes) and finally in ethanol (5 minutes) [11]. All this cleaning process was made under substrate rotation at 60 rpm.

The substrates were slowly introduced in the furnace in order to avoid thermal shocks and maintained for at least 1 h at a few mm above the surface of the solution to obtain thermal equilibrium with the solution. After that, the substrate was introduced in the solution at 1 K above the saturation temperature for 5 minutes to dissolve the outer part of the substrate, followed by decreasing the solution temperature up to several degrees below the saturation temperature in order to growth the epitaxial layer. The LPE growth was carried out for several hours. More details can be seen in Table 2. Finally the substrates with the epitaxial layer were slowly removed from the solution and cooled to room temperature at 20-25 K/h.

2.4 Morphological and optical characterization

The refractive indices of K:RTP and Na:KTP were measured using the dark mode spectra method. For these measurements we used a Metricon prism-coupler and a He-Ne laser to generate 632 nm light.

The morphologies of the surface of the epitaxial layers for the different growth times were studied with a confocal microscope with 20x objective. The equipment used was a Sensofar PLμ 2300 Optical imaging profile with a wavelength of 470 nm.

The composition of the substrates and epitaxial layers was measured by electron probe microanalysis (EPMA) with wavelength dispersive spectroscopy (WDS). The standard used for Rb, Ti, P and O measurements was a undoped RTP, for K measurement a KTP was used and Nb metal was used to determine the Nb concentration and YbF_3 was used for Yb measurements. K_α X-ray lines were used to measure Ti, P and O, while L_α X-ray lines were used for the Rb, Nb and Yb measurements.

3. Results and discussion

3.1. Substrates growth

The saturation temperatures of the three solutions used were 1163 K, 1155 K and 1221 K for RTP, K:RTP and Na:RTP solutions, respectively. As an example, Figure 1 some examples of the obtained crystals. The crystals obtained are colorless, transparents and free of inclusions.

As can be seen in Table 1, the growth rate of K:RTP is similar than the growth rate of undoped RTP, although the solution used to growth K:RTP only contains 10 mol % WO_3, while the solution used to growth RTP contains 20 mol % WO_3. The growth rate of Na:KTP is slightly higher than the growth rates of RTP and K:RTP and the reason could be that the solutions used to growth Na:KTP contains 30 mol % WO_3 and the temperatures of growth are higher, which means less viscous solutions, since the solution viscosity decrease with the WO_3 contents and with the increase of the temperature. When pulling was applied, the crystal dimension in ***c*** crystallographic direction generally is increased.

The composition of the doped crystals was measured by electron probe microanalysis with wavelength dispersion spectroscopy (EPMA-WDS). The compositions obtained for the doped bulk single crystals were $Rb_{0.9}K_{0.1}TiOPO_4$ and $K_{0.97}Na_{0.03}TiOPO_4$, as can be seen in section 3.5.

To obtain substrates, the crystals were cut in slices perpendicular to the ***c*** crystallographic direction or the ***a*** crystallographic direction, depending on the case and polished to optical quality. The roughness of the surfaces obtained was lower than 10 nm and the curvature radius was 8-20 m.

3.2. Predicted lattice mismatch

For a given substrate, the lattice mismatch parameter between the layer and the substrate is limited by a critical value, above which the continuity of the crystalline construction across the substrate-layer interface is impossible. Minimum mismatch, on the opposite, means reduced stress at the layer-substrate interface, and better physical performance. Using the unit cell parameters of the different materials used for substrate and epitaxial layer, it is possible to to calculate the lattice mismatch between the substrate and the epitaxial layer by using the expression: $f_{hkl}=100 \times [(S_{L(hkl)}-S_{S(hkl)})/S_{S(hkl)}]$, where hkl refers to the plane of the substrate and epitaxial layer, $S_{L(hkl)}$ and

$S_{S(hkl)}$ are the areas defined by the periodicity vectors of the layer and the substrate, respectively [11].

Table 3 shows the unit cell parameters of RTP, (Yb,Nb):RTP, K:RTP and Na:RTP used to calculate the lattice mismatch between the substrate and the epitaxial layer. The lattice mismatches are shown in Table 4. The lowest lattice mismatch is obtained is for the KTP/Na:KTP system, due to the small change of the unit cell parameters (Ionic radius of Na^+ 1.24 Å versus ionic radius of K^+ 1.55 Å and the presence of only actual 3% at. substituion). For RTP/K:RTP(100) and RTP/K:RTP(001), also a very low value can be attributed to the plane (100), due to the fact that K^+ introduction in RTP decreases the ***a*** and ***b***, but increases the **c** crystallographic direction (Ionic radius of K^+ 1.55 Å versus Rb^+ 1.63Å and actual 10% at. substitution). The highest lattice mismatch is in (Yb,Nb):RTP/RTP(001) and it is larger that the already described ones for (Yb,Nb):RTP on RTP(100), but we choose this composition of the epitaxial layer, because it maximizes the Yb^{3+} content. In all cases, the surface of the layer defined by the periodicity vectors are higher than the equivalent surface of the substrate, which means than the layer has a compressive stress.

3.3. Refractive index variation

The refractive indices at room temperature and at 632 nm of these crystals are shown in Table 5. In the same Table there are the refractive indices of other crystals used for substrates and epitaxial layers already published in the bibliography.

The variation of refractive indices between the substrate and the epitaxial layer is of great interest for waveguide designing. It is known that a thin epitaxial layer can guide the light if has refractive indices higher than the surrounding, in this case the substrate and air, if no cladding is grown. The contrast of refractive indices between the substrate and the epitaxial layer in every system used in this work has been calculate for different light polarizations and is shown in Table 6. In (Yb,Nb):RTP/RTP, the contrast of refractive indices for polarization along **x** direction is negative and along **y** direction has a very small value (0.0001), this means that guiding light with **x** polarization will be not possible and with **y** polarization very difficult and only with **z** polarization is expected to guide the light. This can be accomplished growing the epitaxial layers in the (001) plane.

In the case of RTP on K:RTP, there's a large variation of the refractive index contrast in n_z and n_y; but is less that the one for the codoped (Nb,Yb) epitaxial layer; however when introducing K^+ in the substrate; it is possible to reach a high variation of the refractive index in n_z of around 0.01.

A similar behavior is observed in KTP/Na:KTP, where the contrast of refractive indices is negative for a polarization and small for c polarization (0.0005), but the refractive index contrast in n_y could be enough for guiding purposes.

3.4. Epitaxial layer growth

The solution compositions were Rb_2O-P_2O_5-TiO_2-Nb_2O_5-Yb_2O_5-WO_3=43.9-23.6-20.7-0.45-1.35-10 (mol %), Rb_2O-P_2O_5-TiO_2-WO_3 = 44.24-18.96-16.8-20 (mol %) and K_2O-P_2O_5-TiO_2 =48-32-20 (mol %) for the growth of (Yb,Nb):RTP/RTP (001), (Yb,Nb):RTP/K:RTP(001), RTP:K:RTP (001) and (100) and KTP/Na:KTP (001), respectively.

In the (Yb,Nb):RTP/RTP LPE experiments generally the epitaxial layers were transparent and without macroscopic defects as can be observed in Figure 2a. As can be seen in Table 2, for (Yb,Nb):RTP/RTP epitaxial layers, the growth temperature was in the range 3-6 K below the saturation temperature and different growth times. As it was expected, the growth rate increased as the growth temperature decreased because of the increasing of the level of supersaturation of the solution and for a given growth temperature the growth rate is practically constant at least up to several hours.

Experiment number 7 was made with the aim to study the effect of the growth time on the layer thickness and the morphology of the surface of the epitaxial layer. In this experiment, the substrate was immersed several mm in the solution and it was pulled in different steps, usually 2 mm every 60 minutes, although sometimes the time interval was slightly different as can be seen in Table 2, where the different step times are summarized. Figure 3 shows the growth rate as a function of the growth time in experiment number 7. As can be seen, up to a growth time of 380 minutes, the layer thickness increases linearly with time, which means a constant growth rate of 0.21 μm/min.

In the case of RTP epitaxial layers grown on K:RTPsubstrates, two different substrate orientations were used, (001) and (100) oriented substrates. The growth temperatures were 2-3 K below the saturation temperature and give similar growth rates than (Yb,Nb):RTP/RTP epitaxial layers grown at 4-6 K below the saturation temperature. This is due to the different WO_3 concentration in the solutions, in the case of RTP/K:RTP the solutions contained 20 mol % WO_3, while in the growth of (Yb,Nb):RTP/RTP the solutions had only 10 mol % WO_3.

In the case of RTP/K:RTP (001) epitaxial growth, the layers have a higher tendency to have cracks and capping effect [12]. If the epitaxial growth is produced at 6 K below

the saturation temperature the number of defects is very high. For this reason LPE experiments were made at 2-3 K below the saturation temperature and the growth time was only 2 h or less. Ref de que la tesis del Jaume ja es menciona que es fragmenten

In the KTP/Na:KTP(100) LPE experiment the growth was made at low supersaturation (growth temperature only 1 K below the saturation temperature) and the growth time was 60 minutes. The WO_3 concentration in the solution was also 20 mol % and the growth rate was only slightly lower than in RTP/K:RTP grown at 2 K below the saturation temperature. The recorded images of the morphologies of the different growth steps of experiment number 7 are shown in Figure 4. It can be observed in Figure 4 that in the first steps of the epitaxial growth, the number of defects is higher than for higher growth times. The defects are mainly oriented along the ***b*** crystallographic direction and, at the initial stages of growth, its size if of the order of a few hundred of nanometers. As can be seen in Figure 4, for a growth time of 380 minutes, the defects are clearly reduced. A possible explanation of this effect is that near the epitaxial layer/substrate interface, the defects are higher in number and size due to the stress existing near the interface produced by the mismatch between the substrate and the layer and when the thickness of the epitaxial layer increase these defects can be partially overcame.

3.5. Compositional characterization

While in the (Yb,Nb):RTP/RTP no diffusion of Yb and Nb from the substrate to the layer was observed, in the case of RTP/K:RTP (001) and (100) a diffusion of K ions was observed as can be seen in Figure 7. This, (Yb,Nb):RTP/RTP can be used for the fabrication of step-index waveguides, while the RTP/K:RTP (001) and (100) samples can be used for the fabrication of graded index waveguides, because the refractive indices depend on the crystal composition and in the interface there is a gradual change of refractive indices due to the gradual compositional change.

A similar behavior was observed in the RTP/K:RTP (100) and in the RTP/K:RTP (001) samples, although it was expected a higher diffusion along (001) direction due to the K and Rb channels in the KTP and RTP structures responsible of the high ionic conductivity in this direction, the diffusion along (100) direction was at a similar level than along (001) direction.

The composition of the substrates and epitaxial layers are shown in Table 6. In the same table there is detailed the kind of interface observed in each case. In (Yb,Nb)RTP/RTP epitaxial layers a sharp compositional change in the epilayer/substrate interface was observed as it has been probed in a previous work [3]. In the case of

RTP/K:RTP (001) and (100) there was observed a region of several tens of μm in the substrate/epitaxial layer interface where there is ion exchange between K and Rb ions, forming a graded interface in composition and consequently also in refractive indices.

From the real stoichiometry of the substrates and the epilayers, the distribution coefficients of the doping ions can be calculated, according to the expressions:

$$K_K = \frac{\{[K]/([K]+[Rb])\}_{crystal}}{\{[K]/([K]+[Rb])\}_{solution}} \text{ for } K^+, \quad K_{Na} = \frac{\{[Na]/([Na]+[K])\}_{crystal}}{\{[Na]/([Na]+[K])\}_{solution}} \text{ for}$$

Na^+, where [*K*], [Na], [Rb] are the K^+, Na^+, Rb^+ concentrations in at. %, respectively. The distribution coefficients of Yb^{3+} and Nb^{5+} were already calculated in a previous work [3].

Thus, the distribution coefficients of the different doping elements are: K_K=1, K_{Na}=0.3, K_{Yb} = 0.14 and K_{Nb}=0.66. If the distribution coefficient of an element is lower than unity, during the crystal growth the solute existing in the solution undergoes richer in this element, but in the case of epitaxial growth this change generally is very small because the weight of the grown epitaxial layer is significantly smaller than the weight of the solute in the solution. In the case of bulk single crystal growth, a distribution coefficient of an element constitutive of the crystal lower than unit can leads to change the composition in the solution.

4. Conclusions

Epitaxial layers of crystals of the $RbTiOPO_4$ family of non-linear optical materials have been grown using the liquid phase epitaxy technique. The crystalline quality of the epitaxial layers grown on the (001) and (100) crystal faces have been studied and after several hours of growth the defects appeared in the substrate/layer interphase are minimized. The refractive indices contrast between the epitaxial layers and the substrates could be suitable for guiding the light in the main part of the cases.

References

[1] C. Zumsteg, C. J. Bierlein, T. E. Gier, $K_xRb_{1-x}TiOPO_4$: A new nonlinear optical material, J. Appl. Phys. 47 (1976) 4980-4985.

[2] P.A. Thomas, A. M. Glazer, B.E. Watts, The crystal structure & Nonlinear optical properties of $KTiOPO_4$ and its structural analogue $KSnOPO_4$, *Acta. Cryst. Sect. B: Sctruct. Sci.* 46(3) (1990) 333-343.

[3] J. Cugat, R. Solé, J. J. Carvajal, M. C. Pujol, X. Mateos, F. Díaz, M. Aguiló, Crystal growth and characterization of $RbTi_{1-x-y}$/ $RbTiOPO_4$(001) non-linear optical epitaxial layers, *CrystEngComm.* 13 (2011) 2015-2022.

[4] M. A. Butt, R. Solé, M. C. Pujol, A. Ródenas, G. Lifante, A. Choudhary, G. S. Murugan, D. P. Shepherd, J. S. Wilkinson, M. Aguiló, F. Díaz, Fabrication of Y-Splitters and Mach-Zehnder Structures on (Yb,Nb):$RbTiOPO_4$/$RbTiOPO_4$ Epitaxial Layers by Reactive Ion Etching, Journal of Lightwave Technology (2015) (in press).

[5] M.E. Hagerman, K.R. Poeppelmeier, Review of the structure and processing defect propertiy relationships of potassium titanyl phosphate: a strategy for novel thin-film photonic devices, Chem. Mater. 7 (4) (1995) 602-621.

[6] X. Mateos, V. Petrov, A. Peña, J.J. Carvajal, M. Aguiló, F. Díaz, P. Segonds, B. Boulanger, Laser operation of Yb^{3+} in the acentric $RbTiOPO_4$ codoped with Nb^{5+}, Optics Letters 32 (13) (2007) 1929-1931.

[7] J. Cugat, R. Solé, M. C. Pujol, J. J. Carvajal, X. Mateos, F. Díaz, M. Aguiló, Waveguiding demonstration on Yb:Nb:$RbTiOPO_4$/$RbTiOPO_4$ (001) epitaxies grown by LPE, Optical Materials, 32 (2010) 1648-1651.

[8] K. Iliev, P. Peshev, V. Nikolov, I. Koseva, Physicochemical properties of high-temperature solutions of the K_2O-P_2O_5-TiO_2-WO_3 system, suitable for the growth of $KTiOPO_4$ (KTP) single-crystals, J. Cryst. Growth. 100 (2990) 219-224.

[9] J.J. Carvajal, V. Nikolov, R. Solé, Jna. Gavaldá, J. Massons, M. Rico, C. Zaldo, M. Aguiló, F. Díaz, Enhancement of the Erbium Concentration in $RbTiOPO_4$ by codoping with Niobium, *Chem.Mater.* **12**(10) (2000) 3171-3180.

[10] H.M. Rietveld, A profile refinement method for nuclear and magnetic structures, J. *Appl. Crystal.* 2 (1969) 65-71.

[11] R. Solé, V. Nikolov, A. Vilalta, J.J. Carvajal, J. Massons, Jna. Gavalda, M. Aguilo, F. Diaz, Liquid phase epitaxy of $KTiOPO_4$ on $KTi_{1-x}Ge_xOPO_4$ substrates, *J. Cryst. Growth* 237-239 (2002) 602-607.

[12] C. Herring, The use of classical macroscopic concepts in surface energy problems, Structure and properties of solid surfaces, ed. by R.G. Gromer, C.S. Smith, University of Chicago Press, Chicago, 1953, pp. 5-72.

[13] J. Cugat, Fabrication and characterization of waveguides on $RbTiOPO_4$ crystals for photonic applications, Ph. D. Thesis, Universitat Rovira i Virgili (2013).

[14] G. M. Loiacono, D. N. Loiacono, R.A. Stolzenberger, Growth and properties of crystals in the system $KTiOPO_4$-$NaTiOPO_4$, J. Cryst. Growth 144 (1994) 223-228.

Figure Captions

Figure 1.- a) As-grown RTP single crystal with pulling, b) As-grown K:RTP single crystal and c) As-grown Na:KTP single crystal

Figure 2.- a) As-grown (Yb,Nb):RTP/RTP (001) and b) as-grown KTP/Na:KTP (001) epitaxial layers.

Figure 3.- Epitaxial thickness as a function of the growth time in experiment number 7.

Figure 4.- Confocal images of the surface morphologies obtained for growth times of a) 90 minutes, b) 110 minutes, c) 170 minutes, d) 230 minutes, e) 320 minutes and f) 380 minutes in a (Yb,Nb):RTP/RTP (001) epitaxial growth in experiment number 7.

Figure 5.- Potassium concentration as a function of the depth in experiment number 9 (Table 4)

Tables

Table 1.- Growth conditions, dimensions and weight of some crystals grown for cutting substrates.

Exp. number	crystal	Cooling rate (K/h) /cooling interval (K)	Pulling (mm)	Crystal dimensions a x b x c (mm^3)	Crystal weight (g)	Growth rate (g/h)
1	RTP	0.1/ 15 K 0.05/15 K	0	15.3 x 18.3 x 12.35	5.74	0.0128
2	RTP	0.1/15 K 0.05/ 18 K	0	15.7 x 16.6 x 15.3	5.98	0.0117
3	RTP	0.1 / 15 K 0.05 /16 K	0	13.6 x 18.4 x 14.2	5.59	0.0119
4	RTP	0.1/ 15 K 0.05 / 19.5 K	2	18.3 x 16.0 x 13.9	6.21	0.0115
5	RTP	0..1/ 15 K 0.05 / 17 K	3	14.5 x 15.8 x 15.9	5.60	0.0114
6	RTP	0.1 /15 K 0.05/ 12 K	4	17.3 x 18.7 x 20.4	9.37	0.0240
7	K:RTP	0.1/ 15 K 0.05/14.7 K	0	16.7 x 17.4 x 6	5.30	0.0119
8	K:RTP	0.1/ 15 K 0.05/14.7 K	0	14.8 x16.0 x 10.4	4.44	0.0100
9	K:RTP	0.1/ 15 K 0.05/14.2 K	0	18. 9 x 15.1 x 9.5	4.57	0.0105
10	Na:KTP	0.1/ 15 K 0.05/13.7 K	0	17.9 x 21.6 x 8.2	5.55	0.0131
11	Na:KTP	0.1/15 K 0.05/ 12.3 K	3	11.9 x 23 x12.5	5.39	0.0136
12	Na:KTP	0.1 / 15 K 0.05 /11.2 K	4	18.2x16.5x13.47	5.70	0.0152

Table 2.- Growth conditions and epitaxial thickness in the LPE experiments.

Exp. number	**Layer/substrate (substrate orientation)**	**Degrees below the T_s (K)**	**Growth time (min)**	**Thickness (μm)**	**Growth rate (μm/min)**
1	(Yb,Nb):RTP/RTP (001)	3	240	75	0.31
2	(Yb,Nb):RTP/RTP (001)	3	320	100	0.31
3	(Yb,Nb):RTP/RTP (001)	4	140	62	0.44
4	(Yb,Nb):RTP/RTP (001)	4	150	60	0.40
5	(Yb,Nb):RTP/RTP (001)	6	130	82	0.63
6	(Yb,Nb):RTP/RTP (001)	6	180	105	0.58
7	(Yb,Nb):RTP/RTP (001)	6	50-110-170-230-320-380	23-34-50.5-69-78-93	0.21
8	RTP/K:RTP (001)	3	120	70	0.58
9	RTP/K:RTP (001)	2	120	55	0.46
10	RTP/K:RTP (001)	2	60	29	0.48
11	RTP/K:RTP (100)	2	60	45	0.75
12	KTP/Na:KTP (001)	1	60	25	0.41

Table 3.- Unit cell parameters of RTP, (Yb,Nb):RTP, K:RTP and Na:RTP expressed in the $Pna2_1$ space group.

crystal	a (Å)	b(Å)	c(Å)	reference
RTP	12.9650(5)	6.5007(3)	10.5576(4)	[3]
(Yb,Nb):RTP	12.9916(7)	6.5152(4)	10.5764(6)	This work*
10 % K:RTP	12.9501(4)	6.4885(2)	10.5619(3)	[13]
KTP	12.8171(3)	6.4046(9)	10.5893(4)	[11]
4% Na:KTP	12.811	6.402	10.592	[14]

These parameters belong to the stoichiometry $RbTi_{0.958}Yb_{0.016}Nb_{0.026}OPO_4$.

Table 4.- Expected lattice mismatch between the substrate and the epitaxial layer.

Epitaxial layer/substrate	Lattice mismatch
(Yb,Nb):RTP/RTP(001)	0.429
RTP/K:RTP(001)	0.303
RTP/K:RTP(100)	0.147
KTP/Na:KTP (001)	0.088

Table 5.- Refractive indices at 632 nm.

crystal	n_x	n_y	n_z	reference
RTP	1.7893	1.8015	1.8897	[3]
(Yb,Nb):RTP	1.7863	1.8016	1.8967	[3]
K:RTP	1.7858	1.7959	1.8843	This work
KTP	1.7613	1.7727	1.8654	[11]
Na:KTP	1.7618	1.7714	1.8649	This work

Table 6.- Refractive index contrast between the substrate and the epilayer.

Epitaxial layer/substrate	**Δn_x**	**Δn_y**	**Δn_z**
(Yb,Nb):RTP/RTP	-0.003	0.0001	0.007
RTP/K:RTP	0.0035	0.0056	0.0054
(Yb,Nb)RTP/K:RTP	0.0005	0.0057	0.0124
KTP/Na:KTP	-0.0005	0.0013	0.0005

Table 7.- Real composition of the substrates and the epitaxial layers and kind of interface.

Epitaxial layer / substrate	**Real stoichiometry**	**Kind of interface (in composition)**
(Yb/Nb):RTP/RTP (001)	$RbTi_{0.958}Yb_{0.016}Nb_{0.026}OPO_4/RbTiOPO_4$	Step interface
RTP/K:RTP(001)	$RbTiOPO_4/Rb_{0.9}K_{0.1}OPO_4$	Graded interface
RTP/K:RTP(100)	$RbTiOPO_4/Rb_{0.9}K_{0.1}OPO_4$	Graded interface
KTP/Na:KTP(001)	$KTiOPO_4/K_{0.97}Na_{0.03}OPO_4$	-

Figure 1.

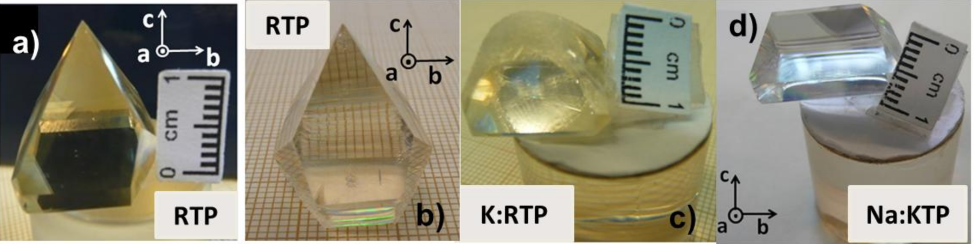

Figure 2

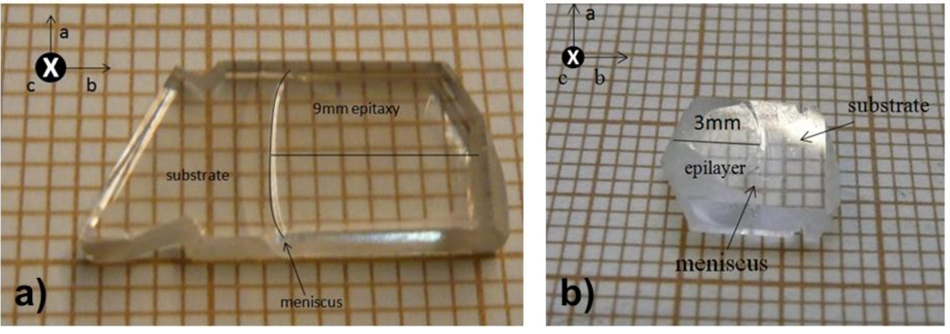

Figure 3

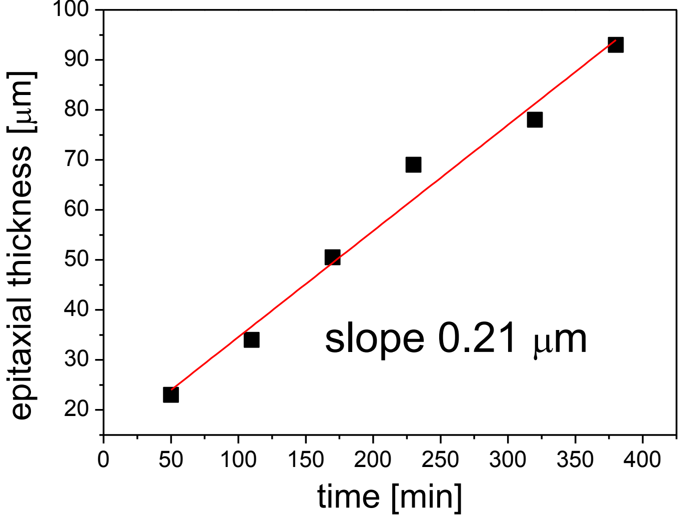

Figure 4

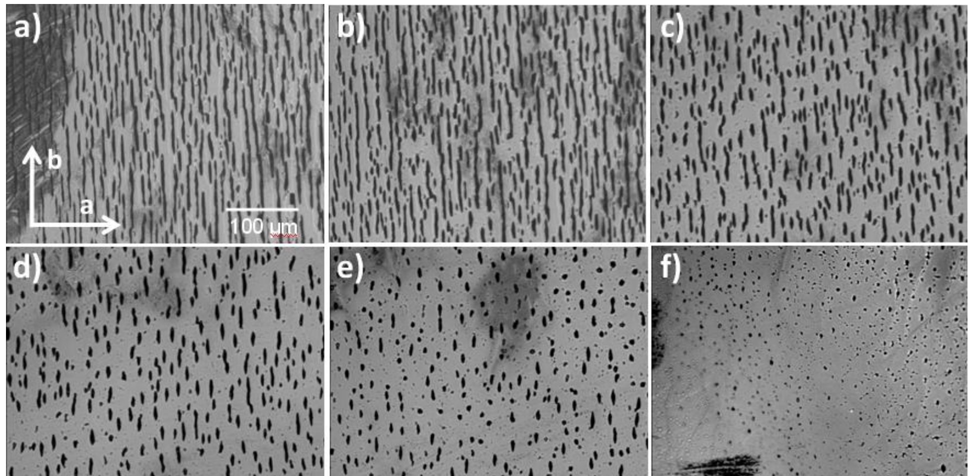

Figure 5

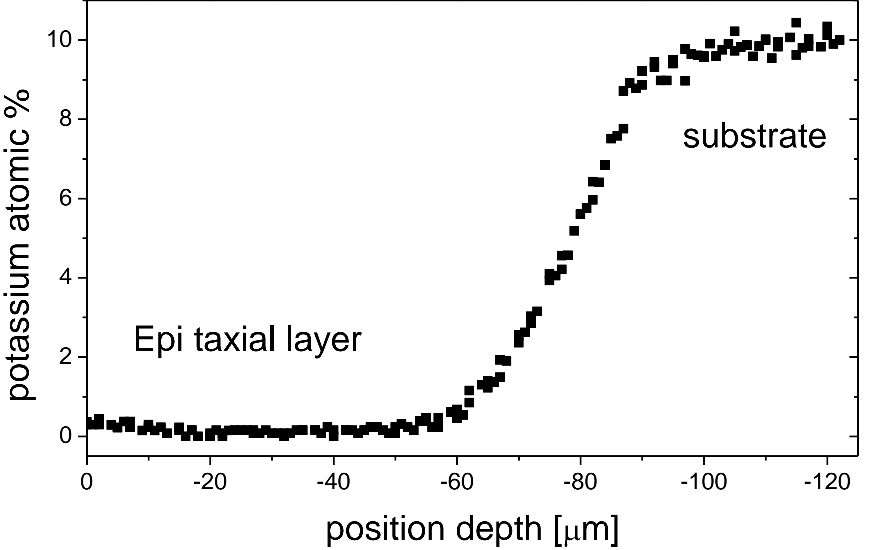

Paper II

"Fabrication of Y-Splitters and Mach-Zehnder Structures on (Yb,Nb):$RbTiOPO_4$/$RbTiOPO_4$ Epitaxial Layers by Reactive Ion Etching"

M. A. Butt, R. Solé, M. C. Pujol, A. Ródenas, G. Lifante, A. Choudhary, G. S. Murugan, D. P. Shepherd, J. S. Wilkinson, M. Aguiló, and F. Díaz.

Accepted in Journal of Lightwave Technology, DOI 10.1109/JLT.2014.2379091, 2014

UNIVERSITAT ROVIRA I VIRGILI
NEW PHOTONIC DEVICES BASED ON NLO(NON-LINEAR OPTICAL) CRYSTALLINE WAVEGUIDES
Muhammad Ali Butt

This article has been accepted for publication in a future issue of this journal, but has not been fully edited. Content may change prior to final publication. Citation imformation:DOI 10.1109/JLT.2014.2379091, Journal of Lightwave Technology

Fabrication of Y-Splitters and Mach-Zehnder Structures on (Yb,Nb):$RbTiOPO_4$/$RbTiOPO_4$ Epitaxial Layers by Reactive Ion Etching

M. A. Butt, R. Solé, M. C. Pujol, A. Ródenas, G. Lifante, A. Choudhary, G. S. Murugan, D. P. Shepherd, J. S. Wilkinson, M. Aguiló, and F. Díaz

***Abstract*—Reactive ion etching of $RbTiOPO_4$ (001) substrates and (Yb,Nb):$RbTiOPO_4$/$RbTiOPO_4$ (001) epitaxial layers has been performed using fluorine chemistry. A maximum etch rate of 8.7 nm/min was obtained, and the deepest etch achieved was 3.5 μm. The (Yb,Nb)-doped epitaxial layers showed a slower etching rate when compared with undoped material. Liquid phase epitaxial growth of cladding layers has also been performed, resulting in a high-quality interface growth without appreciable defects. 9-mm-long Mach Zehnder interferometer (MZI) and 9-mm-long Y-splitter structures were designed and patterned in $RbTiOPO_4$ substrates and (Yb,Nb):$RbTiOPO_4$/$RbTiOPO_4$ (001) epitaxial layers. The structures fabricated in $RbTiOPO_4$ substrates were filled with laser active (Yb,Nb):$RbTiOPO_4$ higher refractive index core material, and finally an $RbTiOPO_4$ cladding was grown on the samples. The refractive index difference between the (Yb,Nb):$RbTiOPO_4$ layer and the $RbTiOPO_4$ substrate at 1.5 μm has been measured and optical waveguiding at this wavelength has been demonstrated.**

***Index Terms*—Integrated Optical Materials, $RbTiOPO_4$, Reactive Ion Etching, optical waves.**

I. INTRODUCTION

$RbTiOPO_4$ (hereafter RTP) belongs to the $KTiOPO_4$ (KTP) family of nonlinear optical crystals. These crystals are orthorhombic and positive biaxial, with a=12.974(2) Å, b=6.494(3) Å and c=10.564(6) Å [1] with the space group $Pna2_1$ and $n_x<n_y<n_z$ (being the X, Y, and Z, the dielectric axes parallel to the crystallographic ***a***, ***b***, and ***c*** directions, respectively). RTP has large electro-optical coefficients (i.e. r_{33}=39.3 pm/V) and, high nonlinear optical coefficients (i.e. d_{33}= 15.6±0.3 pm/V) [2], which make them attractive for electro-optic applications such as modulators and Q-switches [3]. These electro-optic properties also make RTP an attractive material for integrated optical applications for fabrication of active and passive devices. Traditionally, in the KTP family of crystals, such devices are fabricated by ion diffusion techniques; in which a graded refractive index profile is achieved [4] leading to channel waveguides if the diffusion is carried out through an appropriate mask. Ion implantation has been also used as a feasible technique to obtain waveguides with graded refractive index profile in RTP recently [5,6]. Planar optical waveguides have already been demonstrated, for guiding light in the near infrared (NIR) and visible range, based on (Yb,Nb):RTP/RTP (001) epitaxial layers and, in contrast to diffused and ion implanted waveguides, these systems possess a step-index profile [7].

Reactive ion etching (RIE), as commonly is used for structuring dielectric materials such as SiO_2 and $LiNbO_3$ [8-11], could be used to produce channel waveguides in (Yb,Nb):RTP/RTP (001) planar layers and RTP (001) substrates. However, the use of this technique in the KTP family of compounds has not yet been widely explored. Dubs *et al.* reported the preparation of ridge type waveguide structures on $K_{1-x}Rb_xTiOPO_4$/KTP epitaxial layers by electron-cyclotron-resonance reactive ion etching (ECR-RIE) obtaining results in a 3.5 μm depth etch channel [12].

Initially, it would be desirable to use undoped KTP or RTP hosts as active waveguide layer materials if only the electro-optic properties should be used. In this case the substrate material with lower refractive index than the core would be an isostructural material with a ionic substitution in the K^+ or Rb^+ position (Ti or P elements cannot be substituted for any lighter element in order to decrease the refractive index and maintain the crystalline structure) and if in the substrate or in the active epitaxial layer, part of the K^+ or Rb^+ cations are substituted by other monovalent cations for obtaining differences in the refractive index between the substrate and the layer, the refractive index profile along ***c*** direction is graded, because of the high ionic conductivity in this direction in KTP and RTP compounds [13]. This fact induces that the active layer should be the doped one; and the substitution should be preferably in the Ti position; then using the couple (Yb,Nb) already used in the past for RTP, is logical due to the charge compensation in the compound (doping only with Nb^{5+} can create more Rb^+ vacancies [14])

This work was supported by the Spanish Government under the Project MAT2013-47395-C4-4-R, by the Catalan Authority under Project 2014SGR1358. M. Ali Butt thanks the Catalan Government for the FI-DGR fellowship 2012FI-B 00192. A. Choudhary acknowledges an UK Engineering and Physical Sciences Research Council (EPSRC) doctoral prize.

M. A. Butt, , R. Solé, M. C. Pujol, A. Ródenas, M. Aguiló and F. Díaz are with Física i Cristal·lografia de Materials i Nanomaterials (FiCMA-FiCNA) and EMaS, Universitat Rovira i Virgili (URV), Marcel·lí Domingo s/n, E-43007 Tarragona, Spain (email authors: muhammadali.butt@urv.cat, rosam.sole@urv.cat, mariacinta.pujol@urv.cat, airan.rodenas@urv.cat, magdalena.aguiló@urv.cat and f.diaz@urv.cat).

G. Lifante is with the Departamento de Física de Materiales, Universidad Autónoma de Madrid E-28049 Madrid, Spain (email author: gines.lifante@uam.es).

A. Choudhary, G. S. Murugan, D. P. Shepherd and J. S. Wilkinson are with the Optoelectronics Research Centre, University of Southampton, Southampton, SO171BJ, United Kingdom (email authors: ac12g10@orc.soton.ac.uk, smg@orc.soton.ac.uk, dps@orc.soton.ac.uk, jsw@ecs.soton.ac.uk).

0733-8724 © 2015 IEEE. Personal use is permitted, but republication/redistribution requires IEEE permission. See http:// www.ieee.org/publications_standards/publications/rights/index.html for more information.

This article has been accepted for publication in a future issue of this journal, but has not been fully edited. Content may change prior to final publication. Citation imformation:DOI 10.1109/JLT.2014.2379091, Journal of Lightwave Technology

and the future possibility to use Yb^{3+} ion as active ion for laser and SFD emission. Then, the chemical composition of the epitaxies used in this work is (Yb,Nb):RTP layers over undoped RTP, despite the future applications of the designed devices in the present work is only based in the electro-optic properties of these compounds.

Our previous work showed the first exploratory research of the optima conditions for RIE etching in (Yb,Nb):RTP epitaxial layers to obtain channel waveguides with a height around 1.5 µm [15]. In this work, waveguides with larger dimensions than the previous ones reported were designed in order to confine 1.5 µm wavelength radiations; this wavelength is especially interesting in the telecommunications and biomedical fields. The etching has been performed both in the active layer and in the undoped substrate, and consequently, in order to obtain the guiding composite, one or two epitaxial growth processes were required. Finally, the fabricated waveguide structures were optically characterized.

II. WAVEGUIDE FABRICATION

A. *Substrate growth by TSSG and epitaxial growth by LPE*

RTP melts incongruently, and it cannot be grown directly from the melt, then high temperature solution growth and hydrothermal methods have been used traditionally to grow these crystals [16]. In this work, the top-seeded solution growth-slow cooling (TSSG-SC) technique was applied to grow RTP single crystals to be used for substrates [17]. All growth experiments were performed in a vertical tubular single-zone furnace. The solution composition was chosen taking into account the RTP primary crystallization region in solutions with 20 mol% WO_3 [18]. The solution composition used was Rb_2O-P_2O_5-TiO_2-WO_3=44.24-18.96-16.8-20 (mol %). Solutions weighing around 200 g were prepared by mixing Rb_2CO_3 (99%), $NH_4H_2PO_4$ (99%), TiO_2 (99%) and WO_3 (99%). The solution was homogenized at a temperature around 50 K above the expected saturation temperature for a few hours. The saturation temperature was determined with a ***c***-oriented RTP seed crystal in contact with the center of the solution surface and rotating at 60 rpm. For this solution, the saturation temperature was around 1163 K. After that, the supersaturation of the solution was obtained by applying slow cooling to the solution at a rate of 0.1 K/h for the first 15 K and then 0.05 K/h for the next 10-20 K. The crystal rotation was 60 rpm in the initial steps of growth and as the crystal was growing, the rotation was decreased progressively to 40 rpm in order to maintain the convection pattern. In several experiments, when the crystal dimension in the (001) plane was enough, a pulling rate of 1 mm per day was applied in order to increase the crystal dimension along the ***c*** direction. When the crystal was fully grown, it was slowly extracted from the solution and maintained slightly above the solution surface whereas the furnace was cooled at 30-40 K/h to room temperature. Finally, the substrates for LPE growth were obtained by cutting, with a diamond saw, the bulk crystals in slices perpendicular to the crystallographic ***c*** direction. After cutting, the substrates were polished with diamond powder.

The liquid phase epitaxy (LPE) technique was used to obtain (Yb,Nb):RTP/RTP(001) epitaxial layers [19]. The experiments were carried out in a well-isolated vertical cylindrical furnace, with a central region with practically no thermal gradients.

The solution composition used in these LPE experiments was Rb_2O-P_2O_5-TiO_2-Nb_2O_5-Yb_2O_3-WO_3=43.9-23.6-20.7-0.45-1.35-10 (mol %). The reagents used were the same as in the growth of substrates and Yb_2O_3 (99.9 %) and Nb_2O_5 (99.9 %) were used for doping. Cylindrical crucibles of 25 cm^3 were filled with about 95 g of solution. After homogenizing the solution, its saturation temperature was accurately determined in a similar way to that described above for single crystal growth. For this solution composition, the saturation temperature was around 1145 K. The (001) RTP substrates were first cleaned by using a mixture of HNO_3/H_2O in the 50/50 ratio in volume for 5 min, followed by dipping in distilled water (5 min), then in acetone (5 min), and finally in ethanol (5 min). The entire cleaning process was carried out with the substrates rotating at 60 rpm. After that, the substrates were slowly introduced into the furnace using a stepper motor drive to avoid thermal shocks. This process can take 10-12 h depending on the selected speed of motor. Before dipping the substrate into the solution, it was maintained at a few mm above the surface of the solution for at least 1 h in order to obtain thermal equilibrium between the solution and the substrate. Then the substrate was dipped into the solution at a temperature of 1 K above the saturation temperature for 5 min in order to dissolve the outer layer of the substrate. The epitaxial growth was carried out on the RTP substrate at a temperature 3 K below the saturation temperature for 3 h, with the substrate rotating at 60 rpm. After the epitaxial growth process, the sample was withdrawn very slowly from the solution and held a few mm above the solution, whereas the furnace was cooled down to room temperature at a rate of 25 K/h, to avoid thermal shock.

RTP single crystals were obtained by the TSSG-SC technique with dimensions around 16 mm x 20 mm x 15 mm along the crystallographic ***a***, ***b*** and ***c*** directions, respectively. These crystals were transparent, without macroscopic defects and with well-defined morphology, as can be seen in Fig. 1a. After obtaining these crystals, several (001)-oriented substrates were cut and polished, resulting in an average roughness of 15 nm.

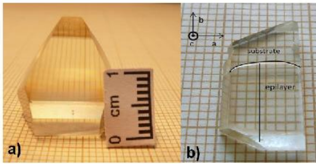

Fig. 1. (a) RTP single crystal, (b) As-grown (Yb,Nb):RTP/RTP epitaxial layer

0733-8724 © 2015 IEEE. Personal use is permitted, but republication/redistribution requires IEEE permission. See http:// www.ieee.org/publications_standards/publications/rights/index.html for more information.

This article has been accepted for publication in a future issue of this journal, but has not been fully edited. Content may change prior to final publication. Citation imformation:DOI 10.1109/JLT.2014.2379091, Journal of Lightwave Technology

The growth rate of the epitaxial layers, after creating a supersaturation by keeping the growth temperature to 3 K below the saturation temperature, was around 0.3 µm/min. The epitaxial layers were polished down to 5 µm thickness after the growth, in order to achieve single mode guiding. A 9-mm-long epitaxial layer grown on a RTP(001) substrate, polished to 5-10 µm thicknesses, is shown in Fig. 1b. In the polished epitaxial layers, the obtained surface roughness was around 5 nm.

B. Pattern design and simulation

The design of the patterns is shown in Fig. 2. A balanced single mode MZI design without any geometrical path length difference between the two arms and with two identical symmetric Y-structures, in which one acts as a splitter and one as a combiner, is shown in Fig. 2.a. Fig. 2.b shows a Y-structure with similar design parameters to act only as a splitter. We have designed MZIs and Y-splitters of length 9 mm with radius of curvature ranging from 50 to 80 mm. It was expected that the Y-junction design, based on an S-line pattern, would give low losses and a large enough separation between the two arms so that there is no evanescent coupling between the branches. It was also expected to give the maximum length in the branches for future applications as an electro-optical modulator. To ensure single-mode behavior of the MZI and Y-splitters at the selected wavelength, the core width and height of the waveguides must be limited depending on the refractive contrast Δn between the waveguide core and the substrate.

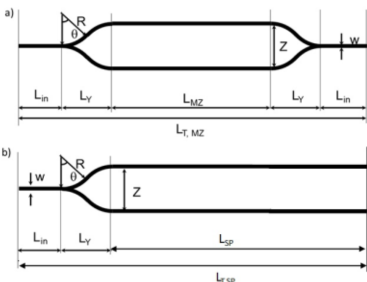

Fig. 2. (a) MZI and (b) Y-splitter design

The guiding properties of the MZIs and Y-splitters were modelled with RsoftBeamPro [20] at a wavelength of 1.5 µm. The dimensions of the designed structures are channels with a width from 6 to 9 µm, and 5 µm in depth. These dimensions were chosen in order to support a fundamental guided optical mode at a wavelength of 1.5 µm. The parameters of the designs are given in Table I.

TABLE I
Parameters of the design

MZI	**Dimensions [µm]**	**Y-splitter**	**Dimensions [µm]**
L_{in}	1000	L_{in}	1000
L_Y	2000	L_Y	2000
L_{MZ}	3000	L_{SP}	6000
w	6	w	6
$L_{T,MZ}$	9000	$L_{T,SP}$	9000
Z	38-42	Z	38-42
R	50,000-80,000	R	50,000-80,000

C. *Sample preparation prior to reactive ion etching procedure*

Prior to fabrication of waveguides by RIE, the RTP samples were clamped on a glass substrate using Unibond power epoxy resin. This step is necessary due to the relatively small size of the samples, which makes it difficult to handle them in spin coating and photolithography processes and reduces the edge bending effect. The curing time of epoxy was around 6-7 h and it allowed heating to 423 K without detachment from the glass. Finally, the sample was cleaned with acetone and iso-propanol using a sonicator.

In order to obtain deep etching, it is necessary to use a highly selective metal mask. We have evaluated Ti, Ni, Al and Cr metals as possible candidates for the metal masks. Metal layer deposition was performed by E-beam evaporation and sputtering techniques. Metal surfaces were evaluated by a molecular imaging atomic force microscope (AFM), model Pico SPM II, without any previous sample preparation, using acoustic mode at a resonance frequency of 75 KHz and a silicon tip of 10 nm radius. The topography and surface roughnesses of the deposited metal layers, analysed by AFM, are shown in Fig. 3. Surface roughness *rms* values calculated with the help of WSxM software were 2.8 nm, 2.6 nm, 150 nm and 100 nm for Ti, Ni, Al and Cr layers, respectively. As observed, for the case of Ti and Ni there are almost flat layers, but in the case of Al and Cr, the layers are composed of grains; which are larger for Al. The presence of these grains leads to the higher value of roughness for Al and Cr layers.

In order to analyze the adhesion and durability of the metal layers on the RTP surface, we performed a tape test five times each to check the adhesion. The Ti layer was completely or partially removed during the first attempt, as can be seen in Fig. 3. In the case of Ni, in the first attempt only significant parts of the Ni layer were removed but in second attempt, Ni was removed as can be observed in Fig. 3. A scratch test was also performed on the Ni layer but didn't show any significant influence on the adhesion. Finally, in the case of Al and Cr there was not observed removal of

0733-8724 © 2015 IEEE. Personal use is permitted, but republication/redistribution requires IEEE permission. See http:// www.ieee.org/publications_standards/publications/rights/index.html for more information.

This article has been accepted for publication in a future issue of this journal, but has not been fully edited. Content may change prior to final publication. Citation imformation:DOI 10.1109/JLT.2014.2379091, Journal of Lightwave Technology

the metal during the tape tests. The scratch test on Al and Cr layers showed a good adhesion in both cases.

Thus the results indicate that Al and Cr are good candidates to be used for metal mask. In order to create a metal mask for the RIE process, the chromium was etched with MS8 chrome chemical etchant and the aluminum was etched with commercially available aluminum enchant.

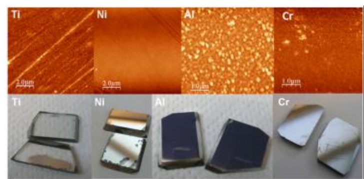

Fig 3. AFM images of the different metal layers and the results of adhesion test

A thin layer of photoresist S1813 was then deposited on the metal layer by spin coating at 5000 rpm for 60 s, obtaining photoresist thicknesses of around 1.3 µm. The samples were then soft baked at 363 K for 30 min.

Y-splitter and MZI patterns were transferred to the photoresist layer using a light field hard mask pattern for the epitaxial layers and a dark field hard mask pattern for the substrates, by standard UV photolithography. The samples with the photoresist and metal layers were carefully aligned with the mask pattern in such a way that the branches of the MZI and 30 m at 393 K.All fabrication steps are illustrated in Fig. 4.

D. Reactive ion etching

The samples containing hard metal mask were etched in an RIE Plasmalab 80Plus, with the etching parameters: 250 W as the RF power, 40 mTorr of pressure and a gas combination of Ar (10 sccm) and SF_6 (10 sccm), which corresponds to parameters optimized in our previous work [15]. A preliminary test was performed to determine the etch rates in (Yb,Nb):RTP, undoped RTP, the metal layers and the photoresist using the etching conditions described above. The samples were etched for 60 min and the etch rates obtained are summarized in Table II.

TABLE II
RIE etch rates

	Etch rate [nm/min]
RTP	10.5
(Yb,Nb):RTP	15.5
PR S1813	36.6
Chromium	0.53
Aluminum	2

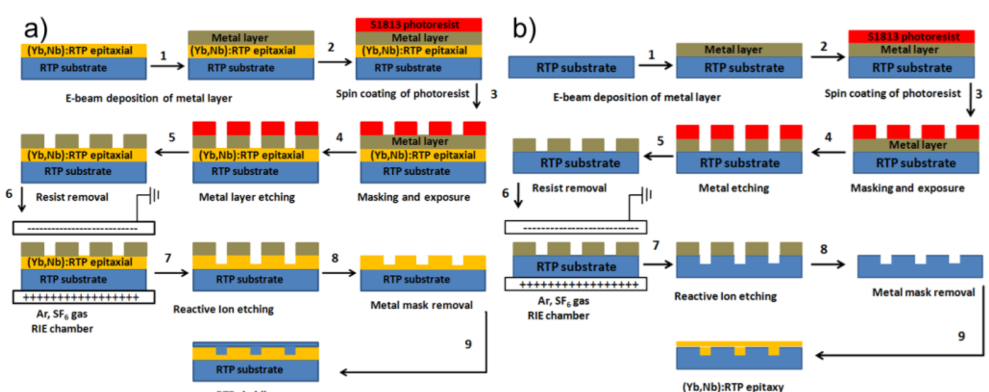

Fig. 4. Steps involved in the fabrication process of the rib waveguides (a) in a (Yb,Nb):RTP epitaxial layer (b) in a RTP substrate.

Y-splitters were parallel to the ***a*** crystallographic direction. A SussMicrotec MA6 mask-aligner was used to expose the samples for 10-12 s at 350 mW/cm^2, using 365-nm-wavelength light. After the exposure, the photoresist was developed by dipping for 45 s in MF-319 developer. Finally, hard baking was performed for

The selectivity (the ratio of the etch rate of RTP compared to the etch rate of the photoresist) for RTP compounds against the photoresist is around 3. This means that it would require a thickness of photoresist around 20 µm to etch 6 µm in RTP, so it is not possible to obtain a smooth and homogeneous thick layer using

0733-8724 © 2015 IEEE. Personal use is permitted, but republication/redistribution requires IEEE permission. See http:// www.ieee.org/publications_standards/publications/rights/index.html for more information.

This article has been accepted for publication in a future issue of this journal, but has not been fully edited. Content may change prior to final publication. Citation imformation:DOI 10.1109/JLT.2014.2379091, Journal of Lightwave Technology

TABLE III
Parameters obtained for the etched designs

Sample	Compound	M	t_{epi}[μm]	t [min]	w_{exp} [μm]	w_r [μm]	d [μm]	Etch rate [nm/min]
Sample 1	(Yb,Nb):RTP	Cr	3.2	213	4	-	1.8	8.2
					6	-		
Sample 2	(Yb,Nb):RTP	Cr	8.8	387	4	7.5-10	2.6	6.7
					6			
Sample 3	(Yb,Nb):RTP	Cr	5	333	5	-	2.8	8.4
					7	-		
Sample 4	(Yb,Nb):RTP	Cr	5	333	4	-	2.9	8.7
					6	-		
Sample 5	(Yb,Nb):RTP	Al	5	624	7	-	2.5	4.0
Sample 6	RTP	Al	-	480	5	13-15	2.5-3.5	6.2
					7			
Sample 7	RTP	Al	-	810	5	-	2.6	3.2
					7			

M= metal, t_{epi} = epitaxial layer thickness, t = etching time, w_{exp} = expected width, w_r = real width and d = etching depth

specifically this photoresist eliminating the possibility of working with this photoresist as a mask.

The selectivity for RTP against Cr was found to be 20 and the selectivity for (Yb,Nb):RTP against Cr was found to be 29. For Al, the selectivity against RTP was 5 and against (Yb,Nb):RTP was 7.8. It has previously been reported [21] that Al masks used in RIE processes using SF_6/O_2 gases show the effect of micromasking if the etched matter from the mask is not properly evacuated and is instead deposited the formed Al_2O_3 on exposed surfaces. Using SF_6, we can also create the AlF volatile species and the AlF_3 as non-volatile species, which can originate also the micromasking.

Table III summarizes all the RIE experiments performed with the different experimental parameters. Extended topography measurements of the channels were performed using a Sensofar PLμ 2300 confocal microscope. The confocal microscope was also used to measure the epitaxial thicknesses. The plasma etching involves two dominant etch mechanisms: physical and chemical. The physical mechanism is the high-energy ion bombardment that erodes the material and the chemical mechanism is the formation of volatile species from reactions on the material surface with the species from the plasma. We expect the volatile species to be TiF_4 (Temperature of sublimation 557 K), PF_3 (Boiling point 172 K), NbF_5 (Boiling point 502 K) and PF_5 (Boiling point 198 K) [22]. As mentioned above, the RIE process employed 250 W RF power, 40 mTorr pressure and gas combination of Ar (10 sccm) and SF_6 (10 sccm).

In Fig. 5, we can observe the etch rate obtained in undoped RTP and (Yb,Nb):RTP in relation to the etching time used. As can be seen in Table III, the average etch rate obtained is in the range of 3.2 to 8.7 nm/min; this etch rate is larger than previously reported for standard RIE of $LiNbO_3$ (around 4 nm/min) [23], although we note that the etching rate of $LiNbO_3$ can be increased after proton exchange to values of 10 nm/min [24]. It can be observed that in the case of short etching times, there is a linear reduction in the etching rate with the time. The potential causes of the low etch rate include too high a pressure of the etching gases, increasing the number of collisions in the gas and a decreasing the number of reactive species reaching the surface and another possible reason, could be an increase of the chemical etching, leading to the formation of sub-products acting as inhibitors on the surface of the etch material, blocking the etching process. Furthermore, in the case of long etching times, there is a significant decrease of the etching rate, both for undoped RTP and (Yb,Nb):RTP. This could be related to the fact that at long etching times, the etching was not only in vertical direction but also in the plane of the sample.

0733-8724 © 2015 IEEE. Personal use is permitted, but republication/redistribution requires IEEE permission. See http:// www.ieee.org/publications_standards/publications/rights/index.html for more information.

This article has been accepted for publication in a future issue of this journal, but has not been fully edited. Content may change prior to final publication. Citation imformation:DOI 10.1109/JLT.2014.2379091, Journal of Lightwave Technology

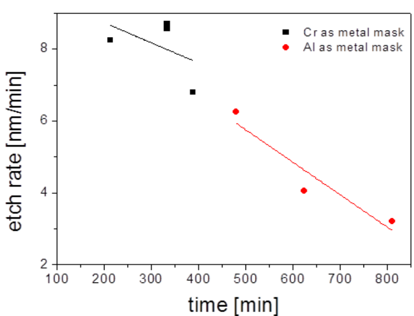

Fig. 5. Etching rate in undoped RTP and (Yb,Nb):RTP versus etching time.

According to Ren *et al.* [11], during RIE etching using gases such as SF_6, CHF_3, etc, gas components could penetrate into the sample, in our case to form bonds with the RTP sample. In order to detect any contamination of the sample by these gases, we have conducted an EDAX test using a FEI Quanta 600 equipment, with an acceleration voltage of 20 kV at a working distance of 10 mm. Sample 7 in Table III was examined for the detection of Al, Cr, Rb, Ti, O, P, S, F and Ar. Fig. 6 shows an ESEM image of this sample image of this sample and the energy dispersive X-ray spectroscopy result where it can be observed that only the peaks of the constituent elements of the sample have been observed. There was no detected presence of any element originating from the gases (S, F, and Ar) or from the hard mask (Al).

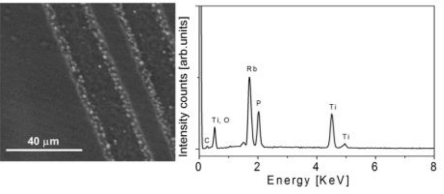

Fig. 6. Energy dispersive X-Ray spectroscopy of etched RTP sample using Al mask (sample 7).

The dimensions of the fabricated structures were evaluated by confocal interferometry, and the results are given in Table III. Width and depth were measured for every device (MZI and Y-splitter). The actual width was observed using an ESEM in sample 2 and sample 6. It is observed that the width of the structures is always larger than expected, especially in the case of the Al mask. In order to elucidate the reason for these results, different photoresist exposure times on the different metal layers were investigated. It was observed that longer exposure times lead to a larger broadening of the channels for the Al mask than in the case of Cr. It can be deduced that Al required less exposure time in order to obtain the desired width of the channels in the photoresist and this can be related to the larger reflectivity (R) of the Al versus Cr in the UV region (R of Al is 92% and R of Cr is 51%). The broadening of the channels obtained in the case of an Al mask could also be due to the fact that, as shown in Table II, the etching rate of Al is larger than for Cr. Therefore, in the case of long etching times, the Al layer could be totally removed, causing etching of the RTP material to take place along the plane as well as perpendicular to the surface.

The surface topography of the rib waveguide for sample 2, measured with confocal microscope, is shown in Fig. 7.a. The epitaxial layer roughness before etching was measured to be around 5 nm and after reactive ion etching it was around 15 nm. After the fabrication process, the samples were examined by environmental scanning electron microscopy (ESEM) with a FEI Quanta 600, with an acceleration voltage of 20 kV at a working distance of 10 mm. An ESEM image of the set of 9-mm-long MZIs fabricated on the (Yb,Nb):RTP deposited on RTP (sample 2) is shown in Fig. 7.b. It can be seen that rather homogenous etching is obtained along the full length of the MZI interferometers.

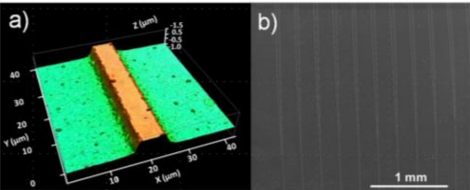

Fig. 7. (a) Surface topography of the rib waveguide obtained in (Yb,Nb):RTP (sample 2) measured with confocal microscope, (b) ESEM image of the top view of (Yb,Nb):RTP (sample 2) etched with RIE with a power 250 W and SF_6 10 sccm, Ar 10 sccm and pressure 40 mTorr.

E. Cladding layer growth

A cladding layer of 200-400 µm thickness of RTP was grown on the channels in order to have centered the mode vertically on the active core region. The cladding would also serve as a protective material, and as demonstrated below by reducing the roughness of the core, it lowers the propagation losses. This cladding layer was grown by following the same procedure as used for the epitaxial layer.

In Fig. 8, an ESEM image of the cross section of an RIE channel realized in a (Yb,Nb):RTP/RTP epitaxial layer (sample 2) is shown. A cladding layer of undoped RTP was also grown on the (Yb,Nb):RTP etched layer. After etching for 387 min, an etch depth of around 2.6 µm in an 8.8-µm-thick epitaxial layer is obtained. As can be observed in Fig. 8, the slab height is around 6 µm with a rib height of 2.6 µm. The channel width is 7.3 µm at the base, making a trapezoid with an angle of 30°. As in the previous case, no visible defects are observed in the interface between the active layer and the cladding.

0733-8724 © 2015 IEEE. Personal use is permitted, but republication/redistribution requires IEEE permission. See http:// www.ieee.org/publications_standards/publications/rights/index.html for more information.

This article has been accepted for publication in a future issue of this journal, but has not been fully edited. Content may change prior to final publication. Citation imformation:DOI 10.1109/JLT.2014.2379091, Journal of Lightwave Technology

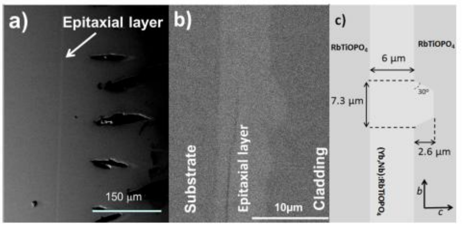

Fig. 8. (a) ESEM image of the general view of the cross section of RIE etched (Yb,Nb):RTP layers and RTP cladding grown also by LPE, (b) ESEM image of the detail of the cross section of RIE etched (Yb,Nb):RTP layers and RTP cladding grown also by LPE. (c) Crosee sectional dimensions of the Fig. 8(b).

In Fig. 9, we can observe a cross-sectional ESEM image of a channel fabricated by RIE in a RTP substrate (sample 6), using an Al mask with structures of 7 µm width. The etching time was 480 min and the etch depth obtained was around 2.5-3.5 µm. The next step was the growth of an (Yb,Nb):RTP layer by LPE. In this case, the solution composition for the layer growth was the same as that used for the epitaxial layer growth and the growth time was 2 h. The supersaturation of the solution was obtained by decreasing the solution temperature to 4 K below the saturation temperature. After another polishing step, a cladding layer of undoped RTP was also grown. Fig. 9 shows that ribs with trapezoidal cross sections were obtained and that there are no appreciable defects at both interfaces, between the epitaxial layer and the RIE etched substrate and between the cladding and the epitaxial layer. The bottom of the channels is found to be approximately 13-15 µm in width, while the channels height is 2.5-3.5 µm and the side wall angle is around 20-30º.

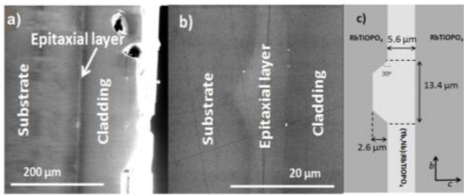

Fig. 9. (a) ESEM image of the general view of the cross section of RIE channels on RTP filled by (Yb,Nb):RTP by LPE and RTP cladding grown also by LPE. (b) ESEM image of the detail the cross section of a RIE channel on RTP filled by (Yb,Nb):RTP by LPE and RTP cladding grown also by LPE. (c) Cross sectional dimensions of the channel of Fig.9 b.

III. OPTICAL CHARACTERIZATION OF THE WAVEGUIDES

Refractive index values at room temperature were measured in undoped RTP and in (Yb,Nb):RTP active layers with a Metricon prism coupler 2010 and a 1.5 µm HeNe laser by the dark mode method. The refractive index difference between the undoped RTP and (Yb,Nb):RTP doped crystals at a wavelength of 1.5 µm were calculated from the refractive index values of undoped RTP acting as a substrate: n_x=1.7559, n_y=1.7630, n_z=1.8375 and (Yb,Nb):RTP acting as an active epitaxial layer n_x=1.7516, n_y=1.7633, n_z=1.8425. Thus, Δn_x=-0.004, Δn_y=0.0003 and Δn_z=0.005 ($\Delta n_i = n_{i,epi} - n_{i,sub}$ being i= x,y and z). The increase of refractive index almost only in the n_z polarization with the presence of Nb in RTP is in agreement with previous works in the literature [25, 26] and in KTP, as well [27], in which was already observed an increase of the birefringence in these crystals (defined as n_z-n_x or n_z-n_y) with the increase of Nb concentration in the crystals (The Yb presence doesn't change this tendency). So, it is important to remark that this refractive index difference allows only guiding in the TM polarization whatever the size of the waveguide but it will be single mode by choosing the appropriate channel waveguide dimensions. Additionally, by using the standard definition for the NA of a fiber (NA = $(n_{core}^2 - n_{crystal}^2)^{1/2}$), the corresponding expected NA is of 0.13.

A vertically polarized (polarization parallel to the Z-axis of the samples) 1.5 µm He-Ne laser with a maximum output power of 1 mW, was coupled into the 9-mm-long devices. The input and output objectives were 5X with 0.10 NA and 20X with 0.40 NA, respectively. The 0.10 NA input objective ensured good NA matching with that expected for the waveguides (~0.13 NA, see below), and also gave a focus spot diameter of ~18 µm (at $1/e^2$ intensity) which matches well with the expected mode field diameters (MFD) of the waveguides. The waveguide mode was excited via careful alignment using an *xyz* translation stage. Near-field mode imaging of the devices was recorded using a FLIR SC7000 IR camera.

Assuming a planar waveguide, the dispersion for a wave propagating along the guide [28], could be calculated using

$$\frac{2\pi}{\lambda}\left(n^2 - n_{eff}^2\right) = m\pi + \phi_{n_a} + \phi_{n_s}$$

where *m* is the mode number, *d* the thickness of the active layer, λ the wavelength of the light in vacuum, in this case 1.5 microns, and n_a and n_s are the air and the substrate refractive indices, respectively, while *n* is the refractive index of the guiding layer, and n_{eff} is the effective refractive index of the propagation mode in the active layer and

$$\phi_{n_j} = arctg\left[\left(\frac{n}{n_j}\right)^{2\rho}\left(\frac{n_{eff}^2 - n_j^2}{n^2 - n_{eff}^2}\right)\right]^2$$

where j = a, s, and ρ = 1 for TM polarization. Next Figure shows the calculated number of modes from these equations for TM polarizations. To confine only one mode for TM polarization we can have a maximum thickness of 8.1 microns (shown in figure 10).

0733-8724 © 2015 IEEE. Personal use is permitted, but republication/redistribution requires IEEE permission. See http:// www.ieee.org/publications_standards/publications/rights/index.html for more information.

This article has been accepted for publication in a future issue of this journal, but has not been fully edited. Content may change prior to final publication. Citation imformation:DOI 10.1109/JLT.2014.2379091, Journal of Lightwave Technology

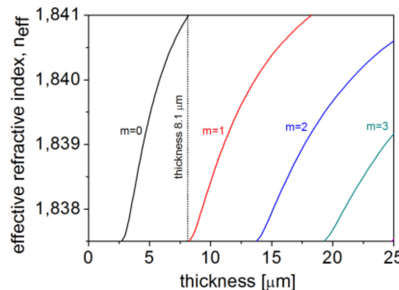

Fig. 10. Propagation modes versus the active layer thickness at 1.5 μm.

Then, going to the 2D waveguides, we use the simulations as a tool to optimize the other dimension, the width of the channel. Figure 11 shows the result of the simulation assuming a rectangular 2D channel, in which the *w* is 6 microns and the *h*, height is 5 microns (X, Y and Z are the optical axis of our samples, being the crystallographic **a**, ***b*** and ***c*** directions, respectively). The first graphic corresponds to the map of refractive index used; the second figure is the confined TM mode and last graphic shows the inexistence of the TE mode with the measured refractive contrast and with these dimensions. Then, the expected TM single–mode conditions, w=6 microns and height 5 microns, with an n_{eff} around 1.839. These conditions of single mode are maintained till a width of 9 microns.

To experimentally characterize the propagation modes, we polished the faces perpendicular to the crystallographic ***a*** direction (X axis), and the light will propagate in this direction. The near field pattern was measured using an IR camera in order to visualize the mode intensity profile at the output of an MZI. Fig. 12.a shows the near-field pattern of the output TM mode guided in a MZI of the sample 2. The horizontal and vertical fundamental TM mode field diameters (MFD) at $1/e^2$ intensity (shown in Figs. 12.c and 12.d, respectively) were measured to be 17.6 μm and 8.3 μm, along the ***b*** (horizontal) and ***c*** (vertical) directions, respectively. Fig. 12.b shows the output TM mode obtained by the simulation. The dimensions of the simulated guided mode are 23.3 μm and 9.6 μm along ***b*** (horizontal) and ***c*** directions (vertical) respectively, and the refractive index contrast used is the one reported above for n_z, 0.005.

A 9-mm-long Y-splitter, fabricated in the sample 2, was also characterized as shown in Fig. 13.a. The Y-splitter is rather well balanced, obtaining an output flux power ratio between the two branches of 0.91. The horizontal and vertical fundamental MFD at $1/e^2$ intensity (shown in Figs. 13.c and 13.d, respectively) were measured to be 19 μm and 16.7 μm (right and left branches, respectively) along the ***b*** direction and 9.6 μm and 9.9 μm (right and left branches, respectively) along the ***c*** direction. The simulation of the modes is plotted in Fig. 13.b. The MFD for the simulated modes were 8.4 μm and 17.6 μm, for the vertical and horizontal directions, respectively. The separation between the centers of two modes emitting from two respective arms is around 36 μm.

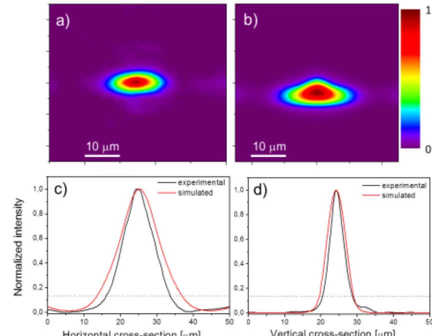

Fig. 12. (a) Near- field TM mode image of the waveguide MZI in the sample 2. (b) Simulated TM mode of the MZI waveguide in the sample 2, (c) Horizontal cross-section of the experimental and simulated TM guided mode, (d) Vertical cross-section of the experimental and simulation TM mode.

We have estimated the total transmission losses corresponding to a single pass transmission as L_T= 10log (P_{out}/P_{in}), where P_{out} is the power measured after the output microscope objective, P_{in} is the power measured before the input microscope objective. In the actual samples fabricated for this work, there are only

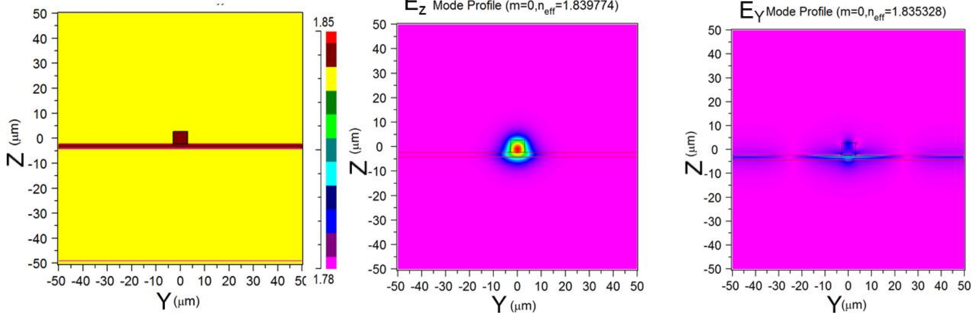

Fig. 11. Simulation of a rectangular 2D cannel, with the w is 6 μm and the h, 5 μm (X,Y,Z are the optical axis of our samples, being the crystallographic *a, b* and *c* directions, respectively). (a) Map of refractive indices, (b) Simulated TM mode, (c) Simulated TE mode.

0733-8724 © 2015 IEEE. Personal use is permitted, but republication/redistribution requires IEEE permission. See http:// www.ieee.org/publications_standards/publications/rights/index.html for more information.

This article has been accepted for publication in a future issue of this journal, but has not been fully edited. Content may change prior to final publication. Citation imformation:DOI 10.1109/JLT.2014.2379091, Journal of Lightwave Technology

MZ and Y-splitter structures as a WGs; so the total transmission losses measured should be the result of the addition of the optical insertion, the Fresnel and the propagation losses; and in the last term, are included the propagation losses of the straight portions of the MZ and the Y-splitter structures (L_{in}, L_{MZ} and L_{SP}) and the propagation losses due to the S-bend and the Y-junction.

The optical insertion losses measured by calculating the $1/e^2$ overlapping between the input laser mode and the output guided mode; are around -1.2 dB for the MZ and -1.5 dB (left output) and -1.2 dB (right output), for the Y-splitter. The Fresnel losses are in both cases around -0.8 dB.

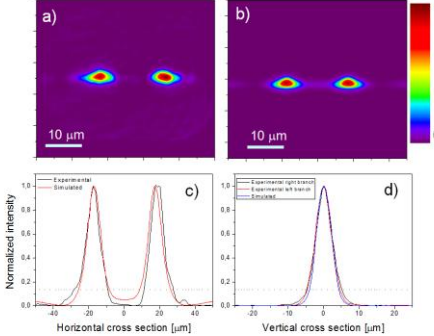

Fig. 13. (a) Near- field TM mode image of a waveguide Y-splitter in the sample 2, (b) Simulated TM mode of the Y-splitter waveguide in the sample 2, (c) Horizontal cross-section of the experimental and simulated guided TM modes, (d) Vertical cross-section of the experimental and simulation TM modes

The measured total transmission losses, L_T, for the MZ were 8.75 dB. Accounting for the insertion losses (1.2 dB) and the Fresnel losses (0.8 dB) we can approximate the propagation losses as 6.7 dB, including the bending and Y-junction losses. For the Y-splitter, a measurement of the total transmission losses, gives us 7.08 dB, making a similar calculation, the total propagation losses (including bending and Y-junction) are around 4.9 dB (assuming 0.9 cm length, they are 5.4 dB/cm). These values are in agreement with the previous reported values, published by Choudhary *et al.* [15], in channel WGs fabricated also by RIE, in which the transmission losses were around >3.5 dB/cm at 980 nm.

IV. CONCLUSIONS

Mach-Zehnder interferometer and Y-splitter structures have been successfully fabricated on RTP (001)-oriented substrates and (Yb,Nb):RTP/RTP (001) epitaxial layers using reactive ion etching. When RTP (001)-oriented substrates were used, an (Yb,Nb):RTP epitaxial layer was grown over the structures made by RIE and finally in both cases, a RTP cladding layer was grown by liquid phase epitaxy in order have the same contrast in the refractive indices in the two interfaces. The Cr and Al layer adhesion to RTP was suitable for transferring the structures from the commercial hard mask to the metal mask in contact with the crystal, before the RIE process was carried out. An etch depth of 2.9 µm with a maximum etching rate of 8.7 nm/min was obtained. The ribs were trapezoidal in shape with a roughness of about 15 nm. Optical waveguiding in the different fabricated structures at a wavelength of 1.5 µm has been demonstrated and characterized.

References

[1] P. A. Thomas, S. C. Mayo, and B. E. Watts, "Crystal structures of $RbTiOAsO_4$, $KTiO(P_{0.58},As_{0.42})O_4$, $RbTiOPO_4$ and $(Rb_{0.465},K_{0.535})TiOPO_4$, and analysis of pseudosymmetry in crystals of the $KTiOPO_4$ family," *Acta Cryst. B,* vol. 48, pp. 401-407, 1992.

[2] M. V. Pack, D. J. Armstrong, and A. V. Smith, "Measurement of the $X^{(2)}$ tensors of $KTiOPO_4$, $KTiOAsO_4$, $RbTiOPO_4$, and $RbTiOAsO_4$ crystals," *Appl. Opt.*, vol. 43, pp. 3319-3323, 2004.

[3] M. N. Satyanarayan, A. Deepthy, and H. L. Bhat, "Potassium titanyl phosphate and its isomorphs: growth, properties, and applications," *Crit. Rev. Solid State Mater. Sci*, vol. 24, pp. 103-191, 1999.

[4] W. P. Risk, "Fabrication and characterization of planar Ion-exchanged $KTiOPO_4$ waveguides for frequency doubling," *Appl. Phys. Lett.*, vol. 58, pp. 19-21, 1991.

[5] L. L. Wang, L. Wang, K. Wang, Q. Lu and H. Ma, "Annealing effect on mono-mode refractive index enhanced $RbTiOPO_4$ waveguides formed by ion implantation," *Opt. Express*, vol. 17, pp. 5069-5074, 2009.

[6] J. Jiao, K. M. Wang, X. L. Wang, F. Chen, L. Wang, L. Wang, Q. M. Lu, H. J. Ma, and R. Nie, "Optical waveguides formed in $RbTiOPO_4$ crystal by 6.0 MeV O^{3+} implantation," *Chin. Phys. Lett.*, vol. 23, pp. 3327-3330, 2006.

[7] J. Cugat, R. Solé, M. C. Pujol, J. J. Carvajal, X. Mateos, F. Díaz, and M. Aguiló,"Waveguiding demonstration on $Yb:Nb:RbTiOPO_4/RbTiOPO_4(001)$ epitaxies grown by LPE," *Opt. Mater.*, vol. 32, pp. 1648-1651, 2010.

[8] L. B. Zhou, F. G. Luo, and M. C. Cao, "Study of the plasma etching process for low-loss SiO_2/ Si optical waveguides," *Thin Solid Films*, vol. 489, pp. 229-234, 2005.

[9] C. Dubs, J. P. Ruske, J. Kräuβlich, and A. Tünnermann, "Rib waveguides based on Zn-Substituted $LiNbO_3$ films grown by liquid phase epitaxy," *Opt. Mater.*, vol. 31, pp. 1650-1657, 2009.

[10] G. Ulliac, N. Courjal, H. M. H. Chong, and R. M. De La Rue, "Batch process for the fabrication of $LiNbO_3$ photonic crystals using proton exchange followed by CHF_3 reactive ion etching," *Opt. Mater.*, vol. 31, pp. 196-200, 2008.

[11] Z. Ren, P. J. Heard, J. M. Marshall, P. A. Thomas, and S. Yu, "Etching characteristics of $LiNbO_3$ in reactive ion etching and inductively coupled plasma," *J. Appl. Phys.*, vol.103, pp. 034109, 2008.

[12] C. Dubs, M. Morgenroth, B. Zeitner, J-P. Ruske, U. Grusemann, J. Delith, Chr. Schmidt, and. A. Tünermann, "Channel waveguides based on epitaxial grown $K_{1-x}Rb_xTiOPO_4$ LPE films," *Zeitschrift fúr kristallographie*, Issue No. 21, pp.189. 2004.

[13] M. Roth, "Stoichiometry and Domain Structure of KTP/Type Nonlinear Optical Crystals," in Handbook of Crystal Growth, Chapter 20, Springer Berlin Heidelberg, 2010, pp. 691-723.

0733-8724 © 2015 IEEE. Personal use is permitted, but republication/redistribution requires IEEE permission. See http:// www.ieee.org/publications_standards/publications/rights/index.html for more information.

This article has been accepted for publication in a future issue of this journal, but has not been fully edited. Content may change prior to final publication. Citation imformation:DOI 10.1109/JLT.2014.2379091, Journal of Lightwave Technology

[14] J. J. Carvajal, J. L. García-Muñoz, R. Solé, Jna. Gavaldà, J. Massons, X. Solans, F. Díaz, and M. Aguiló, “Charge Self-compensation in the Nonlinear Optical Crystals $Rb_{0.855}Ti_{0.955}Nb_{0.045}OPO_4$ and $RbTi_{0.927}Nb_{0.056}Er_{0.017}OPO_4$,” *Chem. Mater*., vol. 15, pp. 2338-2345, 2003.

[15] A. Choudhary, J. Cugat, K. Pradeesh, R. Solé, F. Díaz, M. Aguiló, H. M. H. Chong, and D. P. Shepherd, “Single-mode rib waveguides in (Yb,Nb):$RbTiOPO_4$ by reactive ion etching,” *J. Phys. D*, vol. 46, pp. 145108, 2013.

[16] J. J. Carvajal, M. C. Pujol, and F. Díaz, “High Temperature Solution Growth: Application to laser and Nonlinear Optical Crystals” in *Handbook of Crystal Growth*, Chapter 21, Springer Berlin Heidelberg, 2010, pp. 725-752.

[17] J. J. Carvajal, V. Nikolov, R. Solé, Jna. Gavaldà, J. Massons, M. Aguiló, and F. Díaz, “Crystallization Region, Crystal Growth, and Characterization of Rubidium Titanyl Phosphate Codoped with Niobium and Lanthanide Ions,” *Chem. Mater.*, vol.14, pp. 3136-3142, 2002.

[18] J. J. Carvajal, V. Nikolov, R. Solé, Jna. Gavaldà, J. Massons, M. Rico, C. Zaldo, M. Aguiló, and F. Díaz, “Enhancement of the Erbium Concentration in $RbTiOPO_4$ by Codoping with Niobium,” *Chem. Mater*., vol.13, pp.3171-3080, 2000.

[19] J. Cugat, R. Solé, J. J. Carvajal, M. C. Pujol, X. Mateos, F. Díaz, and M. Aguiló, “Crystal growth and characterization of $RbTi_{1-x-y}$/ $RbTiOPO_4$(001) non-linear optical epitaxial layers,” *CrystEngComm.*, vol.13, pp. 2015-2022, 2011.

[20] RsoftBeamPROP software, Synopsys Optical solutions, v2013.12.

[21] M. Lazar, H. Vang, P. Brosselard, C. Raynaud, P. Cremillieu, J.-L. Leclercq, A. Descamps, S. Scharnholz, and D. Planson, “Deep SiC Etching with RIE,” *Superlattices and Microst,* vol. 40, pp. 388-392, 2006.

[22] M. Köhler, “Etching in Microsystem technology”, Weinheim; New York; Chichester; Brisbane; Singapore; Toronto, Wiley-VCH, 1999.

[23] S. Winnall, and S. Winderbaum, “Lithium Niobate Reactive Ion Etching”, DSTO-TN-0291, DSTO Electronics and Surveillance Research Laboratory, Salisbury South Australia, 2000.

[24] H. Hu, A. P. Milenin, and R. B. Wehrspohn, H. Hermann, W. Sohler, “Plasma etching of proton-exchanged lithium niobate,” *J. Vac. Sci. Technol. A,* vol. 24, pp. 1012-1015, 2006.

[25] J. J. Carvajal, R. Solé, Jna. Gavaldà, J. Massons, M. Rico, C. Zaldo, M. Aguiló and F. Díaz, “Growth and characterization of $RbTiOPO_4$:Nb crystals as a host for rare earth ions”, *J. Alloy. Compd.,* vol. 323-324, pp. 231-235, 2001.

[26] A. Peña, “Ytterbium and erbium doped $RbTi_{1-x}M_xOPO_4$ (M = Nb or Ta) crystals. New laser and nonlinear bifunctional materials,” Ph. D. dissertation, Dept. Phys. Chem. And Inorg., Rovira i Virgili Univ., Tarragona, Spain, 2007.

[27] L. T. Cheng, L. K. Cheng, R. L. Harlow and J. D. Bierlein, “Blue light generation using bulk single crystals of niobium-doped $KTiOPO_4$,” *Appl. Phys. Lett.*, vol. 64, 155-157, 1994.

[28] P. K. Tien and R. Ulrich, “Theory of Prism-coupled and thin-film light guides,” *J. Opt. Soc. Am.*, Vol. 60, pp. 1325-1337,1970.

0733-8724 © 2015 IEEE. Personal use is permitted, but republication/redistribution requires IEEE permission. See http:// www.ieee.org/publications_standards/publications/rights/index.html for more information.

Paper III

"Channel waveguides in $RbTiOPO_4$ crystals produced by Induced Coupled Plasma-Reactive Ion Etching"

M. A. Butt, M. C. Pujol, R. Solé, A. Ródenas, G. Lifante, M. Aguiló, and F. Díaz.

To be submitted to Journal of Lightwave Technology, 2015

Channel waveguide fabrication in $RbTiOPO_4$ planar waveguides by structuring the cladding layer with Induced Coupled Plasma-Reactive Ion etching

M. A. Butt[1], M.C. Pujol[1], R. Solé[1], A. Ródenas[1], G. Lifante[2], M. Aguiló[1] and F. Díaz[1]

Abstract—**Induced Coupled Plasma-Reactive Ion etching has been used to produce the ridge waveguides in $RbTiOPO_4$ crystals. A thin epitaxial layer of doped with Yb^{3+} and Nb^{5+} was grown on the $RbTiOPO_4$ (001) crystallographically oriented substrate to act as a core and an additional layer of RTP was grown over to act as cladding. The cladding layer was structured by using an ICP-RIE process. The guiding was produced by the lateral confinement of the light achieved by a local increase of the effective refractive index of the planar waveguide. The propagating mode was confined in the region far from the lateral walls of the ridge, thus avoiding the losses that could arise from the roughness of the etched walls.**

***Index Terms*—Integrated Optical Materials, $RbTiOPO_4$, Inductively coupled plasma-Reactive Ion Etching, optical waves.**

I. INTRODUCTION

The term integrated optics was first proposed by S. E. Miller [1] in 1960 in order to emphasize the similarity between planar optical circuits technology and the well-established integrated micro-electronic circuits. Miller proposed that various active as well as passive elements can be fabricated on a single platform (substrate) combining and interconnecting them with the help of waveguides. The integration of multiple optical devices on a single platform can clearly reduce the cost of advanced optical systems. Therefore different fabrication techniques were proposed to fabricate waveguides mainly in silicon wafers, and also in semiconductor materials. However, dielectric based photonic platforms are also an interesting alternative for integrated optics devices [2].

This work was supported by the Spanish Government under the Project MAT2013-47395-C4-4-R, by the Catalan Authority under Project 2014SGR1358. M. Ali Butt thanks the Catalan Government for the FI-DGR fellowship 2012FI-B 00192. A.

M. A. Butt, , R. Solé, M. C. Pujol, A. Ródenas, M. Aguiló and F. Díaz are with Física i Cristal·lografia de Materials i Nanomaterials (FiCMA-FiCNA) and EMaS, Universitat Rovira i Virgili (URV), Marcel·lí Domingo s/n, E-43007 Tarragona, Spain (email authors: muhammadali.butt@urv.cat, rosam.sole@urv.cat, mariacinta.pujol@urv.cat, airan.rodenas@urv.cat, magdalena.aguiló@urv.cat and f.diaz@urv.cat).

G. Lifante is with the Departamento de Física de Materiales, Universidad Autónoma de Madrid E-28049 Madrid, Spain (email author: gines.lifante@uam.es).

Rubidium titanyl phosphate, $RbTiOPO_4$ (RTP), belongs to the non-centrosymmetric space group $Pna2_1$ with unit cell parameters of a= 12.974(2) Å, b= 6.494(3) Å, c= 10.564(6) Å [3]. RTP is a biaxial optical crystal which has high nonlinear optical and electro-optical coefficients [4]; these last ones are in the same order than for $LiNbO_3$. RTP is isostructural to the well-known $KTiOPO_4$ (KTP). It although less often used, but it has attracted a great attention as a NLO material. RTP can be considered as an interesting alternative to KTP for phase matched interactions, because its optical damage threshold is around 2 times larger than that of KTP which makes it useful in high power SHG and OPO applications [4,5]. While it has similar nonlinear optical coefficients [6].

Rib waveguides fabricated on (Yb,Nb):RTP by using Ar^+ ion milling technique showed good optical confinement and generation of green light by type II second harmonic generation [7]. The fabrication of Single mode rib waveguides was demonstrated for the first time in (Yb,Nb):$RbTiOPO_4$ by using reactive ion etching technique by A. Choudhary *et al.* [8]. Plasma etching is relatively new techniques in the fabrication of integrated circuits. It was introduced in the seventies, mainly for stripping resists. In the eighties, plasma etching became a mature technique to etch layers and was introduced in the production of integrated circuits. Reactive ion etching was the main technology, but new techniques were developed. In the nineties new techniques, such as electron cyclotron resonance (ECR) and inductively coupled plasmas (ICP) were introduced, with mixed success. The use of plasma etching is widespread in the industry, but contrary to other techniques (e.g lithography), the theoretical understanding of the different mechanisms involved in plasma etching is still very poor.

In this work a fabrication technique combining liquid phase epitaxy (LPE) and ICP-RIE is presented to develop controllable loss channel waveguides in RTP crystals. The main idea of these waveguides is based on the effect of a load waveguide to achieve lateral confinement of light [9]. ICP-RIE process has been optimized for RTP to obtain low loss ridge waveguides with low roughness. The modal sizes and propagation of the fabricated waveguides were measured and compared to the simulated values. The characterization was carried out at 1.5 μm which is the wavelength of interest in telecommunication systems.

II. WAVEGUIDE FABRICATION

A. Substrate growth by TSSG, epitaxial and cladding growth by LPE

RTP melts incongruently below its melting temperature at 1443 K. Therefore, under normal pressure, single crystals cannot be directly grown from the melt. Hydrothermal techniques and high temperature solutions have been successfully reported to grow these crystals. We grew RTP single crystals by using high temperature solution methods, using the top seeded solution growth (TSSG)/ slow cooling technique.All the growth experiments were performed in a vertical tubular single-zone furnace. The solution composition was chosen taking into account the RTP primary crystallization region in solutions with 20 mol % WO_3 [10]. The solution composition used was Rb_2O-P_2O_5-TiO_2 -WO_3= 44.24-18.96-16.8-20 (mol %). In order to reduce the viscosity of the solution, WO_3 has been introduced in the solution The solution was homogenized by maintaining the temperature at about 50-100 K above the expected saturation temperature for 3-5 h. The saturation temperature of the solution was determined by observing the growth/dissolution of the seed in contact with the surface of solution. The supersaturation of the solution was obtained by applying slow cooling to the solution at a rate of 0.1 K/h for the first 15 K and then 0.05 K/h for the next 10-20 K. During the initial stage of growth, the crystal rotation was kept at 60 rpm and as the crystal was growing, the rotation was decreased progressively to 40 rpm in order to maintain the convection pattern. In several experiments, when the crystal dimension in the (001) plane was enough, a pulling rate of 1 mm per day was applied in order to increase the crystal dimension along the ***c*** direction. When the crystal was fully grown, it was slowly extracted from the solution and maintained slightly above the solution surface while the furnace was cooled at 30-40 K/h to room temperature. Finally, the substrates were obtained by cutting the bulk crystal perpendicular to the c- crystallographic direction and polishing it with diamond powder.

The $Rb_{1-x-y}TiYb_xNb_yOPO_4$ epitaxial layers were grown on RTP(001) substrates by Liquid Phase Epitaxial (LPE) method. The epitaxial growth was carried out in a vertical furnace with a wide zone where the temperature differences were practically zero. The solution composition used in these LPE experiments was Rb_2O-P_2O_5-TiO_2-Nb_2O_5-Yb_2O_3-WO_3= 43.9-23.6-20.7-0.45-1.35-10 (mol %). [11]. Careful determination of the saturation temperature of the solution was carried out by measuring the growth/dissolution rate of the crystal seed in contact with the surface of the solution while rotating at constant speed of 60 rpm. RTP substrates were first cleaned by using a mixture of HNO_3/H_2O in the 50/50 ratio in volume for 5 min, followed by dipping in distilled water (5 min), then in acetone (5 min), and finally in ethanol (5 min). The entire cleaning process was carried out with the substrates rotating at 60 rpm. After that, the substrates were slowly introduced into the furnace using a stepper motor drive to avoid thermal shocks and maintain it for 1 h above the surface of solution to obtain thermal equilibrium between the solution and the substrate. Then the substrate was dipped into the solution at a temperature of 1 K above the saturation temperature for 5 min in order to dissolve the outer layer of the substrate. The epitaxial growth was carried out on the RTP substrate at a temperature 3 K below the saturation temperature for 3 h, with the substrate rotating at 60 rpm. After the epitaxial growth process, the sample was extracted slowly from the solution and held a few mm above the solution, while the furnace was cooled down to room temperature at a rate of 25 K/h, to avoid thermal shock.

After that, a cladding layer of undoped RTP was grown by LPE method as mentioned above. Finally, the cladding layer was polished in order to obtain a smooth surface for the deposition of metal mask to be used in ICP-RIE for the microstructuring of the cladding layer. The as-grown RTP single crystal and (Yb,Nb):RTP epitaxial layer grown on polished substrate were shown in figure 1.

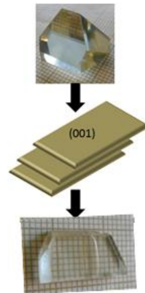

Fig. 1. As grown RTP single crystal, scheme of the cutting process and as grown epitaxy.

B. Pattern design and simulation

The lateral confinement of light in planar waveguide can be introduced by loading a material with different refractive index. A lateral variation of the effective index is induced which depends on the geometry and refractive index of the cladding structured region. As a result, 2D effective index distribution is obtained which is responsible for the lateral confinement of light. The cross-section scheme of the proposed waveguide structure is shown in figure 2.

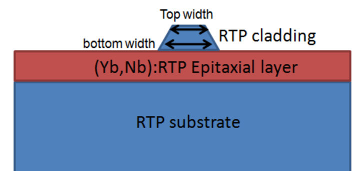

Fig. 2. Cross-section scheme of the proposed waveguide structure.

Different parameters of planar waveguides with cladding structures were simulated with Rsoft beamPro software [12] in order to obtain the optimized parameters for the propagation of fundamental guided optical mode at 1.5 µm as shown in table I. The refractive index values for the undoped RTP and (Yb,Nb):RTP doped crystals at a wavelength of 1.5 µm are: n_x=1.7559, n_y=1.7630, n_z=1.8375 for RTP and n_x=1.7516, n_y=1.7633, n_z=1.8425 for (Yb,Nb).RTP. Thus, Δn_x=-0.004, Δn_y=0.0003 and Δn_z=0.005 ($\Delta n_i = n_{i,epi} - n_{i,sub}$ being i= x,y and z) is the variation of the refractive index, acting RTP and (Yb,Nb):RTP, as substrate/cladding and epitaxial layer, respectively [13]. So, it is important to remark that this refractive index difference allows only guiding in the TM polarization whatever the size of the waveguide but it will be single mode by choosing the appropriate channel waveguide dimensions.

TABLE I.

Parameters for proposed waveguides used in simulation.

Simulation number	Epitaxial layer thickness (µm)	Cladding layer thickness (µm)	Cladding width top(µm)	Cladding width bottom(µm)
a	5	5	15	25
b	5	5	29	35
c	5	5	9.5	15
d	7	5	15	25
e	7	2.5	19	25
f	7	8.5	16.5	25

In accordance to the simulations, the near-field pattern of the modes were obtained and are given in figure 3. The simulation results showed in this figure corresponds to the parameters of table 1. It can be seen that all the stripe loaded waveguides are guiding a single mode with better mode shape and confinement but the mode profile of simulation number 3 is dull and mostly light is lost in the cladding structure, which shows that the dimensions used in this waveguide are not appropriate for guiding the light.

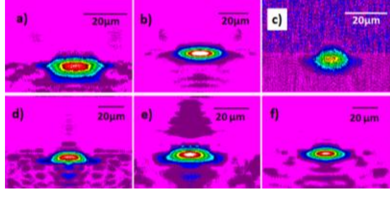

Fig. 3. Simulation results for proposed waveguide at different parameters. The letters a), b), c), d), e) and f) correspond to the simulations with the parameters of table 5.3.

Simulation (b) was further examined from the side view in order to check the penetration of the propagation beam into the substrate or cladding and the losses as shown in figure 4. Figure 4.a) shows the side view of the proposed waveguide. In fig 4 b), it can be observed that there is a small amount of light which penetrate in the substrate depending on the size of the input spot used to couple the waveguide and the total losses also depend on the input beam size. As an example, an input mode of 25 µm and 8 µm in size in horizontal and vertical directions, respectively was used and the total losses obtained were around 0.75 dB.

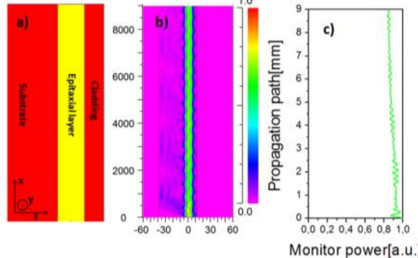

Fig. 4. a) Side view of the proposed waveguide b) Propagation of light in the proposed waveguide c) Variation of launch power in the proposed waveguide.

C. Sample preparation prior to ICP-RIE

A thin layer of (Yb,Nb):RTP was grown on RTP(001) substrate for 2 h and finally polished till 9 µm in order to allow a propagation of fundamental mode at 1.5 µm. Then a cladding layer of RTP was grown over epitaxial layer and polished till 6 µm and the structuring was done in cladding layer without producing any roughness in the epitaxial layer. The cladding layer was grown by following the same procedure as used for the epitaxial layer.

Some test experiments were conducted in order to determine the etching rate of metal layer and RTP with ICP-RIE. We have tried the combination of Al and Cr with different thicknesses. But the combination of Al and Cr at higher layers thickness, for instance 500 nm each was not good; the layers were lifted off during cleaning the sample with acetone. The reason of using the combination of Al and Cr was that, Al showed good adhesion on RTP substrates and Cr has higher selectivity.

The etch rate of Cr is very low and it can work as a perfect hard mask for deep etching but sometimes we were facing some problems with the adhesion of Cr with the sample. It could sustain the tape and scratch test but during cleaning the sample with acetone and ethanol, the layer was removing very fast. In order to ensure the good adhesion of Cr on RTP, we have deposited a thin layer of TiO_2 then progressively decrease the oxygen content in the chamber and moved to Ti. Then started enriching Ti with Cr upto pure Cr. This technique really helped to improve the adhesion of the metal layers which was proved by tape and scratch test.

A thin layer of positive photoresist AZ1505 was spun over the metal layer by spin coating at 5000rpm for 60 s, obtaining a thickness of around 0.5 µm. The sample was then soft baked at 363 K for 30 min. The patterns were transferred on the resist by exposing it by conventional mask aligner and

exposing the sample for 1-2 sec at 350 mW/ cm^2 using a 365 nm wavelength light. After the exposure, the photoresist was developed by dipping it in AZ 726 developer for 45 s. The unwanted parts of the metal layers were chemically etched in order to create a metal mask for ICP-RIE process. Cr layer was etched with MS8 chrome chemical etchant for 3 min. The fabrication process is shown in figure 5.

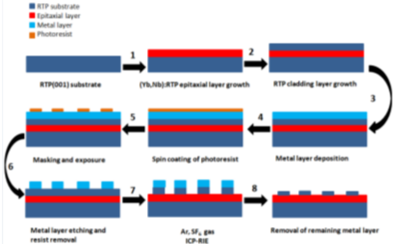

Fig.5. Steps involved in the fabrication of proposed waveguides.

D. Inductively Coupled Plasma Reactive Ion Etching

The preliminary test was performed to determine the etch rates of undoped RTP and Cr metal layer by using Ar(10sccm), SF_6(10sccm), Power=150W, ICP=300W and Pressure=15mTorr. The process was controlled by laser camera with end point feature, which means that the etching process stops when the metal layer with thickness, *d*, is completely removed from the surface of the substrate. The etching rate of RTP and metal layers is shown in table II. As it can be seen that the selectivity, *S*, of Ti-Cr layer combination is relatively higher than Al-Cr layer combination which allows the fabrication of rib waveguides with greater heights. Besides, the achieved etching rate is larger than the ones reported for RTP materials etched by RIE (6.2 nm/min [13]).

TABLE II.
Etch rate and selectivity of metal mask determined by ICP-RIE process.

Etch time[min]	Cr *d* [nm]	Ti *d* [nm]	Al *d* [nm]	RTP Etch rate [nm/min]	Cr Etch rate [nm/min]	S
18	250	10	0	95	14	6.78
30	400	0	400	133	26.66	4.98
45	800	10	0	127	17.8	7.13

After the fabrication process, the samples were examined by environmental scanning microscopy (ESEM) with a FEI Quanta 600, with an acceleration voltage of 20kV at a working distance of 10 mm. Confocal measurements showed a roughness with *rms* values below 8 nm which is very low.
Table III summarizes the dimensions of the obtained waveguides.

TABLE III.
Etched dimensions of the cladding structure.

w_{exp} [μm]	top w_r [μm]	bottom w_r [μm]	Rib height [μm]	*rms* [nm]
20	14.60	21.8	5.75	7.66
25	17.70	25.47	5.43	7.34
30	25.28	31.53	5.70	7.12

w_{exp} = expected width, w_r = real width

In Figure 6, we can observe ESEM images of the channels fabricated by ICP-RIE in a RTP cladding, using an Ti-Cr mask with designed structures of 30 μm in width. Figure 6.a) shows the cross-sectional view of the sample with epitaxial and cladding layer prior to etching. The etching time was 45 min and the etch depth obtained was around 5.7 μm. Ribs with trapezoidal cross section were obtained in the cladding layer as shown in figure 6.b). As reported previously in [13], the sidewalls have some angle, and this creates the trapezoidal shape in the cladding structure. There are no appreciable defects at the interfaces between the RTP substrate- epitaxial layer and the epitaxial layer-cladding layer. The bottom of the channels is found to be approximately 31 μm in width, while at the top the channels width is around 25 μm.

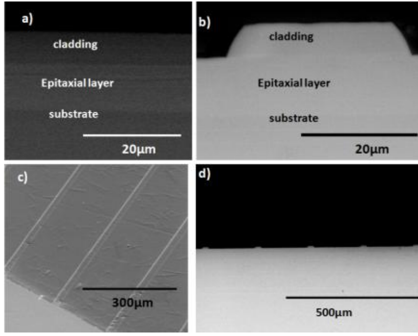

Fig. 6.a) ESEM image of the sample before etching process, b) cross-sectional image of the proposed waveguides.

III. OPTICAL CHARACTERIZATION OF THE WAVEGUIDES

The vertically polarized 1520 nm HeNe laser with a maximum output power of 1mW was coupled to 9 mm long stripe loaded waveguides. The waveguide mode was excited via careful alignment using *xyz* translation stage. To experimentally characterize the propagation mode, we polished the faces perpendicular to the crystallographic ***a*** direction. All the waveguides are single mode in TM configuration. The near field pattern was measured using an IR camera in order to visualize the mode intensity profile at the output of the stripe loaded waveguide; Figure 7. a) shows the near-field pattern of the output mode guided in a channel. The horizontal and vertical fundamental mode field diameters (MFD) at $1/e^2$ intensity (shown in figure 7.c and figure 7.d) were measured to be 26.5 μm and 20.7 μm, along the ***b*** (horizontal) and ***c*** (vertical) directions, respectively. The horizontal fundamental mode field diameter obtained by simulation show an agreement with the experimental results but in case of vertical field diameter it has a contradiction that could be due to big size of coupling mode used in the experiment. Figure 7. b) shows the mode profile of the simulated data with a horizontal and vertical dimensions of 24.72 μm and 12.26 μm respectively.

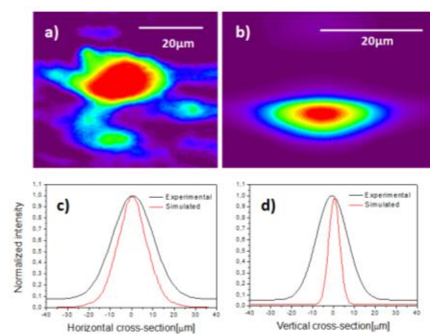

Fig.7. a) Near- field TM mode image of the straight waveguide, b) Simulated TM mode, c) horizontal cross-section of the experimental and simulated guided modes, d) vertical cross-section of the experimental and simulated guided modes.

We have estimated the total transmission losses corresponding to a single pass transmission as L_T= 10log (P_{out}/P_{in}), where P_{out} is the power measured after the output microscope, P_{in} is the power measured before the input microscope objective, then the L_T was around 7 dB in the proposed waveguide. By subtracting the calculated Fresnel and coupling losses from the total insertion loss, the propagation loss can be estimated with a resolution better than 0.37 dB/cm. These values are in lower than previous reported values, published by Choudhary *et al.* [8], in channel WGs fabricated by RIE, in which the transmission losses were around <3.5 dB/cm at 980 nm.

IV. CONCLUSIONS

2D straight channels waveguides have been successfully fabricated by ICP-RIE etching on the RTP cladding in the RTP/(Yb,Nb):RTP/RTP (001) crystals. The cladding and epitaxial layer were grown by LPE. By the use of ICP-RIE versus RIE, the etching time has been reduced and the etch rate increases substantially, and furthermore reducing also the surface roughness of the etched parts. An etch depth of 5.75 microns with a maximum etch rate of 133 nm/min was obtained. Optical waveguiding at a wavelength of 1.5 microns has been demonstrated, with 0.37 dB/cm as propagation loss.

REFERENCES

[1] S. E. Miller, “Integrated optics, An introduction”, *The Bell Sys. Techn. Journal*, **48**, 2059-2068, 1969.
[2] *Towards 2020* – Photonics driving economic growth in Europe**,** Multiannual Strategic Roadmap 2014 – 2020,published by European Technology Platform Photonics21, 2013.
[3] P. A. Thomas, S. C. Mayo, and B. E. Watts, “Crystal structures of $RbTiOAsO_4$, $KTiO(P_{0.58},As_{0.42})O_4$, $RbTiOPO_4$ and $(Rb_{0.465},K_{0.535})TiOPO_4$, and analysis of pseudosymmetry in crystals of the $KTiOPO_4$ family,” *Acta Cryst. B,* vol. 48, pp. 401-407, 1992.
[4] Y. Guillien, B. Menaert, J. P. Feve, P. Segonds, J. Douady, B. Boulanger, O. Pacaud, “Crystal growth and refined Sellmeier equations over the complete transparency range of $RbTiOPO_4$”, *Opt. Mater.* **22**, 155-162, 2003.
[5] Y. S. Oseledchik, A. I. Pisarevsky, A. L.Prosvirnin, V. V. Starshenko, N. V. Svitanko, “Nonlinear optical properties of the flux grown $RbTiOPO_4$ crystal”, *Opt. Mater*. **3**, 237-242, 1994.
[6] L.K. Cheng, J.D. Bierlein, “KTP and isomorphs- recent progress in device and material development”, *Ferroelect.* **142**, 209-228, 1993.
[7] J. Cugat, A. Choudhary, R. Solé, J. Massons, D. Shepherd, F. Díaz, M. Aguiló, “Ar^+ ion milling rib waveguides on nonlinear optical (Yb,Nb): RTP/RTP epitaxial layers”, *Opt Mat. Express,* **3**, 1912-1917, 2013.
[8] A. Choudhary, J. Cugat, K. Pradeesh, R. Solé, F. Díaz, M. Aguiló, H. M. H. Chong, and D. P. Shepherd, “Single-mode rib waveguides in (Yb,Nb):$RbTiOPO_4$ by reactive ion etching,” *J. Phys. D*, vol. 46, pp. 145108, 2013.
[9] J. Martínez de Mendívil, J. Hoyo, J. Solís, M.C. Pujol, M. Aguiló, F. Díaz and G. Lifante, Channel waveguide fabrication technique in $KY(WO_4)_2$ combining liquid-phase-epitaxy and beam-multiplexed fs-laser writing. Submitted to J. Lightwave technology, 2015.
[10] J. J. Carvajal, V. Nikolov, R. Solé, Jna. Gavaldà, J. Massons, M. Aguiló, and F. Díaz, “Crystallization Region, Crystal Growth, and Characterization of Rubidium Titanyl Phosphate Codoped with Niobium and Lanthanide Ions,” *Chem. Mater.*, vol.14, pp. 3136-3142, 2002.
[11] J. Cugat, R. Solé, J. J. Carvajal, M. C. Pujol, X. Mateos, F. Díaz, and M. Aguiló, “Crystal growth and characterization of $RbTi_{1-x-y}$/ $RbTiOPO_4$(001) non-linear optical epitaxial layers,” *CrystEngComm.*, vol.13, pp. 2015-2022, 2011.
[12] RsoftBeamPROP software, Synopsys Optical solutions, v2013.12.
[13] M. A. Butt, R. Solé, M. C. Pujol, A. Ródenas, G. Lifante, A. Choudhary, G. S. Murugan, D. P. Sheperd, J. S. Wilkinson, M. Aguiló, and F. Díaz. Fabrication of Y-Splitters and Mach-Zehnder Structures on (Yb,Nb):$RbTiOPO_4$/RTP(001) epitaxial layers by Reactive Ion etching. Accepted in J. Lightwave technology, 2014.

Paper IV

"Channel waveguides and Mach-Zehnder structures on $RbTiOPO_4$ by Cs^+ ion exchange"

M. A. Butt, M. C. Pujol, R. Solé, A. Ródenas, G. Lifante, J. S. Wilkinson, M. Aguiló and F. Díaz

Submitted to Optical Materials Express, 2015

Channel waveguides and Mach-Zehnder structures on $RbTiOPO_4$ by Cs^+ ion exchange

M. A. Butt[1], M. C. Pujol[1], R. Solé[1], A. Ródenas[1], G. Lifante[2], J. S. Wilkinson[3], M. Aguiló[1] and F. Díaz[1]

1. Física i Cristal·lografia de Materials i Nanomaterials (FiCMA-FiCNA) andEMaS, Universitat Rovira i Virgili (URV), Marcel·lí Domingo 1, E-43007 Tarragona, Spain
2. Departamento de Física de Materiales, Universidad Autónoma de Madrid 28049 Madrid, Spain
3. Optoelectronics Research Centre, University of Southampton, Southampton, SO171BJ, United Kingdom
** mariacinta.pujol@urv.cat, rosam.sole@urv.cat*

Abstract: Cs^+ ion exchange in $RbTiOPO_4$ and (Yb,Nb):RTP/RTP(001) has been used to locally increase the refractive indicesfor waveguide circuit fabrication. Ti maskswere fabricated on RTP samples by conventional photolithography. Cs^+exchange was done using a $CsNO_3$ melt at 698 K during 2 h. Elemental analysis confirms an exponential Cs^+ profile with a variable depth. Apparently the Cs^+exchange is disfavored in the doped epitaxial sample. The refractive index variation is higher forn_z than for$n_{x,y}$. Near-field images of the guided modes at 633, 1064 and 1520 nm wererecorded. The optical characterization shows propagation losses of 5 dB/cm at 1520 nm.

©2015 Optical Society of America

OCIS codes:130.2790guided waves; 130.3130 integrated optics materials.

References and links

1. P. A. Thomas, S. C. Mayo, and B. E. Watts, “Crystal structures of $RbTiOAsO_4$, $KTiO(P_{0.58},As_{0.42})O_4$, $RbTiOPO_4$ and$(Rb_{0.465},K_{0.535})TiOPO_4$, and analysis of pseudosymmetry in crystals of the $KTiOPO_4$ family,” ActaCryst. B **48**(4), 401-407 (1992).
2. M. N. Satyanarayan, A. Deepthy, and H. L. Bhat, “Potassium Titanyl Phosphate and its isomorphs: Growth, properties and applications,’’ Crit. Rev. Solid State Mater. Sci. **24**(2), 103-191 (1999).
3. S. Yu, A. I. Oseledchik, A. L. Pisarevsky, V. V. Prosvirnin, N. V. Starshenko, and N. V. Svitanko, “Nonlinear optical properties of the flux grown $RbTiOPO_4$ crystal,’’ Opt. Mater. **3**(4), 237-242 (1994).
4. Y. Guillien, B. Ménaert, J. P. Féve, P. Segonds, J. Douady, B. Boulanger, and O. Pacaud, “Crystal growth and refined Sellmeier equations over the complete transparency range of $RbTiOPO_4$,” Opt. Mater. **22**(2), 155-162 (2003).
5. J. D. Bierlein, D. B. Laubacher, J. B. Brown and C. J. van der Poel, “Balanced phase matching in segmented $KTiOPO_4$ waveguides,’’ Appl. Phys. Lett. **56**(18), 1725-1727 (1990).
6. G. Lifante, *Integrated Photonics: Fundamentals* (Wiley, 2003).
7. T. Suhara and M. Fujimura, *Waveguide Nonlinear-Optic Devices* (Springer, 2003).
8. T. L. Koch, F. J. Leonberger, and P. G. Suchoski, *Handbook of Optics, Integrated Optics* (McGraw-Hill, 1995).
9. J. D. Bierlein, A. Ferretti, L. H. Brixner, and W. Y. Hsu, “Fabrication and characterization of optical waveguides in $KTiOPO_4$,” Appl. Phys. Lett. **50**(18), 1216-1918 (1987).
10. J. D. Bierlein, and H. Vanherzeele, “Potassium titanyl phosphate: properties and new applications,’’ J. Opt. Soc. Am. B,**6**(4), 622-633 (1989).
11. M. G. Roelofs, A. Ferretti, and J. D. Bierlein, “Proton-exchanged and ammonium-exchanged waveguides in $KTiOPO_4$,” J. Appl. Phys. **73**(8), 3608-3613 (1993).
12. L. Zhang, P. J. Chandler, P. D. Townsend, Z. T. Alwahai, and A. J. McCaffery, “Second-harmonic generation in ion-implanted $KTiOPO_4$ planar waveguides,” Electron. Lett. **28**(16), 1478-1480 (1992).
13. N. Yu. Korkishko,V. A. Fedorov, *Ion Exchange in Single Crystals for Integrated Optics and Optoelectronics*
(Cambridge International Science publishing 1999).
14. M. Roth, *Springer Handbook of Crystal Growth.Stoichiometry and domain structure of KTP-Type Nonlinear Optical Crystals.*Chapter 20 (Eds: G. Dhanaraj, K. Byrappa, V. Prasad, M. Dudley, Springer-Verlag Berlin Heidelberg 2010), pp. 691-723.
15. V. D. Kugel, G. Roseman, N. Angert, E. Yaschin, and M. Roth, “Domain inversion in $KTiOPO_4$ crystal near the Curie point,” J. Appl. Phys. **76**(8), 4823-4826 (1994).

16. Jna. Gavaldà, J. J. Carvajal, X. Mateos, M. Aguiló, and F. Díaz, "Dielectric properties of Yb^{3+} and Nb^{5+} doped $RbTiOPO_4$ single crystals," J. Appl. Phys. **111**(3), 034106 (2012).
17. J. Cugat, R. Solé, J. J. Carvajal, X. Mateos,J. Massons, G. Lifante, F. Díaz, and M. Aguiló, "Channel waveguides on $RbTiOPO_4$ by Cs^+ ion exchange," Opt. Lett. **38**(3),323-325 (2013).
18. P. U. M. Sastry, M. S. Somayazulu, and A. Sequiera,"Influence of some partial substitutions on conductivity and dielectric behaviour of potassium titanyl phosphate," Mater. Res. Bull. **27**(12), 1385-1392 (1992).
19. J. J. Carvajal, M. C. Pujol and F. Díaz, Springer Handbook of Crystal Growth. High-Temperature Solution Growth: Application to Laser and Nonlinear Optical Crystals. Chapter 21 (Eds: G. Dhanaraj, K. Byrappa, V. Prasad, M. Dudley, Springer-Verlag Berlin Heidelberg 2010), pp. 725-757.
20. J. J. Carvajal, V. Nikolov V., R. Solé, Jna. Gavaldà, J. Massons, M. Rico, C. Zaldo, M. Aguiló, and F. Díaz. "Enhancement of Erbium Concentration in $RbTiOPO_4$ by Codoping with Niobium,"Chem. Mater. **12**(10), 3171-3180 (2000).
21. J. Cugat, R. M. Solé, J. J. Carvajal, M. C. Pujol, X. Mateos, F. Díaz, and M. Aguiló, "Crystal growth and characterization of $RbTi_{1-x-y}Yb_xNb_yOPO_4/RbTiOPO_4(001)$ non-linear optical epitaxial layers," CrystEngComm, **13**(6), 2015-2022 (2011).
22. Ytterbium and erbium doped $RbTi_{1-x}M_xOPO_4$ (M = Nb or Ta) crystals. New laser and nonlinear bifunctional materials, Alexandra Peña Revellez, Thesis 2007.
23. J. Guo, B. Raghothamachar, M. Dudley, J. J. Carvajal, A. Butt, M. C. Pujol, R. Solé, X. Mateos, J. Massons, M. Aguiló, F. Díaz, "Effect of doping on crystalline quality of rubidium titanyl phosphate (RTP) crystals grown by the TSSG method," MRS Proceedings, 1698 (2014).
24. V. I. Voronkova, V. K. Yanovskii, T. Yu. Losevskaya, and S. Yu. Stefanovich, "Electrical and nonlinear optical properties of $KTiOPO_4$ single crystals doped by Nb or Sb," J. Appl. Phys. **94**, 1954-1958 (2003).
25. A. Peña, B. Ménaert, B. Boulanger, F. Laurell, C.Canalias, V. Pasiskevicius, P.Segonds, C.Félix, J. Debray, and S. Pairis, "Template-growth of periodically domain-structured $KTiOPO_4$ [Invited]," Opt. Mater. Express, **1**(2), 185-191 (2011).
26. K. S.Buritskii, E. M. Dianov, V. A. Maslov, V. A. Chernykh, and E. A. Shcherbakov, "Measurement of optical anisotropy in KTP:Rb waveguides," Kvant. Electron. **17**(10), 1369–1370 (1990).
27. K. S. Buritskii, E. M. Dianov, V. A. Maslov, S. Tsygankov, V. A. Chernykh, and E. A. Shcherbakov, "Measurement of optical strength of diffused planar Rb:KTP waveguides," Kvant. Electron.**17**(4), 494–495 (1990).

1. Introduction

$KTiOPO_4$ (KTP) and its isostructural $RbTiOPO_4$ (RTP) are well known crystalline dielectric materials with excellent properties for non-linear optical applications. They crystallize in the noncentrosymmetric orthorhombic space group $Pna2_1$and for RTP, the unit cell parameters area=12.974(2)Å, b=6.494(3)Å and c=10.564(6)Å [1]. RTP has similar non-linear optical coefficients to KTP [2], a higher laser damage threshold (~2 times larger than that of KTP) [3, 4], a wide range of wavelength and angular acceptance for frequency doubling, high chemical stability, and low photorefractive damage susceptibility [5]. Another important nonlinear material is $LiNbO_3$ (LN), which is broadly used for integrated optics (IO) [6,7]. RTP has a higher damage threshold than LN and similarly large electro-optic coefficients [8]. Both LN and RTP could be used as platform for various IO electro-optical (EO) applications such as modulators and Q-switches. In general, IO devices interface efficiently with optical fibers and can reduce the cost in complex circuits by eliminating the need for separate and individual packaging of each circuit element.

Depending of the refractive index distribution, waveguides (WG) can be classified into two types: graded-index and step-index WGs. In the literature, different methods of fabrication of graded-index WG, such as ion exchange [9, 10], proton exchange [11], and ion implantation [12], have been successfully used on KTP.

KTP is a classical ionic conductor, and the vacancy assisted one dimensional ionic conductivity is present. It is known that the ionic conductivity of KTP crystals along the [001] direction is significantly higher than along the other crystallographic directions

[13].The highly anisotropic behavior ensures high aspect ratio with low lateral ion exchangeWG, in contrast with LN. Ionic conductivity, directly related to the feasibility of the ion exchange, is favored by the presence of K^+ vacancies and also affected by the c+ or c- surface nature. KTP/ RTP are known ferroelectric materials, with c+ and c- domains. For WG preparation in KTP, the ion exchangebehavior on the c+ surface is different from that on the c- surface. Compared with the c+ face, the index change Δn obtained on the c- face is larger, whereas the exchange depth d is smaller [14]. KTP crystals grown from highly concentrated solutions usually crystallize in the paraelectric phase above the Curie temperature, T_c. The ferroelectric domain structure is formed upon post growth cooling, so that the crystals grown with high temperature growth method result in multi domain structures [14, 15].

Literature related to WG with graded-index in RTP is scarce. Even though the Rb^+ ion is larger than the K^+ ion, RTP is also a conventional ionic conductor [16] and vacancy-assisted one dimensional ionic conductivity is also expected. The ionic conductivity of RTP along the [001] direction is lower than that of KTP, but also higher than the ionic conductivity along the other directions [16]. This difference in ionic conductivity between KTP and RTP is due to the different ionic radii of Rb^+ and K^+. The higher ionic radius of Rb^+ contributes to a decrease in its mobility through the channels along the ***c***direction of the crystal lattice. In any case, the ionic conductivity of RTP along ***c*** direction is high enough to allow Cs^+exchange into the RTP crystal lattice with concentrations high enough to allow the formation of optical WGs with vertical channel walls parallel to the polar [001] axis.For anideally controlled ionexchange process it is necessary to know the distribution of c+/c- ferroelectric domains. In RTP, the $T_c$covers the range from 1043 to 1073 K and the growth temperature used in the TSSG-SC technique in self-flux is usually around 1173 K; so RTP crystals are also obtained in the paraelectric phase.Recently, Cs^+ ion exchange channel WGs on RTP have been reported [17]. Cs^+ ions were used for the exchange process because they produce an increase in the refractive index and its ionic radius is similar to the radius of Rb^+. Up to now, no exchange on (Yb,Nb) doped RTP epitaxial layer has been described. It is known that the doping with Nb^{5+}increases the ionic conductivity in KTP [18] due to the increase of vacancies at the K^+ sites. Also in RTP, Nb^{5+} doping increases the ionic conductivity. However, the doping couple (Yb,Nb) doesn't change the ionic conductivity along the***c*** direction in comparison with RTP, but interestingly it increases significantly the ionic conductivity along ***a*** crystallographic direction [16], so the (Yb,Nb) codoping is not expected to favor the unidirectional exchange process.

The motivation of the current work is to demonstratethe Cs^+exchange process for fabricating integrated optic devices such asY-splitters and Mach-Zehnder structures (MZ) on RTP (001) substrates and (Yb,Nb):RTP epitaxial layers, and to optically characterize the WG structures obtained.

2.Experimental section

Substrate growth:RTP single crystals were grown by applying theTop Seeded Solution Growth-Slow Cooling (TSSG-SC) technique[19].A vertical tubular single zone furnace was used in all growths experiments. The solution weighed around 200g and its composition was Rb_2O-P_2O_5-TiO_2-WO_3=44.24-18.96-16.8-20(mol%), located into the RTP primary crystallization region in solutions with 20 mol% WO_3 [20].The WO_3 has been introduced in the solution to decrease its viscosity and thus favors the crystal growth. The starting precursors were Rb_2CO_3 (99%), $NH_4H_2PO_4$ (99%), TiO_2 (99%) and WO_3 (99%). The homogenization of the solution was performed at 50 K above the

expected saturation temperature for a few hours. The saturation temperature was determined by measuring the apparent no growth/no dissolution in a***c*-oriented-seed RTP crystal in contact with the center of the solution surface with a micrometer. The saturation temperature of the above RTP solution composition is around 1163 K. Supersaturation was created by applying a slow cooling rate of 0.1 K/h for the first 15 K and then 0.05 K/h for the next 10-20 K. Rotation was applied to the crystal, starting at 60 rpm in the initial steps of growth and as the crystal was growing, the rotation was decreased progressively to 40 rpm in order try to maintain the convection pattern. In several experiments, when the crystal dimension in the (001) plane was enough, a pulling rate of 1 mm per day was applied in order to increase the crystal dimension along the ***c*** direction. When the crystal was fully grown, it was slowly extracted from the solution and maintained slightly above the solution surface while cooled at 30-40 K/hto room temperature. The crystals obtained were colorless and transparent, without macroscopic defects and with well-defined morphology as can be seen in the Figure 1.Substrates of 1.5 mmthickness werecut from RTP single crystals as plates parallel to the (001) plane and then polished resulting in an average surface roughness of 15 nm.

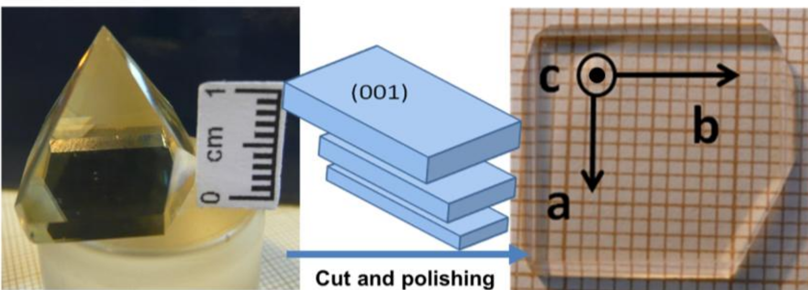

Fig.1. RTP bulk single crystal grown by TSSG-SC and a cut and polished RTP(001) oriented substrate.

Epitaxial layer fabrication: Epitaxial layers of (Yb,Nb):RTP/RTP(001) were grown by liquid phase epitaxy (LPE) [21].The solution composition used for LPE experiments was Rb_2O-P_2O_5-TiO_2-Nb_2O_5-Yb_2O_3-WO_3= 43.9-23.6-20.7-0.45-1.35-10 (mol %). The reagents used were the same as in the growth of substrates, additionally, Yb_2O_3 (99.9 %) and Nb_2O_5 (99.9 %) were used for doping. Cylindrical crucibles of 25 cm^3 were filled with about 95 g of solution. A well-isolated vertical cylindrical furnace was used, and the crucible was located in a central region of the furnace to obtain a zero vertical thermal gradient in the solution. The solution was homogenized by maintaining at temperatures above the saturation temperature and the determination of the saturation temperature was performed as described above for bulk crystal growth. The RTP(001) substrates were cleaned before introducing them into the solution, whichinvolved the immersion of the substrate in a mixture of HNO_3/H_2O at a 50/50 ratio by volume for 5 min, followed by dipping in distilled water(5 min), then in acetone (5 min) and finally in ethanol (5 min) with a rotation of 60 rpm. After that, the substrates were slowlyintroduced into the furnace using a stepper motor drive to avoid thermal shocks. Before dipping the substrate into the solution, it was held at a few mm above the surface of the solution for at least 1 h in order to obtain thermal equilibrium between the solution and the substrate. Then, the substrate was dipped into the solution at a temperature of 1 K above the saturation temperature for 5 min in order to dissolve the outer layer of the substrate. Supersaturation was created by decreasing the temperature 3 K below the

saturationtemperature, also rotating at 60 rpm. The growth temperatures were around 1045 K. After 3 h of growth, the sample was extracted very slowly from the solution and held a few mm above it, while the furnace was cooled down to room temperature at a rate of 25 K/h.

Waveguide pattern design: The designs of the waveguide patternsare shown in Figure 2. The first consists in a symmetric single mode Mach-Zehnder (MZ) design (Figure 2(a)) without any geometrical path length difference between the two arms and with two identical symmetric Y-structures, the first one acting as a splitter and the second one acting as a combiner. The Y–junction design is based on an S-line pattern, to give low bending losses and a large enough separation between the two arms to minimize the evanescent coupling between the two branches. The long length of the branches is desired for incorporation of electrodes for electro-optic modulation.9mm length MZstructures with radius of curvature rangingfrom 50 to 80 mm were designed. Figure 2(b), shows the bentWGdesign based on the same parameters as that of MZ, intended to give additional information on the losses in the MZ waveguide bends. The set of MZs were designed with a length of 9 mm with a separation of 38-42 μm between two arms which gives evanescentcoupling free propagation and large radius of curvature provides smooth bend for minimum bending losses. Figure 2(c), shows a straight WGdesign included in the photolithographic mask to aid alignment and troubleshooting. The width, *w*, of the channels has been fixed to 6 μm. The geometrical parameters of the designs are given in Table 1.

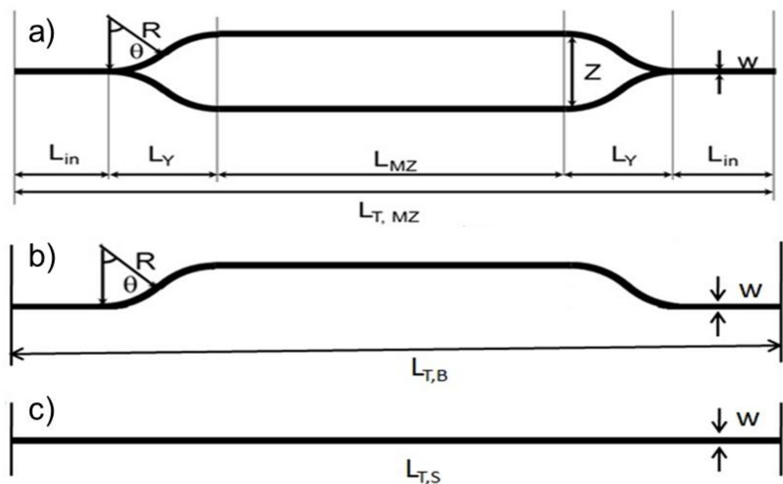

Fig. 2. Pattern design of (a) MZ, (b) S-bend WG, (c) straight WG.

Table 1. Geometrical parameters of the designs.

	L_{in}	L_Y	L_{MZ}	$L_{T,MZ}$	Z	R	$L_{T,B}$	$L_{T,S}$
Dimensions [μm]	1000	2000	3000	9000	38-42	50,000-80,000	9000	9000

Mask preparation: In order to fabricate a dark field mask, a commercially available glass plate coated with chromium and photoresist was used and designs were written on the photoresist with the help of laser lithography. After developing the exposed parts, the designs were transferred on the Cr mask by etching it with commercially available MS8 chrome etchant. This dark field mask in turn was used to transfer the patterns on the RTP samples. This mask contains the patterns of straight WG, S-bend WG and MZs. For the preparation of a hard mask on the RTP samples, a 200nm-thick Ti layer was sputtered onto the RTP at a rate of 0.7Å/sec with DC power of 200W using an AJA sputtering system. A layer of photoresist (AZ 1505 from Microchemicals) was then spin-coated onto the Ti-RTP sample and designs were transferred into the resist by using the dark field mask described above using conventional photolithography on an MG 1410 mask aligner. After developing the exposed parts, the designs were transferred into the Ti mask by etching with H_2O_2:NH_4OH in a 2:1 molar ratio.

Ion exchangeprocess: The ion exchange process was conducted in a vertical tubular single zone furnace. The crucible filled with $CsNO_3$ was placed in the furnace where the temperature gradient was almost zero. The sample was previously heated in the furnace to obtain the thermal equilibrium with the melt and then immersed to a depth of 6 mmdepth (the plane of the sample is parallel to the surface of the solutionhorizontally) in a $CsNO_3$ salt melt maintained at 698K for 2h and rotated at 40rpm in order to obtain a good homogeneity in the liquid. Finally, the sample was slowly extracted from the melt and cooled down at 25K/h in order to avoid thermal stress.Provided that the ion exchange processing temperature remains at 698 K, theexchange process does not introduce any detectable surface defects. The steps for the sample fabrication process are shown in Figure 3.

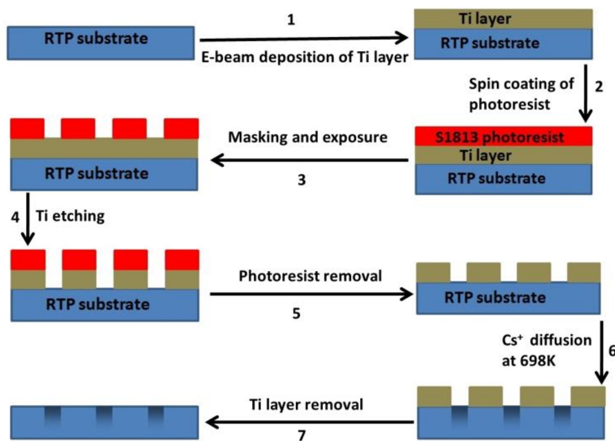

Fig. 3.Steps for the fabrication of the Cs^+ion exchangeWG in RTP.

In this work, Cs^+-exchange RTP WGs were fabricated along three different crystallographic directions (see table 2). For future applicationsinsecond harmonic generation doubling (SHG) in RTP and self-frequency doubling (SFD) in Yb-doped RTP, the straight channel WG propagation directions werechosen to be parallel to the direction of type II ($e^{\omega}+o^{\omega}\rightarrow e^{2\omega}$) phase matching for 1.05 μmwavelength.These directions areparallel to the [180] direction in RTP (θ=90º, φ=76º) and along [120] direction (θ=90º, φ=45º) in (Yb,Nb):RTP as described in ref. [22]. On a second RTP sample, the straight, S-bend and MZWGswere fabricated along the ***b*** crystallographic direction, in which the sample had the longest dimension. All the samples were fabricated under the same conditions. Table 2 summarizes the description of the fabricated WGs.

Table 2. Description of the fabricated WGs.

Sample	WG [uvw] propagation direction	WG types
RTP(001)	***b***	Straight,S-bend,MZ
(Yb,Nb):RTP/RTP(001)	[120]	Straight WG
RTP(001)	[180]*	Straight WG

*the angle between the ***a*** and [180] is 76º.

Modal characterization: The end faces perpendicular to the channels were polished in the three different samples, to image the near field intensity distribution of the guided modes. A 20X microscope objective (NA=0.4) was used to couple the light into the input side of the devices and images were collected with a visible camera through a 20X microscope output objective (NA=0.4). Straight WGs fabricated along the [180] direction were characterized at three different wavelengths: 633, 1064and 1520 nm using HeNe and diode lasers.

Loss evaluation: In order to estimate the propagation losses of the channel WGs, the fundamental mode was excited in the channel using an x-y-z stage. A 20X microscope objective was used to collect the transmitted light. The beam power was measured before the input microscope objective as well as after the output microscope objective. The expression applied to estimate the total insertion losses, L_I, was the corresponding to the single pass transmission method,

$$L_I = -10*\log_{10}(P_{wg}/P_{no\text{-}wg}), \quad (1)$$

Where P_{wg} is the power measured after the output microscope objective with the WG inserted, and $P_{no\text{-}wg}$ is the power measured with both input and output objectives aligned but without the WG. The Fresnel losses L_{Fr}, coupling losses L_C, and the propagation losses L_{Prop}, are the terms whose summation is assumed to give the total transmission insertion losses, $L_I=L_{Fr}+L_C+L_{Prop}$. Coupling losses were evaluated by calculating the overlapping integral of WG output modes and input objective focal spot intensity distributions.

3. Results and discussion

RTP bulk crystal domain map: We have studied the ferroelectric domain structures in an RTP bulk single crystal. The variety of the domain boundaries depends directly on the growth sector number, the kinetics of growth of them, and then directly from the growth method and composition of the flux used for growth [14]; so the description here is for the crystals grown as described before. Two single crystals have been cut in slices perpendicular to the ***c*** crystallographic direction; the resulting plates have been submitted to selective chemical etching in a 2:1 (mol ratio) solution of KOH: KNO_3 for 30 min at 353Kto visualize the domains. It is known that molten salts containing hydroxide attack the negative face (c^-), while the positive face is left essentially untouched.

Roth [14] reported the growth sectors present in KTP and RTP crystals. As can be seen in Figure 4, mainly in the plates perpendicular to ***c***direction, there are four main growth sectors, displayed and labelled trough the developed faces in the morphology, the {201} and the {011}sectors, as observed before [23]. In KTP it has been reported that these two sectors are usually monodomain; however as can be observed in Figure 4, it seems that in RTP the {201}has grown as monodomain, but the {011} sector is multidomain. The domain present in the {201} sector has a domain boundary coincident with the edge boundaryof the growth sector, and can be labelled as a full-size edge; but the small domainswith irregular shapelocated inside the {011} growth sector, theypresent intra-sector domain boundaries dispersed type [14].

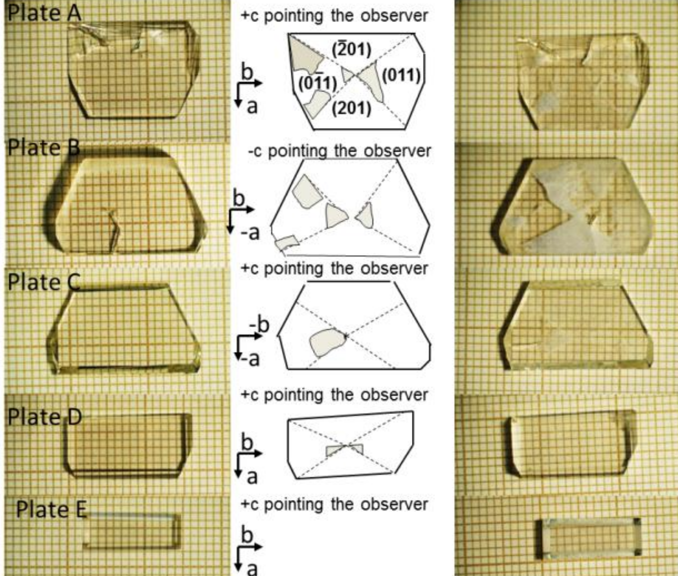

Fig. 4. Cut and polished plates of RTP from a single RTP bulk single crystal, on the left, before the wet chemistry attack, on the right after the wet chemical attack. The attacked parts have been highlighted to help to visualize them.

As no reversal domain technique has been applied to our RTP (001) cut samples, it can be predicted that along the diffused channelparallel to the ***b*** crystallographic direction

and [180] direction, there can be different ion exchangebehavior, because more probably the channel is travelling along different ferroelectric domains.

The epitaxial doped samples are also grown over the Curie temperature (it is expectedthat the T_c is decreased with the presence of Nb^{5+} [24]), so they are grown as paraelectric samples and no transfer of the domain structure of the substrate can be done [25]. In these samples, the transition from paraelectric phase to ferroelectric phase is done through the cooling period. In this case, as the samples are grown by LPE method on the (001) face, which is not a natural face, a ferroelectric multidomain is also expected [25].Figure 5 shows an epitaxial sample after the wet etching. As can be observed, it is multidomain, as expected.

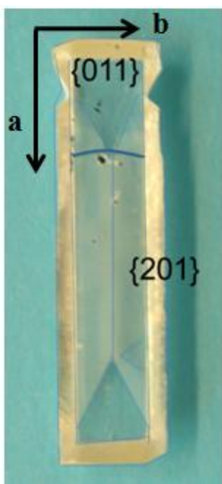

Fig. 5.(Yb,Nb):RTP/RTP(001) epitaxial layer after wet etching.

Ion exchange results: The exchange of Cs^+ as a function of the depth in the RTP samples was measured by electron probe microanalysis (EPMA) with a JEOL JXA-8230 electron microprobe instrument in thewavelength dispersive mode. The accelerating voltage was 15 kV and the beam current 20 nA. The standards used were RTP for Rb, Ti, P and O measurements and CsI for Cs measurement. The analyses were made using the LαX-ray lines for $Rb^+$and Cs^+ and Kαlines for Ti, P and O. The measurements of Rb, Ti, P and O were performed for duration of 10 s and for 30 s in the case of Cs^+. The matrix effect was corrected using the CITZAF procedure.
Figure 6 shows the Cs^+ concentration in weight per cent as a function of the distance from the crystal surfacein three different channels in the RTP and two other channels in a (Yb,Nb):RTP epitaxial layer. As can be observed,there's no reproducibility of the exchange in the different channels, whichmay be due to each channel being located in a different crystal growth sector, and then, different ferroelectric domains. It can be also observed that the quantity of Cs^+ introduced in RTP is larger than in the doped (Yb,Nb):RTP. This may be expected due to the similar or lower ionic conductivity when RTP is doped with Yb and Nb [16]. In Gavaldà*et al.*, the Nb content of the sample was larger than in the epitaxial sample reported in this work, and the ytterbium concentration was similar; and it was observedthat the couple (Yb,Nb) has similar ionic conductivity than RTP along ***c***, but when compared with single doped Nb samples, the

codoping(Yb,Nb) decreases the ionic conductivity along ***c***, so the tendency observed in our samples, is in agreement with the reported tendency of the ionic conductivity. Generally, the Cs^+ concentration decreases with depth and the exchange region is as minimum 6-7 μm.

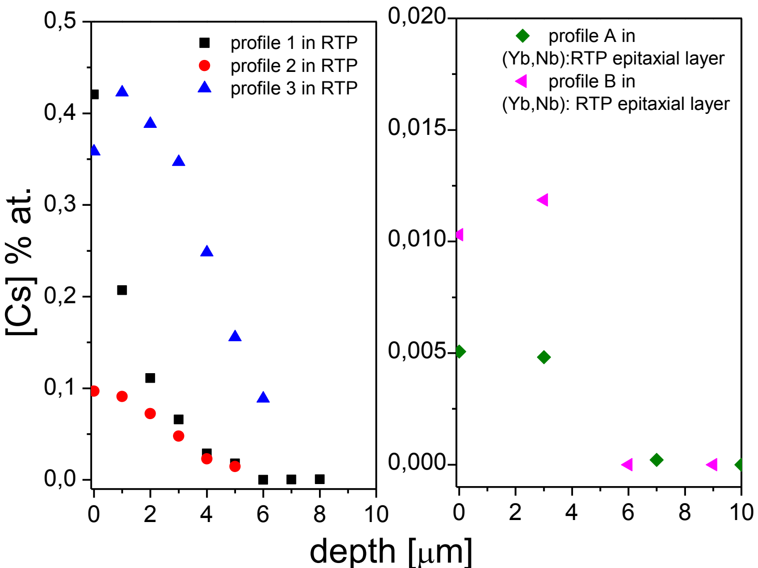

Fig. 6. Cs concentration in the channel as a function of the depth in the RTP substrate and (Yb,Nb):RTP epitaxial layer.

To determine the width of the exchanged channels, we observe the channelsby ESEM,after the exchange process. Figure 7 shows the ESEM images. It can be observed that Ti mask layer was removed from the edges of the WG allowing the Cs^+ ions to diffuse in these parts which in turn forms a wider dimension of WG than expected. It can also be seen that the part of the substrate which was directly exposed to the melt shows some chemical etching effects. These inhomogeneities in the channel width along the WG can scattering when light propagates along it.

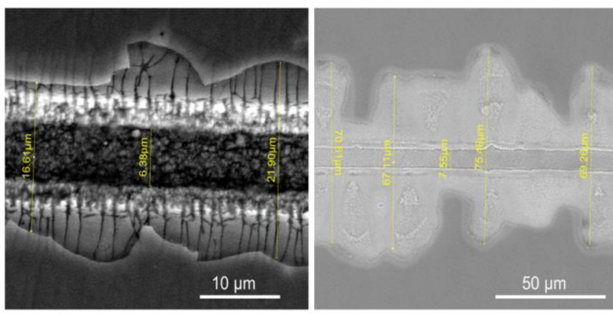

Fig.7. ESEM images of the top view of (a) Cs:RTP(001) coated with a patterned Ti layer (b) Cs:(Yb,Nb):RTP/RTP (001) sample coated with a patterned Ti layer.

Modal characterization In the straight, S-bend and MZ WGs realized in RTP (001),light at a wavelength of 633 nm was only guided in the TM polarization. Figure 8(a), shows the mode intensity profile of the guided light in a straight WGwith mode field diameters (MFD, at $1/e^2$ intensity)of 43 μm x 22 μm for the horizontal and vertical profiles, respectively. Figure 8(b) shows a profile for the guided light in an S-bend WG with mode field diameter (MFD) dimensions of 33 μm x 18 μm for the horizontal and vertical profiles, respectively. Figure 8(c) shows a profile of a MZoutput with a MFD of 52 μm x 26 μm of horizontal and vertical profiles, respectively. In the same sample straight, S-bend and MZWGs were measured; in the WGs it was only possible to observe guiding in the TM configuration at 633nm.

The MFD were in the range from 30-50 μm in the horizontal and 20-25 μm in the vertical directions, respectively. A correlation can be found between the horizontal dimension of the WGwith the sizes of the mode in horizontal dimension, observing at the ESEM images of the "diffused region"(as an example see Figure 7).Inprevious work where the Cs^+exchange was also done in a channel along the ***b*** direction in a RTP (001) substrate with the same experimental conditions [17], the size of the modes for guided light at 633 nm, was 9.7μm x 7.5μm, horizontal and vertical dimensions, respectively, despite the observed exchange depth being around 20 μm.

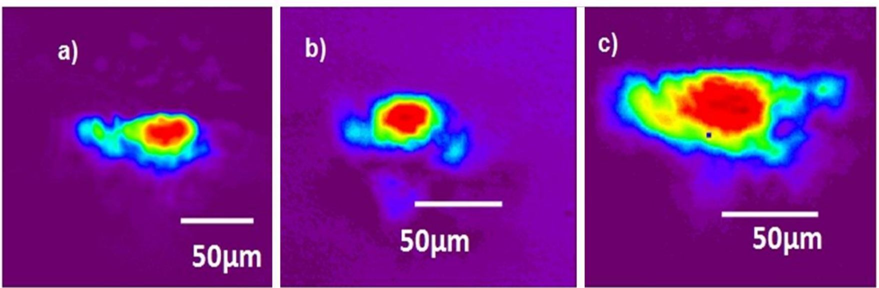

Fig.8.(a) Near field mode intensity profile from a9mm long straight WG (b) of the output guided modes in a 9 mm long S-bend WG, (c) of the output guided mode in 9 mm long MZ at 633 nm.

Straight WGs fabricated along the [120] directionin RTP(001) were characterized using the same optical apparatus as described above with wavelengths of 633 nm, 1064 nm and 1520 nm in the TE and TM polarizations. The near field mode intensity profiles for the straight waveguides are shown in Figure 9.

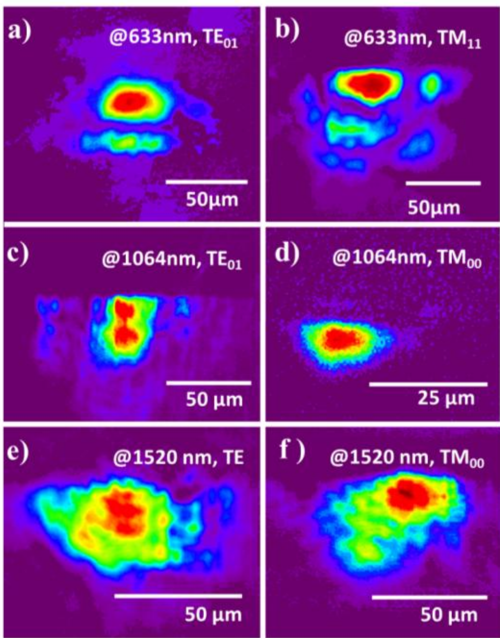

Fig. 9.(a) Near field image of the TE_{01} mode at 633 nm of a straight WG, (b) Near field image of TM_{11} mode at633 nm of a straight WG, (c) Near field image of the TE_{01} at 1064 nm of a straight WG, (d) measured near field image of the TM_{00} at 1064 nm of a straight WG, (e) Near field image of the TE mode at 1520 nm of a straight WG, (f) Near field image of the TM_{00} mode at 1520 nm of a straight WG.

It can be observed that almost all the WGs are multimode and support more modes at shorter wavelengths as expected. The successful guidance in both polarizations may allow the generation of SHG by type II configuration in future applications. Comparing the WGs fabricated in RTP along ***b*** and along [180], we can highlight that the guided modes are not similar, due to the different index contrast produced by the different Cs^+ concentration profiles. Further, for this last sample, we have observed the TE_{01} and TM_{11} modes at 633 nm, which means that this WG can support at least 2 TE modes and 4 TM modes indicating that $\Delta n_{(001)\ plane} << \Delta n_z$.In previous works, Bierlein and Vanherzeele (1989) [10], in the WG fabricated by ion exchange in KTP, reported that the obtained Δn was isotropic ($\Delta n_x=\Delta n_y=\Delta n_z$), however later Buritskii*et al.* [26,27] determined that in the case of Rb^+ diffused KTP WG, the $\Delta n_x \sim 2\ \Delta n_z$.

Straight WGs were fabricated by Cs^+exchange on (Yb,Nb) doped epitaxial sample RTP in order to examine the effect of (Yb, Nb) doping ions on Cs^+exchange. Cs:(Yb,Nb):RTP/RTP(001) straight WGs fabricated along [120] were characterized as described above at 633 nm. In this case light was only confined and guided in the TM polarization. The near -field mode intensity profiles of a straight WG are shown in Figure 10.

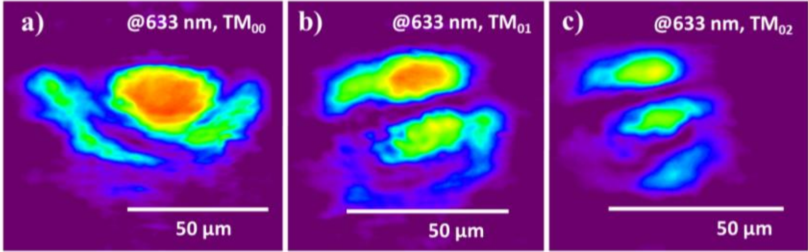

Fig.10. TM modes of straight WGs fabricated on Cs^+ exchanged (Yb,Nb):RTP/RTP(001) along the [120] direction.

When comparing the guiding properties of the Cs diffused sample in RTP with that in the (Yb,Nb):RTP, it can be inferred that there is a larger refractive index contrast in the RTP samples (in agreement with the EPMA measurements), in which guiding has been observed in both polarizations, TE and TM; also the TM_{11} mode has been observed, implying that the waveguide supports a minimum of 5 modes.

Table 3. Losses evaluation in Cs^+ exchanged WGs.

Sample	λ [nm]	Pol.	WG	[uvw]	L_C [dB]	L_{Fr}[dB]	L_I [dB]	L_{Prop}[dB /cm]
RTP(001)	633	TM	Straight	***b***	10.0	0.9	22.6	11.3
	633	TM	S-Bend	***b***	8.1	0.9	23.4	15.8
	633	TM	MZ	***b***	11.5	0.9	21.7	10.4
	633	TE	Straight	[180]	7.5	0.7	14.5	5.7
	633	TM	Straight	[180]	7.0	0.7	25.2	15.9
	1064	TE	Straight	[180]	5.9	0.7	27.3	18.8
	1064	TM	Straight	[180]	1.4	0.7	30.9	26.1
	1520	TE	Straight	[180]	11.4	0.7	19.3	6.6
	1520	**TM**	**Straight**	**[180]**	**10.6**	**0.7**	**16.8**	**5.0**
(Yb,Nb):RTP/RTP(001)	633	TM	Straight	[120]	2.8	0.9	21.8	15.5

Loss calculation of the samples: Using the expression (1), we estimated an upper limit on the propagation losses of themeasured TM and TE guided modes. For the sample with all designs, we have evaluated the total losses, and they are summarized in Table 3. In all WGs, propagation lossesare around 15-30dB, rather large. The contribution to the total losses due to the S-bend and Y-splitter cannot be distinguished due to the large deviation in the loss measurements. As described above, the waveguide width varies strongly along the waveguides, due to the different ferroelectric domains along the WG and the over etching of the Ti masks, resulting in these rather high losses and large variation of values.

Conclusions

In summary, waveguides based on Cs^+exchangein $RbTiOPO_4$(001) and (Yb,Nb):$RbTiOPO_4$ have been fabricated in different configurations: straight, S-bendand MZs. The Cs^+exchange profiles achieved are not reproducible in a single sample due to

the presence of different ferroelectric domains. The Cs^+exchange is favored in the undopedRTP(001) samples when compared with doped epitaxial (Yb,Nb):$RbTiOPO_4$/RTP(001). All waveguides confinedlight, with the observed near field mode intensity distributions larger than expected, taking into account the measured diffused region. High total losses were obtained due to scattering and microbending effects generated by the inhomogeneitiesalong the Cs^+ exchanged region.

Acknowledgments This work was supported by the Spanish Government under Projects MAT2011-29255-C02-02, and MAT2013-47395-C4-4-R/1-R, by the Catalan Authority under Project 2014SGR1358. M. Ali Butt thanks the Catalan Government for the FI-DGR fellowship 2012FI-B 00192.

UNIVERSITAT ROVIRA I VIRGILI
NEW PHOTONIC DEVICES BASED ON NLO(NON-LINEAR OPTICAL) CRYSTALLINE WAVEGUIDES
Muhammad Ali Butt